Measurement and On-chip Control of a Niobium Persistent Current Qubit

by

Donald S. Crankshaw

B.S. in Electrical Engineering, University of South Carolina (1996),

M.S. in Electrical Engineering, Massachusetts Institute of Technology (1998)

Submitted to the Department of Electrical Engineering and Computer Science in Partial Fulfillment of the Requirements for the Degree of

Doctor of Philosophy in Electrical Engineering

at the

Massachusetts Institute Of Technology

June 2003

Author .....
Department of Electrical Engineering and Computer Science
May 16, 2003

Certified by .....
Terry P. Orlando
Professor of Electrical Engineering
Thesis Supervisor

Accepted by .....
Arthur C. Smith
Chairman, Department Committee on Graduate Students

Measurement and On-chip Control of a Niobium Persistent Current Qubit

by

Donald S. Crankshaw

Submitted to the Department of Electrical Engineering and Computer Science
on May 16, 2003, in partial fulfillment of the
requirements for the degree of
Doctor of Philosophy

ABSTRACT

The persistent current qubit is a superconducting ring interrupted by three Josephson junctions. Its two quantum states have circulating currents in opposite directions which can be measured by a dc SQUID magnetometer. This work examines a persistent current qubit fabricated in niobium, using Lincoln Laboratory's DPARTS process. Measurements of the niobium qubit show a promisingly high subgap resistance, demonstrate discrete energy levels, and give good estimates of the qubit parameters as fabricated. Although the variances on the qubit parameters are large, it is possible to design a qubit whose parameters are in the quantum regime.

Additionally, we show how the qubit can be integrated with on-chip electronics while taking into account decoherence. A dc SQUID oscillator has been designed which can deliver an oscillating field at 10 GHz without reducing the decoherence time below 1 microsecond. The oscillator is shown to deliver power to the measurement device, although the qubit rotation has not yet been observed.

Thesis Supervisor: Terry P. Orlando
Title: Professor of Electrical Engineering

Acknowledgments

During my time at MIT, a number of people contributed not only to my career here, but to my overall well-being. First, I would like to thank my mother and father, who instilled in me a love of language and a love of science, a hunger for knowledge, and a hope in God.

When I first came to MIT, I worked for Professor Fonstad. While I ultimately decided to pursue a different research area, much of what I learned about MIT, scientific research, and microfabrication came from Professor Fonstad and his students, among them Isako Hoshino, Janet Pan, Henry Choy, Joseph Ahadian, and Joanna London.

For the remainder of my time here, I worked for Professor Orlando on superconductors. Professor Orlando encouraged me to pursue this research and gave me direction, and he has managed my work while not micro-managing it, which is a difficult feat. Enrique Trías and Amy Duwell taught me how to measure Josephson junctions and how to understand them. Ken Segall and Daniel Nakada worked with me to figure out how to measure the qubit, while Lin Tian reasoned out how it should work. Janice Lee, Bhuwan Singh, Bryan Cord, and David Berns are even now learning how to continue my work, and their questions have given me new insights.

Much of the work I did relied upon the assistance of our collaborators. From Delft, I would like to thank Hans Mooij, Caspar van der Wal, and Alexander ter Haar, who performed the first measurements on the qubit and showed us what was necessary to do ours. From Harvard, I would like to thank Michael Tinkham, Nina Markovic, and Sergio Valenzuala. Their dilution refrigerator and their expertise made our low temperature measurements possible. From the University of Rochester, I would like to thank Mark Bocko, Marc Feldman, Jonathan Habif, and Xinxiang Zhou, for their help in designing the RSFQ circuits featured in this work. Finally, I would like to thank the people at Lincoln Laboratory, including Karl Berggren, Jay Sage, and Will Oliver, for their work in fabricating our designs.

The Graduate Christian Fellowship formed the basis for most of my relationships outside of work, and I am grateful to Kevin Ford, Todd Hastings, Steven Mascaro, Debbie Mascaro, and the many others who helped me to grow spiritually as well as academically. I owe an even greater debt to the Hardcore Bible Study in all its incarnations, and to its participants, both old and new, including Jason Heine, Amy Black, Tom Lee, Tim Chow, Mark and Heather McConnally, Pat and Debbie Walton, George and Jane Greco, Tim Finegan, Cynthia Lo, David Chan, and Susan Kern.

Finally, and most importantly, I must thank my God, by whom and through whom all this is possible.

Table of Contents

List of Figures

Chapter 1

Introduction

1.1 Superconducting Quantum Phenomena

At its heart, low temperature superconductivity is a macroscopic quantum phenomenon [1]. Because the vast sea of superelectrons in a superconductor maintains phase coherence, its effects takes place even when billions of superelectrons interact. For this reason, it is a useful system for studying the intersection between quantum and classical mechanics [2-8]. Recent studies of these systems have produced evidence that even a large superconducting ring, on a scale ranging from a few microns to hundreds of microns, can maintain a quantum superposition of states which have 10^9 electrons circulating in the ring [29,30]. These states are sometimes called macroscopic since they require coherence across a large number of particles.

The experiments which show this large-scale quantum coherence are the culmination of many years of research which demonstrated the quantum nature of superconductors [9-16]. The recent interest in quantum computation has invigorated this research, leading to the search for a system suitable for use in a quantum system. The flux quantum systems mentioned above [29,30] must compete with other superconducting quantum systems, including quantized charge states [26,27] and quantized levels in the energy potential of a single Josephson junction [51]. The next step will be to develop one or more of these superconducting quantum systems into a viable quantum bit, or qubit, a quantum system which serves as the fundamental unit of data in quantum computation.

In this thesis, I look at the persistent current qubit, one of the first systems to display superposition of macroscopic states. The focus of this project is to test whether this qubit can be fabricated in niobium, and then to see whether it can be monolithically integrated with superconducting control electronics. To this point most of the superconducting quantum systems have been fabricated in aluminum using shadow evaporation, which produces high quality, small size Josephson junctions, the nonlinear circuit elements nec-

essary for creating superconducting quantum systems. However, using the Josephson junction fabrication process developed by Lincoln Laboratory [45], which has produced niobium junctions of promisingly high quality, we will attempt to produce a superconducting qubit in niobium, which is the predominant material system used for classical superconducting electronics. By producing the qubit in this same material system, we can draw on the collective experience of niobium electronic design to produce complex on-chip control circuitry. This thesis covers both the qubit by itself, and when coupled to an oscillator monolithically integrated with the qubit in this material system.

1.2 Quantum Computation

By exploiting quantum mechanics, quantum computation offers completely new approaches to solving certain computational problems. The most famous examples of these are Grover's algorithm and Shor's algorithm. Grover's algorithm allows an unordered search of N objects to take place in $N^{1/2}$ time [17] as opposed to the usual N time, while Shor's algorithm accomplishes the factoring of a large number of N bits in N^2 time [18] as opposed to $\exp(N^{1/3})$ time. They accomplish these feats by using quantum mechanical properties which allow an exponentially large number of inputs to be processed simultaneously.

The two physical concepts central to quantum computation are superposition and entanglement. It is possible to place a quantum system into a combination of states, so that it is not just in one state or another, it is in a *superposition* of both with some relative phase. A quantum bit, or qubit, may be in the state $\alpha|0> + \beta|1>$ rather than just one of the classical 0 and 1 states. α and β are complex numbers which follow the relation $|\alpha|^2+|\beta|^2=1$. When classically measured, the qubit is found in the $|0>$ state with a probability $|\alpha|^2$ and in the $|1>$ state with a probability $|\beta|^2$. Two classical bits can be combined to form a register, which may hold one of four states: 00, 01, 10, and 11. A register of qubits, on the other hand, can hold all four of those states at once. The power of a quantum computer increases exponentially as you add qubits, as n qubits can represent 2^n states. A qubit register requires *entanglement* as well as superposition. When two quantum systems interact, they become a single quantum system. Consider the register with two qubits.

Entanglement allows the numbers |00> and |11> to be placed in the register simultaneously with the same weight. Without entanglement, the two qubits would be independent, and each would be in a superposition which was one-half |0> and one-half |1>. Measuring the two independent qubits would be just as likely to give 01 or 10 as 00 or 11. If the two qubits are entangled, then the qubits remain interrelated, and measuring the register will produce 00 or 11, not 01 or 10. Measuring one qubit in effect measures all of the entangled qubits, as the quantum state will collapse for all the qubits, and measurements on them in any order will only produce one of the values in the register. In the previous example, each of the numbers had the same probability of being read in the measurement. It is generally not useful to measure a random number (unless we are building a random number generator). Instead, we will be looking for a single answer, which a quantum register will produce if the weight of the solution we want goes to one while the weights of all incorrect values go to zero. Most quantum algorithms start with a large number of inputs of the same probability. In each step, the correct result becomes more probable, while the incorrect results become less probable, so that when the output is read, the correct result is found with a high degree of fidelity.

Numerous physical systems have been put forward as quantum computers, from nuclear spins in a single molecule to charge states in arrays of quantum boxes [19,20]. Any quantum system with at least two states may be used as a qubit in a quantum computer as long as it satisfies five criteria [21,22]. First, it must be possible to prepare the qubit in a desired initial state. Second, it must be possible to coherently rotate it into a precise superposition of the |0> and |1> states, with both the correct weight and the correct phase. Third, it must be possible to measure the qubit and determine its state. Measuring a qubit will project it into the classical state of either 0 or 1. It would take an ensemble measurement to determine the exact weight of 0 and 1 (the values of $\alpha^*\alpha$ and $\beta^*\beta$, respectively), but the only requirement is that the measurement needs to distinguish between the two states. Fourth, one must be able to couple two qubits together in order to entangle them. Finally, the qubit must maintain coherence long enough to perform a calculation. While external and internal sources of noise cause the qubit to continually lose phase information, if the noise is small enough, the quantum computer can still produce useful calculations before it loses too much information. If the quantum computer's decoherence

time is 10^4 times longer than the operation time, quantum error correction algorithms can be implemented to extend the lifetime of the quantum computer indefinitely.

1.3 Superconductors

A superconductor, like the idealized perfect conductor, has no resistance to the flow of electrons. Additionally, superconductors are perfectly diamagnetic, repelling any magnetic field which attempts to penetrate them. This is not true of perfect conductors, which only resist changes in magnetic field. While the lack of resistance makes superconductors interesting enough for use in quantum systems, superconductors are even more promising due to macroscopic quantum coherence. This makes it possible to build macroscopic quantum systems, quantum devices where the measurable quantities are relatively large.

The charge carrier in a superconductor is the superelectron. This consists of a pair of electrons with opposite spins, called a Cooper pair, which couple together through the intermediation of the lattice with a binding energy of 2Δ. Δ is called the gap energy. A Cooper pair has no net scattering, since when one electron scatters, the paired electron scatters in the opposite direction. Electrons will only couple in this manner below a certain temperature, called the critical temperature, which varies for different materials. At any temperature above absolute zero, the superconductor will have both paired and unpaired electrons. The unpaired electrons are quasiparticles, which are at a higher energy than the superelectrons, and there is an energy difference of Δ between the lowest energy quasiparticle and the highest energy paired electron. Generally, no Cooper pair lasts long, and they constantly break apart only to reform between different pairs of electrons.

The superfluid, the whole sea of superelectrons, behaves quantum mechanically. In a superconductor, the entire ensemble of superelectrons may be described by a single macroscopic quantum wavefunction with a phase and amplitude, as in Equation (1-1).

$$\Psi = \sqrt{N^*}\exp(i\theta) \tag{1-1}$$

The amplitude is equal to $\sqrt{N^*}$, where N^* is the density of superelectrons. The superelectron current depends on the vector potential of the magnetic field and on the phase varia-

tion of the wavefunction, as in Equation (1-2).

$$\Lambda \boldsymbol{J}_S = -\left(\boldsymbol{A} - \frac{\hbar}{q^*}\nabla\theta\right) \tag{1-2}$$

Here $\boldsymbol{A}$ is the vector potential and θ is the phase, Λ is from the first London equation and q^* is the charge of the superelectron. The vector potential is defined as $\nabla\times\boldsymbol{A}\equiv\boldsymbol{B}$, where $\boldsymbol{B}$ is the magnetic field. This does not uniquely define the vector potential (any value $\nabla\chi$ may be added to $\boldsymbol{A}$ without altering $\boldsymbol{B}$), but neither is the phase uniquely defined. These gauge variations do not affect any physical measurables as long as we deal with them consistently. A sharp phase difference can develop through a break between two superconductors, but for any solid piece of superconductor, any variation in it must be accompanied by a flow of current or a change in the vector potential, $\boldsymbol{A}$. Consider the phase difference around a loop of superconducting material. By definition, the vector potential traced around a loop is equal to the magnetic flux penetrating it. If one can trace a path around the superconducting loop along which no supercurrent flows--which is often the case, as the current usually flows at the edges of the superconductor and there is a zero current path along its center--then the phase drop around the loop is proportional to the amount of magnetic flux penetrating the loop. However, a phase difference in a loop would imply that the starting and ending point had two different phases, which is not allowed unless the phase difference is a multiple of 2π, since only then would $\exp(i\theta)$ be identical for both values. This requires flux quantization, where flux penetrating a closed superconducting loop must be a multiple of the flux quantum, Φ_0, the amount of flux which causes a full 2π drop in the quantum wavefunction's phase. Φ_0 is equal to $h/2e$, Planck's constant divided by the charge of a superelectron. The superconductor maintains this quantization by developing a current around the loop, along the edges of the superconductor, which either adds or subtracts flux from the total magnetic flux penetrating the loop until it is an inte-

gral number of flux quanta.

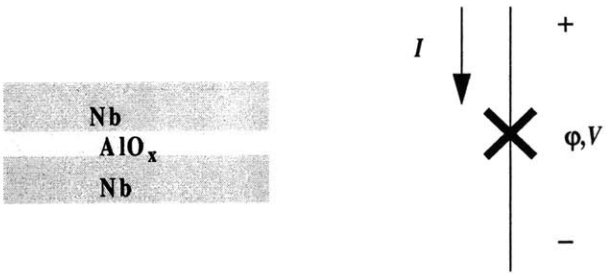

FIGURE 1-1. A Josephson junction. (a) The physical representation of two superconducting electrodes (Nb) separated by an insulator (AlO_x) and (b) The circuit symbol showing current, phase, and voltage.

Figure 1-1 shows a Josephson junction, a small insulating break between two superconductors across which a phase drop can develop. These junctions have a number of interesting properties. First, superelectrons can tunnel across the junction without seeing a resistance. The supercurrent which flows through a Josephson junction is equal to $I=I_c \sin \varphi$. I_c is the critical current, the maximum current which can flow through the junction without breaking up Cooper pairs, while φ is the gauge-invariant phase difference between the superfluid wavefunctions on either side of the insulator, as in Equation (1-3).

$$\varphi = \theta_2 - \theta_1 - \int_1^2 \boldsymbol{A} \cdot \partial \boldsymbol{l} \qquad \textbf{(1-3)}$$

The vector potential once again plays a role, although this effect is rarely significant unless a great deal of magnetic flux penetrates an insulator. The voltage across the junction is proportional to the rate at which the phase changes, or $V=(\Phi_0/2\pi)d\varphi/dt$. Since the junction consists of two conducting plates separated by an insulator, it has a capacitive structure that obeys the relationship $q=C_jV$, where q is the charge on the junction and C_j is the junction capacitance. This capacitance is in parallel with the Josephson element, the conceptual device which follows the Josephson relation. At low currents, the junction looks like an inductor since the rate at which the current changes depends on its voltage. This Josephson inductance has a value of $L_J=\Phi_0/2\pi I_c$. Current can also flow through the junction normally, when normal electrons (quasiparticles) tunnel across the barrier, which acts as a resistance. This can be modeled by a resistor in parallel with the capacitor and

supercurrent elements of the junction, which gives the Resistively-Capacitively-Shunted Junction (RCSJ) model shown in Figure 1-2. The resistance varies depending on the bias of the junction. When the current flowing through the junction is less than the critical current, this is the subgap resistance, which is discussed in more detail in Section 2.8.4. It plays a significant role in damping and dissipation, so we will define a junction quality factor in the same way we would define it for an RLC resonator, $Q = \sqrt{2\pi I_c R^2 C_j/\Phi_0}$, which we will use as a measure of the dissipation effects of the resistance. However, if we use Q as a measure of the total damping seen by a Josephson junction (and in any case where we measure Q, we cannot separate the junction from the environment), R consists of not just the subgap resistance, but a parallel combination of the subgap resistance and the shunting resistance of the environment. When the junction is at a finite voltage, the junction model has a resistance called the normal resistance, R_n. The Stewart-McCumber parameter, $\beta_C=2\pi I_c R_n^2 C_j/\Phi_0$, is a measure of the qubit's damping when determining the junction dynamics at a finite voltage. A shunt resistance, either from the circuit environment or intentionally added, may reduce β_C. When using the junction in a quantum system, we keep the junction biased below its critical current, so the relevant resistance is the subgap resistance, which is very large and can be neglected. Instead, the environmental shunting resistance usually dominates to cause dissipation and decoherence, although every attempt is made to isolate the junction from its environment.

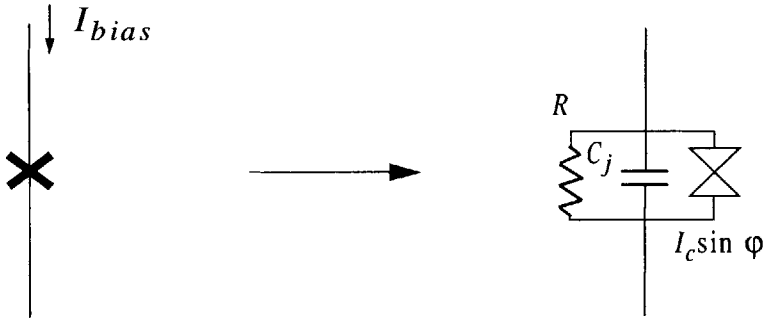

FIGURE 1-2. The Josephson junction and the RCSJ (Resistively Capacitively Shunted Junction) circuit model. The hourglass figure is the supercurrent branch, which follows the Josephson relation.

The energy of a Josephson junction is a combination of the energy stored in the supercurrent ($W_i=E_J(1-\cos\varphi)$ where $E_J=\Phi_0 I_c/2\pi$) and the energy stored in the capacitor ($W_v=(1/2)C_j V^2=(1/2)C_j(\Phi_0/2\pi)^2(d\varphi/dt)^2$). Energy may also be dissipated by the resistor,

but we will assume that the resistance is high and neglect its dissipation. A Hamiltonian which describes a Josephson system can designate one of these as the potential energy (usually W_i) and one as the kinetic energy (W_v). This gives Equation (1-4), where $M=C_j(\Phi_0/2\pi)^2$ is the effective mass of the junction.

$$H = T + U = \frac{1}{2}M\dot{\varphi}^2 + E_J(1 - \cos\varphi) \tag{1-4}$$

The addition of a Josephson junction to a superconducting loop modifies flux quantization, since the superconducting loop is no longer closed and the additional phase drop across the junction is now allowed in the loop. This phase difference is added to the phase drop induced by the penetrating magnetic flux, giving a total phase difference around the loop, which must be a multiple of 2π. This is fluxoid quantization. The self-inductance of the loop compared to the Josephson inductance of the junction determines how large a role the circulating current plays in quantizing the magnetic field. When the self-inductance is much smaller than the Josephson inductance, then the maximum supercurrent which can flow through the junctions is not large enough to quantize the field, and the phase drop across the junctions dominates. When the inductance of the loop is much larger than the junction's Josephson inductance, then the current needed to quantize the flux doesn't require a large phase in the junctions, and the junction simply lets flux quanta in or out of the loop as the total flux is quantized by the circulating current. Often, the two inductances are of the same scale and must both be considered.

1.4 The Persistent Current Qubit

The qubit investigated in this project is a superconducting loop interrupted by three Josephson junctions, called the persistent current qubit [23]. This design is descended from the rf SQUID quantum system first proposed by Leggett and Caldeira [1], but has several advantages. With the right parameters, the rf SQUID, a superconducting loop interrupted by a single junction, can form a double well potential when biased by an external magnetic field of nearly half a flux quantum. These wells correspond to different fluxoid quantizations, with zero or one fluxoid quanta in the loop. These two states have circulating currents in opposite directions, opposing the applied flux in one direction and

reinforcing it in the other direction, to push the flux in the loop toward an integral number of flux quanta. Either way, it reinforces a quantized fluxoid value to give a total phase drop of 0 around the loop (absorbing the multiples of 2π into the junctions themselves). When biased at exactly half a flux quantum, the wells are equal in energy. Thus the lowest energy states are the symmetric and antisymmetric occupation of both wells. When biased slightly off of half a flux quantum, one well has a lower energy than the other. Thus the two lowest energy states are occupation of the lower energy well and occupation of the higher energy well, corresponding to current circulating in one direction or the other. This forms a measurable quantum system, as a magnetometer can detect the flux in the loop and distinguish the circulating current of the two states. Since there is one junction, there is a single degree of freedom.

The persistent current qubit has two degrees of freedom, rather than one. With three junctions, it would have three degrees of freedom, but the small inductance of the loop does not produce enough magnetic field to significantly effect the total magnetic field through the loop. This means that the externally applied magnetic flux and the phases of the junctions, φ_i, must sum to a multiple of 2π, removing one degree of freedom by restricting φ_3 to be $\varphi_2-\varphi_1-2\pi f$. The term $f=\Phi_{ext}/\Phi_0$ is the frustration, the externally applied flux, Φ_{ext}, in units of flux quanta. Of course, the PC qubit does have some inductance, so while we may neglect the third degree of freedom for now we will reconsider it later. The small inductance nevertheless produces a field sufficient to measure. The current of the lowest energy state produces a flux of approximately -1 $m\Phi_0$. In the first excited state, the circulating current is in the opposite direction, producing a flux of about 1 $m\Phi_0$. This is sufficient to measure with a dc SQUID, a sensitive, superconducting magnetometer.

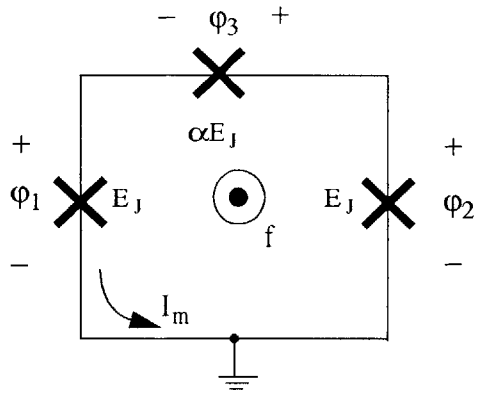

FIGURE 1-3. The Persistent Current Qubit. Circulating current in opposite directions define the two states. The third junction is smaller than the other two junctions, which are the same size.

The PC qubit is shown in Figure 1-3. This brief discussion of its operation is more fully explained in [24]. The Hamiltonian of the qubit is given by Equation (1-5), which sums the energy of each of the three junctions: each has a charge energy equal to $C_jV^2/2$, which is considered the kinetic energy, and a current energy equal to $E_J(1-\cos\varphi)$, which is considered the potential energy. Summing all three of these gives Equation (1-5).

$$H = \frac{1}{2}\left(\frac{\Phi_0}{2\pi}\right)^2 C_j\dot{\varphi}_1^2 + \frac{1}{2}\left(\frac{\Phi_0}{2\pi}\right)^2 C_j\dot{\varphi}_2^2 + \frac{1}{2}\left(\frac{\Phi_0}{2\pi}\right)^2 \alpha C_j\dot{\varphi}_3^2 + E_J[2+\alpha-\cos\varphi_1-\cos\varphi_2-\alpha\cos\varphi_3] \qquad \textbf{(1-5)}$$

In this equation, α is the scaling factor for the third junction shown in the figure, which is smaller than the other two. When we apply the constraint that $\varphi_3=\varphi_2-\varphi_1-2\pi f$, and change to the new variables φ_m and φ_p, such that $\varphi_m=(\varphi_1-\varphi_2)/2$ and $\varphi_p=(\varphi_1+\varphi_2)/2$, this Hamiltonian simplifies to Equation (1-6), which has two rather than three dimensions.

$$H = \frac{1}{2}M_p\dot{\varphi}_p^2 + \frac{1}{2}M_m\dot{\varphi}_m^2 + E_J[2+\alpha-2\cos\varphi_p\cos\varphi_m-\alpha\cos(2\varphi_m+2\pi f)] \qquad \textbf{(1-6)}$$

M_p and M_m are the masses associated with the new variables, where $M_p = 2\left(\frac{\Phi_0}{2\pi}\right)^2 C_j$ and $M_m = (2+4\alpha)\left(\frac{\Phi_0}{2\pi}\right)^2 C_j$. Converting the classical Hamiltonian into a quantum mechanical Hamiltonian requires converting the conjugate variables into quantum operators. The converted Hamiltonian is given in Equation (1-7).

$$\hat{H} = \frac{-\hbar^2}{2M_p}\frac{\partial^2}{\partial\varphi_p^2} + \frac{-\hbar^2}{2M_m}\frac{\partial^2}{\partial\varphi_m^2} + E_J[2+\alpha-2\cos\varphi_p\cos\varphi_m-\alpha\cos(2\varphi_m+2\pi f)] \qquad \textbf{(1-7)}$$

The potential energy, $U=E_J[2+\alpha-2\cos\varphi_p\cos\varphi_m-\alpha\cos(2\varphi_m+2\pi f)]$, is periodic in two dimensions. When the qubit is biased near half a flux quantum, *e.g.* f=0.495, each unit cell of the periodic potential has two wells, one with a slightly higher energy than the other, as can be seen in Figure 1-4(a). The tunneling between the wells, T_{in}, happens at a much higher rate than tunneling between cells, T_{out}, which has to go through a high barrier. Part (b) of the figure projects the potential into one dimension and shows the two lowest energy states. The ground state occupies one well, while the first excited state occupies the other. The accompanying energy band diagram, calculated numerically from the Hamiltonian, clearly shows the energy difference between the two states. There are higher energy levels as well, to which the qubit may be excited, but these are not used intentionally. Also shown is the circulating current, which goes in opposite directions for the two lowest levels. Since the qubit has a small inductance, its circulating current produces only a small field, which is nevertheless large enough to be measured using a dc SQUID magnetometer.

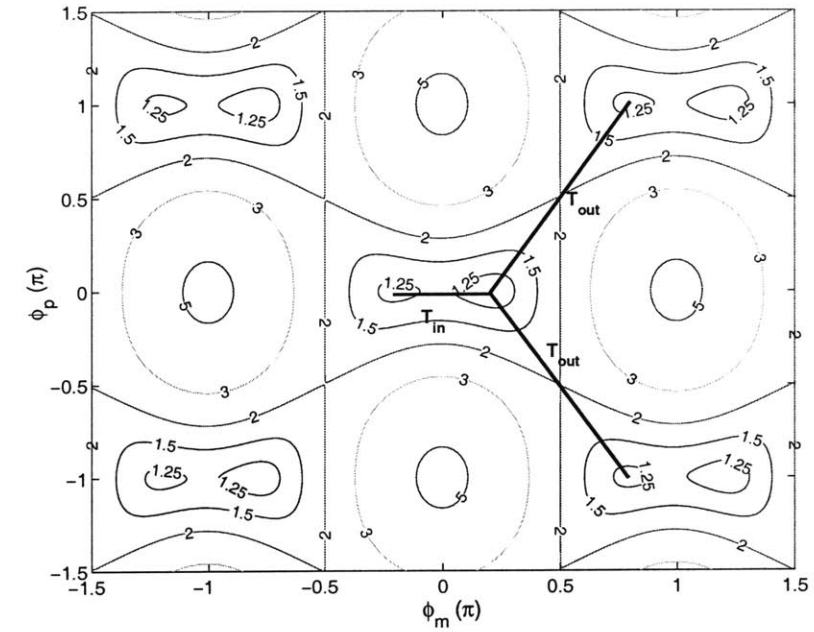

(a)

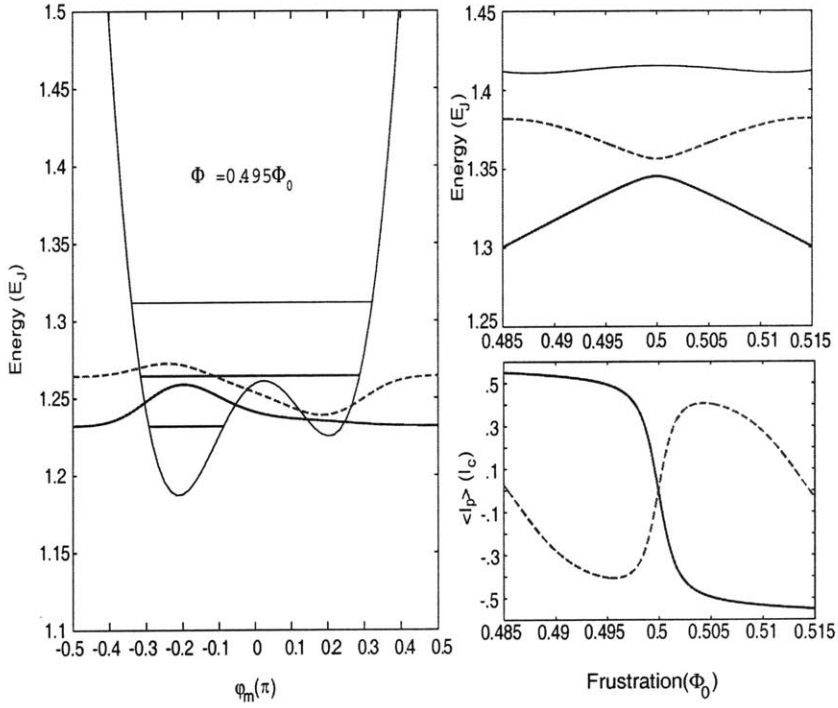

(b)

FIGURE 1-4. (a)Two dimensional potential energy of the persistent current qubit. The phase may move from one potential well to another following the T_{in} path, which has a much smaller potential barrier than the T_{out} path. (b) Energy band diagram showing the first two energy levels as a function of external flux, along with one-dimensional potential energy diagrams showing the double well potential at different flux biases. There are higher energy levels not shown here. Finally, a diagram of the circulating current for each of the energy levels at different flux biases.

The PC qubit has several advantages over the rf SQUID. It is physically much smaller, on the scale of 5 μm rather than 100 μm, since the rf SQUID requires a geometric inductance somewhat larger than the Josephson inductance in order to have a double well potential, while the PC qubit's geometric inductance does not play a role in its potential. This smaller size means that the PC qubit takes up less space on a microchip, making it possible to produce a large array of such qubits on a single chip. Its smaller inductance also makes it less vulnerable to magnetic coupling with unwanted noise sources, and makes it less likely to radiatively decohere.

This system meets the criteria for a qubit. First, it can be set in a desired ground state given the proper bias and enough time to decohere. Second, it can be placed into a superposition of two quantum mechanical states. This can be done by a microwave oscillator producing a magnetic field at the energy difference between the two states, or by a non-adiabatic magnetic flux pulse moving the qubit from f=0.495 to f=0.5, where it will rotate between the |0> and |1> states. This is a simplistic view of the procedure, but it is possible to rotate the qubit through all possible complex phases using some combination of the two methods. Third, the two quantum states of the qubit have distinct characteristics which can be measured, specifically circulating currents in opposite directions whose field can be detected by a dc SQUID. Fourth, the qubits can influence one another by mutual inductive coupling. This may be done either by physical proximity, or by using a "transformer," a superconducting loop which couples magnetic field from one qubit to another. This opens up the possibility of a "transformer" loop which may be switched on and off to create controllable coupling. The coupling allows the formation of gates and entangled systems between the two qubits. Finally, while decoherence time is difficult to measure until the qubit is fabricated and tested, it is believed to be long enough to allow not only simple computations, but the error correction necessary for arbitrarily long quantum computation.

1.5 Measurements

Measurements were performed on a persistent current qubit with a dc SQUID magnetometer to detect its flux state. The samples were fabricated at Lincoln Labora-

tory's foundry in a niobium trilayer process at critical current densities of 730 A/cm^2, 365 A/cm^2, and 70 A/cm^2. The measurements were performed at a range of temperatures from 15 mK to 2 K, over which a transition from quantum tunneling to thermal activation was observed. The thermal activation data shows that the shape and position of the step changes with temperature, as shown in Figure 1-5, and with measurement rate. This change is due to the time-dependent measurement process which tests one state before the other. By modeling this effect, we can derive significant information about the parameters of the qubit, including the Josephson energy of the junctions, E_J, the relative size of the smaller junction, α, and the quality factor, Q, of the qubit. For the sample which we tested with a critical current density of 730 A/cm^2, these values were found to be 4000 μeV for E_J, 0.58 for α, and 4x10^5 for Q. For the sample measured at 365 A/cm^2, these values were found to be 2400 μeV for E_J, 0.59 for α, and 3x10^5 for Q.

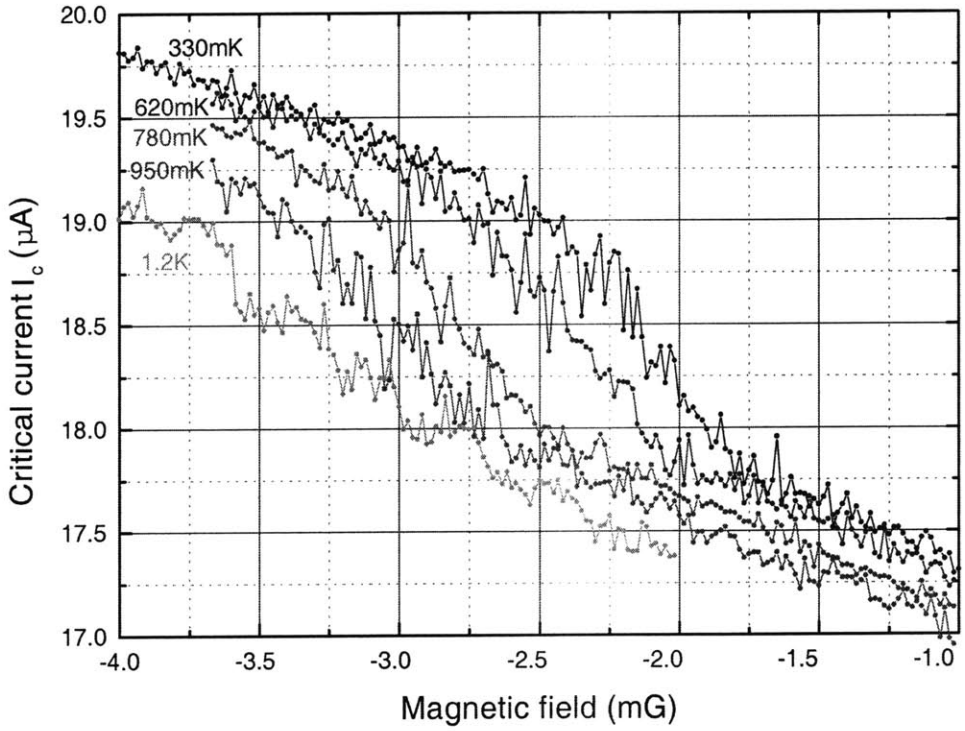

FIGURE 1-5. The temperature dependence of the qubit step signature. As temperature increases, the qubit step becomes wider and shifts to the left, towards the higher switching current.

The data taken at lower temperatures showed strong evidence of quantum tunneling. Since the effective flux of the qubit changes as the current bias on the measuring

device is ramped, the ability to link stripes in the data (which represent qubit state transitions at specific external flux and current biases) to lines of constant effective flux, as shown in Figure 1-6, provides strong evidence of resonant macroscopic quantum tunneling at discrete flux biases. The flux biases which give these high tunneling rates allow us to calculate the energy levels of the qubit and the charging energy, E_C, which is 3 μeV, which produces energy bands which match up well with the observed resonant tunneling. This charging energy is for the lower critical current sample, but E_C does not vary much with critical current density, so it is expected to be similar for all samples.

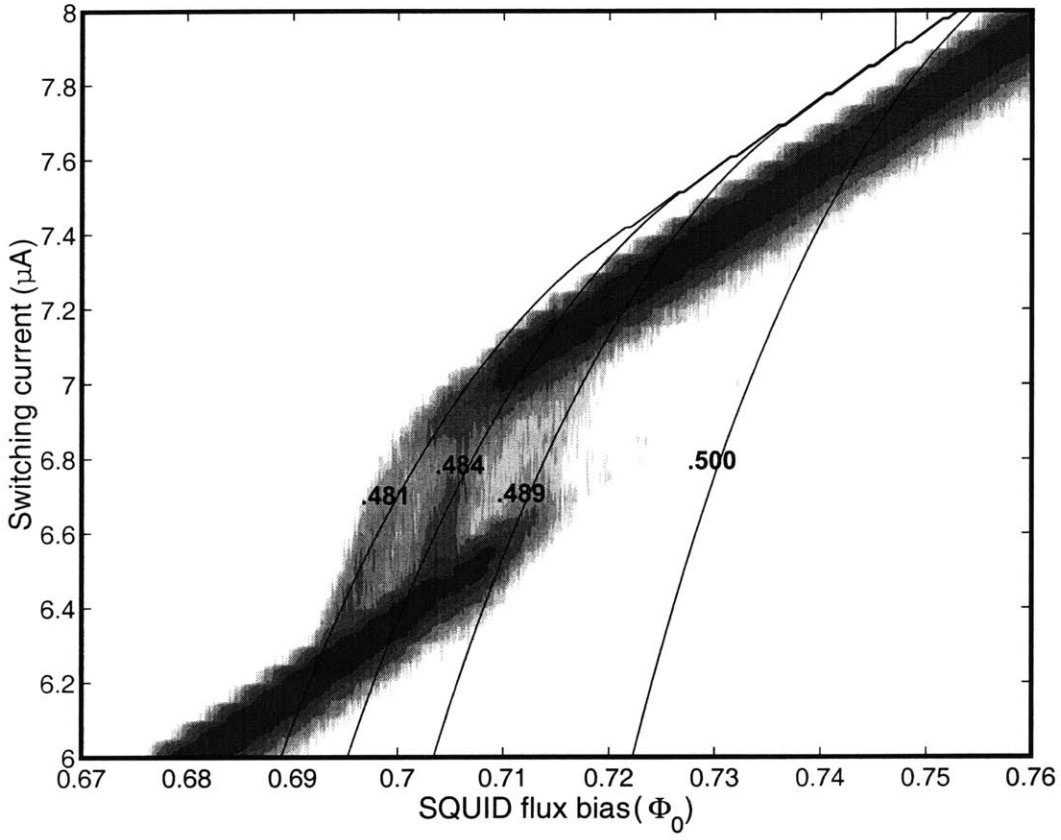

FIGURE 1-6. This contour plot for a qubit prepared in the R state includes lines of constant f_q'. These lines, whose numbers indicate the effective flux bias of the qubit along the line, mark where there is a level alignment and enhanced quantum tunneling. Near some lines, there may be more than one quantum level in close proximity. There are only a few points near the f_q'=0.5 line, indicating deep wells with little quantum tunneling.

1.6 The Oscillator

In addition to the measurements on the ground state of the qubit, an oscillator was designed in order to serve as the means of driving the qubit between its two quantum

states via a magnetic field oscillating at the frequency of the energy difference. The oscillator is a simple dc SQUID whose amplitude and frequency can be controlled by a combination of flux and current bias. The oscillator is shown in Figure 1-7.

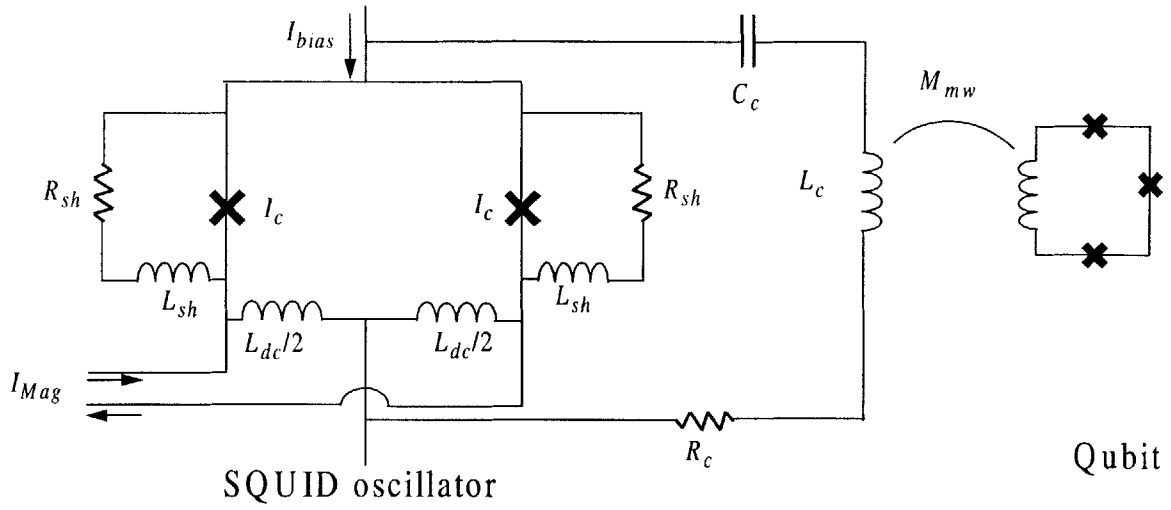

FIGURE 1-7. Circuit diagram of the SQUID oscillator.

The oscillator was designed to minimize decoherence while delivering sufficient amplitude to cause the qubit to rotate with a Rabi frequency of nearly 100 MHz. The decoherence time is calculated using the spin-boson model for the qubit's interaction with the environment. The desired qubit rotation can be achieved as long as the oscillator's amplitude is at least 1 $m\Phi_0$ and the decoherence time is greater than 100 ns, which are achievable in the designed dc SQUID oscillator for frequencies near 10 GHz. While the qubit rotation has not yet been measured, the oscillator delivers enough power to suppress the switching current of the SQUID, as shown in Figure 1-8.

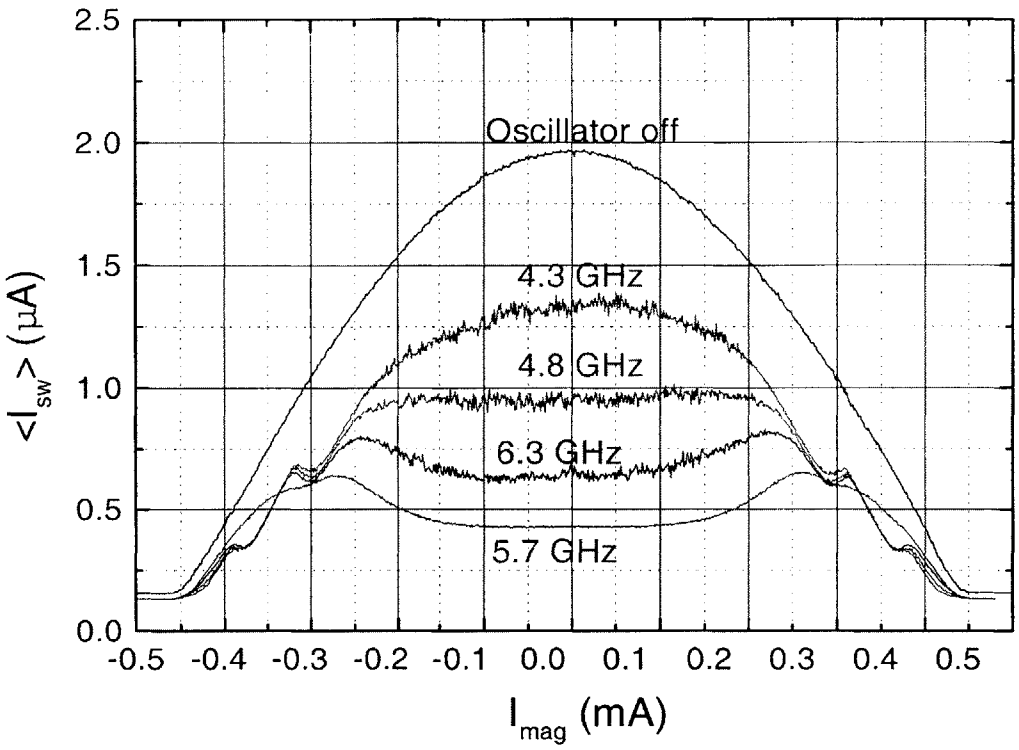

FIGURE 1-8. The mean switching current for the measurement SQUID when the SQUID oscillator is at various frequencies. The magnetic field bias of the oscillator is kept at f_{osc}=0.26, while the current bias is changed to produce different oscillation frequencies.

1.7 Outline

This first chapter has introduced the idea of quantum computation and explained how superconductors act quantum mechanically even at the macroscopic scale. It also introduced the persistent current qubit and gave a brief quantum mechanical description. Finally, this chapter showed some of the main results of this work.

Chapter 2 discusses the persistent current qubit in more detail, including the system Hamiltonian, numerical simulations of it, and the effect of the small inductance of the ring. Methods of calculating decoherence from the circuit environment of the qubit are also covered. Finally, this chapter explains the fabrication process and the difficulties involved in reliably achieving the required parameters.

Chapter 3 discusses the dc SQUID, the device used to measure the qubit's state. It covers theoretical operation of the SQUID and the experimental set-up of the measurements. The SQUID design is discussed, including the calculation of the SQUID's contri-

bution to decoherence.

Chapter 4 discusses the measurements, both at high temperatures (from 300 mK to 1.2 K) and low temperatures (15 mK to 300 mK). The measurements show thermal activation at high temperature and quantum tunneling at low temperature. At high temperatures, the measurement time and thermal activation help to determine the qubit's parameters. At low temperatures, the discrete levels of each well of the qubit are visible and provide further parameters for the qubit. Some careful analysis allows us to consider the influence of the measurement device on the qubit. Two samples have been thoroughly tested so far, one at 730 A/cm^2 and the other at 360 A/cm^2, and preliminary results are available for a sample with a critical current density at 70 A/cm^2.

Chapter 5 discusses Josephson junction oscillators. Measurements on arrays of overdamped junctions are presented, along with the means of calculating the power from a superconducting oscillator using a detector junction. An overdamped dc SQUID oscillator which can be used to drive the qubit without causing undue decoherence is also presented, along with preliminary results.

Chapter 6 discusses RSFQ electronics, a digital logic technology using Josephson junctions. After describing fundamental RSFQ cells, two RSFQ circuits are discussed: a Variable Duty Cycle Oscillator (VDCO) with on-chip timing, and an oscillator with off-chip timing. The VDCO has been designed and fabricated, but not yet tested. The oscillator with off-chip timing has been designed, but fabrication is not yet complete.

Chapter 7 concludes this work by reviewing the results and niobium's prospects for superconductive quantum computation, and pointing out the direction for future work.

Chapter 2

Analysis, Design, and Fabrication of the PC Qubit

2.1 Introduction

The purpose of this chapter is to quantum mechanically describe the persistent current qubit and establish its design criteria. Section 2.2 begins with a simpler quantum mechanical system, the quantum box, and describes the Hamiltonian, which is then discretized so it can be numerically simulated. The same is done for the persistent current qubit in Section 2.3. Once the principle is laid out, such complications as the extra degree of freedom introduced by the self-inductance (Section 2.5) and a time-dependent perturbation (Section 2.7) can be discussed. Finally, the parameters necessary for successful qubit operation are discussed in Section 2.8, and Section 2.9 judges the fabrication capabilities of the foundry which we used by those criteria.

2.2 The Quantum Mechanical Josephson junction

The system in Figure 2-1 is sometimes called a quantum box. It consists of a single junction which is grounded on one end. On the other end is a charge island, the "box," which is capacitively coupled to the outside world. This quantum box summarizes most of the principles necessary to model the PC qubit, and analyzing it will give us the tools we need to do numerical simulations.

The dual variables in this system are charge and phase, and it can therefore be modeled in either the charge basis or the phase basis. Here, we are concerned primarily with the phase basis, which is inherently continuous and so must be discretized in order to calculate numerically.

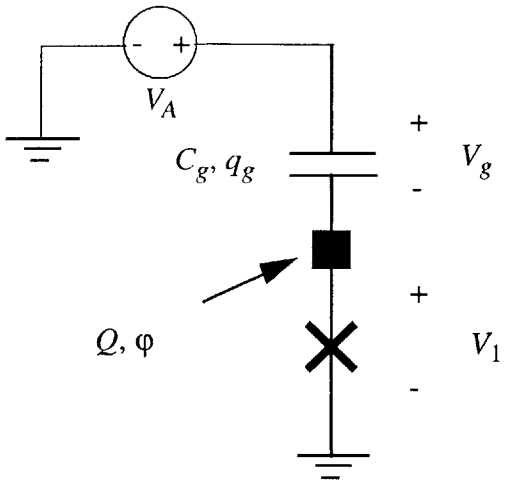

FIGURE 2-1. The Quantum Box.

A Hamiltonian sums up the equations of motions in a system by the energies. Forming a Hamiltonian requires calculating the kinetic and potential energies, T and U respectively. Here we define the potential energy as the charge across the capacitance:

$$T = \frac{1}{2}\sum_k C_k V_k^{\,2} - q_g V_A \tag{2-1}$$

$$T = \frac{1}{2}(C_j + C_g)\left(\frac{\Phi_0}{2\pi}\right)^2 \dot{\varphi}^2 - \frac{1}{2}C_g V_A^2 \tag{2-2}$$

The potential energy is the Josephson energy, $U = E_J(1 - \cos\varphi)$. This classification is arbitrary: the Josephson energy could just as easily be defined as kinetic energy and the electrical energy as potential. The electrical energy includes the energy stored in each of the capacitors minus the work done by the source, which is equal to the work required to produce the applied voltage. The shape of the energy band structure is determined by the two energy constants: E_C and E_J. E_C is the electrical energy constant, which equals $e^2/2C_j$, the energy of one electron charge on the capacitor of the junction. E_J is the Josephson energy, which is the energy of the Josephson junction when it is at its maximum superconducting current, and it is equal to $\Phi_0 I_c/2\pi$.

Since we want to put the Hamiltonian in the form $H = \frac{P^2}{2M} + E_J(1 - \cos\varphi)$, we need to define the momentum in a consistent manner. We define the Lagrangian L as T-U. We can introduce a simple shift to the Lagrangian, equivalent to changing to a constant veloc-

ity frame of reference, to change the Lagrangian to $L = T - U - \left(\frac{\Phi_0}{2\pi}\right)C_g V_A \dot{\varphi}$. The canonical momentum is defined as $P = \frac{\partial L}{\partial \dot{\varphi}} = \left(\frac{\Phi_0}{2\pi}\right)^2 (C_j + C_g)\dot{\varphi} - \left(\frac{\Phi_0}{2\pi}\right)C_g V_A$. The shift gives P a more physical meaning: it is proportional to the charge on the island, $P=(\Phi_0/2\pi)q$. This definition of P also allows us to define M. Clearly φ has the same role as x in the usual Hamiltonian. From $P = M\dot{x} \Rightarrow M\dot{\varphi}$, we can determine M in this case as $M = \left(\frac{\Phi_0}{2\pi}\right)^2 (C_j + C_g)$. The $(\Phi_0/2\pi)C_g V_A$ term is simply a constant shift. The classical Hamiltonian is defined by Equation (2-3), which expands to Equation (2-4), where q^I is the induced charge, $C_g V_A$ [24].

$$H = \sum_i P_i \dot{\varphi}_i - L \tag{2-3}$$

$$H = \frac{1}{2M}\left(P + \frac{\Phi_0}{2\pi} q^I\right)^2 + U \tag{2-4}$$

In order to transform this equation from a classical Hamiltonian operator to a quantum Hamiltonian operator, the variables must become operators. In phase space, the operators should be $\hat{\varphi} = \varphi$ and $\hat{P} = \frac{\hbar}{i}\frac{\partial}{\partial \varphi}$, in analogy to the real space operators $\hat{x} = x$ and $\hat{P} = \frac{\hbar}{i}\frac{\partial}{\partial x}$. The wavefunction can be written as a sum of plane-wave solutions in this coordinate system as $\Psi(\varphi)=\sum_m c_m \exp(-im\varphi)$, where m is the number of Cooper pairs on the island, which is always an integral number. Now we define k to be the number of Cooper pairs induced by V_A, $-C_g V_A/2e$. While the total number of Cooper pairs, m, must be integral, k need not be. Now the plane wave solutions are $\exp(-ik\varphi)\exp(-i(m-k)\varphi)$. The second term, while it is not a solution to the Hamiltonian in Equation (2-4), is a solution to the simpler Hamiltonian $H = P^2/2M + U$, since we've moved the induced charge. So if $\Psi(\varphi)$ is a solution to Equation (2-4), then $\exp(ik\varphi)\Psi(\varphi)$ is a solution to the transformed Hamiltonian.

We've considered the solution, $\Psi(\varphi)$, to be a sum of plane waves, which corresponds to charge states. If we're looking for a solution in terms of phase rather than charge, then the basis functions are impulses, resulting in a Hamiltonian matrix of $H_{\varphi_0, \varphi_0'} = \langle e^{-ik\varphi}\delta(\varphi - \varphi_0')|\hat{H}|e^{ik\varphi}\delta(\varphi - \varphi_0)\rangle$. Note that we are using the transformed Hamiltonian, and thus the $\Psi(\varphi)$ solution is multiplied by $\exp(ik\varphi)$. Phase is continuous, thus there are an infinite number of φ_0 basis functions, resulting in an infinite H matrix. A sufficient approximation can be achieved by discretizing the phase space, which is periodic in 2π,

into A points in one 2π period, where one hundred points is generally a sufficient approximation. Δ is the phase distance between points. N is the total number of points, over all S periods. When we discretize the phase space, $\varphi \rightarrow n\Delta$, and $e^{ik\varphi}\Psi(\varphi) \rightarrow e^{ikn\Delta}\Psi[n]$,

$$\hat{P}e^{ik\varphi}\Psi(\varphi) = \frac{\hbar}{i}\nabla(e^{ik\varphi}\Psi(\varphi)) \rightarrow \frac{\hbar}{i\Delta}(e^{ik\Delta(n+1)}\Psi[n+1] - e^{ik\Delta n}\Psi[n]), \quad \text{and}$$

$$\hat{P}^2(e^{ik\varphi}\Psi(\varphi)) = -\hbar^2\nabla^2(e^{ik\varphi}\Psi(\varphi)) \rightarrow -\frac{\hbar^2}{\Delta^2}\{e^{ik\Delta(n+1)}\Psi[n+1] - 2e^{ik\Delta n}\Psi[n] + e^{ik\Delta(n-1)}\Psi[n-1]\}.$$

The next step is to determine the $H_{\varphi 0,\varphi 0'}$ values. We can write $|\Psi_{n_0}\rangle = c_n\delta[n-n_0]$ in n, or phase, space, normalizing it as in Equation (2-5) as

$$\langle\Psi_{n_0}|\Psi_{n_0}\rangle = \sum_{n=0}^{N-1} c_n^2\delta[n-n_0]\delta[n-n_0] = 1 \tag{2-5}$$

Finally, we write this as the discretized Hamiltonian matrix element in Equation (2-6).

$$\begin{aligned} H_{n_0,n_0'} &= \langle e^{-ikn\Delta}\Psi_{n_0'}|\hat{H}|e^{ikn\Delta}\Psi_{n_0}\rangle \\ H_{n_0,n_0'} &= -\frac{\hbar^2}{2M\Delta^2}\{e^{ik\Delta}\delta_{n_0',n_0-1} + e^{-ik\Delta}\delta_{n_0',n_0+1} - 2\delta_{n_0',n_0}\} \\ &+ E_J(1-\cos(\Delta n_0))\delta_{n_0',n_0} \end{aligned} \tag{2-6}$$

This matrix equation describes the Hamiltonian for a single junction. Finding the eigenvalues determines the energy levels of this quantum system, while the eigenvectors gives the discretized forms of the wavefunctions in phase space.

2.3 The Persistent Current Qubit

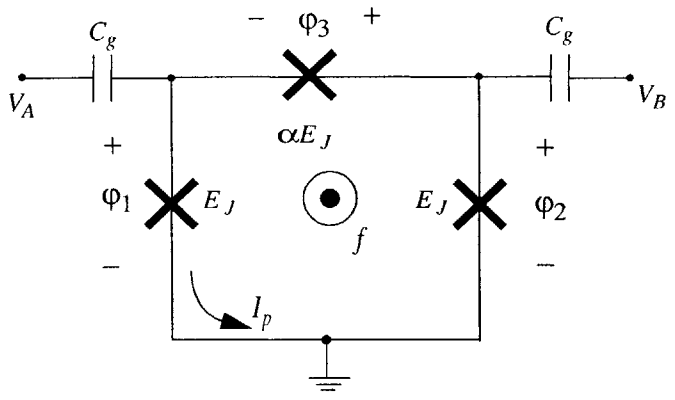

FIGURE 2-2. The Persistent Current Qubit. Circulating current in opposite directions define the two states.

The Hamiltonian for the three junction qubit is naturally more complex, but the approach is the same. The largest difference is that the persistent current qubit Hamiltonian has two dimensions rather than one, and this two dimensional problem now has two variables to discretize, n_+ and n_-. These are not discretizations of the phase differences for each junction, which would be φ_1 (n_1) and φ_2 (n_2), but rather they are discretizations of the sum and difference variables $\varphi_p=(\varphi_1+\varphi_2)/2$ and $\varphi_m=(\varphi_1-\varphi_2)/2$ used as the basis in Equation (2-7).

$$H = \frac{1}{2}M_p\dot{\varphi}_p^2 + \frac{1}{2}M_m\dot{\varphi}_m^2 + E_J[2 + \alpha - 2\cos\varphi_p\cos\varphi_m - \alpha\cos(2\varphi_m + 2\pi f)] \qquad \textbf{(2-7)}$$

The delta functions are now products of a delta function in each dimension, such that describing the nearest neighbor interaction over one dimension is the product $\delta_{(n+)',(n+)+1}\delta_{(n-)',(n-)}$, while the other dimension is $\delta_{(n+)',(n+)}\delta_{(n-)',(n-)+1}$. The masses are now $M_p=(\Phi_0/2\pi)^2 2(C_j+C_g)$ and $M_m=(\Phi_0/2\pi)^2 2(C_j+2\alpha_C C_j+C_g)$, while $k_+=-C_g(V_A+V_B)/2e$ and $k_-=-C_g(V_A-V_B)/2e$. α_C is the ratio between the capacitances of the smallest junction and the larger junctions. Ideally, $\alpha_C=\alpha$, but that is not necessarily the case. The Hamiltonian operator for the qubit is given in its usual form in Equation (2-8).

$$H = \frac{-\hbar^2}{2M_p}\frac{\partial^2}{\partial\varphi_p^2} + \frac{-\hbar^2}{2M_m}\frac{\partial^2}{\partial\varphi_m^2} + E_J[2 + \alpha - 2\cos\varphi_p\cos\varphi_m - \alpha\cos(2\varphi_m + 2\pi f)] \qquad \textbf{(2-8)}$$

When discretized, this becomes Equation (2-9). Since each delta function product must be represented in the Hamiltonian, such that $\delta_{(n+)',(n+)}\delta_{(n-)',(n-)}$, $\delta_{(n+)',(n+)}\delta_{(n-)',(n-)+1}$, $\delta_{(n+)',(n+)+1}\delta_{(n-)',(n-)}$, and $\delta_{(n+)',(n+)+1}\delta_{(n-)',(n-)+1}$ all require separate columns in the matrix, the size of the matrix, which was AxA for the one dimensional problem, is now A_+A_- x A_+A_-. While the resolution may vary, the matrix has effectively squared in size.

$$
\begin{aligned}
H_{n_+n_-,n_+'n_-'} &= \langle e^{-i(k_+n_+ + k_-n_-)}\Psi_{n_+'n_-'}|\hat{H}|e^{i(k_+n_+ + k_-n_-)}\Psi_{n_+n_-}\rangle \\
H_{n_+n_-,n_+'n_-'} &= -\frac{\hbar^2}{2M_p\Delta_+^2}\left\{e^{ik_+\Delta_+}\delta_{n_+',n_+-1} + e^{-ik_+\Delta_+}\delta_{n_+',n_++1} - 2\delta_{n_+',n_+}\right\}\delta_{n_-',n_-} \\
&-\frac{\hbar^2}{2M_m\Delta_-^2}\left\{e^{ik_-\Delta_-}\delta_{n_-',n_--1} + e^{-ik_-\Delta_-}\delta_{n_-',n_-+1} - 2\delta_{n_-',n_-}\right\}\delta_{n_+',n_+} \\
&+ E_J\{2+\alpha-2\cos(n_+\Delta_+)\cos(n_-\Delta_-) - \alpha\cos(2\varphi_m + 2\pi f)\}\delta_{n_+',n_+}\delta_{n_-',n_-}
\end{aligned}
\tag{2-9}
$$

2.4 The Simple Harmonic Oscillator Approximation

It is often useful to reduce the qubit to a simple harmonic oscillator approximation for each well. The SHO approximation cannot account for tunneling between the two wells, which is the quantum effect which we use for quantum computation, but it can give us the resonant frequency of the wells in each dimension, the variance of the variables' uncertainties, and the approximate level spacing when the each well is deep enough to have multiple quantum levels. We start with Equation (2-10), the Hamiltonian for the qubit.

$$
H = \frac{1}{2}M_p\dot{\varphi}_p^2 + \frac{1}{2}M_m\dot{\varphi}_m^2 + E_J[2+\alpha-2\cos\varphi_p\cos\varphi_m - \alpha\cos(2\varphi_m + 2\pi f)] \tag{2-10}
$$

The simple harmonic oscillator approximation has the form in Equation (2-11), where $\varphi_{p,0}$ and $\varphi_{m,0}$ are at the minimum of the qubit's well and represent an offset of the SHO solution's origin from the qubit's origins.

$$
H = \frac{1}{2}M_p\dot{\varphi}_p^2 + \frac{1}{2}M_m\dot{\varphi}_m^2 + \frac{1}{2}M_p\omega_p^2(\varphi_p - \varphi_{p,0})^2 + \frac{1}{2}M_m\omega_m^2(\varphi_m - \varphi_{m,0})^2 \tag{2-11}
$$

It is possible to find a simple harmonic oscillator approximation for any system which is in a stable state (at a minimum of the potential), if the third-order or higher terms are negligible. The potential for the qubit is given below:

$$U = E_J[2 + \alpha - 2\cos\varphi_p\cos\varphi_m - \alpha\cos(2\varphi_m + 2\pi f)] \tag{2-12}$$

The first derivatives, in Equation (2-13), go to zero at the minimum at $\varphi_{p,0}$ and $\varphi_{m,0}$. $\varphi_{p,0} = 0$, while $\varphi_{m,0}$ must be solved from the first derivative.

$$\begin{aligned}\frac{\partial U}{\partial \varphi_p} &= 2E_J\sin\varphi_p\cos\varphi_m \\ \frac{\partial U}{\partial \varphi_m} &= 2E_J\cos\varphi_p\sin\varphi_m + 2\alpha E_J\sin(2\varphi_m + 2\pi f)\end{aligned} \tag{2-13}$$

The second derivatives, in Equation (2-14), give us the curvature of the wells. Taking the values of the curvature in each dimension at $(\varphi_{p,0},\varphi_{m,0})$ allows us to apply the simple harmonic oscillator approximation.

$$\begin{aligned}\frac{\partial^2 U}{\partial \varphi_p^2} &= 2E_J\cos\varphi_p\cos\varphi_m \\ \frac{\partial^2 U}{\partial \varphi_m^2} &= 2E_J\cos\varphi_p\cos\varphi_m + 4\alpha E_J\cos(2\varphi_m + 2\pi f)\end{aligned} \tag{2-14}$$

The simple harmonic oscillator in two dimensions has the potential:

$$U = \frac{1}{2}M_p\omega_p^2(\varphi_p - \langle\varphi_p\rangle)^2 + \frac{1}{2}M_m\omega_m^2(\varphi_m - \langle\varphi_m\rangle)^2. \tag{2-15}$$

In Equation (2-16), the first derivatives of this simple harmonic oscillator potential go to zero when $\varphi_p=\varphi_{p,0}$ and $\varphi_m=\varphi_{m,0}$.

$$\begin{aligned}\frac{\partial U}{\partial \varphi_p} &= M_p\omega_p(\varphi_p - \langle\varphi_p\rangle) \\ \frac{\partial U}{\partial \varphi_m} &= M_m\omega_m(\varphi_m - \langle\varphi_m\rangle)\end{aligned} \tag{2-16}$$

The second derivatives, in Equation (2-17), are positive and constant.

$$\begin{aligned}\frac{\partial^2 U}{\partial \varphi_p^2} &= M_p\omega_p^2 \\ \frac{\partial^2 U}{\partial \varphi_m^2} &= M_m\omega_m^2\end{aligned} \tag{2-17}$$

Setting the second derivatives of the simple harmonic oscillator potential equal to the second derivatives of the qubit potential, as shown in Equation (2-18), gives us the

relationship we need to approximate the qubit with the simple harmonic oscillator solution.

$$\begin{aligned} M_p\omega_p^2 &= 2E_J\cos\varphi_{m,0} \\ M_m\omega_m^2 &= 2E_J\cos\varphi_{m,0} + 4\alpha E_J\cos(2\varphi_{m,0} + 2\pi f) \end{aligned} \tag{2-18}$$

Recall that the effective masses in the φ_p and φ_m directions are $M_p=(\Phi_0/2\pi)^2 2C_j$ and $M_m=(\Phi_0/2\pi)^2(2+4\alpha_C)C_j$ when we neglect C_g. We'll use the charging energy, $E_C=e^2/2C_j$, and the definition that $\Phi_0/2\pi=\hbar/2e$, to rewrite the masses as $M_p=\hbar^2/4E_C$ and $M_m=(1+2\alpha_C)\hbar^2/4E_C$. Substituting gives the values for ω_p and ω_m, the resonant frequencies of the qubit wells in each direction, as shown in Equation (2-19).

$$\begin{aligned} \omega_p &= \frac{2}{\hbar}\sqrt{2\cos\varphi_{m,0}}\sqrt{E_J E_C} \\ \omega_m &= \frac{2}{\hbar}\sqrt{\frac{2\cos\varphi_{m,0} + 4\alpha\cos(2\varphi_{m,0} + 2\pi f)}{1+2\alpha_C}}\sqrt{E_J E_C} \end{aligned} \tag{2-19}$$

At f=1/2, $\cos\varphi_{m,0}=1/2\alpha$, and Equation (2-19) simplifies to Equation (2-20).

$$\begin{aligned} \omega_p &= \frac{2}{\hbar}\sqrt{\frac{1}{\alpha}}\sqrt{E_J E_C} \\ \omega_m &= \frac{2}{\hbar}\sqrt{\frac{4\alpha^2 - 1}{\alpha(1+2\alpha_C)}}\sqrt{E_J E_C} \end{aligned} \tag{2-20}$$

The variance in φ of the ground state of the simple harmonic oscillator is $\Delta\varphi = \sqrt{\frac{\hbar}{2M\omega_0}}$, so when we subtitute variables into this equation we get Equation (2-21), the approximate width of the ground state of the qubit in both the φ_p and φ_m dimensions.

$$\begin{aligned} \Delta\varphi_p &= \alpha^{1/4}\left(\frac{E_J}{E_C}\right)^{-1/4} \\ \Delta\varphi_m &= \left(\frac{\alpha}{(1+2\alpha_C)(4\alpha^2-1)}\right)^{1/4}\left(\frac{E_J}{E_C}\right)^{-1/4} \end{aligned} \tag{2-21}$$

We wrote the width in terms of E_J/E_C. This ratio is important for defining the regime in which the qubit is operating, and it will reappear often. For the persistent current qubit, this ratio should be near 100.

2.5 Inductance Effects on the Persistent Current Qubit

Up to this point, the inductance of the qubit has been assumed to be zero so that it constrains $\varphi_1-\varphi_2+\varphi_3 = -2\pi f$, where f is the frustration. As the inductance gets larger, this

constraint relaxes, and the two-dimensional problem becomes three-dimensional. Physically, there is an additional energy due to flux stored in the loop, which is equal to $(\Phi_0/2\pi)^2(\varphi_1-\varphi_2+\varphi_3+2\pi f)^2/2L$, where L is the inductance of the qubit. Since the potential is quadratic, it looks like a simple harmonic oscillator (SHO), although SHO solutions may not hold when other potential energies in the system have similar energy scales. When the inductance is small, then the potential energy well is deep, and the standard deviation of $(\varphi_1-\varphi_2+\varphi_3+2\pi f)$ is very small while the energy gap between levels of the SHO is very large. When the inductance is large, the quadratic potential is shallow, so that $(\varphi_1-\varphi_2+\varphi_3+2\pi f)$ has a larger spread and the energy spacing is smaller and more likely to be on the same order as the energy difference of the two circulating current qubit states. As noted above, the numerical simulation becomes increasingly difficult as more dimensions are added, requiring for the three-dimensional problem a matrix of the size $A_1A_2A_3$ x $A_1A_2A_3$. This is intractable on most computers, thus encouraging us to find an analytical approach to solving it. The solution we find is only appropriate to small inductances, where the physical inductance is at least an two orders of magnitude smaller than the Josephson inductance, but it provides a more complete solution than neglecting the inductance completely.

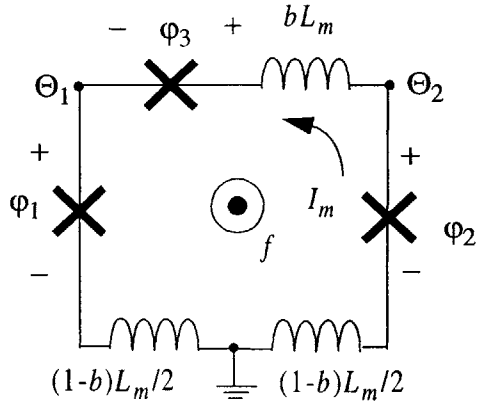

FIGURE 2-3. The three junction qubit with inductance. The inductance has been distributed on all three branches. Doing this, and using branch as opposed to junction phases, the three dimensional model reduces to a simpler form, the sum of the two dimensional model, a simple harmonic oscillator, and a correction term.

The first requirement is to choose the appropriate basis. There are many possibili-

ties, but in this case, we will choose to use a basis of Θ_1, Θ_2, and I_m, as shown in the diagram in Figure 2-3. This gives us the equalities in Equation (2-22) for converting the previous variables. The value of b is arbitrary, as long as it is less than 1, so we can define its value so that it eliminates any products of the time derivative of I_m and the time derivative of Θ_1 or Θ_2.

$$\begin{aligned}
\varphi_1 &= \Theta_1 - \frac{1-b}{2}\left(\frac{2\pi}{\Phi_0}\right)(L_m I_m + \Phi_{ext}) \\
\varphi_2 &= \Theta_2 + \frac{1-b}{2}\left(\frac{2\pi}{\Phi_0}\right)(L_m I_m + \Phi_{ext}) \\
\varphi_3 &= \Theta_2 - \Theta_1 - b\left(\frac{2\pi}{\Phi_0}\right)(L_m I_m + \Phi_{ext}) \\
b &= \frac{1}{1+2\alpha}
\end{aligned} \tag{2-22}$$

Due to the complexity of the problem, it is simpler to deal with the kinetic and potential energy components of the Hamiltonian separately. The kinetic energy term for this system is given by

$$T = \frac{1}{2}C_j\left(\frac{\Phi_0}{2\pi}\right)^2 \dot{\varphi}_1^2 + \frac{1}{2}C_j\left(\frac{\Phi_0}{2\pi}\right)^2 \dot{\varphi}_2^2 + \frac{1}{2}\alpha C_j\left(\frac{\Phi_0}{2\pi}\right)^2 \dot{\varphi}_3^2 \tag{2-23}$$

Substituting for φ_1, φ_2, and φ_3 in Equation (2-23), gives

$$T = \frac{1}{2}C_j\left(\frac{\Phi_0}{2\pi}\right)^2 [(1+\alpha)\dot{\Theta}_1^2 + (1+\alpha)\dot{\Theta}_2^2 - 2\alpha\dot{\Theta}_1\dot{\Theta}_2] + \frac{\alpha}{1+2\alpha}C_j L_m^2 \dot{I}_m^2 \tag{2-24}$$

This is where the odd distribution of the inductance pays off. The above kinetic energy can easily be resolved into Equation (2-25).

$$= \frac{1}{2}M_p\dot{\Theta}_p^2 + \frac{1}{2}M_m\dot{\Theta}_m^2 + \frac{\alpha}{1+2\alpha}C_j L_m^2 \dot{I}_m^2 \tag{2-25}$$

where $M_p = 2\left(\frac{\Phi_0}{2\pi}\right)^2 C_j$, $M_m = (2+4\alpha)\left(\frac{\Phi_0}{2\pi}\right)^2 C_j$, $\Theta_p = \frac{\Theta_1+\Theta_2}{2}$, and $\Theta_m = \frac{\Theta_1-\Theta_2}{2}$.

The potential energy term in the original variables is

$$U = E_J(2+\alpha-\cos\varphi_1-\cos\varphi_2-\alpha\cos\varphi_3) + \frac{(\varphi_1-\varphi_2+\varphi_3+2\pi f)^2}{2L_m}\left(\frac{\Phi_0}{2\pi}\right)^2 \quad . \tag{2-26}$$

Once again, we replace the variables φ_1, φ_2, and φ_3 with Θ_1, Θ_2, and I_m to change Equation (2-26) to Equation (2-27).

$$\begin{aligned}
U = E_J\Big[2+\alpha-2\cos\Theta_p\cos\Big(\Theta_m - \frac{1-b}{2}\Big(\frac{2\pi}{\Phi_0}\Big)(L_m I_m + \Phi_{ext})\Big) - \\
\alpha\cos\Big(-2\Theta_m - b\Big(\frac{2\pi}{\Phi_0}\Big)(L_m I_m + \Phi_{ext})\Big)\Big] + \frac{1}{2}L_m I_m^2
\end{aligned} \tag{2-27}$$

By defining $\tilde{\Theta}_m = \Theta_m - (1-b)2\pi f$, we can make the Hamiltonian's form more

closely resemble that of the zero-inductance qubit. This does not affect the kinetic energy, T, since $\dot{\tilde{\Theta}}_m = \dot{\Theta}_m$.

$$U = E_J\left[2+\alpha-2\cos\Theta_p\cos\left(\tilde{\Theta}_m-\frac{\alpha}{1+2\alpha}\left(\frac{2\pi}{\Phi_0}\right)L_m I_m\right)-\right.$$
$$\left.\alpha\cos\left(2\tilde{\Theta}_m+2\pi f+\frac{1}{1+2\alpha}\left(\frac{2\pi}{\Phi_0}\right)L_m I_m\right)\right]+\frac{1}{2}L_m I_m^2 \tag{2-28}$$

By expanding the equation, as shown in Appendix I, we can separate the Hamiltonian into three independent parts.

$$H = H_q(\Theta_p, \tilde{\Theta}_m) + H_{ho}(\tilde{I}_m) + E_{cor}(\langle\Theta_p\rangle, \langle\tilde{\Theta}_m\rangle) \tag{2-29}$$

Since the terms are independent, it's possible to utilize the original qubit solution and a simple harmonic oscillator solution without alteration. The final solution for the energy bands is given by Equation (2-31). Note that the harmonic oscillator term does not alter the shape of the bands: it adds a constant energy offset to the qubit's original energy bands, and then causes them to be repeated at equal intervals of $\hbar\omega_0$, where

$$\omega_0 = \frac{2}{\hbar}\sqrt{\frac{\alpha}{1+2\alpha}}\sqrt{E_J E_C/\beta_L} \tag{2-30}$$

As long as $\hbar\omega_0 >> \hbar\omega_m$, the scale of the qubit energy levels, these extra levels have little influence on the operation of the qubit. This is true for small $\beta_L < 0.01$

$$E = E_q(f)+\left(n+\frac{1}{2}\right)\hbar\omega_0-\frac{1}{2}L_m I_c^2\left(\frac{\alpha}{1+2\alpha}\right)^2\left(\sin(2\langle\tilde{\Theta}_m\rangle+2\pi f)-2\cos\langle\Theta_p\rangle\sin\langle\tilde{\Theta}_m\rangle\right)^2 \tag{2-31}$$

The expectation value $\langle\Theta_p\rangle$ is always 0. We can approximate the value for $\langle\tilde{\Theta}_m\rangle$, $\langle\tilde{\Theta}_m\rangle = -2f\text{acos}\left(\frac{1}{2\alpha}\right)$ for the first energy band. Figure 2-4 plots the location of the energy minimum from the classical potential, showing that the location of the minimum is almost linear in f, close to our approximation. The second energy band has the same expectation value until the potential goes from a single to a double well, as shown in Figure 2-5. Here it becomes $\langle\tilde{\Theta}_m\rangle = 2f\text{acos}\left(\frac{1}{2\alpha}\right)$. The point where this changes looks like a maximum of the second energy band. Using these values this gives Equation (2-32).

$$\frac{E(f)}{E_J} = \frac{E_q(f)}{E_J}+\left(n+\frac{1}{2}\right)2\sqrt{\frac{1}{\beta_L}\frac{E_c}{E_J}\frac{1+2\alpha}{\alpha}}$$
$$-\frac{1}{2}\beta_L\left(\frac{\alpha}{1+2\alpha}\right)^2\left[\sin\left(2f\left(\pi\mp 2\,\text{acos}\frac{1}{2\alpha}\right)\right)-2\sin\left(2f\left(\mp\text{acos}\frac{1}{2\alpha}\right)\right)\right]^2 \tag{2-32}$$

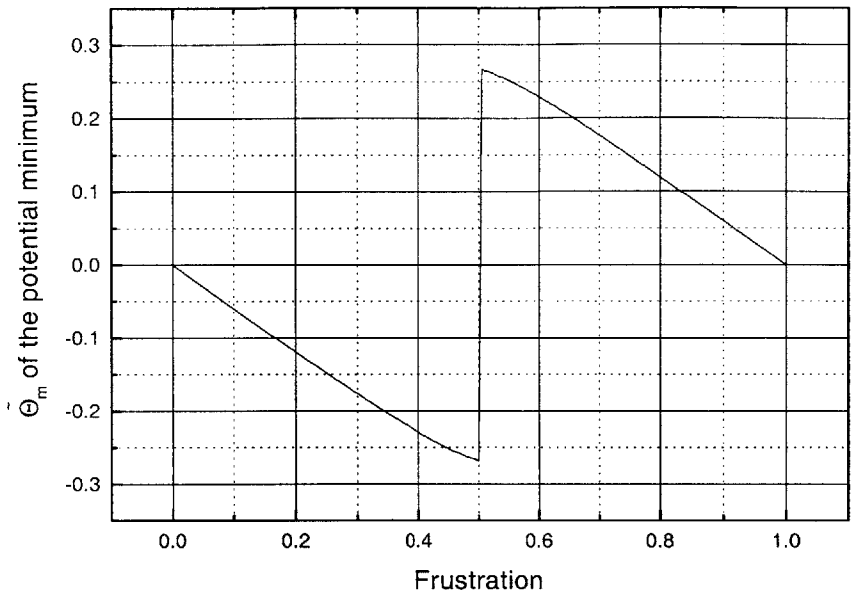

FIGURE 2-4. Θ_m for the minimum of the classic potential of the qubit versus frustration.

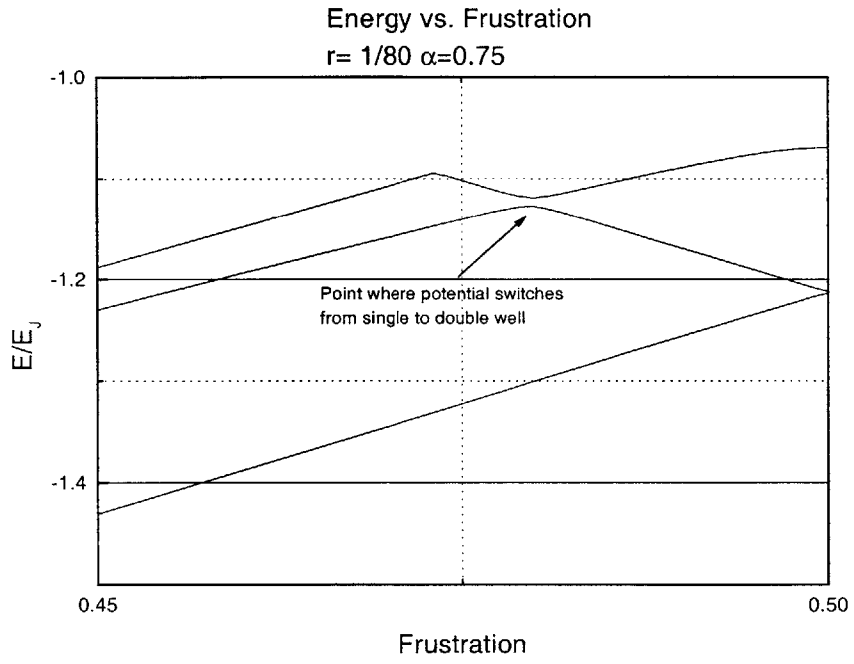

FIGURE 2-5. The energy bands versus frustration showing where the potential switches from single to double well.

We have used the expectation value of the phase, and then taken the cosine or sine of it. While this is accurate to the first order, we can use a more precise formulation of it by calculating the expectation values of the sine and cosine numerically from the wave-functions. Expanding the cosine to second order should be sufficient since the deviations are small and centered around zero, $\langle\cos\Theta\rangle = 1 - \langle\frac{\Theta^2}{2}\rangle = 1 - \frac{\Delta\Theta^2}{2}$. The sine term is more complicated, since it is not centered around zero, but applying some basic trigonometric identities can resolve that difficulty and give the proper formulation: $\langle\sin\Theta\rangle = \langle\sin(\Theta - \langle\Theta\rangle + \langle\Theta\rangle)\rangle = \langle\sin(\Theta - \langle\Theta\rangle)\cos\langle\Theta\rangle + \cos(\Theta - \langle\Theta\rangle)\sin\langle\Theta\rangle\rangle$. The first sine term inside the brackets is an odd function operating on a symmetric wavefunction centered around zero, so its expectation value can is zero with good accuracy. The second term reduces to $\langle\cos(\Theta - \langle\Theta\rangle)\rangle\sin\langle\Theta\rangle$, which is easily resolved using our previous identity to be $\left(1 - \frac{\Delta\Theta^2}{2}\right)\sin\langle\Theta\rangle$. From the Harmonic oscillator approximation of the qubit, we have the values of $\Delta\Theta_p^2$ and $\Delta\tilde{\Theta}_m^2$, given in Equation (2-33) and Equation (2-34).

$$\Delta\Theta_p^2 = \frac{1}{\sqrt{\frac{1}{\alpha}\left(\frac{E_J}{E_C}\right)}} \tag{2-33}$$

$$\Delta\tilde{\Theta}_m^2 = \frac{1}{(1+2\alpha)\sqrt{\frac{2\alpha-1}{\alpha}\left(\frac{E_J}{E_C}\right)}} \tag{2-34}$$

Applying these techniques, the Hamiltonian becomes Equation (2-35).

$$\begin{aligned} H = {} & \frac{1}{2}M_p\dot{\Theta}_p^2 + \frac{1}{2}M_m\dot{\tilde{\Theta}}_m^2 + E_J[2 + \alpha - 2\cos\Theta_p\cos\tilde{\Theta}_m - \alpha\cos(2\tilde{\Theta}_m + 2\pi f)] \\ & + \frac{\alpha}{1+2\alpha}C_jL_m^2\dot{\tilde{I}}_m^2 + \frac{1}{2}L_m\tilde{I}_m^2 \\ & - \frac{1}{2}L_mI_c^2\left(\frac{\alpha}{1+2\alpha}\right)^2(\sin(2\langle\tilde{\Theta}_m\rangle + 2\pi f)\langle\cos(2\tilde{\Theta}_m - 2\langle\tilde{\Theta}_m\rangle)\rangle - \\ & 2\langle\cos\Theta_p\rangle\langle\cos(\tilde{\Theta}_m - \langle\tilde{\Theta}_m\rangle)\rangle\sin\langle\tilde{\Theta}_m\rangle)\,\hat{}\,2 \end{aligned} \tag{2-35}$$

When applied to the final equation, Equation (2-32), we get Equation (2-36).

$$\begin{aligned} \frac{E(f)}{E_J} = {} & \frac{E_q(f)}{E_J} + \left(n + \frac{1}{2}\right)2\sqrt{\frac{1}{\beta}\frac{E_c}{E_J}\frac{1+2\alpha}{\alpha}} \\ & - \frac{1}{2}\beta\left(\frac{\alpha}{1+2\alpha}\right)^2\left[\sin\left(2f\left(\pi \mp 2\,\mathrm{acos}\frac{1}{2\alpha}\right)\right)(1 - 2\Delta\tilde{\Theta}_m^2) - 2\left(1 - \frac{\Delta\tilde{\Theta}_m^2}{2}\right)\left(1 - \frac{\Delta\Theta_p^2}{2}\right)\sin\left(2f\left(\mp\,\mathrm{acos}\frac{1}{2\alpha}\right)\right)\right]^2 \end{aligned} \tag{2-36}$$

This gives the energy bands shown in Figure 2-6, which shows the minimal change

in the energy band shape due to the inductance. The energy offset due to the harmonic oscillator term was subtracted from the inductance-influenced energy bands in order to make the comparison between the energy bands easier. The result shows very little difference between the energy bands. It is safe to say that the inductance has little effect as long as the β_L is less than 0.01 for E_J/E_C=80.

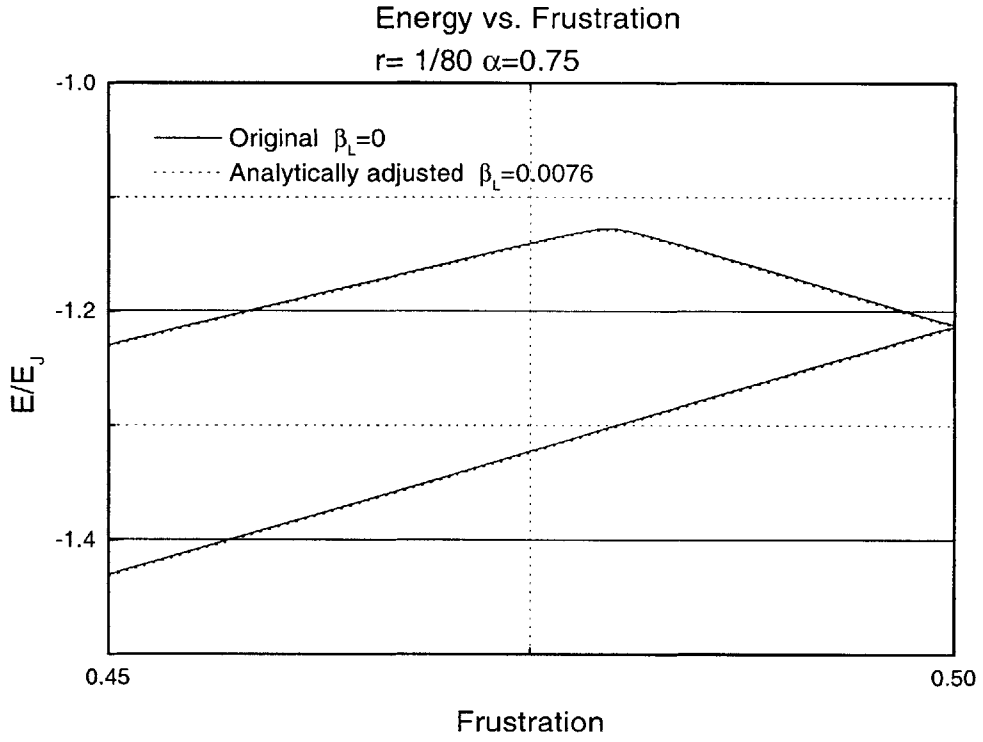

FIGURE 2-6. The energy bands versus frustration for both the original qubit and adjusted for inductive influence.

2.6 Two-state Model of the Qubit

If we consider only the first two states of the qubit, we can represent it using a tight binding model. Consider the bases to be the wavefunction localized either in one well or the other, which gives the matrix in Equation (2-37):

$$\boldsymbol{H}\begin{bmatrix} c_l \\ c_r \end{bmatrix} = \begin{bmatrix} H_{ll} & H_{lr} \\ H_{rl} & H_{rr} \end{bmatrix}\begin{bmatrix} c_l \\ c_r \end{bmatrix} = E\begin{bmatrix} c_l \\ c_r \end{bmatrix} \tag{2-37}$$

c_r and c_l are the complex coefficients of the wavefunctions on the right hand well and the left hand well, ψ_r and ψ_l. The various terms are $H_{ll} = \langle\psi_l|\hat{H}|\psi_l\rangle$, $H_{lr} = \langle\psi_l|\hat{H}|\psi_r\rangle$, $H_{rl} = \langle\psi_r|\hat{H}|\psi_l\rangle$, and $H_{rr} = \langle\psi_r|\hat{H}|\psi_r\rangle$. The eigenvalues of the Hamiltonian matrix, E, are the energies of the levels in the energy band, while the eigenvectors indicate the distribution of the states for these energies.

If the energy is offset so that 0 is the midpoint between the first two energy bands, then $\boldsymbol{H}$ becomes the form shown in Equation (2-38). Here ε is the energy bias, the energy difference between the potential energy of the left well minimum for the current value of f and its value at f=1/2. It is negative when f<1/2, and linear as long as f is near 1/2. Δ is tunneling matrix element between the two wells. The energies of the two levels are $E_{0,1} = \mp\sqrt{\varepsilon^2 + \Delta^2}$. Here, we assume that the qubit is biased slightly below f=1/2.

$$\boldsymbol{H} = \begin{bmatrix} \varepsilon & -\Delta \\ -\Delta & -\varepsilon \end{bmatrix} \tag{2-38}$$

$$v_0 = \begin{bmatrix} \cos(\theta/2) \\ \sin(\theta/2) \end{bmatrix} \qquad v_1 = \begin{bmatrix} -\sin(\theta/2) \\ \cos(\theta/2) \end{bmatrix} \tag{2-39}$$

The eigenvectors of this Hamiltonian are given in Equation (2-39), where θ=-atan (Δ/ε). It is easier to work with the eigenvectors $\begin{bmatrix} 1 \\ 0 \end{bmatrix}$ and $\begin{bmatrix} 0 \\ 1 \end{bmatrix}$, such that the first element of the vector represents occupation of the ground state of the system and the second element represents occupation of the first excited state. This can be done by multiplying the eigenvectors by the rotating matrix $\boldsymbol{D}(\theta)$ in Equation (2-40). The Hamiltonian in this rotated frame becomes $\boldsymbol{H_D}=\boldsymbol{D}^{\mathrm{T}}(\theta)\boldsymbol{H}\boldsymbol{D}(\theta)=-\sqrt{\varepsilon^2 + \Delta^2}\sigma_z$. When Δ and ε are perturbed, such as would happen with a change in frustration, this becomes $\boldsymbol{H_D}=-\sqrt{\varepsilon_0^2 + \Delta_0^2}\sigma_z+\delta\boldsymbol{H_D}$, where $\delta\boldsymbol{H_D}=\delta\varepsilon[\cos(\theta)\sigma_z-\sin(\theta)\sigma_x]-\delta\Delta[\sin(\theta)\sigma_z+\cos(\theta)\sigma_x]$. ε changes linearly with f, while Δ depends on the barrier height between the two wells, which also has an f dependence but

changes little while f remains near 0.5. Thus the qubit can be rotated by varying f.

$$D(\theta) = \begin{bmatrix} \cos\left(\frac{\theta}{2}\right) & -\sin\left(\frac{\theta}{2}\right) \\ \sin\left(\frac{\theta}{2}\right) & \cos\left(\frac{\theta}{2}\right) \end{bmatrix} \tag{2-40}$$

2.7 Time-Dependent Perturbation of the Qubit

The previous section shows that changes in the magnetic field bias can alter the state of the PC qubit. Numerical simulations provide some insight into how this works. As shown in Section 2.6, the steady-state qubit has a σ_z rotation in its basis states. Disturbing its steady-state bias results in a σ_x rotation dependent on the change in the bias. A quantum mechanical simulation of this rotation provides insight into the workings of the qubit and assists in the development of experimental methods to manipulate the qubit. We will start the qubit at f=0.495, with the energy eigenvalues of E_i^{Ψ} and eigenvectors of ψ_i, where i=0,1,... are the ground state, the first excited state, and then higher energy levels. The time evolution of each eigenstate is given by Equation (2-41):

$$\psi_i(t) = \psi_i(0)\exp\left(-i\frac{E_i^{\Psi}}{\hbar}t\right) \tag{2-41}$$

The overall wavefunction has the form $\Psi = \sum a_i\psi_i$. The difference in energies gives different phase rotations to each eigenstate, which gives rise to the σ_z rotation discussed earlier. Changing the bias to f=0.5 at t_0 results in a Hamiltonian with a different set of eigenvectors, ϕ_i, with their own energy eigenvalues, E_i^{ϕ}. When the bias is changed to this value, the old wavefunction is projected onto the new basis states, and the new states follow a time evolution similar to the form of Equation (2-41), but with different values. The new wavefunction thus follows the form of Equation (2-42).

$$\Psi(t) = \sum_i \langle\varphi_i|\Psi(t_0)\rangle\varphi_i\exp\left(-i\frac{E_i^{\phi}}{\hbar}t\right) \tag{2-42}$$

When this is projected back onto the ψ_i eigenvectors, the coefficients of the ψ_i eigenvectors have rotated according to the time spent at the f=0.5 bias. At f=0.5, the two

eigenvectors are the symmetric and antisymmetric populations of both wells, while at f=0.495, they are the population of one well or the other. It is qualitatively obvious, given that the ground state and the first excited state rotate at different rates at f=0.5, that the first two eigenvectors at f=0.495 will alternate in population when moved to f=0.5. Clearly, $\exp(-i\omega_0 t)\begin{bmatrix}0.5\\0.5\end{bmatrix}$ and $\exp(-i\omega_1 t)\begin{bmatrix}0.5\\-0.5\end{bmatrix}$ will rotate through $\begin{bmatrix}1\\0\end{bmatrix}$ and $\begin{bmatrix}0\\1\end{bmatrix}$ at a frequency of $(\omega_1-\omega_0)/2$, as Equation (2-43) shows.

$$\Psi(t) = e^{-i\omega_0 t}\begin{bmatrix}0.5\\0.5\end{bmatrix} + e^{-i\omega_1 t}\begin{bmatrix}0.5\\-0.5\end{bmatrix}$$

$$\Psi(t) = e^{-i\left(\frac{\omega_0+\omega_1}{2}\right)t}\left[e^{i\left(\frac{\omega_1-\omega_0}{2}\right)t}\begin{bmatrix}0.5\\0.5\end{bmatrix} + e^{-i\left(\frac{\omega_1-\omega_0}{2}\right)t}\begin{bmatrix}0.5\\-0.5\end{bmatrix}\right] \qquad \textbf{(2-43)}$$

$$\Psi(t)) = e^{-i\left(\frac{\omega_0+\omega_1}{2}\right)t}\begin{bmatrix}\cos\left(\frac{\omega_1-\omega_0}{2}t\right)\\ \sin\left(\frac{\omega_1-\omega_0}{2}t\right)\end{bmatrix}$$

This problem can be solved numerically, starting with a solution of the Hamiltonian matrix as in Equation (2-9). Then, following the method discussed above, the wavefunction is projected onto its new basis, time-evolved, then projected back, resulting in a rotation of the qubit between its $|0\rangle$ and $|1\rangle$ states in the basis of f=0.495.

This can be applied to more complex changes in f than the simple pulse from f=0.495 to 0.5. Instead, the frustration could oscillate with an amplitude of 0.001 Φ_0 at a frequency equal to the level splitting, providing an on-resonance driving field. This should also cause a σ_x rotation between the two states. Numerically, this is solved by discretizing the sine wave in time and solving the eigenstates and eigenvectors at each discretized point and then evolving.

The Bloch sphere represents the complete complex phase of a two state system, $\alpha|0\rangle+\beta|1\rangle$, in the spherical coordinate system: $r=|\alpha|^2+|\beta|^2$, $\phi=\text{atan}(Im(\beta/\alpha)/Re(\beta/\alpha))$, and $\theta=2\tan^{-1}(|\beta|/|\alpha|)$. Usually, an arrow connects the origin at r=0 with the point on the Bloch sphere representing the state of the quantum system. As long as the system is truly two

state, r=1, thus resulting in a sphere of possible values for the qubit. When the arrow points straight up, α=1 and β=0. When it is straight down, α=0 and β=1. In between, θ gives the relative population of the two states, while ϕ gives the relative phase between them. σ_x, σ_y, and σ_z rotations are rotations around the x, y, and z axes of the Bloch sphere respectively. Figure 2-7 shows Bloch sphere diagrams with the paths of the qubit for a pulse input and for an oscillating input. The pulse input causes a fast, straight evolution, mostly σ_x with some deviations due to the fact that we began at a flux bias where the eigenvectors were not purely states of opposite circulating current. The oscillating input causes a slower rotation that also precesses at the rate of the σ_z rotation.

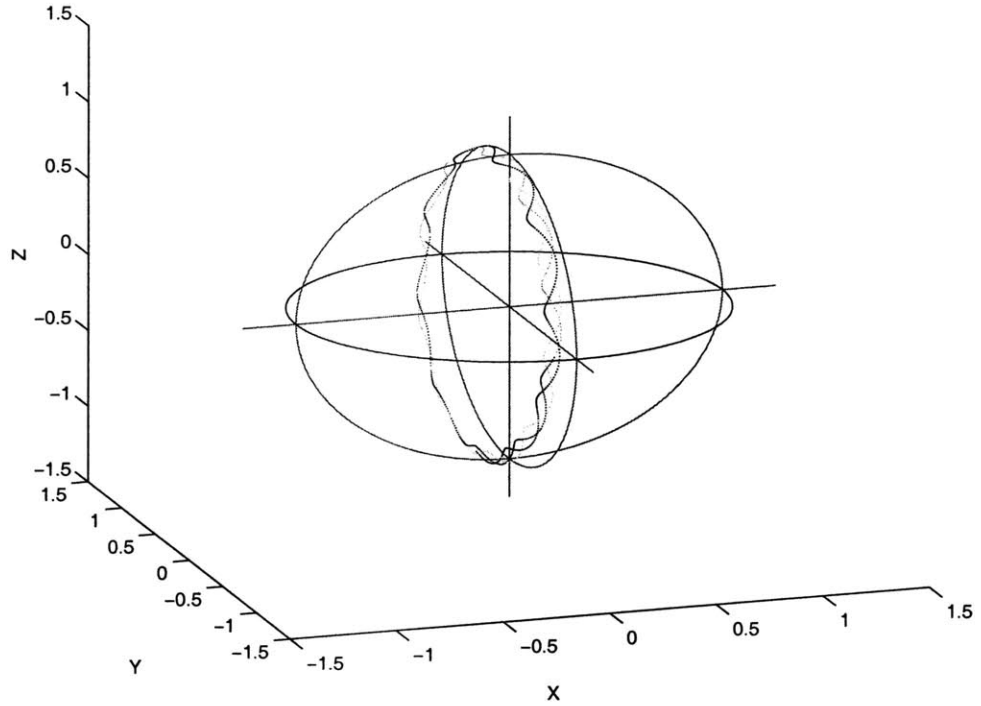

(a)

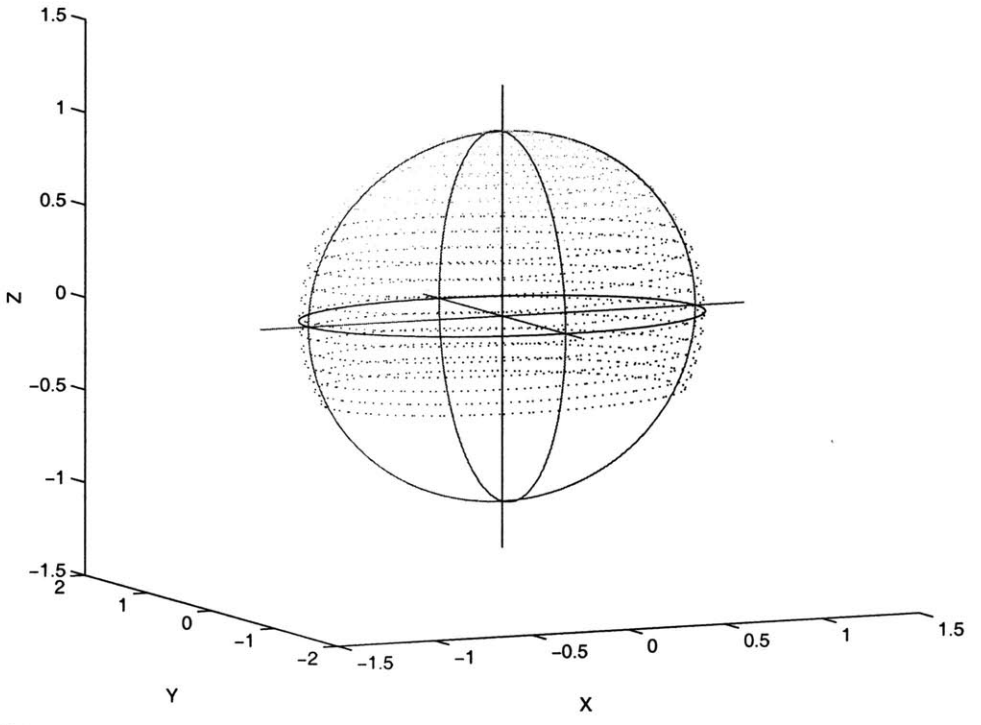

(b)

FIGURE 2-7. The time evolution of the qubit under different perturbations. (a) shows the result of a pulse function from 0.495 Φ_0 to 0.500 Φ_0, while (b) shows the result of an oscillating field around 0.495 Φ_0, with an amplitude of 0.001Φ_0.

2.8 Fabrication requirements

In trying to manufacture a qubit implementation, we must determine the range of parameters which will give a suitable quantum system so that an appropriate manufacturing process can be found. We utilize the foundries available at Lincoln Laboratory, TRW, and HYPRES for niobium trilayer superconducting circuits. If any or all can produce the required parameters, then manufacturing the persistent current qubit in niobium is possible.

2.8.1 E_J/E_C

The ratio between the Josephson energy and the charging energy of each junction determines the regime of operation. If E_J/E_C is too small, the circuit will be in the charging regime and will act like a charge qubit. If it is too large, the device will act like a current-biased Josephson junction qubit, where the two lowest energy states are in the same well with no measurable difference between them, rather than in different wells which give circulating currents in opposite directions. The ratio necessary for the persistent current qubit to attain the desired mode of operation is approximately 100, with some flexibility for variation between 10 and 1000. Figure 2-8 shows the energy bands for various E_J/E_C values. The slope of the band versus frustration indicates the circulating current. The circulating currents of the ground state and first excited state are in opposite directions, producing a clear difference in magnetic field produced by the qubit, only when the first two energy levels have opposite slopes. When E_J/E_C=1, the system is in the charging regime, and the bands do not vary with frustration, although they do vary with voltage, which is not shown. For E_J/E_C=10000, the first and second bands are parallel at f=0.495 (the preferred bias point), representing two harmonic oscillator states in the same well and with the same circulating current. It's only for E_J/E_C~100 that the first two states vary with f and have opposite circulating current. All these results assume α=0.8.

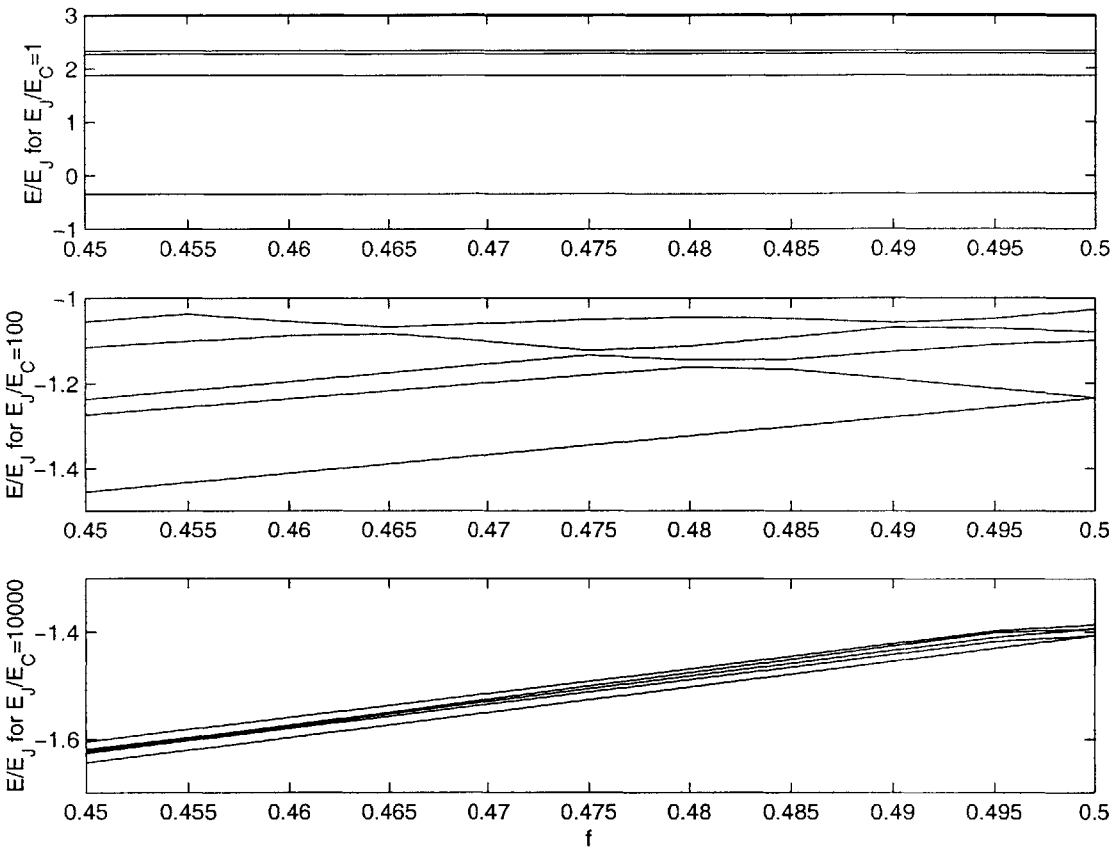

FIGURE 2-8. Energy bands for E_J/E_C = 1, 100, and 10000. Values between 10 and 1000 are suitable for a persistent current qubit.

Most of the other parameters, such as the tunneling frequency, the level splitting, and the Rabi frequency, have a strong dependence on the E_J/E_C ratio. Equation (2-44) gives the value for E_J/E_C in terms of junction size and critical current density. Here p is the length of the junction, while J_C is the critical current density. Figure 2-9 shows the range of values which give the appropriate E_J/E_C ratio.

$$\frac{E_J}{E_C} = \frac{\frac{\Phi_0}{2\pi}I_c}{\frac{e^2}{2C_j}} = \frac{\Phi_0}{\pi e^2}(40fF/\mu m^2)p^4 J_C \qquad \textbf{(2-44)}$$

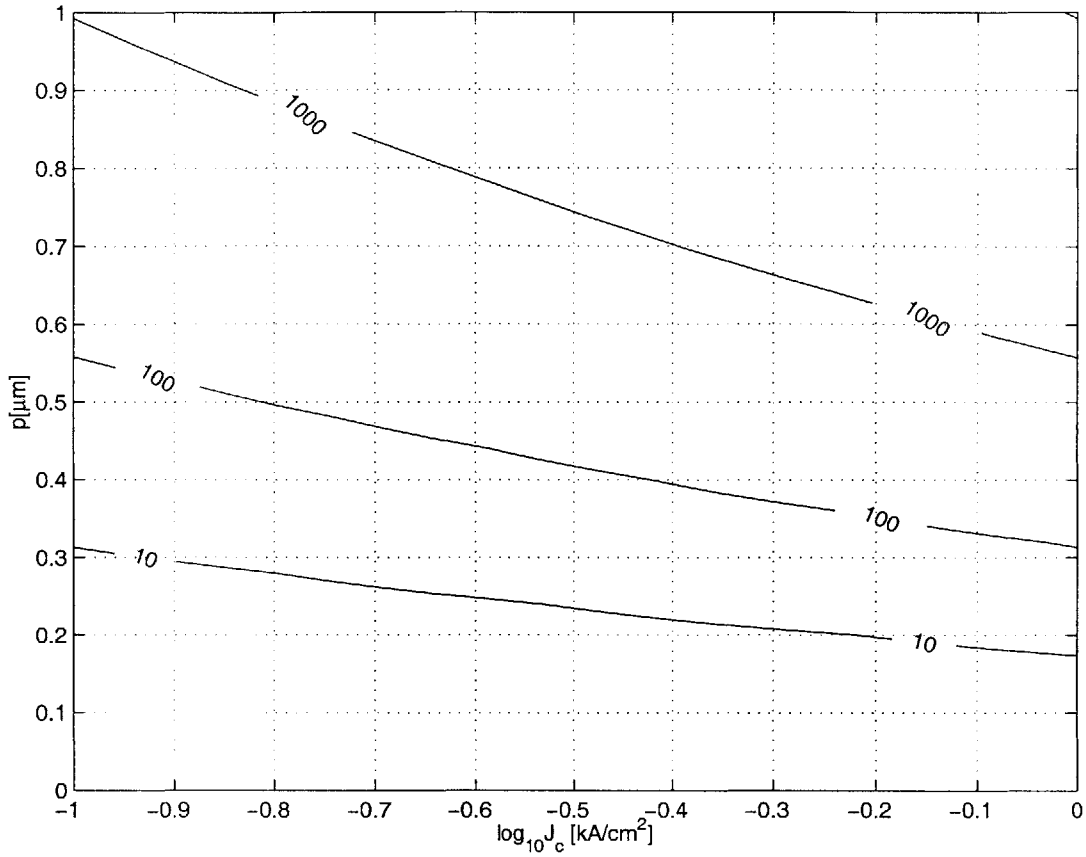

FIGURE 2-9. E_J/E_C plotted against junction length and critical current density. Values between 10 and 1000 are suitable for a persistent current qubit.

2.8.2 β_L requirements

The persistent current qubit design assumes that the quantum system has no self inductance. This is obviously not completely true, since any superconducting loop will have some inductance. The ratio of the loop inductance, L_q, to the Josephson inductance, L_J, is called β_L. As long as the inductance is negligible, *i.e.* $\beta_L << 1$, then the quantum system's characteristics are not significantly affected by the inductance. The requirement we'll assume is that β_L must be less than 0.01. In order to calculate β_L, we'll assume that minimum loop diameter is four times the length of the junction, and calculate the inductance from the formula $L_m = \mu_0 d$ (which holds as long as the wire width is of the same order as the distance between the wires). This is a worst case estimate, as it should be possible to reduce the loop size with some refinement. L_J comes directly from the junction charac-

teristics, $L_J=\Phi_0/(2\pi I_c)$. This gives the formula for β_L which is shown in Equation (2-45).

$$\beta_L = \frac{L_q}{L_J} = \mu_0 d \frac{2\pi I_c}{\Phi_0} = \frac{8\pi\mu_0}{\Phi_0} p^3 J_c \tag{2-45}$$

With these restrictions, the contour in Figure 2-10 shows which values of junction length and current density gives the proper β_L.

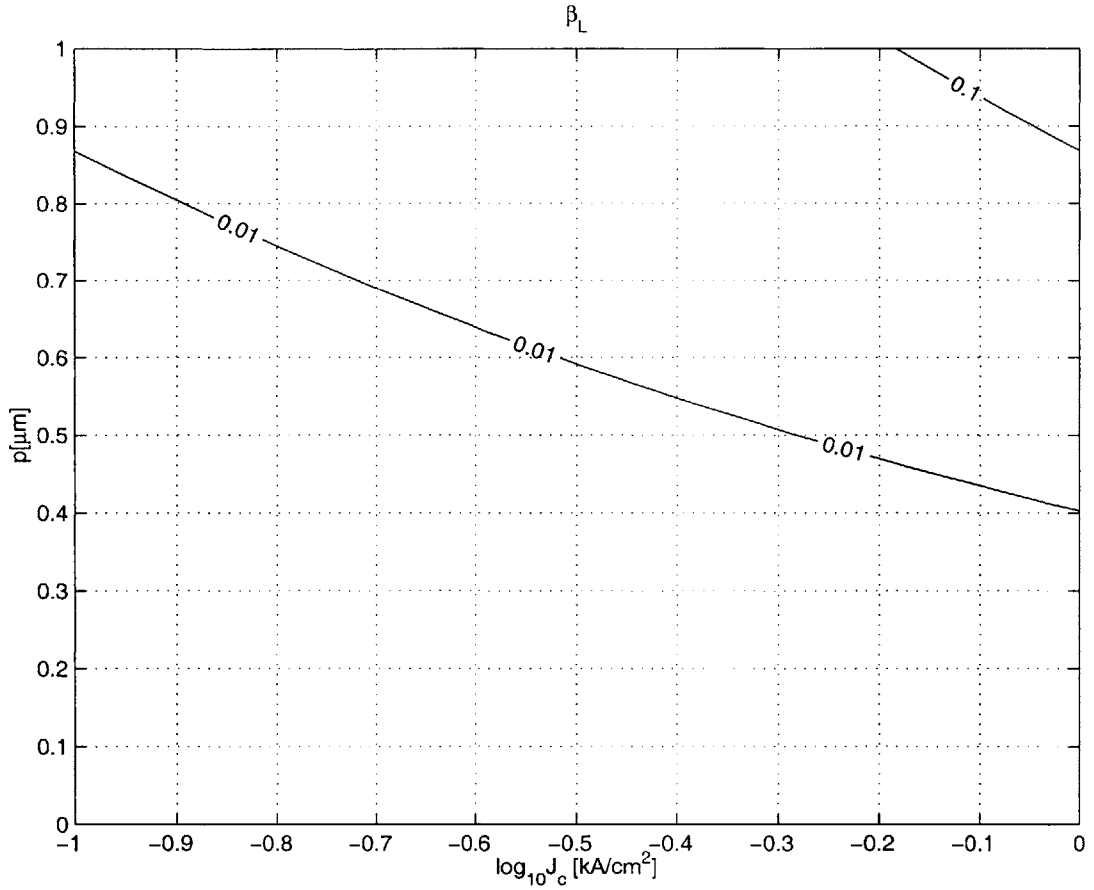

FIGURE 2-10. β_L plotted against junction length and critical current density. Values less than 0.01 are suitable for a persistent current qubit. The ring diameter is assumed to be $4p$.

2.8.3 Operation Parameters

Considering α and E_J/E_C to be the dominant parameters to ensure that the design operates as a persistent current qubit, what it takes to manipulate the PC qubit also depends on its parameters. The first of these is the level splitting between the first two energy levels at the bias point (we will hold the flux bias point of the qubit at f=0.495). This determines the frequency at which the qubit must be driven. This must be of the

same order of the tunnel splitting at f=0.5, to ensure that the two wavefunctions have enough overlap to allow driving. Looking at Figure 2-11, we can see that the requirements for the first two parameters will keep the level splitting within the desired frequency range. This value is calculated from simulations of the quantum system, as in Section 2.3.

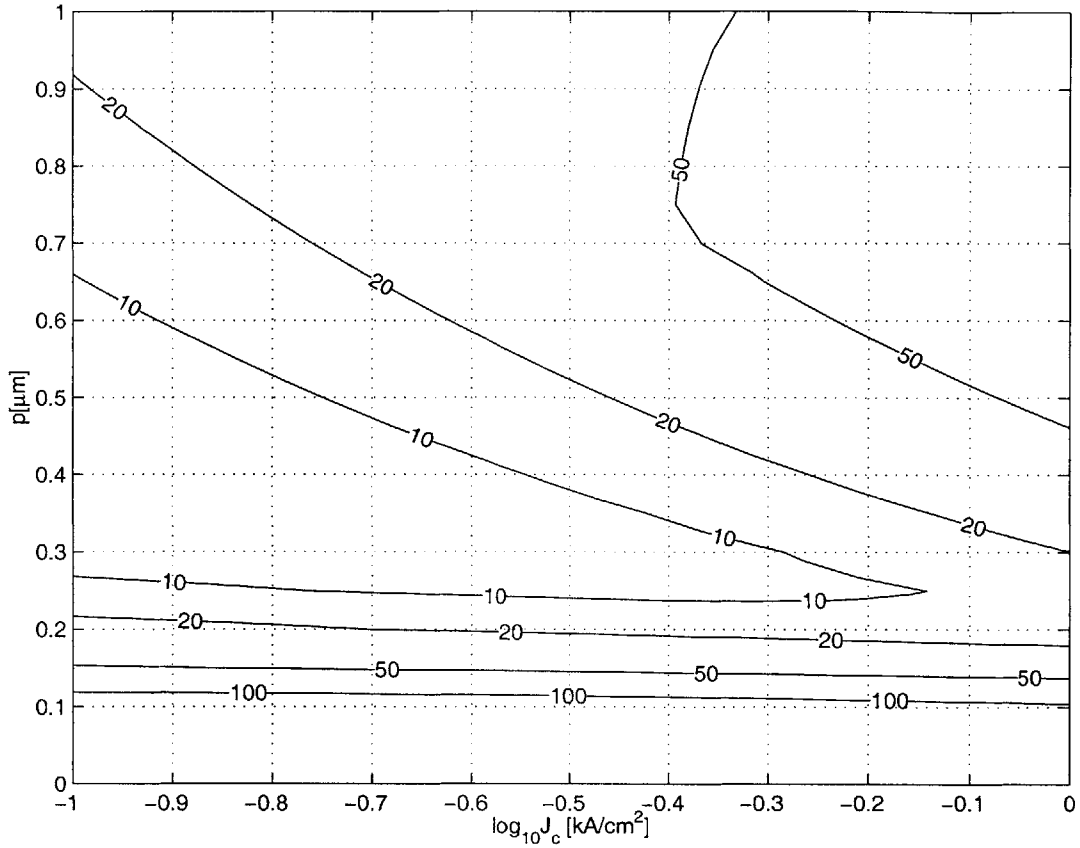

FIGURE 2-11. Energy difference, in GHz, between first and second levels at f=0.495 in the PC qubit, shown as a contour on axes of junction length and critical current density.

Starting with $\delta \boldsymbol{H}_D = \delta\varepsilon[\cos(\theta)\sigma_z - \sin(\theta)\sigma_x] - \delta\Delta[\sin(\theta)\sigma_z + \cos(\theta)\sigma_x]$, which appeared in Section 2.6, we can follow the method used in Appendix C of [24] in order to calculate the Rabi frequency. Equation (2-46) follows this through to get the value for $\delta\varepsilon$.

$$\delta\varepsilon = \frac{\partial\varepsilon}{\partial f}\delta f$$
$$\frac{\partial}{\partial f}\varepsilon = 2\pi\alpha E_J \sin(2\varphi_m^0) = 2\pi E_J\sqrt{1-\frac{1}{4\alpha^2}} \qquad \textbf{(2-46)}$$

We can use the definition that $\sin(\theta)=-\Delta_0/(\varepsilon_0^2+\Delta_0^2)^{1/2}$ to give Equation (2-47).

$$\nu_{Rabi} = \frac{\delta\varepsilon}{h}\sin(\theta)$$

$$\nu_{Rabi} = \delta\varepsilon\left(\frac{\Delta_0}{\sqrt{\varepsilon_0^2+\Delta_0^2}}\right) = 4.9\frac{E_J}{h}\delta f\frac{\Delta_0}{\sqrt{\varepsilon_0^2+\Delta_0^2}} \quad \textbf{(2-47)}$$

Figure 2-12 plots the Rabi frequency of the device when driven at the frequency of the level splitting with an oscillating field of amplitude $0.001\Phi_0$. The basic requirement for quantum computation is that the Rabi frequency be 10^4 times faster than the decoherence times. Useful experiments can be done when the operation time is only 10 times faster. An operation time of up to 100 MHz is available in the regime where other considerations have already constrained the qubit parameters.

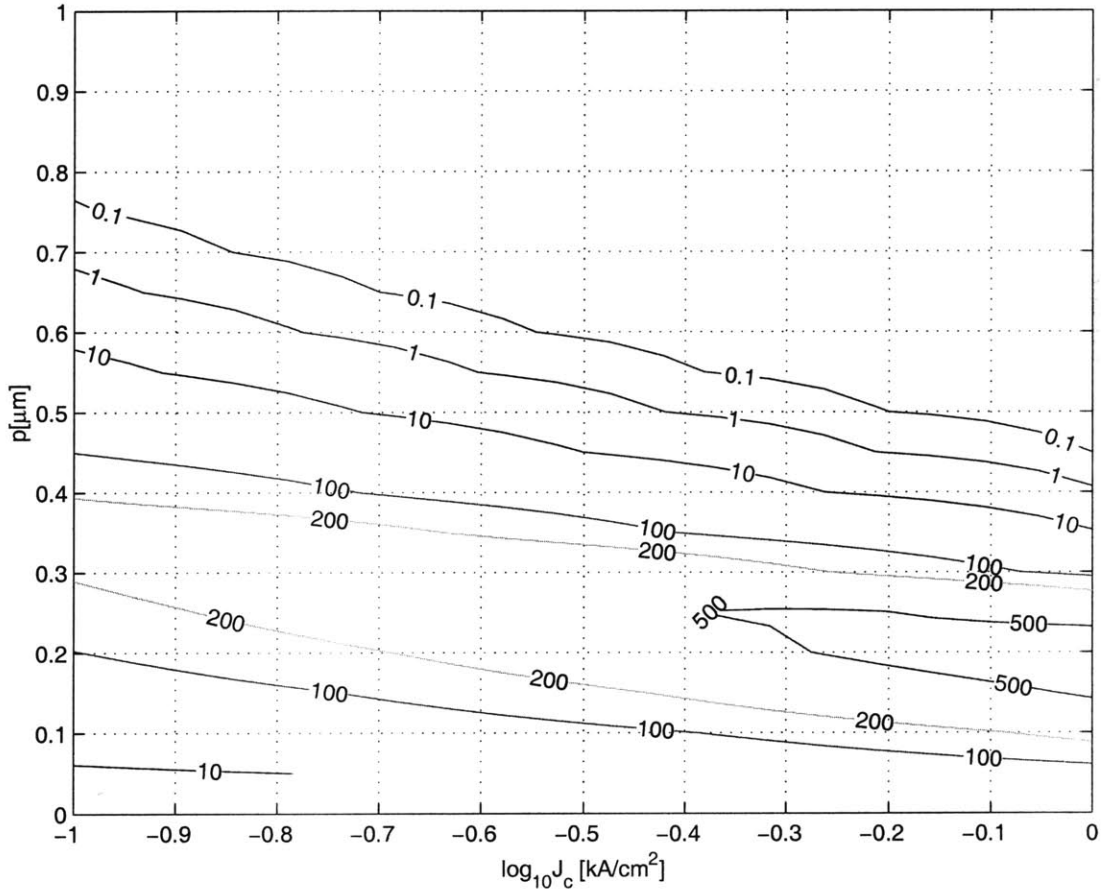

FIGURE 2-12. Rabi frequency of the PC qubit, in MHz, numerically calculated when f=0.495 and the applied oscillating field is $0.001\Phi_0$ with a frequency of the energy difference between levels 1 and 2, shown as a contour on axes of junction length and critical current density.

2.8.4 Subgap Resistance

At nonzero temperatures, normal electrons (quasiparticles) co-exist with super-electrons in the superconductor due to thermal activation above the energy gap. These quasiparticles can quantum mechanically tunnel across the insulating barrier of the Josephson junction, thus seeing a resistive normal channel parallel to the superconductive channel. When the Josephson junction is current biased below its critical current, there are few quasiparticles to tunnel across the channel, and it has an effective resistance, called the subgap resistance, inversely proportional to the number of quasiparticles, which decreases exponentially with temperature. Thus, $R_{sg} \approx R_n \exp(\Delta_0/(k_B T))$, where R_n is the normal resistance, and Δ_0 is the energy gap. This assumes that the junction perfectly follows BCS theory, ignoring defects in the junction. The quality factor of the junction, Q, estimates the damping of the junction and is equal to $\omega_0 R C_j$, where ω_0 is the plasma frequency, R is the junction's resistance, and C_j is the junction capacitance. R is ideally the subgap resistance, but it must be taken in parallel with any shunting resistance which the environment provides at the plasma frequency of the junction. For a junction whose leads are directly connected to the environment, this is usually 100 Ω or smaller. Actually measuring the subgap resistance is difficult [56,58], since it is difficult to avoid an environmental shunting resistance on the order of 1 MΩ. At best, a minimum subgap resistance value can be found, and measurements of the Lincoln Laboratory junctions indicate that the subgap resistance is greater than 10 MΩ.

The qubit has no direct connection to the environment, so the shunting impedance is coupled to the circuit through the SQUID leads. Additionally, the qubit design is a loop with three junctions, and rather than using the subgap resistance and capacitance of each of the three junctions individually, they must be considered together and for each dimension. We've determined how to do this for the capacitance when finding M_p and M_m, the effective masses in the φ_p and φ_m directions: $C_p=2C_j$ and $C_m=(2+4\alpha_C)C_j$. It is plausible to do the same for the resistance by calculating the amount of dissipation caused by φ_p and φ_m respectively, which can be solved quite simply. Each junction causes V^2/R power dis-

sipation, where $V=(\Phi_0/2\pi)(d\varphi/dt)$, which is shown in Equation (2-48).

$$P = \frac{V_1^2}{R_1} + \frac{V_2^2}{R_2} + \frac{V_3^2}{R_3} = \left(\frac{\Phi_0}{2\pi}\right)^2\left(\frac{\dot{\varphi}_1^2}{R_1} + \frac{\dot{\varphi}_2^2}{R_2} + \frac{\dot{\varphi}_3^2}{R_3}\right) \tag{2-48}$$

By replacing the gauge-invariant phase difference for each junction with their φ_p and φ_m equivalents, we get Equation (2-49).

$$P = \left(\frac{\Phi_0}{2\pi}\right)^2\left(\frac{(\dot{\varphi}_p + \dot{\varphi}_m)^2}{R_{sg}} + \frac{(\dot{\varphi}_p - \dot{\varphi}_m)^2}{R_{sg}} + \frac{(2\dot{\varphi}_m)^2}{R_{sg}/\alpha}\right) \tag{2-49}$$

R_{sg} is the subgap resistance of the larger two junctions, which are assumed to be equivalent. Since the critical current is αI_c in the smaller junction, and the resistance is inversely related to the critical current, R_{sg}/α is the subgap resistance of the smaller junction. Separating out φ_p and φ_m gives us R_p and R_m in Equation (2-50).

$$\begin{aligned} P &= \left(\frac{\Phi_0}{2\pi}\right)^2\left(\frac{2\dot{\varphi}_p^2}{R_{sg}} + \frac{(2+4\alpha)\dot{\varphi}_m^2}{R_{sg}}\right) \\ R_p &= \frac{R_{sg}}{2} \qquad R_m = \frac{R_{sg}}{2+4\alpha} \end{aligned} \tag{2-50}$$

Johnson-Nyquist noise across these subgap resistances generates fluctuations in the normal current, which causes decoherence to the qubit. Lin Tian has estimated [64] the decoherence due to a subgap resistance to be Equation (2-51), although in the form shown here the subgap resistance has been replaced with the qubit equivalent, R_m.

$$\tau_\phi = \frac{2e^2R_m}{\hbar\nu}\left(\frac{\varepsilon}{\Delta}\right)^2 \qquad \tau_r = \frac{2e^2R_m}{k_BT} \tag{2-51}$$

While R_p does contribute to dissipation, R_m's role in the qubit is closest to that of R_{sg} for the single junction. Even if R_p contributes in the same way as R_m, R_m's smaller size (less than half of R_p, since α is always greater than 0.5) would cause it to be the predominant source of decoherence. ε and Δ are the energy bias and tunnel splitting used in Section 1.4, while ν is the frequency of the total energy difference. If $R_{sg}>10^{10}$ Ω, then the dephasing time due to the subgap resistance should not interfere with the ability to perform 10^4 operations. A subgap resistance of 10^7 Ω should be sufficient to observe Rabi oscillations.

2.9 The Lincoln Laboratory Fabrication Process

The three-junction qubit which we use is fabricated in Lincoln Laboratory's foundry, using a doubly-planarized trilayer process. The trilayer process is a standard fabrication technique for niobium superconductive electronics which has been refined over more than a decade.

2.9.1 The trilayer

The Lincoln process [45] starts with a 150 mm diameter silicon substrate with a thermally grown oxide layer 0.5 μm thick. On top of this is sputtered a layer of niobium 0.15 μm thick to form the base electrode of the Josephson junctions. This layer covers the entire surface of the wafer, and is called M2. On top of this is sputtered 6 nm of aluminum, which is then oxidized to form the insulating barrier of Al_2O_3. The amount of oxidation is adjusted according to the desired current density. Any unoxidized aluminum becomes superconducting along with the niobium according to the proximity effect [48]. On top of the oxidized aluminum a layer of 0.25 microns of niobium is sputtered, forming the counter-electrode, called M3. At this point the entire wafer is one large Josephson junction, which is next reduced to the desired Josephson junctions by photolithographic patterning followed by reactive ion etching. The first etch removes M3 except for where the junctions are located. Then a wet etch removes the aluminum oxide, which is only exposed where the M3 has already been removed. Finally, the M2 is patterned with photoresist and etched away anywhere there is no photoresist to protect it. M2 serves a dual purpose: it's a wiring layer as well as the base electrode of the junctions. All these steps are in parts (a) through (f) of Figure 2-13.

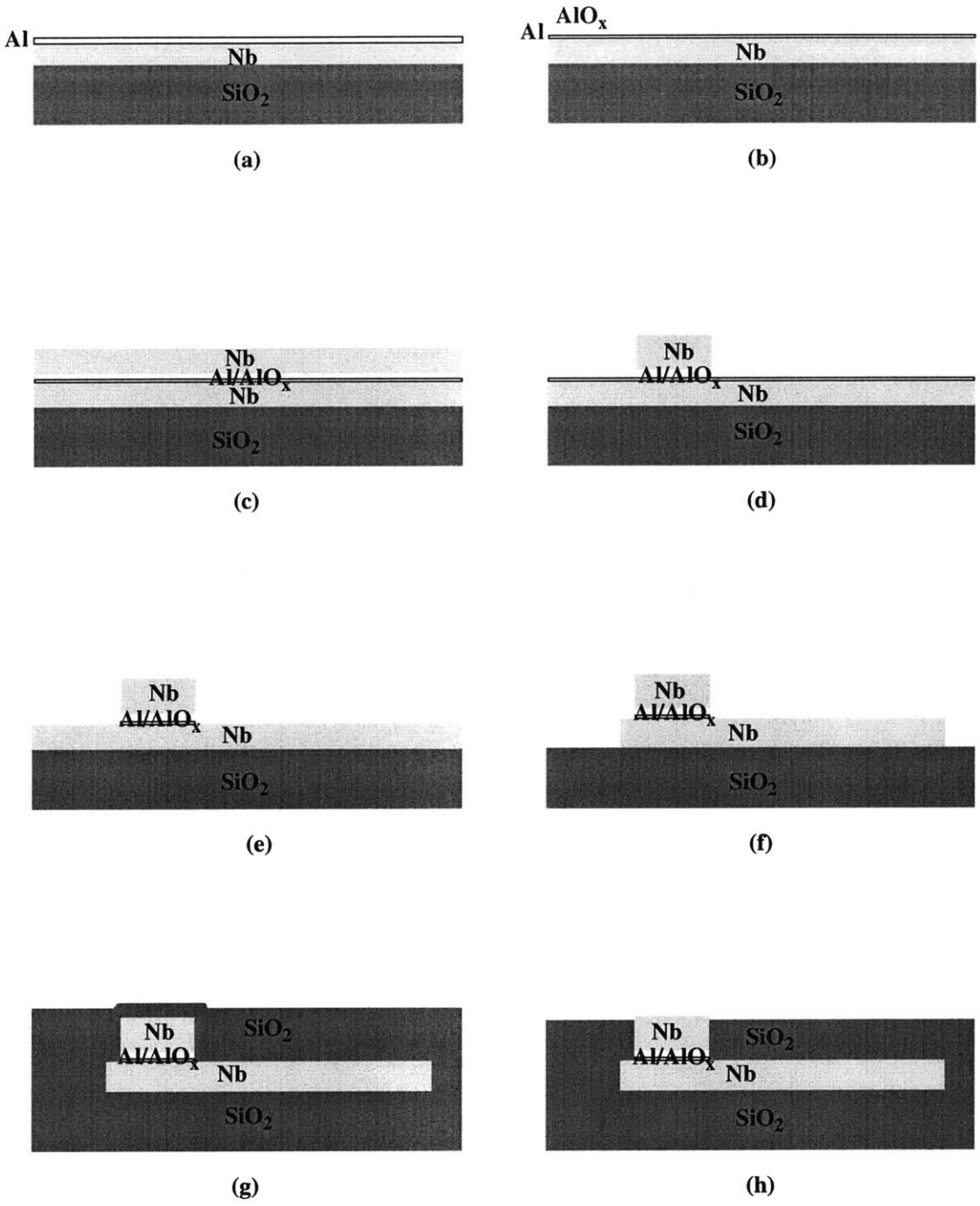

FIGURE 2-13. A cross-section of the Lincoln Laboratory DPARTS (Doubly Planarized All-Refractory Technology for Superconductive electronics) fabrication process. (a) shows the deposited aluminum on top of niobium. (b) shows the AlO_x grown on top of the Al. (c) is after the deposition of the counter-electrode niobium. (d) shows the result after the counter-electrode is etched to define the junctions. Then the AlO_x is wet etched, as shown in (e), after which the base-electrode is etched to define the wiring layer, as shown in (f). Then a layer of SiO_2 is deposited by PECVD, in (g), and then polished by CMP to expose the counter-electrode, as in (h).

2.9.2 Double planarization and wiring

Once the junctions and the first wiring layers have been defined by etching M2 and M3 respectively, a thick layer of silicon oxide is deposited by PECVD (plasma enhanced chemical vapor deposition). This is then planarized by CMP (chemical mechanical polish), which grinds away the oxide to expose M3. This is shown in Figure 2-13(g and h). Lift-off is used to pattern the resistors (R1), by creating a photolithographic pattern which has no photoresist in those areas where the resistors will be. Electron beam evaporation deposits 10 nm of titanium, then 90 nm of palladium. Acetone removes the resist, taking the excess resistor material with it. The resistors have a resistivity of 0.6 Ω/sq. Then vias are defined by photolithographic patterning, then etched into the oxide by rf RIE. Another layer of niobium (M4) is deposited by sputtering a thickness of 0.25 μm. M4 directly contacts both M3 and R1 (which are left exposed thus far in the process) in order to connect the junctions and resistors to the circuit. It also connects to M2 through the vias. Then the M4 is patterned by photolithography and etched by RIE. (The result is shown in Figure 2-14.)

This is followed by more oxide deposition, another planarization, etching more vias, the deposition of another 0.4 μm of niobium (M5, the ground plane), which is then patterned and etched. These remaining steps are done the same way as those described above. The final step uses lift-off to form contact pads (30 nm titanium, 360 nm palladium, 50 nm gold) for off-chip connections.

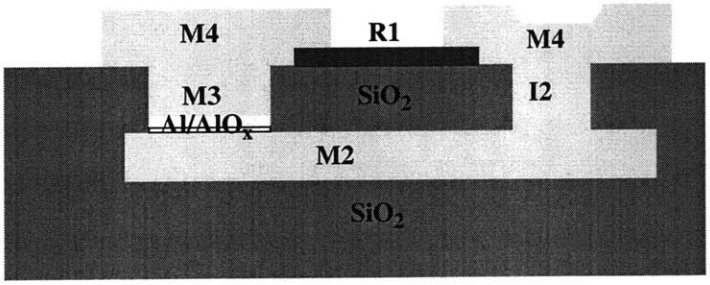

FIGURE 2-14. The Lincoln Laboratory DPARTS (Doubly Planarized All-Refractory Technology for Superconductive electronics) fabrication process, after the addition of the R1 and M4 layers.

2.9.3 Variance in Critical Parameters

2.9.3.1 Resistivity of R1

The Ti/Pd resistors presented two main concerns. The first was that the Ti layer, used primarily to provide adhesion for the Pd layer, would go superconducting at low temperatures. Titanium normally goes superconducting at 390 mK, but the resistors used in this process maintained their resistivity all the way down to 15 mK. This may be due to alloying of the titanium and palladium, or the titanium layer is thinner than the coherence length. The second concern is due to the lift-off process used to form the resistors. The narrower the resistor, the greater the resistance, but when the resistor metals are evaporated into a narrow opening in the resist, there is some physical undercut of the resistors (due to metal being removed along with the resist) and greater resistivity at the edge of the resistors. Thus the design rules give a formula for calculating resistance which depends on the width of the resistor.

2.9.3.2 Capacitance between M2 and M4

Many of our designs require a capacitor, such as for the shunt for our SQUIDs, or for the filter for our oscillators. These uses of capacitances are uncommon for RSFQ, which is what the Lincoln Laboratory DPARTS process was designed for. The simplest way to design a capacitor is simply to put two metal layers on top of one another, in this case M2 and M4. However, the capacitance of this is not well measured and must be calculated using the formula $C=A(\varepsilon/d)$. $C_0=\varepsilon/d=0.2$ fF/μm^2 is the specific capacitance. Thus far the experiments have indicated that this value of the specific capacitance is close, but the variance has yet to be properly measured.

2.9.3.3 Critical Current Density

Critical current density is one of the most exhaustively measured and continuously refined metrics of fabrication quality. Unfortunately, most work has aimed at large critical current densities, on the order of 1-10 kA/cm^2. For superconducting circuits with quantum properties, the critical current density must go in the other direction, aiming for 100-500 A/cm^2. The exact process to hit these densities is not completely refined yet, so many of the wafers are significantly off the mark. Wafers fabricated for 100 A/cm^2 may be

somewhere between 67 A/cm^2 and 200 A/cm^2, while those fabricated for 500 A/cm^2 may range between 350 A/cm^2 and 750 A/cm^2. Since each of these represents a slightly different aluminum sputtering and thermal oxidation recipe in an attempt to hit the target precisely, there are not enough wafers completed using the same recipe to accurately calculate a variance. Lincoln Laboratory's fabrication team should be able to target the critical current densities more accurately within the next few of fabrication runs.

What is more easily done is calculating the variance in the critical current density across the wafer, measuring Josephson junctions located in various locations on the wafer. This comes to about 5%, which is a reasonably small variance across a wafer [62]. The variance of the critical current density across any 5 mm by 5 mm chip is even smaller.

2.9.3.4 Undercutting and Anodization

Defining the critical current of a Josephson junction requires knowing both the critical current density and the size of the junction. Lincoln's process, and indeed, most trilayer processes which create small (submicron) junctions, encounter a problem with undercutting [62]. The junctions appear to be smaller than the defined junction size by about 0.3 or 0.4 μm in each dimension. In SEM images, the junction actually appears to be smaller, with rounded edges. The cause of undercutting is not well known, although a possible explanation is cracking at the junction edge which causes separation between the M3 layer and the oxide. This is represented in Figure 2-15(a) and (b) as a greater distance between the two metal layers, as if the tunneling barrier is thicker. Since the critical current density falls off exponentially with the thickness of the barrier, while the specific capacitance is inversely proportional to the thickness of the insulator between electrodes, then the effective junction size would look much smaller to the critical current, which cannot tunnel at all through the thicker barrier, than to the capacitance, which sees the thicker barrier only as a slightly smaller capacitance. The α is also affected by the undercut, as the area reduction is not directly proportional to the original area, and α must be recalculated from the new sizes. In fact, even the approximation that the undercutting reduces each dimension by 0.3 or 0.4 μm breaks down for small junctions, as the corners see a greater undercut which rounds the shape of the junction. Additionally, the difference between the critical current reduction and the capacitance reduction requires two different

values, α and α_C, for the ratio of the smaller critical current and smaller capacitance, respectively. While this complicates matters, it is perfectly possible to incorporate these separate variables into the qubit Hamiltonian, and in fact, one of the earliest simulations, programmed by Lin Tian, allows for different values for these two variables.

In order to reduce the variance in critical currents caused by undercutting, an anodization process was introduced directly after the patterning of the M3 layer, as shown in Figure 2-15 (c) and (d). The wafer was placed in a solution of tartaric acid and ammonium hydroxide, where it was connected to a power supply (with a Pt wafer on the other side), so that it served as the anode. This fully oxidized any exposed niobium, as well as the exposed aluminum oxide. Then the remaining processing steps were performed. The anodization did not remove the undercutting (anodization itself might be expected to eat away at the material on the junction's sides), but it did reduce the variance in the undercutting, making it a constant 0.3 on large junctions. Smaller junctions, at 1 μm or less, are still rounded by the undercutting, and continue to show additional variance. Moreover, the difference in the undercutting relevant to the critical current and the undercutting relevant to the capacitance is still noticeable. Lincoln Laboratory is continuing to work on reducing the undercutting in their process and make it more uniform when it does occur.

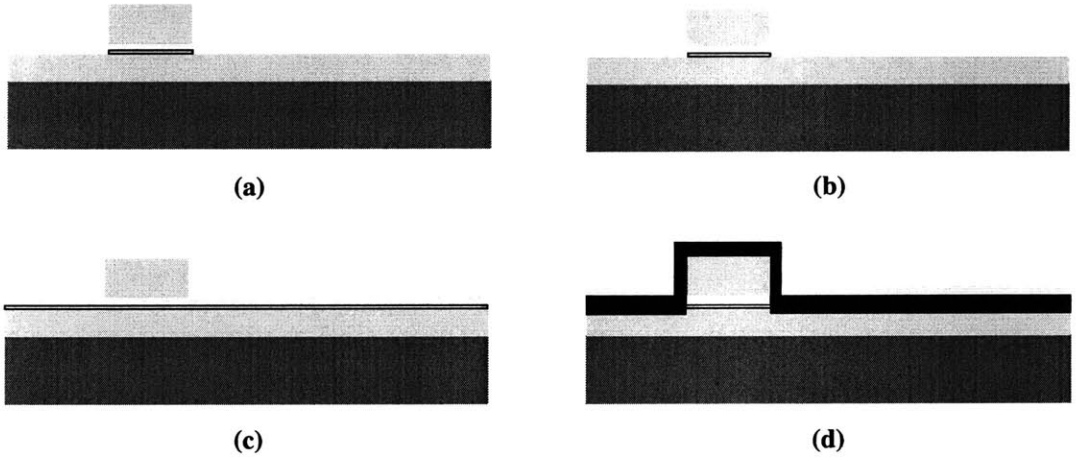

FIGURE 2-15. The undercutting of the junction represented as cracking between the niobium and aluminum oxide layers. (a) shows the junction without undercut, while (b) shows the junction with undercut. Anodizing the wafer early in the process helps to make the undercutting more uniform. (c) is before anodization, while (d) is after.

2.9.4 Qubit Requirements

In order to achieve the requirements of the qubit, we need an E_J/E_C between 10 and 1000, an α and α_C between 0.5 and 1, a β_L<0.01, and a subgap resistance greater than 10^{10} Ω. These fabrication parameters will give us the operational parameters needed to operate the qubit. Figure 2-9 shows the junction size and critical current density to get E_J/E_C on the order of 100. The Lincoln laboratory process can produce junctions lithographically 1 μm on each side, which become effectively.55 μm on a side given a rounded undercut. The process can also produce critical current densities of 100 A/cm^2 or less, so it should be able to reach an E_J/E_C of 100. This should easily meet the β_L requirements as well. Since a junction can be made as small as 0.9 μm lithographically, which is effectively 0.44 μm on a side with undercut, this gives an α of 0.63. The α_C is approximately 0.75. R_{sg} is harder to measure, but our experiments indicate that the total resistance, which consists of the subgap resistance in parallel with the environmental shunt, is greater than $10^8\Omega$ when the critical current density is about 400 A/cm^2 and the temperature is 300 mK. R_{sg} is inversely proportional with the critical current density and becomes exponentially larger as temperature decreases. These parameters are within the boundaries required to fabricate a persistent current qubit.

2.10 Summary

This chapter covered the fundamentals of the persistent current qubit, discussing its Hamiltonian and its numerical approximation, then covering various approximations of the qubit Hamiltonian. These provided simple ways to calculate the qubit's energy bands, resonant frequencies, and wavefunctions. We could then apply similar methods to a numerical calculation of the qubit's time-dependent evolution. Finally, we discussed the parameters necessary for fabricating the qubit. Our analysis indicates that the qubit can be fabricated to meet our requirements using Lincoln Laboratory's foundry process.

Chapter 3

The DC SQUID Magnetometer

3.1 Introduction

Since the qubit's two states have opposite circulating currents, and thus opposite magnetizations, a sensitive magnetic field detector is needed to measure the state of the qubit. This chapter introduces the dc SQUID, a magnetometer whose effective critical current changes with magnetic field. Its sensitivity is high enough to detect the change in the magnetic field caused by the qubit's change of states, which is about 0.001 Φ_0.

Section 3.2 gives an overview of the dc SQUID. Section 3.3 covers processes by which the dc SQUID switches from the supercurrent to the voltage state, while Section 3.4 explains how these processes give a distribution of switching currents whose mean translates into the value of the magnetic field. Next, Section 3.5 discusses the technique to perform an ensemble measurement of the SQUID's switching current, covering the electronic circuits used to perform the measurements. Section 3.6 then discusses another measurement technique which is being explored, measuring the time rather than the current at which the SQUID switches. The requirements of the measurement device are covered in Section 3.7. Finally, the quantum model of the SQUID is discussed in Section 3.8.

3.2 The DC SQUID

The dc SQUID is a superconducting magnetometer consisting of two Josephson junctions in parallel, as shown in Figure 3-1. Any magnetic flux inside of the loop sets up a phase difference between the two junctions, which changes an effective critical current of the two junction system. This modification of the effective critical current allows us to measure the small magnetic field changes induced by the qubit.

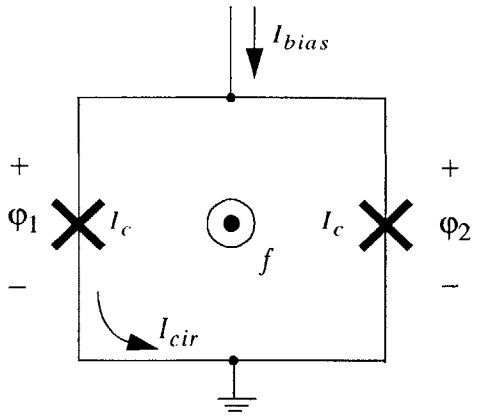

FIGURE 3-1. Circuit diagram of the dc SQUID (Superconducting QUantum Interference Device).

The total bias current through the SQUID, I_{bias}, equals the sum of the currents, as in Equation (3-1). The circulating current in the SQUID, I_{cir}, is equal to the difference of the currents, as in Equation (3-2).

$$I_{bias} = i_1 + i_2 = I_c \sin\varphi_1 + I_c \sin\varphi_2 = 2I_c \sin\left(\frac{\varphi_1 + \varphi_2}{2}\right)\cos\left(\frac{\varphi_1 - \varphi_2}{2}\right) \tag{3-1}$$

$$I_{cir} = i_1 - i_2 = I_c \sin\varphi_1 - I_c \sin\varphi_2 = I_c \cos\left(\frac{\varphi_1 + \varphi_2}{2}\right)\sin\left(\frac{\varphi_1 - \varphi_2}{2}\right) \tag{3-2}$$

To simplify matters, we use the variables $\varphi_p=(\varphi_1+\varphi_2)/2$ and $\varphi_m=(\varphi_1-\varphi_2)/2$. It is sometimes useful to refer to φ_p as the external variable, since it couples most directly with I_{bias}, and to refer to φ_m as the internal variable. These transformations give Equation (3-3).

$$\begin{aligned} I_{bias} &= 2I_c \cos\varphi_m \sin\varphi_p \\ I_{cir} &= I_c \sin\varphi_m \cos\varphi_p \end{aligned} \tag{3-3}$$

These two equations are true only so long as the SQUID remains in the superconducting state. When the applied current exceeds the effective critical current (the maximum current which Equation (3-1) allows for the value of φ_m), it switches to the voltage state and the equation no longer applies.

Flux quantization gives the phase around the loop to be $\varphi_1-\varphi_2=2\pi n + 2\pi\Phi/\Phi_0$. Φ is the total magnetic flux through the loop, and it is equal to the sum of the externally applied bias magnetic flux and the self-induced magnetic flux, as well as the magnetic flux from any mutual inductive source (such as the PC qubit). If there is no mutually coupled

device and the self inductance is small, which happens when $\beta_L=L_m/L_J<<1$, then the only significant source of magnetic field is the externally applied flux, Φ_{ext}, so that $\varphi_m=\pi n+\pi f$, where the frustration, f, is Φ_{ext}/Φ_0. This means that the bias current, as defined in Equation (3-3), can be written as $2I_c\cos(\pi f+\pi n)\sin(\varphi_p)$.

The switching current is now the maximum value of I_{bias} for a specified value of f and n. The maximum is reached whenever $\sin(\varphi_p)$ is -1 or 1, so that $I_{c,eff}=2I_c|\cos(\pi f+\pi n)|$. Since adding a multiple of π to an angle only changes the sign of its cosine, the πn term is unnecessary, giving Equation (3-4).

$$I_{c,eff} = 2I_c|\cos(\pi f)| \tag{3-4}$$

When β_L is significant, then fluxoid quantization requires that $2\varphi_m=2\pi(f-L_mI_{cir}/\Phi_0)$, and the calculation for the circulating current must be solved self-consistently, since it both influences and depends upon φ_m. Figure 3-2 shows how the effective critical current changes with flux, both with a small and a large inductance.

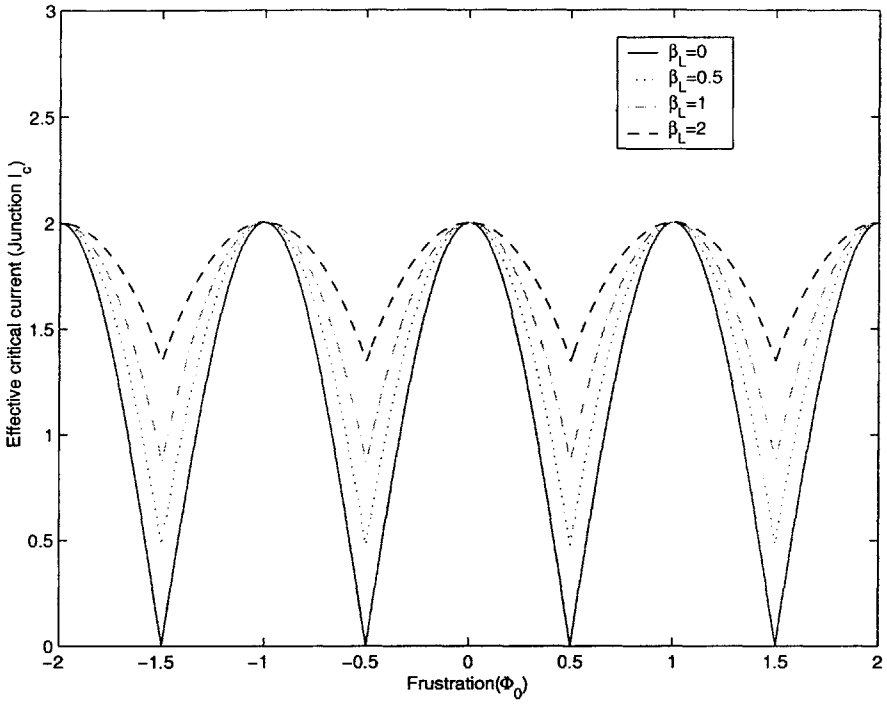

FIGURE 3-2. Effective critical current of the dc SQUID versus frustration for various values of β_L.

3.3 Escape Rates for the Measurement Process

Once the bias current in a dc SQUID surpasses its effective critical current, the SQUID switches to the voltage state. If the SQUID is underdamped, then it is hysteretic, and once it switches to its voltage state, it cannot return to the superconducting state until the bias current is reduced to its return current which is well below the critical current. This strong hysteretic signal, shown in Figure 3-3, provide the measurement which indicates the state of the qubit.

Due to the statistical processes of thermal activation and incoherent quantum tunneling, the SQUID can switch to the voltage state even when I_{bias} is below $I_{c,eff}$. These statistical processes are often calculated by modeling the dc SQUID as a single Josephson junction with a critical current of $I_{c,eff}$. The exact current at which it switches can be determined by calculating the rate of the escape of a particle from a well. Once the particle escapes, the SQUID's undamped oscillations will keep it in the voltage state, and Equation (3-3) no longer applies.

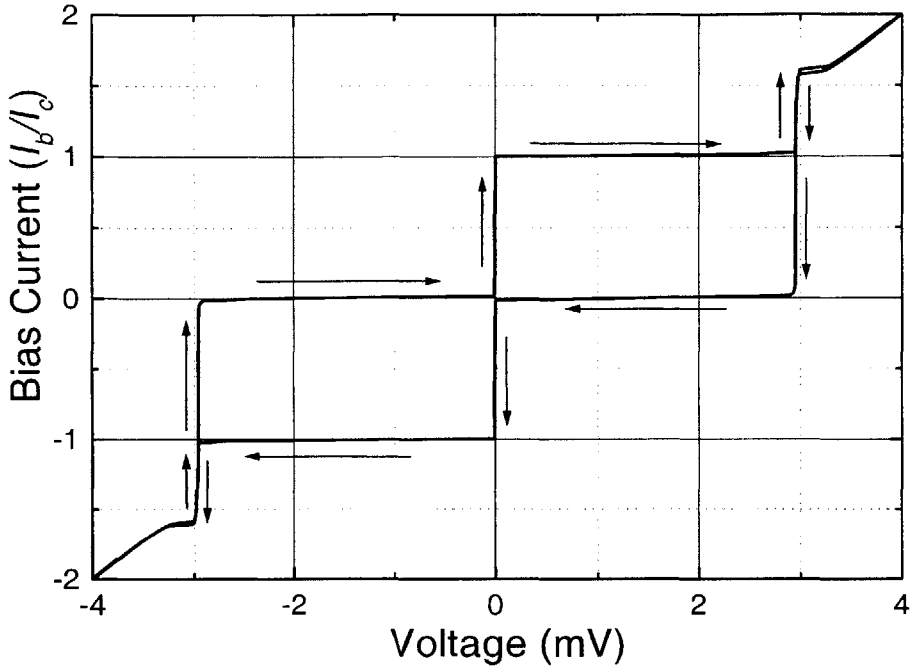

FIGURE 3-3. Current-voltage characteristic for an underdamped dc SQUID.

3.3.1 Thermal Activation Escape Rate

Assuming a negligibly small inductance, the dc SQUID has a potential energy determined coming from its Josephson energy and the work done by the current source. It is analogous to the potential energy of a current-biased Josephson junction, $U(\varphi) = E_J(-\cos\varphi - I_{bias}\varphi/I_c)$, which gives the potential shown in Figure 3-4. When the bias current, I_{bias}, is zero, the potential is sinusoidal. As the current is increased, the potential tilts, giving it a "washboard" shape. Eventually the washboard is tilted so far that no barrier exists between the wells anymore, and the junction switches to the voltage state. Even before this occurs, the barrier becomes small enough that the phase particle (the quantum mechanical wavefunction representing the phase) may escape by either thermal excitation or incoherent quantum mechanical tunneling. By calculating the barrier height, and consequently the escape rate, at a certain bias current, the probability of escape over a time interval may be determined. This allows us to determine the SQUID's switching current.

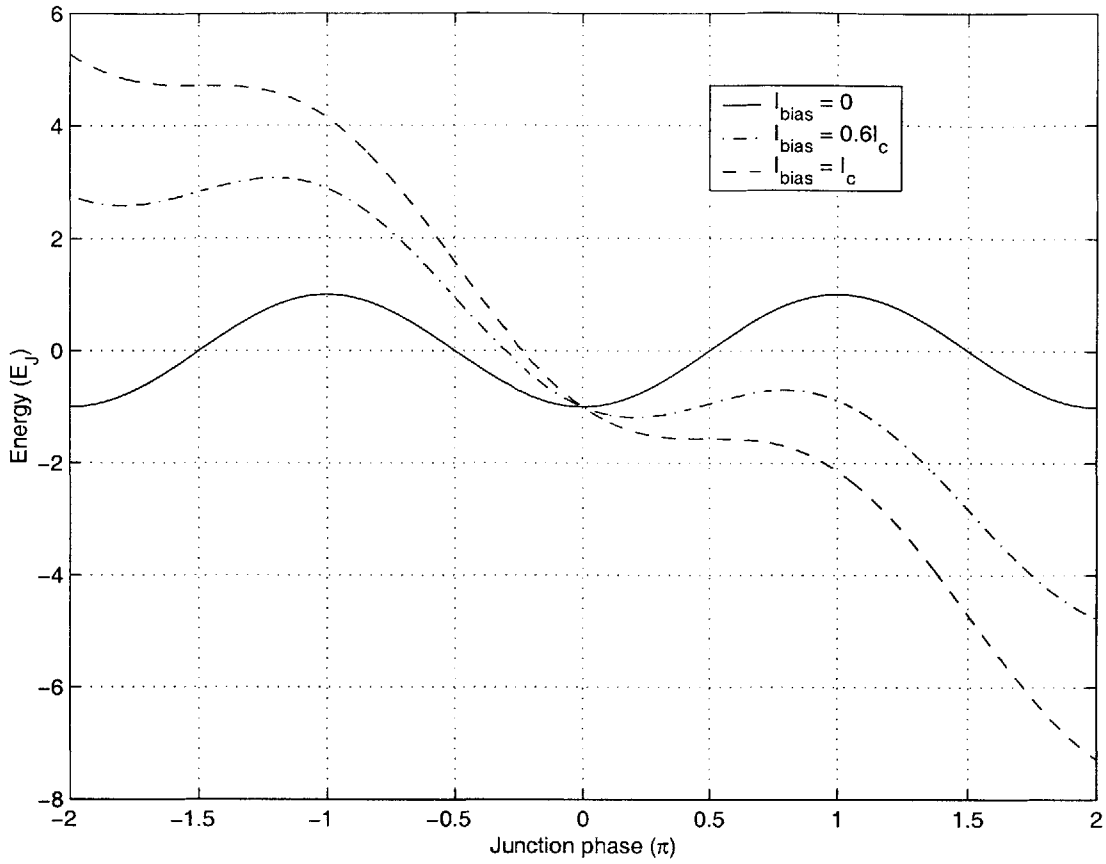

FIGURE 3-4. The potential energy of a single junction when biased at various currents.

The maxima and minima of the potential are at the zeroes of the derivative of U in φ. The second derivative distinguishes between them, since it is positive at the minimum and negative at the maximum, giving the results in Equation (3-5).

$$\frac{dU}{d\varphi} = E_J\left(\sin\varphi - \frac{I_{bias}}{I_c}\right) \qquad \frac{d^2U}{d\varphi^2} = E_J\cos\varphi$$
$$\varphi_{min} = \text{asin}\left(\frac{I_{bias}}{I_c}\right) \quad \varphi_{max} = \pi - \text{asin}\left(\frac{I_{bias}}{I_c}\right) \tag{3-5}$$

The barrier is simply the local maximum of the potential minus the local minimum of the potential at a smaller φ, which gives the form in Equation (3-6).

$$\Delta U = U(\varphi_{max}) - U(\varphi_{min}) = 2E_J\left(\sqrt{1-\left(\frac{I_{bias}}{I_c}\right)^2} - \frac{I_{bias}}{I_c}\text{acos}\left(\frac{I_{bias}}{I_c}\right)\right) \tag{3-6}$$

The energy can also be used to calculate the oscillation frequency of the phase particle in the well. Using a simple harmonic oscillator approximation gives the frequency with

which the particle "attempts" to escape the well. Equation (3-7) calculates this based on the curvature of the well and the effective mass of the phase particle, which is proportional to the capacitance of the junction, as shown in Section 2.2.

$$\omega_0 = \sqrt{\frac{\partial^2}{\partial\varphi^2}U(\varphi_{min})/m_\varphi}$$

$$\omega_0 = \sqrt{\frac{(\Phi_0/2\pi)I_c\cos\varphi_{min}}{(\Phi_0/2\pi)^2 C_j}} \tag{3-7}$$

$$\omega_0 = \frac{1}{\sqrt{L_j C_j}}\left(1-\left(\frac{I_{bias}}{I_c}\right)^2\right)^{1/4}$$

From these, the escape rate is simply the attempt rate times the rate of activation over the barrier. For thermal activation, this is $\Gamma = \alpha_d \frac{\omega_0}{2\pi} e^{-\frac{\Delta U}{k_B T}}$ [4]. α_d is the damping parameter, which depends on a quality factor Q, the temperature, and the barrier height: $\alpha_d = \frac{7.2\Delta U}{Qk_B T}$ for large Q. Although a value for Q can be calculated for an isolated junction from the its inherent properties, this value is inaccurate due to the shunting from the environment. It is more useful to determine Q, and thus dervie the environmental shunting, from the measurement. This is discussed in more detail in Section 2.8.4.

Unlike a single junction, the SQUID has a two dimensional potential through which the phase may escape. This is given by Equation (3-8).

$$U(\varphi_1, \varphi_2) = E_J\left(-\cos\varphi_1 - \cos\varphi_2 - \varphi_1\frac{I_{bias}}{2I_c} - \varphi_2\frac{I_{bias}}{2I_c} + \frac{(\varphi_1 - \varphi_2 - 2\pi f)^2}{2\beta_L}\right) \tag{3-8}$$

When this is transformed to the φ_m and φ_p variable space, this becomes Equation (3-9).

$$U(\varphi_p, \varphi_m) = E_J\left(-2\cos\varphi_m\cos\varphi_p - \varphi_p\frac{I_{bias}}{I_c} + \frac{(2\varphi_m - 2\pi f)^2}{2\beta_L}\right) \tag{3-9}$$

This gives a sinusoidal potential periodic in one dimension and quadratic in the other, which tilts when a bias current is applied. The inductance term is what confines the potential with a quadratic potential well, similar to its effect on the PC qubit. The quadratic well is orthogonal to the direction of the tilt, giving the overall potential landscape the shape of a valley with a downward slope in the direction of φ_p. The cosine potential causes hills in the valley. When β_L is very small, the constraint is such that the phase particle is only free to move in a single dimension (the valley has very steep walls), making it

effectively one dimensional. In this case, the smallest barrier to escape is in the φ_p direction and $\varphi_m=\pi f$ (or nearly so), and the problem is the same as for a single junction, in Equation (3-6), except that the capacitance is $2C_J$ and the current is $I_{c,eff}$. Once again, we use the first and second derivatives of the potential to find the maximum and the minimum, resulting in Equation (3-11).

$$\frac{dU}{d\varphi_p} = E_J\left(2|\cos\pi f|\sin\varphi_p - \frac{I_{bias}}{I_c}\right) \qquad \frac{d^2U}{d\varphi_p^2} = E_J 2|\cos\pi f|\cos\varphi_p$$
$$\varphi_{p,min} = \operatorname{asin}\left(\frac{I_{bias}}{2I_c|\cos\pi f|}\right) \quad \varphi_{p,max} = \pi - \operatorname{asin}\left(\frac{I_{bias}}{2I_c|\cos\pi f|}\right) \tag{3-10}$$

This gives ΔU from the difference of the potentials at $\varphi_{p,min}$ and $\varphi_{p,max}$ in Equation (3-11).

$$\Delta U = U(\varphi_{max}) - U(\varphi_{min}) = 4(|\cos\pi f|E_J)\left(\sqrt{1-\left(\frac{I_{bias}}{2I_c|\cos\pi f|}\right)^2} - \frac{I_{bias}}{2I_c|\cos\pi f|}\operatorname{acos}\left(\frac{I_{bias}}{2I_c|\cos\pi f|}\right)\right) \tag{3-11}$$

We can define $I_{c,eff}=2I_c|\cos\pi f|$ and $E_{J,eff}=2I_{c,eff}(\Phi_0/2\pi)=2|\cos\pi f|E_J$. With those definitions, the above equation reduces to the equation for a single junction, resulting in the form in Equation (3-12).

$$\Delta U = 2E_{J,eff}\left(\sqrt{1-\left(\frac{I_{bias}}{I_{c,eff}}\right)^2} - \frac{I_{bias}}{I_{c,eff}}\operatorname{acos}\left(\frac{I_{bias}}{I_{c,eff}}\right)\right) \tag{3-12}$$

The equations for the frequency also look similar, as in Equation (3-13).

$$\omega_0 = \sqrt{\frac{\partial^2}{\partial\varphi_p^2}U(\varphi_{p,min})/m_p}$$
$$\omega_0 = \sqrt{\frac{(\Phi_0/2\pi)2I_c(|\cos\pi f|\cos\varphi_{p,min})}{(\Phi_0/2\pi)^2 2C_J}} \tag{3-13}$$
$$\omega_0 = \frac{1}{\sqrt{L_{J,eff}C_{eff}}}\left(1-\left(\frac{I_b}{I_{c,eff}}\right)^2\right)^{1/4}$$

Between these two formulae, it is apparent that the SQUID, though a two-dimensional system, can be reduced to one dimensional system which behaves like a single junction with an adjustable critical current whenever β_L is small. $L_{J,eff} = \Phi_0/(2\pi I_{c,eff})$. Often we place an external capacitance across the SQUID in order to shunt it, in which case $C_{eff} = 2C_J+C_S$, where C_S is the shunting capacitance. Figure 3-5 shows the escape rate for thermal activation.

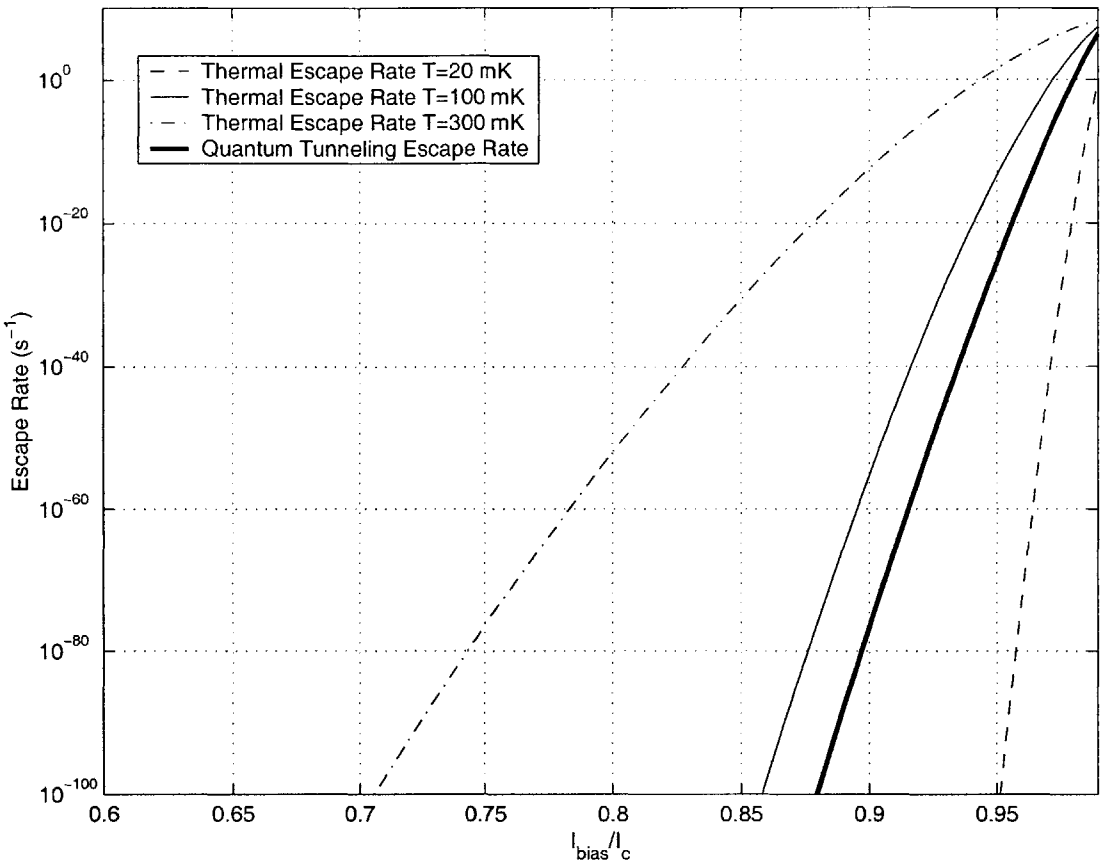

FIGURE 3-5. Escape rate for the dc SQUID varies with bias current at various temperatures. This graph applies to the device measuring the qubit, with a 2 pF shunt capacitor and an I_c of 5.25 μA in each junction. The heavy line shows the quantum tunneling escape rate, which does not depend on temperature. It is about equal to the thermal escape rate at 100 mK, and is dominant at lower temperatures.

3.3.2 Quantum Tunneling Escape Rate

So far, only thermal activation has been discussed as the means for the SQUID to switch. It is also possible for the SQUID to tunnel out of its potential well quantum mechanically. The potential from which the phase particle must tunnel is still that shown in Figure 3-4. The rate of tunneling may be calculated using the WKB (Wentzel-Kramers-Brillouin) approximation, as in Equation (3-14).

$$\Gamma = K\omega_0\left(\frac{\Delta U}{\hbar\omega_0}\right)^{1/2}\exp\left(-\int_{\varphi_i}^{\varphi_f}\frac{1}{\hbar}\sqrt{2m(U(\varphi)-E_0)}d\varphi\right) \qquad \textbf{(3-14)}$$

K is a constant, φ_i and φ_f are the initial and final points in φ in which the tunneling takes place. These are determined by the intersection of the barrier with the ground state

energy (E_0) of the particle in the well. ΔU is the height of the barrier, and ω_0 is the frequency of the ground state. Leggett solved this equation explicitly for a cubic potential [34], which approximates a Josephson junction (or a SQUID), to give Equation (3-15).

$$\Gamma = \omega_0\left(\frac{60\Delta U}{\hbar\omega_0}\right)^{1/2}\left(\frac{18}{5\pi}\right)^{1/2}\exp\left(-\frac{36}{5}\frac{\Delta U}{\hbar\omega_0}\right) \tag{3-15}$$

As before, ΔU and ω_0 are functions of the bias current and the magnetic field, given in Equation (3-16).

$$\begin{aligned}\Delta U &= 4|\cos\pi f|E_J\left(\sqrt{1-\left(\frac{I_{bias}}{I_{c,eff}}\right)^2}-\frac{I_{bias}}{I_{c,eff}}\operatorname{acos}\left(\frac{I_{bias}}{I_{c,eff}}\right)\right)\\ \omega_0 &= \frac{1}{\sqrt{L_{J,eff}C_{eff}}}\left(1-\left(\frac{I_b}{I_{c,eff}}\right)^2\right)^{1/4}\end{aligned} \tag{3-16}$$

3.4 Simulations of Escape Probability in the DC SQUID

The probability of escape is distinct from the escape rate. Γ is a generic escape rate which may be either thermal activation, quantum tunneling, or some combination. In Equation (3-17) we have a probability of escape within an infinitesimally small unit of time.

$$P_{esc}(t+dt)-P_{esc}(t) = (1-P_{esc}(t))\Gamma dt \tag{3-17}$$

The probability that the phase particle escapes within time dt is the escape rate times dt times the probability that it has not already escaped. Since $dP_{esc}(t)/dt=(P_{esc}(t+dt)-P_{esc}(t))/dt$, we can solve Equation (3-17) for $P_{esc}(t)$, giving us Equation (3-18).

$$\begin{aligned}dP_{esc}(t) &= (1-P_{esc}(t))\Gamma dt\\ -\ln(1-P_{esc}(t)) &= \Gamma t\\ 1-P_{esc}(t) &= e^{-\Gamma t}\end{aligned} \tag{3-18}$$

We define $P(t)=1-P_{esc}(t)$ as the probability that the particle remains in the well. This gives the simple equation $P(t) = e^{-\Gamma t}$, the usual exponential decay rate that one expects.

It is still necessary to determine Γ when two escape rates exist. Consider both probabilities: escaping from the well due to thermal activation, $P_{therm}(t) = e^{-\Gamma_{therm}t}$, and

escaping from the well due to quantum tunneling, $P_{quant}(t) = e^{-\Gamma_{quant}t}$. The probability that the SQUID remains in the zero voltage state rather than escaping by either means is $P(t) = P_{quant}(t) \times P_{therm}(t) = e^{-\Gamma_{quant}t} \times e^{-\Gamma_{therm}t} = e^{-(\Gamma_{quant} + \Gamma_{therm})t}$. The total escape rate is equal to the sum of the two rates, $\Gamma_{tot}=\Gamma_{therm}+\Gamma_{quant}$, if they are independent. (This is a good approximation in this potential, since thermally-assisted tunneling is not statistically favorable.) This satisfies the escape rate in the two temperature extremes. At absolute zero, thermal activation is frozen out, and the total rate is equal to Γ_{quant} when $\Gamma_{therm} \rightarrow 0$. At high temperatures, thermal activation completely overwhelms the quantum tunneling, and the escape rate looks like Γ_{therm} when $\Gamma_{therm} >> \Gamma_{quant}$.

The next challenge is to find the probability of the phase particle's escape as the SQUID bias current is ramped. While analytically complex, a simple numerical solution can be achieved by discretizing the ramping of the SQUID bias current into a series of steps, where the current is held constant for a period of Δt before it is increased to the next value. Then the probability of the phase particle escaping at any particular current, I, is given by Equation (3-19), which is simply the probability that a particle would escape at this current in time Δt times the probability that it has not escaped already.

$$P_{esc}(I_i) = (1 - e^{-\Gamma(I)\Delta t})\left(1 - \sum_{j<i} P_{esc}(I_j)\right) \tag{3-19}$$

A computer program can solve this problem by sequentially calculating the probability of escape at each current step. The analytical, continuous problem stated in Equation (3-20) is more difficult to solve. $p_{esc}(t)$ is the probability density of escaping within time dt.

$$p_{esc}(I)dI = \Gamma(I)dt\left(1 - \int_0^t p_{esc}(u)du\right) \tag{3-20}$$

Another approach uses a Monte Carlo method. In this, the probability of escape at each current is calculated individually to be $P(I_i) = e^{-\Gamma(I_i)\Delta t}$ A one-dimensional array of uniformly distributed random numbers between 0 and 1 is created, each element of the array corresponding to one step in the SQUID bias current. The first element whose value exceeds the probability is marked as the escape point, and the corresponding current is the switching current. New random arrays must be created on the order of a thousand times in

order to produce a histogram of switching currents. While slower than the numerical solution of Equation (3-19), this method allows the addition of noise to the bias current or the magnetic field, or even the effect of a qubit changing states. While this would be a highly complex correlation to solve analytically, a Monte Carlo simulation can easily produce an approximate solution. The results of both types of simulations, numerical integration and Monte Carlo, are compared to the measurement results in Figure 3-10.

3.5 Experimental set-up

Measuring the dc SQUID requires ramping the bias current of the SQUID until it switches, recording that current, and then repeating the measurement between 500-10,000 times in order to make an ensemble measurement. While each switching event is stochastic, with a sizable variance, taking enough measurements reduces the variance of the mean, making for an accurate measurement of the magnetic field from the mean switching current. In order to determine the viability of niobium, we want to reproduce the experiments on Al done at Delft with our Nb sample, starting with the ground state experiments, where we take an ensemble measurement of the switching current of the dc SQUID, shown in Figure 3-6, for each magnetic field step as we sweep it. The dc SQUID should follow the standard SQUID effective critical current, $2I_c|\cos\pi f|$ (allowing for the statistical variation due to thermal activation and quantum tunneling), except where the qubit disturbs it. Because of the noise requirements of this measurement, all equipment connected directly to the dc SQUID must be battery powered, since ac powered devices transfer noise to the SQUID and increase the standard deviation of the switching current.

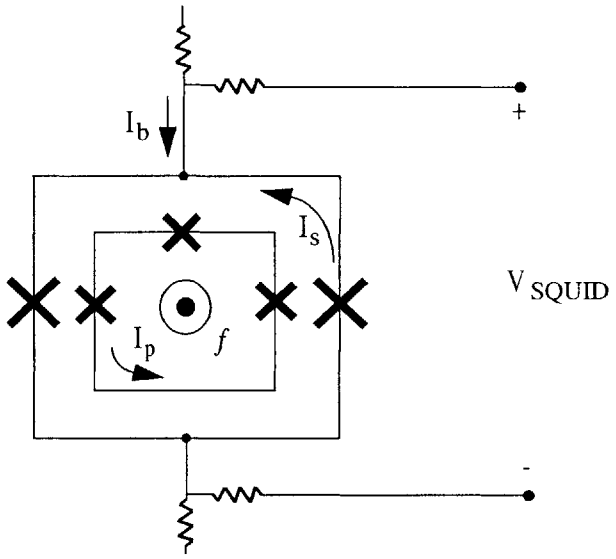

FIGURE 3-6. The dc SQUID and the qubit. On the order of 500 to 10,000 measurements must be taken of the switching current in order to determine the state of the qubit.

The central component of the measuring equipment is the sample-and-hold circuit shown in Figure 3-7. This device measures the dc SQUID's current quickly enough to get a high resolution measurement of the switching current. A sample-and-hold IC (an AD783J from Analog Devices) reads a voltage measure of the current (V_{cur}), while an amplified version of the voltage (V_{volt}) across the junction is measured by a high speed, 7 ns comparator (AD8516). The potentiometer sets the threshold voltage of the comparator. When the junction voltage (amplified 500 times) exceeds this threshold voltage, the inverse output of the comparator ($\overline{Q}$) is sent to the sample-and-hold. The AD783J holds on a low input, so it locks onto the V_{cur} when the junction switches. Simultaneously, the comparator output is used as an external trigger (V_{trig}) sent to the DMM which measures the held voltage (V_{meas}). The sample-and-hold circuit is accurate and can sample accurately (at least 1 part in a 1000) from an input with frequencies ranging from dc to 1 kHz. This allows high resolution measurements on the dc SQUID switching current.

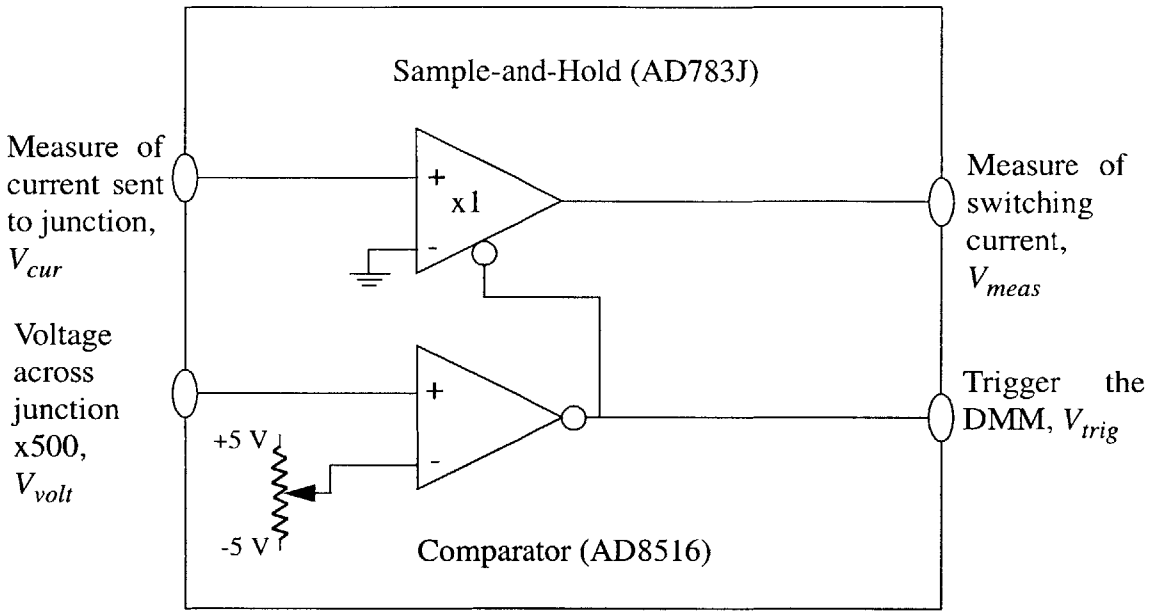

FIGURE 3-7. Sample-and-hold circuit used to detect the switching current of the dc SQUID.

The digital multimeter records the output of the sample-and-hold circuit, V_{meas}, when it receives the trigger signal, V_{trig}. The multimeter can store up to five hundred measurements, which it then downloads to a computer. The multimeter and the computer are the only parts of this measurement which must run off an ac power line. Everything else, from the function generator which sweeps the current to the amplifier which magnifies the voltage output, runs off batteries. The ac powered components are all at least one degree of separation from the superconducting device, so that their noise influence is minuscule. The full circuit is shown in Figure 3-8, and draws 30-40 mA from the battery. Four sealed lead acid batteries, each with a charge of 5 amp-hours, provide the two rails with 12 V and -12 V, with two batteries in parallel providing for each rail. The total of four batteries provide enough power for about 250 hours between rechargings. Three of the four-battery packs were made, allowing recharging of two of them while the third is in use. The magnetic field, which is not electronically coupled to the rest of the setup, is controlled by a Yokogawa programmable dc source, which supplies current (or voltage) to an accuracy of 1 part in 10^4 with very low noise.

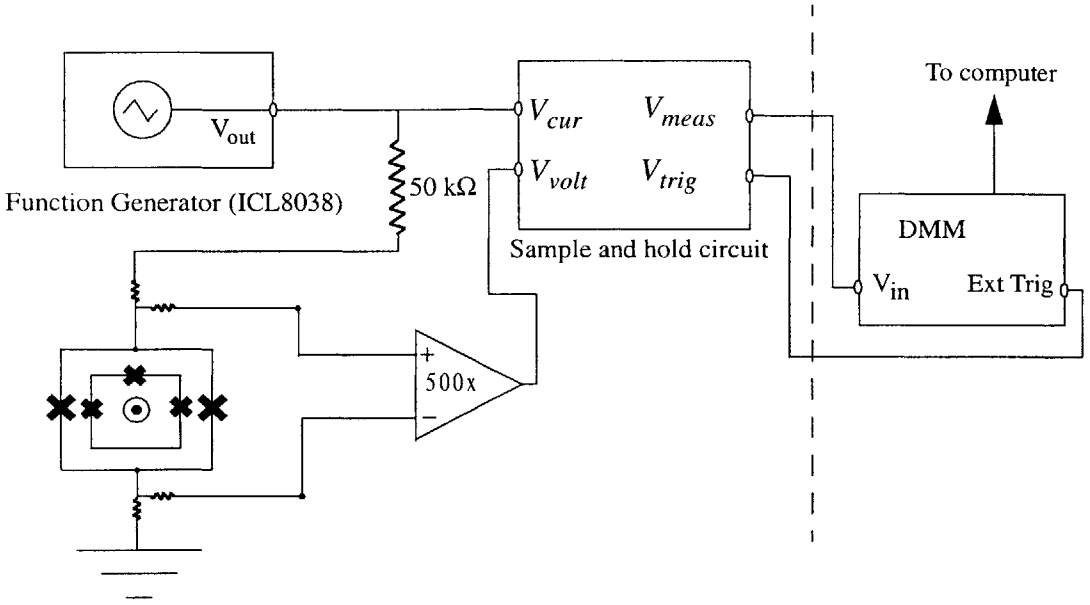

FIGURE 3-8. Setup used to measure switching current of dc SQUID. Everything to the left of the dashed line is battery powered, while everything to the right is plugged into an ac wall outlet.

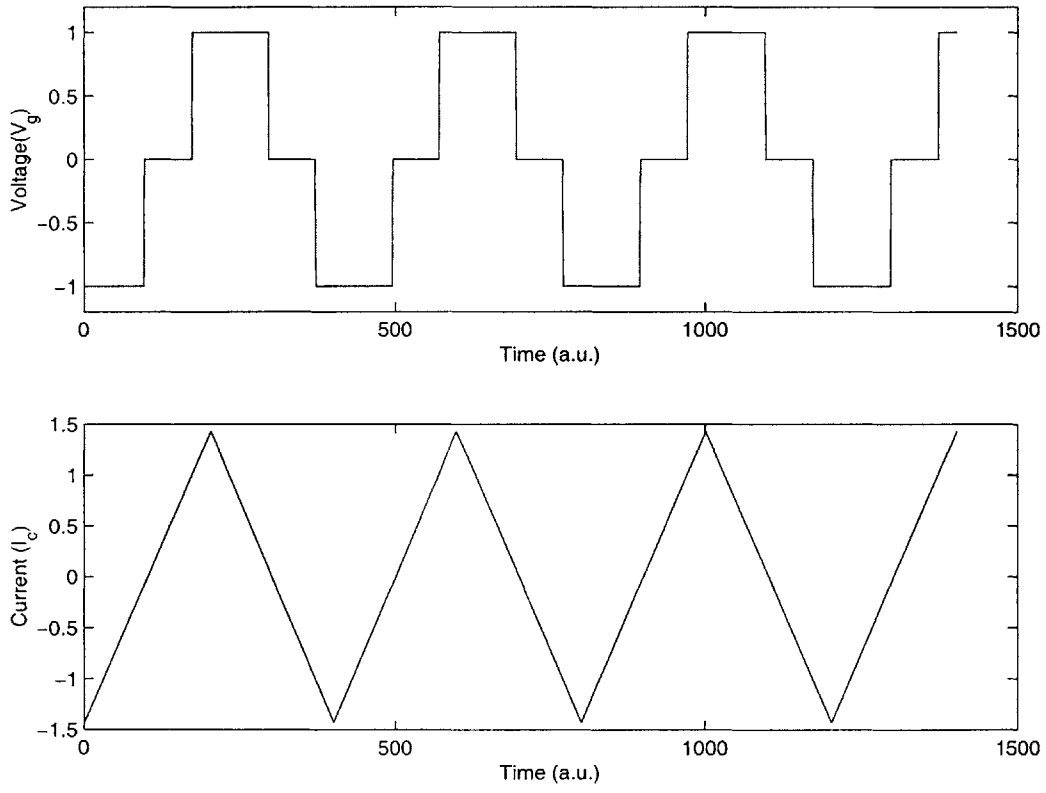

FIGURE 3-9. Current through the SQUID over time and the corresponding voltage. A large number of such ramps (500-2000) are needed to make a single histogram.

This setup was first tested on a dc SQUID made with junctions of 1.2x1.2 μm^2 and a current density of 730 A/cm^2. It has a critical current of about 22 μA. The SQUID has 2 pF in parallel with it in order to increase the weight of the internal variable (see Section 3.8). The SQUID can resolve variations in the field of 0.001 Φ_0 with 1000 measurements of the switching current. At 400 mK and f=0, the mean switching current is 21.6 μA, and its measured standard deviation is 70 nA. Simulations using the Monte Carlo technique give a mean of 21.5 μA and a standard deviation of 42.5 nA, while using the formulation in Equation (3-19) gives a mean of 21.5 μA and a standard deviation of 30 nA. The histograms associated with these values are shown in Figure 3-10. The standard deviation is greater for the experiment than the simulation, which may be due to noise in the experimental apparatus.

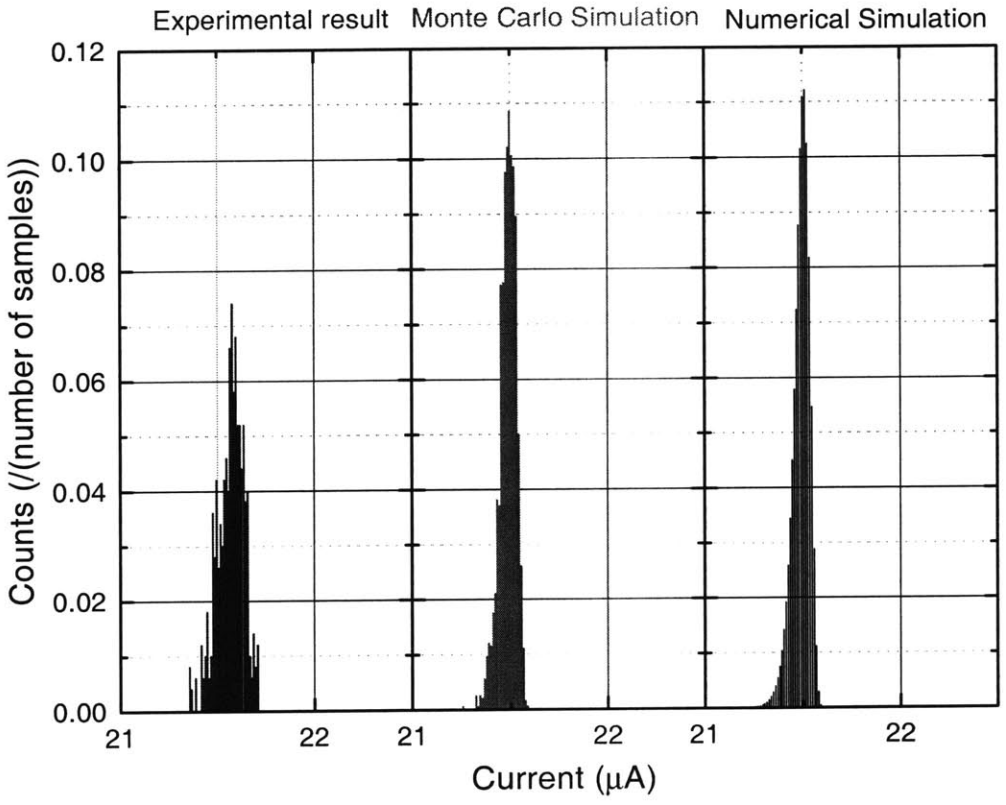

FIGURE 3-10. Switching histogram of the SQUID, both from the experiment, and from the Monte Carlo and numerical simulation. For all three, the temperature is 400 mK, for a SQUID with 1.2x1.2 μm^2 junctions and 730 $\mu A/cm^2$ critical current. The specific capacitance is 40 fF/μm^2 and there are 2 pF in parallel with the SQUID.

3.6 Timing Experiment

The initial experiments looked for the *current* where the SQUID switched in order to determine the flux which the SQUID was detecting. However, it is equally valid to measure the *time* it takes the SQUID to switch when it is biased at a certain current. The escape rate increases exponentially with changes in current, but does not change at all in time. Since the probability of escape has an exponential dependence on both rate and time, $1\text{-}P_{esc}(t) = e^{-\Gamma t}$, a time measurement is potentially more sensitive. In cases where the qubit state is changing over time, a time measurement can give more detailed information than the current measurement. Finally, the current measurement requires a changing bias current. Because the circulating current of the SQUID inductively couples to the qubit, the influence of the SQUID on the qubit changes with its bias current. Thus it is useful to keep the SQUID at a constant bias current, so its influence on the qubit remains constant.

In order to measure the time to escape, the bias current of the SQUID is rapidly increased to a point just below its effective critical current. Then the circuit measures the length of time between when the current reaches this point and when the SQUID switches. This is done with the analog integrator shown in Figure 3-11, which consists of a comparator and an op-amp integrator which has a linear voltage ramp. The comparator switches when the bias current of the SQUID reaches a certain preset point. A comparator ensures that the ramp rate is independent of the actual amplitude of the current, since it rails the voltage input of the integrator to a constant value. When the input goes below the threshold current, the comparator reverses the inputs on the integrating op-amp, causing the capacitor to charge to the negative rail. In order to make sure that the integrator always starts at the same place (with the capacitor charged to the negative rail), the comparator off-time needs to be longer than the on-time.

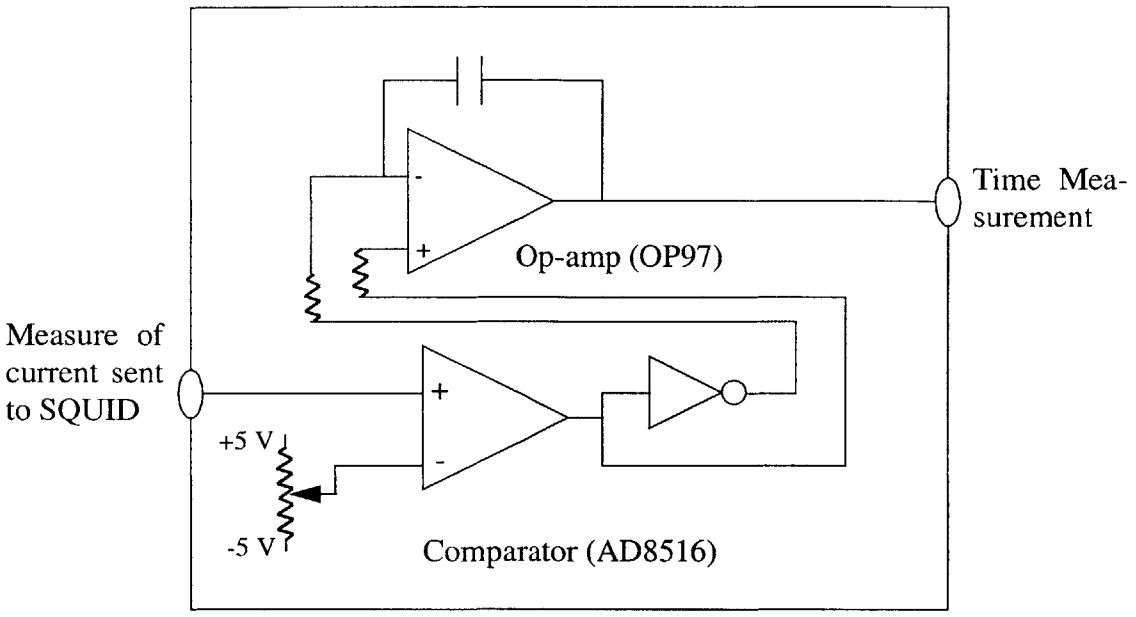

FIGURE 3-11. Op-amp integrator. The operational amplifier charges the capacitor when the negative input is 5 V and the positive input is 0 V, and discharges it when the negative input is 0 V and the positive input is 5 V. The comparator switches on when the current to the SQUID ramps up.

The insertion of the integrator is the only real difference between the circuit to measure the escape time, shown in Figure 3-12, and the circuit which measures the switching current, in Figure 3-8. (The function generator is also replaced with an ac function generator and an optical isolator, which is only necessary to give more control to the wavefunction.) In the new setup, when the SQUID switches, the sample-and-hold captures the value of the integrator, an analog measurement of the escape time, and sends it to the DMM. The program which reads the value of the DMM for escape time is identical to that which reads switching current, although it may need to be calibrated to convert its new input to time rather than current.

This setup has been tested, and it does work. The limiting factor has less to do with the experimental setup than with the nature of the timing experiment. Because the SQUID is more sensitive to the bias current than to the time, the most difficult task is to select a bias current where the timing experiment can work. Since $I_{c,eff}$ depends on the flux bias, a different bias current is necessary for each flux bias, so taking measurements at differing flux biases requires inordinate work. Overall, this setup will be useful when taking time ordered measurements, but not before.

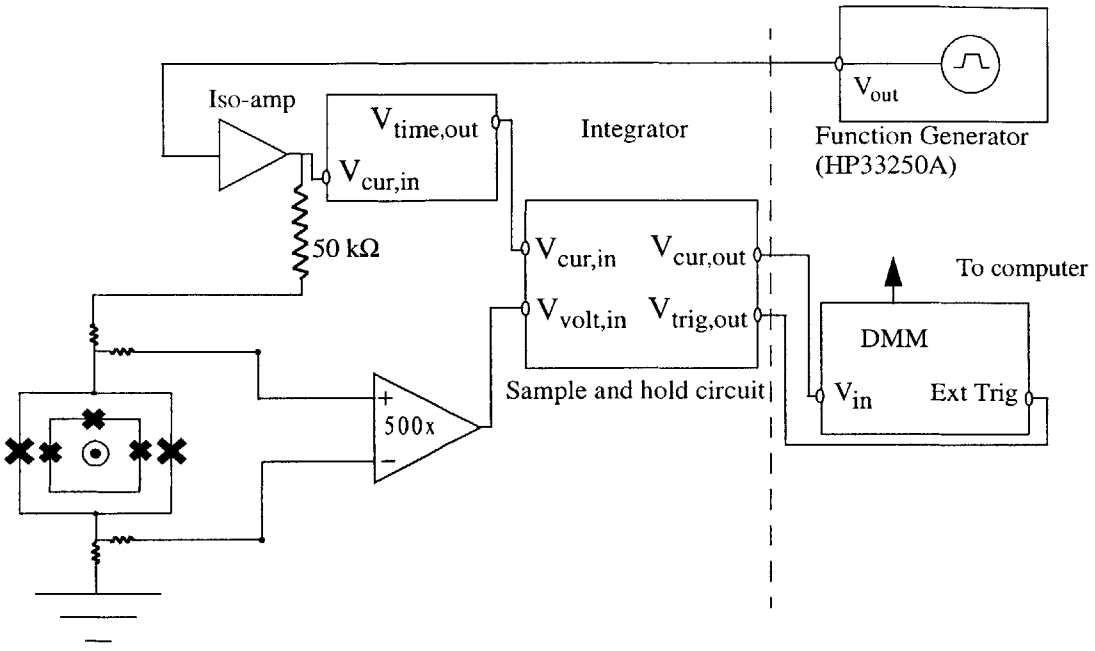

FIGURE 3-12. The setup used to measure the switching time of the dc SQUID. Everything to the left of the dashed line is battery powered, while everything to the right is plugged into an ac wall outlet. The function generator delivers a square wave at about 40% duty cycle. When it goes high, the integrator starts increasing in voltage. When the SQUID switches, the sample-and-hold samples the value of the integrator, which is then measured by the DMM. Repeated measurements produce a histogram of switching times.

3.7 Requirements for the SQUID

3.7.1 Decoherence through the SQUID

The most difficult aspect of interfacing with the qubit is doing so without causing excessive decoherence. Decoherence is the process whereby quantum systems lose information, becoming more classical. There are two rates associated with this: dephasing time and relaxation time. Dephasing time is the characteristic time in which the quantum system loses phase information. For a qubit in state $\alpha|0\rangle + \beta|1\rangle$, α and β are complex numbers, and thus have a relative phase to one another and to the other qubits. The dephasing time describes the rate that this relative phase information is lost while the probability distribution between the states remains the same, that is $|\alpha|^2$ and $|\beta|^2$ remain constant. Thus, while a dephased qubit can no longer be used for calculations, a classical measurement made on it will still produce reliable information, i.e. the same probability distribution as it would have had before the dephasing. Relaxation time is the time it takes for the qubit to

relax to its ground state, thereby losing any measurable information. When the qubit has fully relaxed, it has also dephased, since the relative phase information is lost when it is entirely in one state. The characteristic times which we calculate are the exponential decays to dephase or relax, so it is possible that the rate of decay of the phase information may be slower than that of the state information, leading to a slightly slower dephasing than relaxation rate in Equation (3-21). Nevertheless, once the system is fully relaxed, it is also fully dephased.

Relaxation and dephasing times may be found by applying the spin-boson model to the qubit. The spin-boson model is a special case of the dissipative two-state system, where a spin is coupled to a bath of harmonic oscillators. This is a good model for the PC qubit's coupling to the environment, although it has some weaknesses. Most critical, it assumes a two-state spin. Although the circulating current has similar magnetic properties to a nuclear spin, it has a number of higher states which are not taken into account. Still, it does provide a good starting point to calculate decoherence. The relevant equations give dephasing and decoherence times in terms of the spectral density of the environmental noise, $J(\omega)$ [33].

$$\tau_r^{-1} = \frac{1}{2}\left(\frac{\Delta}{\nu}\right)^2 J(\omega)\coth\left(\frac{\hbar\omega}{2k_BT}\right) \quad \text{and} \quad \tau_\phi^{-1} = \frac{\tau_r^{-1}}{2} + \frac{1}{2}\left(\frac{\varepsilon}{\nu}\right)^2 \lim_{\omega\to 0}\left[J(\omega)\coth\left(\frac{\hbar\omega}{2k_BT}\right)\right] \tag{3-21}$$

τ_r and τ_ϕ are the relaxation and dephasing times, respectively. The ω in the relaxation rate is the frequency corresponding to the energy difference (ν) between the two states. Δ and ε are the tunnel splitting and energy bias, respectively, and are related to ν by $\nu^2=\Delta^2+\varepsilon^2$. The tunnel splitting is the energy difference of the symmetric and antisymmetric wave-function at f=1/2, while the energy bias is the energy difference between the minimum of the two wells in the potential. It varies linearly with f near f=1/2, passing through zero at exactly half a flux quantum. $J(\omega)$ is the environmental spectral density function, defined in Equation (3-22).

$$J(\omega) = \frac{\pi}{2}\sum_i \frac{c_i^2}{C_i\omega_i}\delta(\omega-\omega_i) \tag{3-22}$$

$J(\omega)$ is calculated from the fluctuations in the energy levels of the qubit ε, $J(\omega)=\langle\delta\nu\ \delta\nu\rangle_\omega/\hbar^2\coth(\hbar\omega/2k_BT)=\langle\delta\varepsilon\ \delta\varepsilon\rangle_\omega/\hbar^2\coth(\hbar\omega/2k_BT)$, which is true at those biases where $\varepsilon>>\Delta$.

To find $J(\omega)$, various theoretical methods have been developed [46,47]. Here we use the intuitive method of van der Wal [47]. The most direct source of noise are field fluctuations due to noise in the circulating current in the dc SQUID, which traces back to the Johnson-Nyquist noise in the environment. The Johnson-Nyquist noise can be calculated from the real part of the impedance seen by the SQUID. Since the resistive noise source is located outside of the magnetometer, it is evenly divided between the two branches of the SQUID (as in Figure 3-13) when the impedance of each branch is equal, which is the case as long as the junctions are equal and equally-biased, which is the case when the bias current is off.

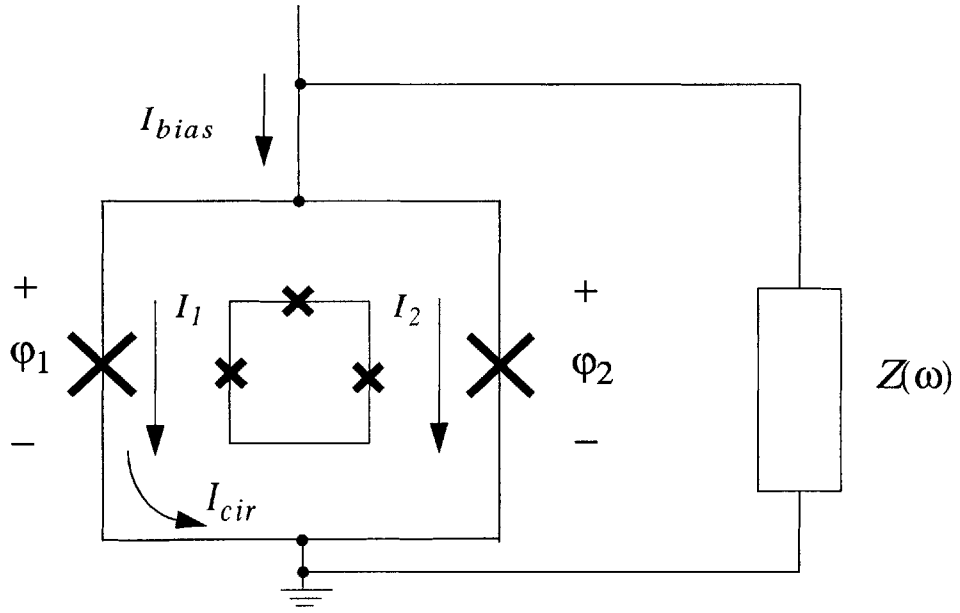

FIGURE 3-13. Circuit diagram of the dc SQUID and the impedance seen by it. The Johnson noise from the impedance couples indirectly to the circulating current of the dc SQUID to decohere the qubit.

If the coupling of each of the two branches to the qubit is equal and opposite, the total noise is zero. As the bias current is increased, however, the difference in the current in either branch (due to the circulating current which the external bias flux produces in the SQUID) creates different linear characteristics in the branches. Here we repeat Equation (3-3) for reference.

$$\begin{aligned} I_{bias} &= 2I_c \cos\varphi_m \sin\varphi_p \\ I_{cir} &= I_c \sin\varphi_m \cos\varphi_p \end{aligned} \tag{3-23}$$

Recall that $\varphi_m=(\varphi_1-\varphi_2)/2=\pi\Phi_{sq}/\Phi_0$, where Φ_{sq} is the magnetic flux threading the SQUID and Φ_{sq}/Φ_0 can be written as f. φ_p follows the bias current. While I_{cir} directly couples to the qubit, environmental noise appears as fluctuations in the I_{bias}. The fluctuations in I_{bias} can be translated into fluctuations of I_{cir} through $\delta\varphi_p$ in Equation (3-24).

$$\begin{aligned}\delta I_{bias} &= 2I_c\cos\varphi_m\cos\bar{\varphi}_p\delta\varphi_p \\ \delta I_{cir} &= I_c\sin\varphi_m\sin\bar{\varphi}_p\delta\varphi_p\end{aligned} \tag{3-24}$$

This gives the relationship in Section 3-25 between δI_{cir} and δI_{bias}.

$$\delta I_{cir} = \frac{1}{2}\tan\varphi_m\tan\bar{\varphi}_p\delta I_{bias} \tag{3-25}$$

Likewise, fluctuations in the voltage can be related to fluctuations in the current across the SQUID by the relation in Equation (3-26), which uses the Josephson inductance of the two junctions in parallel to relate the two.

$$i\omega\delta I_{bias} = 2I_c\cos\varphi_m\cos\bar{\varphi}_p\frac{2e}{\hbar}\delta V \tag{3-26}$$

This yields Equation (3-27) for fluctuations in the SQUID circulating current.

$$\delta I_{cir} = \frac{1}{i\omega}I_c\sin\varphi_m\sin\bar{\varphi}_p\frac{2e}{\hbar}\delta V \tag{3-27}$$

I_p is the circulating current in the qubit, which is proportional to the slope of the energy bands, such that $2I_p=\delta\varepsilon/\delta\Phi$. Since $\delta\varepsilon=2I_p\delta\Phi$, and $\delta\Phi$ is a small change in flux in the qubit which is caused by the circuit environment through $M\delta I_{cir}$, we can write the deviation in ε as Equation (3-28).

$$\delta\varepsilon = 2I_pM\left(\frac{1}{i\omega}I_c\sin\varphi_m\sin\bar{\varphi}_p\frac{2e}{\hbar}\delta V\right) \tag{3-28}$$

Substituting $I_c\sin\bar{\varphi}_p=I_{bias}/2\cos\varphi_m$ and finding the autocorrelation function $\langle\delta\varepsilon\ \delta\varepsilon\rangle_\omega$ gives Equation (3-30).

$$\langle\delta\varepsilon\ \ \delta\varepsilon\rangle_\omega = \hbar\left(\frac{2e}{\hbar}\right)^2\frac{4}{\omega}M^2I_p^2I_{bias}^2(\tan\varphi_m)^2\Re\{Z_t(\omega)\} \tag{3-29}$$

Since the Johnson-Nyquist noise gives a value for $\langle\delta V\ \delta V\rangle_\omega=Re\{Z_t(\omega)\}\coth(\hbar\omega/2k_BT)$.

$$\langle\delta\varepsilon\ \ \delta\varepsilon\rangle_\omega = \hbar\left(\frac{2e}{\hbar}\right)^2\frac{4}{\omega}M^2I_p^2I_{bias}^2(\tan\varphi_m)^2\Re\{Z_t(\omega)\}\coth\left(\frac{\hbar\omega}{2k_BT}\right) \tag{3-30}$$

This finally gives the value of $J(\omega)$ in Equation (3-31).

$$J(\omega) = \left(\frac{2e}{\hbar}\right)^2 \frac{4}{\hbar\omega} M^2 I_p^2 I_{bias}^2 (\tan\varphi_{int})^2 \Re\{Z_t(\omega)\} \tag{3-31}$$

Here, $Z_t(\omega)$ is the impedance which the SQUID sees in parallel with the SQUID itself, as shown Figure 3-13. The total environment includes the SQUID itself; its Josephson inductance and capacitance must be included, in parallel with the external impedance from the environment: $Z_t(\omega) = Z(\omega)||Z_{SQUID}(\omega)$. Notice that the decoherence caused by the SQUID is proportional to its bias current. Thus, when the SQUID is unbiased, it should not contribute to decoherence at all, as we predicted when we noted that the SQUID is symmetric, and in the unbiased SQUID, the noise is divided equally between each branch, and the two branches' inductive coupling to the SQUID cancel each other out.

3.7.2 Measurement Requirements

The first design objective for the SQUID is to cause minimum decoherence to the qubit. The second design objective is to narrow the standard deviation of the switching current, which improves the resolution of the measurement. As noted above, many measurements must be taken on the SQUID in order to determine the field in the qubit. In order to determine the state of the qubit with a given number of measurements, the mean switching current of the SQUID when the qubit is in the |0> state, $\langle I_{sw}(|0\rangle)\rangle$, must differ from the mean switching current in the |1> state, $\langle I_{sw}(|1\rangle)\rangle$, by a value significantly greater than σ_{mean} (ideally, by at least $3\sigma_{mean}$), which is the standard deviation of the mean switching current. $\sigma_{mean}=\sigma_{sw}/N^{1/2}$, where σ_{sw} is the standard deviation of the switching current for each measurement and N is the number of measurements taken. The more measurements taken, the closer the measured mean will be to the true mean. Since the standard deviation of the mean varies with the square root of the number of measurements, the number of measurements (and thus the time required to take the ensemble measurement) must be increased by a factor of 4 in order to reduce the standard deviation of the mean by a factor of 2. Any technique which decreases σ_{sw} by a factor of 2 would reduce the time to take the measurement by a factor of 4.

In Delft's initial experiments, they minimized the critical current of the SQUID in order to minimize back action from the SQUID to the qubit. In their operating regime ($\omega >> \omega_{LC} = \frac{1}{\sqrt{L_J C}}$, where L_J and C are the Josephson inductance and the capacitance of the SQUID respectively), Equation (3-32) describes the spectral density of the noise, where R is the environmental resistance and C_{eff} is the capacitance seen by the SQUID.

$$J(\omega) = \frac{(2\pi)^2}{h}\frac{1}{\omega^3}\left(\frac{MI_pI_{bias}}{\Phi_0}\right)^2(\tan\varphi_{int})^2\frac{1}{RC_{eff}^2} \quad \text{for } \omega \gg \omega_{LC} \tag{3-32}$$

Coherence times vary with $1/J(\omega)$. Decoherence increases with the square of the bias current, thus encouraging the minimization of the critical current of the SQUID. Delft also uses a large external capacitance to shunt the SQUID. Not only does this lengthen the coherence times, it was believed that it would decrease the width of the histogram (experimental evidence has failed to demonstrate this, however). It effectively makes φ_p harder to change, increasing the accompanying mass m_p, thus requiring more energy to switch the junction to the voltage state.

This is not the only regime in which it is possible to operate the SQUID, however. If one works in a regime where $\omega << \omega_{LC}$, the dependence looks more like Equation (3-33).

$$J(\omega) = \frac{\omega}{\hbar c}\left(\frac{MI_pI_{bias}}{I_{c,\,eff}}\right)^2(\tan\varphi_m)^2\frac{1}{R} \quad \text{for } \omega \ll \omega_{LC} \tag{3-33}$$

In this case the dependence on $I_{c,eff}$ and C_{eff} disappears. This is not an obvious advantage, since it quickly becomes apparent that $J(\omega)$ increases linearly with ω. This means that there is no longer a $1/\omega^3$ fall off, and at first glance it will give a shorter decoherence time than can be obtained in the other regime. However, as I_c increases, the width of the histogram as a proportion of critical current narrows rapidly.

Since the SQUID does not decohere the qubit until a bias current is introduced, the idea of a rapid measurement of the qubit is ideal. In this case, the SQUID's current is rapidly ramped up, in a time on the order of a microsecond, which is faster than the relaxation time. In the first round of experiments, the instrumentation needed to measure the switching current could only accurately measure the current up to a few kilohertz, since it needed to accurately determine where the SQUID switched to one part in a thousand. In other words, the measurement of the SQUID current had to be accurate to one part in a thousand

with a 1 ms measuring time. If the histograms are sufficiently narrow, the resolution of the switching current can subsequently decrease. It may be possible to rapidly increase the current and hold it for a time on the order of 1 μs so that it is very likely to switch if the qubit contains one value, and very unlikely to switch if it contains another. This can only work if the current distributions for the two states of the qubit are very distinct, however. If so, a large number of measurements can be taken very quickly while fewer measurements are actually needed, which is the ideal.

The qubit designs which have been fabricated at Lincoln use a SQUID with a larger junction size, and hence critical current, than those at Delft. This thesis discusses the testing of those qubits, and whether their operation in a different regime is an advantage. They have a shunt capacitor of 2 pF, a self inductance of 70 pH, and a critical current for each junction of 10.5 μA, 5.3 μA, and 1.1 μA of each junction for the samples at current densities of 730 A/cm^2, 370 A/cm^2, and 67 A/cm^2 respectively. These give dephasing times of 2 ns, 7 ns, and 1 μs, and relaxation times of 13 ns, 35 ns, and 100 μs.

3.8 The SQUID as a Quantum System

Thus far we have treated the SQUID as a classical device. In the case of the dc SQUID measuring the qubit, it is more correct to view the SQUID as two coupled quantum systems. Moreover, if the internal and external variables of the SQUID are considered separately, there are three coupled systems, although the external variable is the least quantum in nature. This is covered fully in Lin Tian's thesis [64]. Here, we quickly review a simple technique in order to extract a few useful results.

The Hamiltonian for the SQUID by itself is given in Equation (3-34).

$$H_{SQUID} = \frac{P_p^2}{2M_p} + \frac{P_m^2}{2M_m} + \left(\frac{\Phi_0}{2\pi}\right)^2 \frac{(2\varphi_m - 2\pi f)^2}{2L} - 2E_J \cos\varphi_p \cos\varphi_m - \left(\frac{\Phi_0}{2\pi}\right) I_b \varphi_p \qquad \textbf{(3-34)}$$

The full quantum system, excluding the decohering environment, appears in Equation (3-35).

$$H = H_q + \frac{P_m^2}{2M_m} + \frac{1}{2}M_m\omega_m^2(\tilde{\varphi}_m + q_0\sigma_z)^2 + \frac{P_p^2}{2M_p} + \frac{1}{2}M_p\omega_p^2\tilde{\varphi}_p^2 + \delta_I\tilde{\varphi}_m\tilde{\varphi}_p \qquad \textbf{(3-35)}$$

H_q is the Hamiltonian for the isolated qubit [53]. Here, the external and internal degrees

of freedom of the SQUID have been approximated by simple harmonic oscillators. The masses of the internal and external variables are $M_m=(\Phi_0/2\pi)^2(2C_J)$ and $M_p=(\Phi_0/2\pi)^2(2C_J+C_s)$, where C_s is the external capacitance in parallel with the SQUID. C_{eff}, as in Section 3.2, is equal to $2C_J+C_s$. The means of getting from Equation (3-34) to Equation (3-35) is expressed in Equation (3-36) for the external variable, φ_p.

$$\begin{aligned}
\frac{\partial U}{\partial \varphi_p} &= E_J\left(2\cos\langle\varphi_m\rangle\sin\langle\varphi_p\rangle - \frac{I_{bias}}{I_c}\right) \\
\frac{\partial^2 U}{\partial \varphi_p^2} &= 2E_J\cos\langle\varphi_m\rangle\cos\langle\varphi_p\rangle \\
m_p\omega_p^2 &= \frac{\partial^2 U}{\partial \varphi_p^2} = 2E_J\cos\langle\varphi_m\rangle\cos\langle\varphi_p\rangle
\end{aligned} \tag{3-36}$$

Equation (3-37) shows how to develop the simple harmonic oscillator approximation for the internal variable, φ_m.

$$\begin{aligned}
\frac{\partial U}{\partial \varphi_m} &= E_J\left(2\sin\langle\varphi_m\rangle\cos\langle\varphi_p\rangle - \frac{2(2\langle\varphi_m\rangle - 2\pi f)}{\beta_L}\right) \\
\frac{\partial^2 U}{\partial \varphi_m^2} &= E_J\left(2\cos\langle\varphi_m\rangle\cos\langle\varphi_p\rangle - \frac{4}{\beta_L}\right) \\
m_m\omega_m^2 &= \frac{\partial^2 U}{\partial \varphi_m^2} = E_J\left(2\cos\langle\varphi_m\rangle\cos\langle\varphi_p\rangle - \frac{4}{\beta_L}\right)
\end{aligned} \tag{3-37}$$

The potential is expanded to $U(\varphi_i)=K_0+K_1\varphi_i+K_2\varphi_i^2/2$. The center of the oscillator is at the stable point of $K_1=dU/d\varphi_i=0$. K_0 is an offset and may be discarded, leaving K_2, which is equivalent to $M\omega^2$ in a simple harmonic oscillator. $\tilde{\varphi}_m=\varphi_m-\langle\varphi_m\rangle$ and $\tilde{\varphi}_p=\varphi_p-\langle\varphi_p\rangle$. The values of the expectation values of φ_p and φ_m, along with the ω_p and ω_m, are defined in Equation (3-38).

$$\begin{aligned}
\langle\varphi_p\rangle &= \operatorname{asin}\left(\frac{I_{bias}}{I_{c,\,eff}}\right) \quad \langle\varphi_m\rangle \cong \pi f \\
\omega_p &= \frac{1}{\sqrt{L_{J,\,eff}(2C_J)}}\left(1-\left(\frac{I_{bias}}{I_{c,\,eff}}\right)^2\right)^{1/4} \\
\omega_m &= \sqrt{\frac{1}{L_{J,\,eff}(2C_J)}\left(1-\left(\frac{I_b}{I_{c,\,eff}}\right)^2\right)^{1/2} + \frac{2}{L_S C_J}}
\end{aligned} \tag{3-38}$$

We have already assumed that β_L is small, and that the $2/L_mC_J$ term dominates for ω_m. The resonant frequencies and offsets of the oscillators depend on the bias current and the magnetic field through the SQUID. σ_z measures the state of the qubit, and transfers this to

an offset of magnitude +/- q_0 in φ_m. The interaction between $\tilde{\varphi}_m$ and $\tilde{\varphi}_p$ is determined by the term $\delta_I \tilde{\varphi}_m \tilde{\varphi}_p$, where δ_I is the strength of the interaction.

The width in φ_m decreases with the self inductance of the SQUID, as Equation (3-39) quantifies.

$$\Delta\varphi_m = \sqrt{\frac{\hbar}{4\sqrt{2}}\left(\frac{2\pi}{\Phi_0}\right)^2 \sqrt{\frac{L_S}{C}}} \tag{3-39}$$

The Hamiltonian in Equation (3-35) approximates the system, but it leaves out the effect of the quantum width of the qubit phase, whose influence on the SQUID is not as narrowly defined as $q_0\sigma_z$. A better formulation would be $q'I_p$, where I_p is the quantum variable corresponding to the circulating current in the qubit. The new variable, q', is approximately equal to $q_0/\langle I_p \rangle$, where $\langle I_p \rangle$ is the expectation value of the circulating current. Determining the wavefunction I_p requires a fuller definition of H_q which includes the self inductance, as in Section 2.5. If the width of I_p is much smaller than the expectation value, $\langle I_p \rangle$, which is true for the small β_L where we design our qubit, then the $q_0\sigma_z$ is a sufficiently accurate approximation.

The quantum model for the SQUID is important if it is necessary to consider the SQUID and the qubit as an entangled quantum system. It can also be used to derive the means whereby environmental noise couples to the qubit and causes decoherence, as Tian has done.

3.9 Summary

This chapter has explained how the dc SQUID is used to measure the state of the qubit. It details how the switching current histogram relates to the actual state of the qubit. We produce this histogram using a function generator which sends a triangle wave bias current to the SQUID and a sample-and-hold circuit which captures the current value where the SQUID switches to the voltage state. By taking ensemble measurements of a 1000 samples, we can measure a change in the magnetic field on the order of 0.001 Φ_0, which is sufficient to detect the state of the qubit. The dc SQUID is a sensitive flux meter whose coupling to the qubit transfers limited noise since the noise across each branch cou-

ples to the qubit antisymmetrically and the two cancel out at zero current bias.

Chapter 4

Measurements on a Persistent Current Qubit

4.1 Introduction

We have performed experiments on the persistent current qubit in order to measure its signal, and used the data we have taken to derive the parameters of the qubit. This information tells us much about the quality of the fabrication process. This chapter starts by explaining what measurements have been taken, in Section 4.2, and which devices have been measured, in Section 4.3. Then Section 4.4 covers the data taken at temperatures above 300 mK, and explains how the time-ordered measurements account for the change in the qubit step location with temperature and measurement rate. This information is used to extract the parameters of the qubit. Next the measurements taken in a dilution refrigerator, at temperatures ranging from 20 mK to 300 mK, are introduced in Section 4.5. After pointing out the features of the ground state measurements, we explain the need for state preparation and show how it is done. This leads to the hysteresis measurements and their explanation. These results give evidence for quantum energy level crossings and for back action from the measurement SQUID, both of which are explained. When these low temperature results are compared to the qubit's quantum model, we are able to use the locations of the level crossings in order to extract the remaining parameters.

4.2 Measurement Technique

The DC SQUID discussed in Chapter 3 serves as the magnetometer to detect the state of the Persistent Current Qubit. As Figure 4-1 shows, the circulating current of the ground state of the PC qubit changes direction as the magnetic flux bias of the qubit passes through f_q=0.5. This change in the circulating current produces a change in magnetic field which the magnetometer can detect. Since the background magnetic field which biases the qubit also biases the SQUID, the magnetometer measures the sum of the background flux and the flux generated by the qubit. It is preferable to measure the qubit state change

at a flux bias where the SQUID is sensitive to small field changes. By making the SQUID and qubit different sizes, we can have the SQUID frustration, f_S, at 0.75, when f_q=0.5. At this is the point the SQUID is sensitive to changes in magnetic field without the ambiguity of a double well in the SQUID potential, so the changing of the circulating current of the qubit's ground state should result in a noticeable change in the SQUID's switching current.

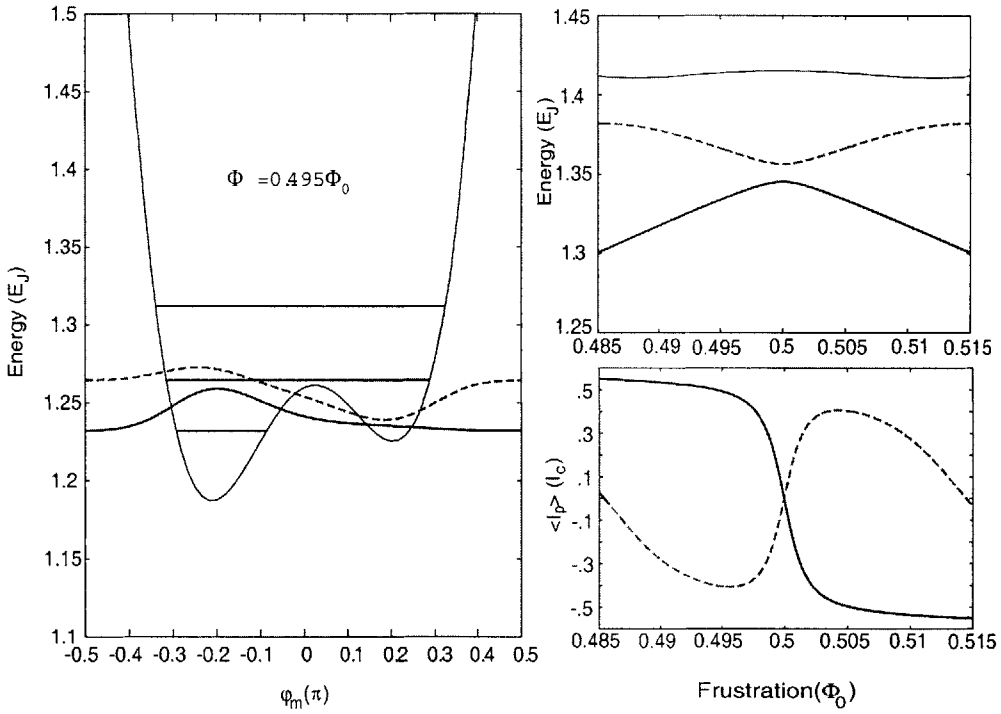

FIGURE 4-1. The levels in the qubit (left) along with the energy band diagram and the circulating currents at various frustrations (right).

4.3 The Samples

Our experiments have been on a SQUID and qubit combination, shown in Figure 4-2, where both the devices are fabricated in Lincoln Laboratory's trilayer process in a single fabrication run. The qubit is placed inside of the SQUID, both for maximum mutual inductive coupling and because this configuration gives symmetrical coupling of the two SQUID branches. This is what causes noise coupled from the SQUID to the qubit to cancel out unless the SQUID is current biased, as is discussed in Section 3.7.1. We have tested three critical current densities, one at 730 A/cm^2, one at 370 A/cm^2, and one at 67

A/cm^2. There are two large capacitors connected on either side of the SQUID. These effectively increase the mass of the SQUID's external variable, lowering the SQUID's resonance and helping to decrease decoherence.

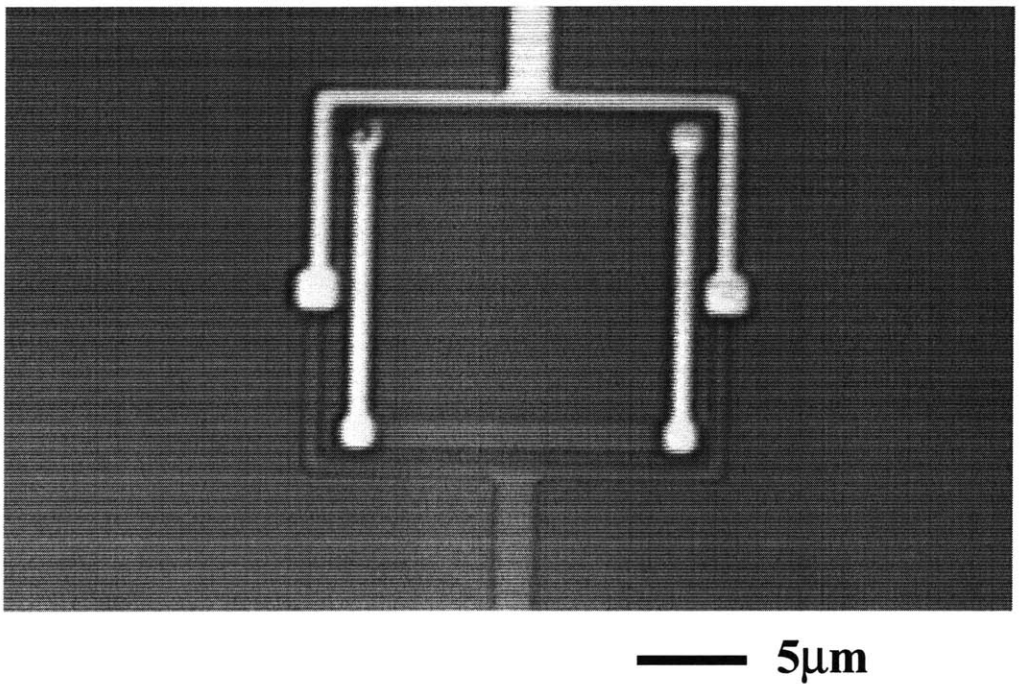

FIGURE 4-2. A micrograph of the SQUID and qubit combination which are measured in this project.

4.4 The Qubit above 300 mK

4.4.1 Experimental Results

Measurements confirm the existence of this change in circulating current in the qubit. In the switching current curve of the SQUID, this looks like a sudden change, or step, in the mean of an ensemble switching current measurement. The experimental technique is described in Section 3.5. The results are shown in Figure 4-3, plotting the mean switching current of the SQUID versus the magnetic field, which shows a small step where the qubit bias is f_q=0.5. These first measurements were done at 300 mK according to the He-3 probe thermometer, but the thermometer is not calibrated, and we believe that the actual temperature of the sample is closer to 400 mK.

There are numerous approaches to normalizing the step in order to separate the qubit magnetization from the flux bias magnetization. The first method of "subtracting the background" works best when the step appears in the linear part of the SQUID curve. In this case, one can simply draw a straight line through the step parallel with the SQUID curve at that point, then subtract the switching current indicated by the line from the measured mean switching current. This gives Figure 4-3 (b and c), which show a pronounced step, but the edges are not straight lines due to the non-linearity of the SQUID curve. Another method is to take a lobe of the SQUID curve in which no step appears and subtract that from a curve in which the step does appear, which works better but it does not take into account that the change of the qubit's circulating current introduces a flux jump to the SQUID which alters the effective magnetic field of the SQUID curve. These methods, which subtract a normalization value from the switching current of the SQUID curve rather than mapping the switching current to the effective magnetic field, cannot adequately describe the qubit's state change. The best method takes this into account, by taking a region of the SQUID curve where no step appears, and determine what value of magnetic field corresponds to each mean switching current. Then we map each point in the step, which is the mean of an ensemble measurement of the switching current, to the corresponding magnetic field. This should give us a straight line (due to the linearly changing flux bias) which includes the step (due to the qubit). Subtracting the linear flux bias, we get a good measurement of the change of the qubit's magnetization.

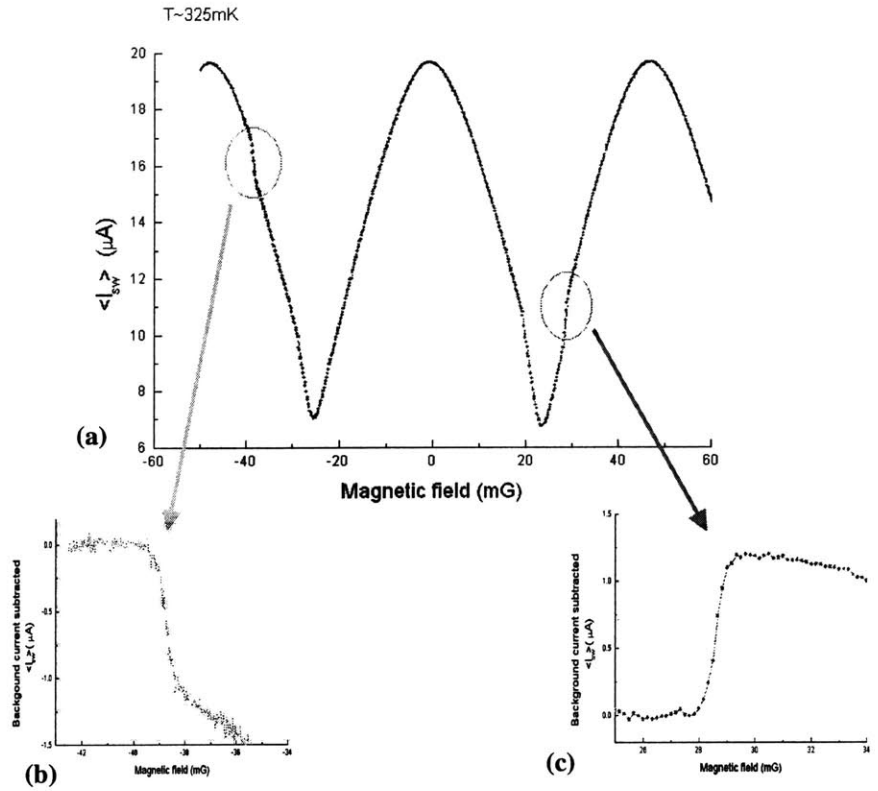

FIGURE 4-3. (a) The SQUID curve in response to a magnetic field. It has a periodicity corresponding to one flux quantum through the SQUID. Steps appear in the curve around f_S=0.75 and -0.75, corresponding to the switching point of the PC qubit. (b) and (c) show the steps at f_S=-0.75 and 0.75, respectively, once a SQUID curve without the step has been subtracted off.

Each point in the SQUID switching current curve is an average of 500 switching events. A close look at the histogram of switching events near the qubit step reveals two peaks, allowing us to distinguish the number of switching events corresponding to each qubit state in the measurement. As Figure 4-4 shows, the two peaks vary in height as the qubit moves through f_q=0.5. This allows for a fourth technique to observe the step. If the histograms have two peaks, then we can count the measurements in one peak and then the other, and produce a probability curve which shows the probability for each direction of the circulating current. This method is only useful when the two peaks are clearly distinguishable, which becomes less true at higher temperatures.

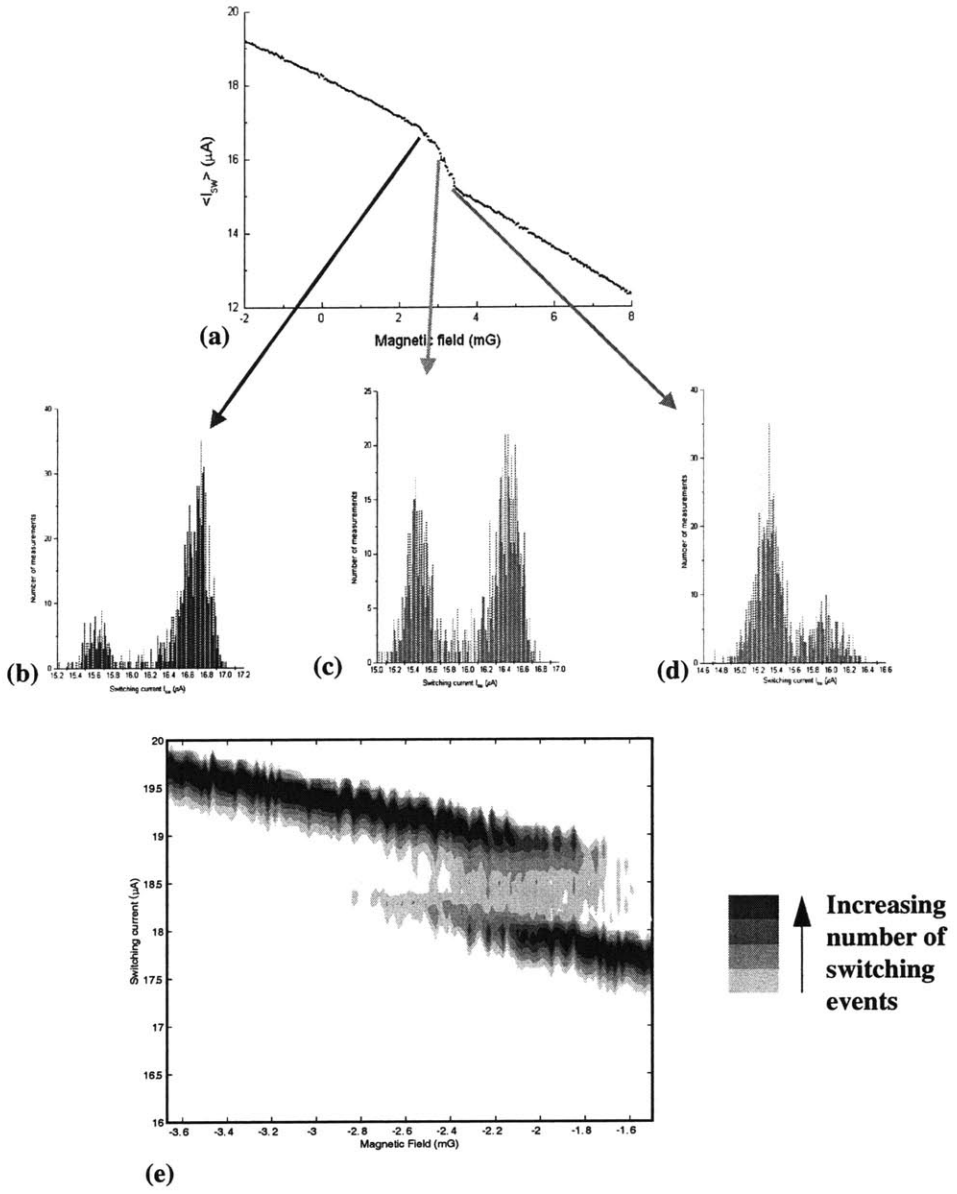

FIGURE 4-4. (a) The signature step of the PC qubit in the average dc SQUID switching current. Looking at the measurements taken at each point reveals bimodal histograms, with the heights of the peaks varying as the flux bias of the qubit changes. (b) Bimodal histogram favoring the higher switching current for f_q<-0.5 (c) Bimodal histogram where the peaks are about even, where f_q=-0.5. (d) Bimodal histogram favoring the lower switching current, where f_q>-0.5. (e) Another way of looking at the data: a contour plot where each vertical slice represents the histogram at a certain magnetic field value. The shade of grey indicates the number of switching events appearing at each bias current value of the SQUID.

While we can measure the qubit in each state, there is no clear correlation between sequential measurements. The state in which we measure the qubit each time is random, although the probability has a clear dependence on the flux bias. The qubit must have some mechanism for changing states in between measurements. Each state is energeti-

cally stable, corresponding to a minimum in the energy potential, and there are four possible ways for the qubit to escape its energy well. The first is thermal excitation. The second is incoherent quantum tunneling, in which the phase particle tunnels from one well to the other, but does not coherently occupy both wells. Third, the phase particle can coherently tunnel, reaching a superposition of the two circulating current states. Finally, changes in the qubit's flux bias alter the depth and shape of the potential wells, so it may cause the qubit to change states by eliminating the barrier, or at least reducing the barrier sufficiently to greatly enhance one or more of the other three mechanisms. One such change to the qubit's flux bias may be due to back action from the DC SQUID, which, for the samples with high current density, has a large circulating current which couples by mutual inductance to the qubit. By measuring the qubit step signature against temperature and measurement rate, we can explore the possible sources of the qubit state change.

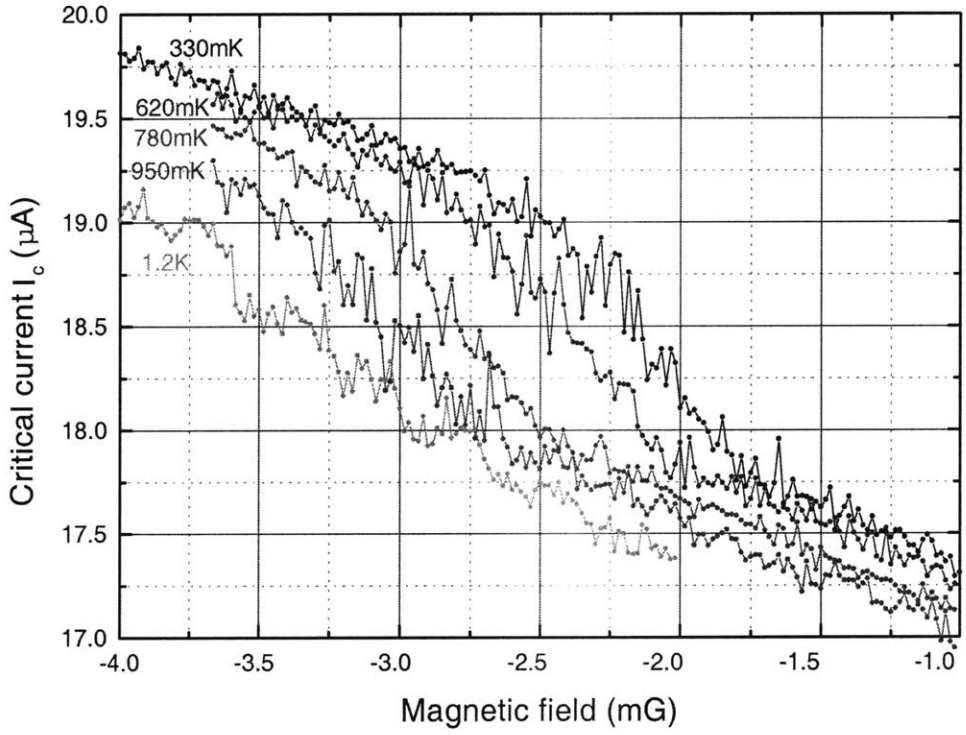

FIGURE 4-5. The temperature dependence of the qubit step signature. As temperature increases, the qubit step becomes wider and shifts to the left, towards the higher switching current.

As the temperature rises, the magnetic field at which the step occurs shifts towards a greater magnitude of the switching current. The step also becomes wider, as shown in Figure 4-5. A similar effect is observed at lower rates of sweeping the bias current (see

Figure 4-6). That measurement rate and temperature have similar effects suggest that classical thermal activation is the best explanation for this phenomenon. The data shown in these two figures is from the sample with a critical current density of 730 A/cm^2.

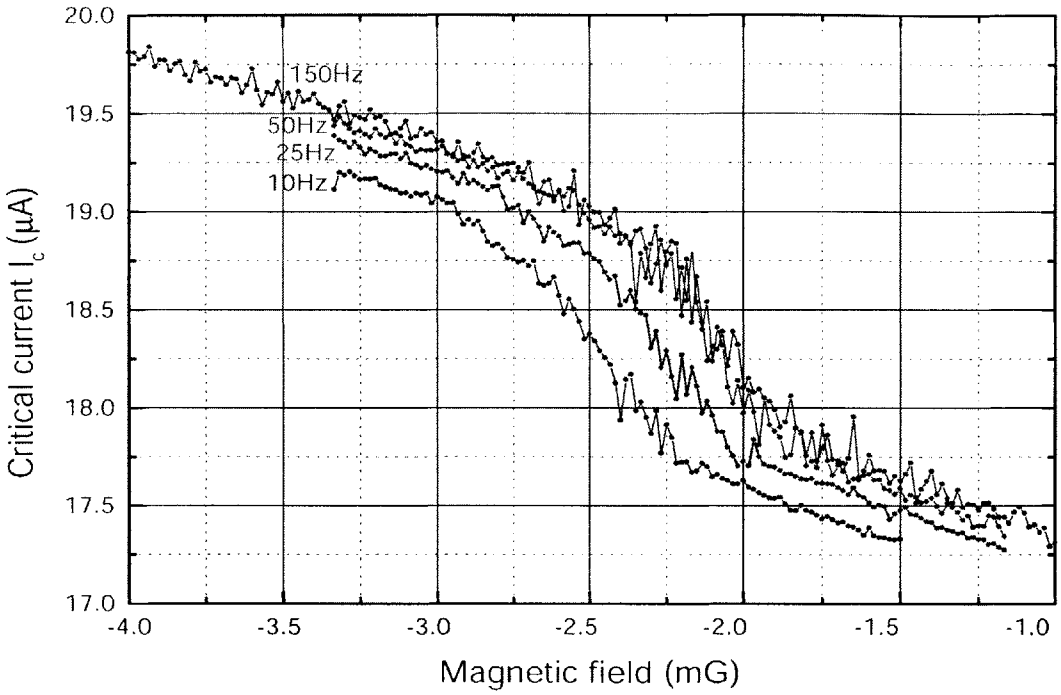

FIGURE 4-6. The dependence of the qubit step signature on the measurement rate. As the frequency of the measurement decreases, the qubit step becomes wider and shifts to the left, towards higher magnitude switching current.

A clearer picture of the phenomenon can be obtained by looking at the individual histograms. The contour plots in Figure 4-7 are one way of doing this, similar to the plot shown in Figure 4-4(e). It has the same axes of Figure 4-5 and Figure 4-6, but rather than a plot where each point represents the mean of a histogram, this contour plot shows the number of switching events at each flux and current bias point, so the a vertical line through the plot represents a single histogram. In these plots, it is clear that there are switching events between the two histogram peaks, and that the number of those switching events increase with temperature. Although it is expected that the histogram would grow wider with temperature due to the thermal activation's contribution to probabilistic switching of the SQUID, this is a separate phenomena, as the observed width of the SQUID switching current variance away from the qubit step is not large enough to account for the number of events between the two peaks.

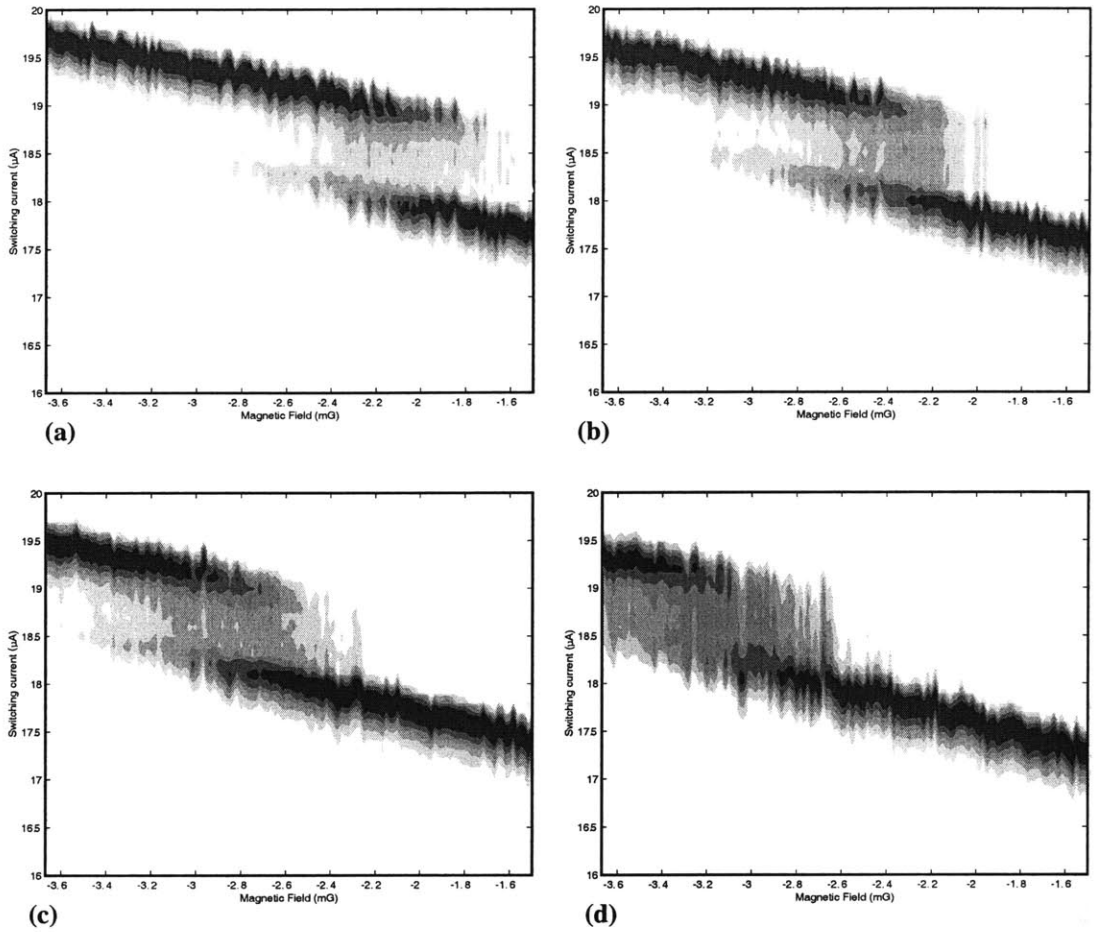

FIGURE 4-7. Each of these four contour plots show the number of switching events at the specified magnetic field bias and current bias. Each plot occurs for the same measurement rate, 150 Hz, but at a different temperature, (a) 420 mK, (b) 620 mK, (c) 780 mK, and (d) 950 mK. As the temperature increases, so does the number of switching events between the mean switching currents for the two states of the qubit. The curves shift to the left, towards the top of the lobe in the SQUID curve.

Similar contour plots show the results for different measurement rates in Figure 4-8. Slowing down the ramping of the SQUID bias current has a similar effect to raising the temperature, although it takes a much larger change in rate to produce the same effect as a small change in temperature. Qualitatively, slowing down the ramp rate results in more switching points in between the two peaks, and pushes the midpoint of the step to the left.

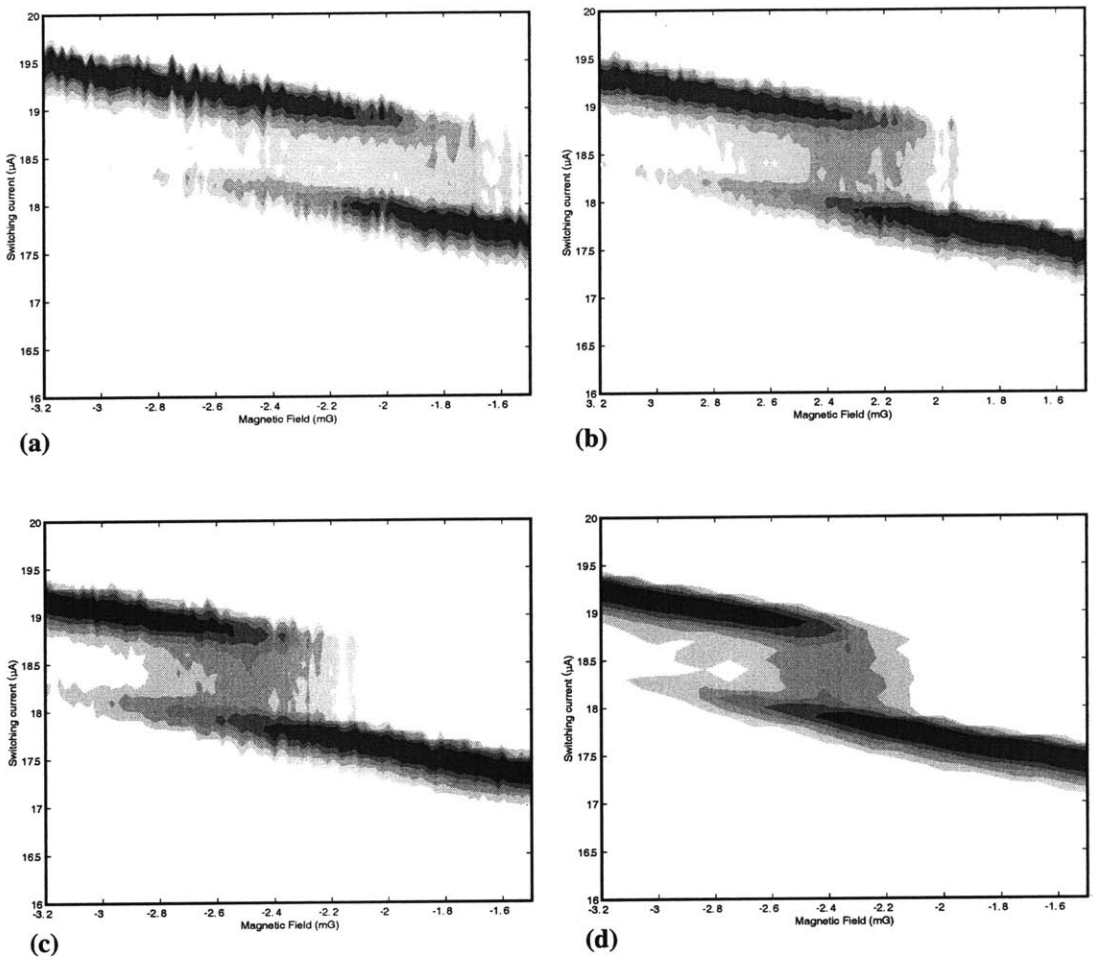

FIGURE 4-8. As above, these four contour plots show the number of switching events at the specified magnetic field bias and current bias. Each plot occurs at the same temperature, 330 mK, but a different ramp rate, (a) τ_{ramp}=2.5 ms, (b) τ_{ramp}=10 ms, (c) τ_{ramp}= 25 ms, and (d) τ_{ramp}=125 ms. As the rate increases, so do the number of switching events between the mean switching currents for the two states of the qubit, although more slowly than for temperature. The curves shift to the left, towards the top of the lobe in the SQUID curve.

4.4.2 Analysis

We will define **R**, the right state, as the qubit state where the persistent current in the qubit is circulating counter-clockwise, which produces a lower SQUID switching current in the step shown in the above plots. **L**, the left state, has circulating current in the clockwise direction and produces a higher SQUID switching current in the plots. **L** indicates that the qubit wavefunction is localized in the left well, while **R** indicates that it is localized in the right well. They do not have a direct correspondence to the ground and first excited states since, as Figure 4-1 shows, the direction of the circulating current of the first two states exchange places as the f_q goes through 0.5, while **L** and **R** consistently

refer to the same circulating current direction.

Both Figure 4-5 and Figure 4-6 show the step moving to the left as temperature is increased and rate is decreased. Both of these plots focus on a single step, where the transition from **L** to **R** is from left to right. As Figure 4-3 shows, while the L to R transition is still from left to right, at this location in the SQUID, **L** results in a lower switching current and **R** causes a higher switching current. In this case, the step moves to the right as temperature is increased and rate is decreased. We will focus on the case shown in Figure 4-5 and Figure 4-6.

The timescales involved in the measurements, illustrated in Figure 4-9, help to explain these results. τ_{hist} is the time to take the full ensemble of measurements necessary to assemble a histogram of switching events, while τ_{ramp} is the time to take one measurement out of the ensemble. τ_{ramp} is more strictly defined as the time to ramp the current from 0 μA to $2I_c$, its maximum, so it is approximately one-quarter of the period of the triangle wave signal sent to the SQUID. τ_{meas} is the time it takes to distinguish between the two states of the qubit. Specifically, τ_{meas} is the time to ramp from the mean SQUID switching current for one state of the qubit (in this case, the **R** state) to the mean switching current for the other state of the qubit (the **L** state). This quantifies the non-instantaneous measurement, where it requires a finite time to sweep the bias current of the SQUID. The state of the qubit determines the flux which the SQUID sees, influencing the current bias and time at which it switches. Since the two states are separated by about 1 μA in the SQUID's switching current, this time corresponds to 1/320th of the total SQUID period. At 150 Hz, τ_{ramp}=1.6 ms, and τ_{meas}=20 μs.

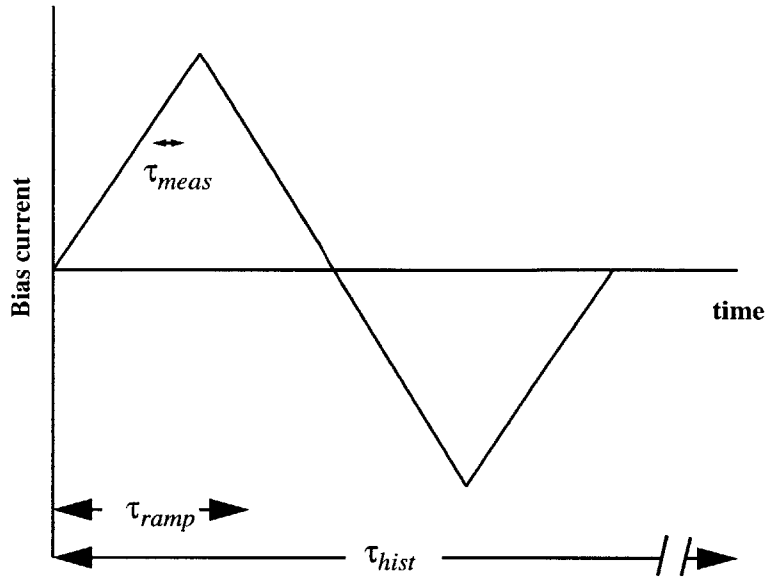

FIGURE 4-9. A single oscillation of the current corresponds to τ_{ramp}. A histogram consists of 500-2000 ramps, and thus takes τ_{hist}~1000τ_{ramp}. The time it takes to distinguish between the two states of the qubit are much smaller. Since it only takes about 1 μA to do so, and the full oscillation has an amplitude of 20 μA, τ_{meas}~(1/320)τ_{ramp}.

Figure 4-10 illustrates these switching timescales along with the possible switching currents. ***B*** is the switching current to measure the qubit in **R** and ***D*** corresponds to the qubit in **L**. Say that the qubit is in **L** when the SQUID bias reaches point ***A*** on this curve. If it changes to **R** by ***B***, then the SQUID will measure it as **R**. If it changes to **R** at point ***C***, however, then the SQUID will immediately switch to the voltage state, and a switching current halfway between **R** and **L** will be recorded for that event. If it waits until point ***D*** to change to **R**, then the SQUID will measure **L** regardless. Now, consider the qubit in state **R** at point ***A***. If it changes to **L** at ***B***, then there's a roughly even chance that the SQUID will measure **L** rather than **R**. If it has not changed from **R** by the time the bias current reaches ***C*** or ***D***, however, the SQUID has already switched, so it will have measured **R** regardless. So the time in between the two switching points ***B*** and ***D***, τ_{meas}, gives the time during which the qubit may change from **L** to **R** and give a false reading, while it is too late for the qubit to change from **R** to **L**. If the rate at which the qubit moves between the two wells is on the order of τ_{meas}, then the SQUID shows a higher preference for the lower switching current than the average state of the qubit warrants, and the mean switching current will average towards **R**.

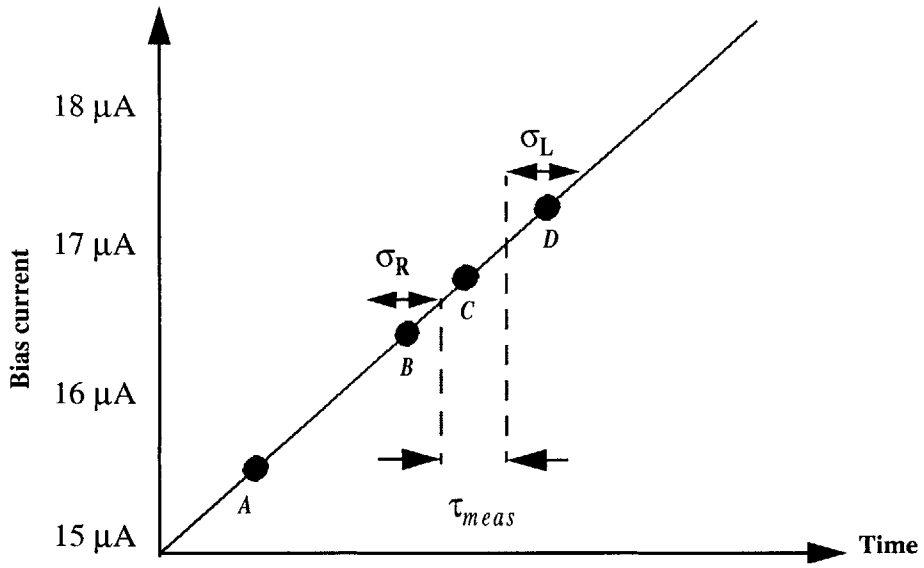

FIGURE 4-10. This magnification details the time over which the SQUID measures the qubit. Since the switching of the SQUID is stochastic, there is some standard deviation of the switching current no matter what state the qubit is in. σ_L shows the standard deviation of the SQUID when the qubit is in state L, while σ_R shows the standard deviation of the SQUID when the qubit is in state R. *A, B, C, D* are different points where the state of the qubit are considered.

The characteristic time for the state of the qubit to change states, τ_{therm}, comes from the thermal escape rate of the qubit's phase particle from its well. The equation for it is identical to that for the SQUID thermal escape rate, namely $\tau_{therm}^{-1} = \Gamma_{therm} = \frac{7.2\Delta U \omega_0}{Qk_BT\,2\pi} e^{-\frac{\Delta U}{k_BT}}$, where ω_0 is the attempt frequency, ΔU is the energy barrier, and Q is the quality factor (see Section 2.8.4). τ_{therm} depends on the frustration, and since the potential for the qubit is double-welled, it's necessary to consider the escape rate in each direction separately, since it may be easier for the qubit to move in one direction than the other. This is clear in Figure 4-11, where the right well is much deeper than the left. The barrier for the phase particle traveling from well **L** to well **R**, $\Delta U_{\mathbf{LR}}$, is much smaller than the barrier to travel from well **R** to well **L**, $\Delta U_{\mathbf{RL}}$. In this case, $\tau_{\mathbf{LR}} \ll \tau_{\mathbf{RL}}$. The wells change in depth as the frustration of the qubit changes, so that $\tau_{therm} = \tau_{\mathbf{LR}} = \tau_{\mathbf{RL}}$ only at f=0.5. At temperatures where τ_{therm} is smaller than τ_{meas} at f=0.5, the position of the midpoint of the step will shift to a magnetic field bias which gives a qubit frustration where $\tau_{\mathbf{LR}} \sim \tau_{meas}$, and there is less probability that the qubit will change to state **R** within the measurement time.

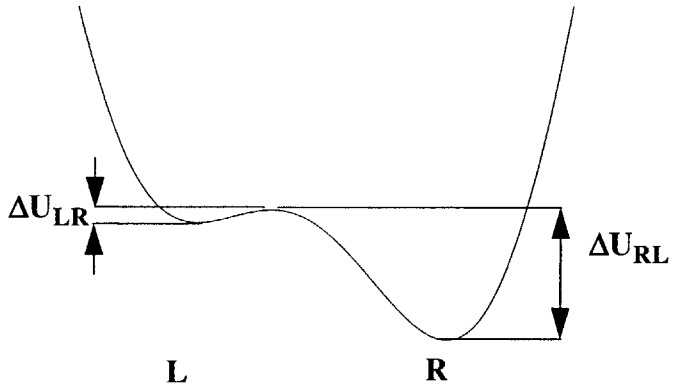

FIGURE 4-11. The double well potential of the persistent current qubit. A particle traveling from L to R sees a smaller barrier than a particle traveling from R to L.

In order to do a simulation of the SQUID switching current in response to the qubit, we need to calculate $\tau_{\mathbf{LR}}$ and $\tau_{\mathbf{RL}}$, which we can get from $\Delta U_{ij}(f_q)$ and $\omega_i(f_q)$. These variables is not particularly hard to calculate, since we have the potential energy for the qubit, repeated here in Equation (4-1).

$$U = E_J[2 + \alpha - 2\cos\varphi_p\cos\varphi_m - \alpha\cos(2\varphi_m + 2\pi f_q)] \tag{4-1}$$

Symmetry reduces the number of calculations we have to do, since $\Delta U_{\mathbf{RL}}(f)=\Delta U_{\mathbf{LR}}(1-f)$. It is necessary to simplify this equation by reducing it to a single dimension, namely the dimension through which the phase particle tunnels, φ_m, where $\varphi_p=0$. ΔU is simply the difference between the minimum and the maximum, and at the minimum, $\sqrt{\frac{\partial^2 U}{\partial\varphi_m^2}\frac{1}{M_m}}$ gives $\omega_{\mathbf{L}}$ or $\omega_{\mathbf{R}}$. This can easily be worked out in the same way that the SQUID's switching current was in Section 3.3.1. Since ΔU is nearly linear near $f_q=0.5$, a simple approximation for $\Delta U_{\mathbf{RL}}$ is given in Equation (4-2). The negative option assumes a step where the ground state when $f_q<0.5$ is **L** and the ground state when $f_q>0.5$ is **R**, as in Figure 4-3(b), which is the focus for the current discussion. Notice that in the steps we have been looking at occur around $f_q=-0.5$, which does not alter the problem since the potential is periodic in f_q, and it is appropriate to simply add or subtract an integer value to f_q to bring it between 0 and 1.

$$\Delta U_{\mathbf{LR}}(f_q) = 3.5E_J(f_q - 0.5) + \Delta U(0.5) \quad \textbf{(4-2)}$$

The Monte Carlo method of determining the histogram, described in Section 3.4, is useful for solving this problem. On each current ramp of the SQUID, the qubit is placed in a random state with a probability determined by the relative rates, such that the probability of the qubit phase particle starting in well **R** is $P_{\mathbf{R}} = \Gamma_{\mathbf{LR}}/(\Gamma_{\mathbf{LR}}+\Gamma_{\mathbf{RL}})$. Then a Monte Carlo method similar to that used in the SQUID is applied to the qubit. Its probability of being thermally activated such that it switches from its current well is calculated from $\Gamma(f_q)$ and Δt, and a pseudorandom number generator determines whether it actually changes wells or not during that time interval. This determines where it changes wells, and when it changes state it also affects the SQUID's state. The Monte Carlo simulation is simultaneously applied to the SQUID, exactly as described in Section 3.4, so that its switching is affected by the changes in the qubit signal as well as its own probabilistic switching times. The simulated result is qualitatively the same as the measured result, as shown in Figure 4-12.

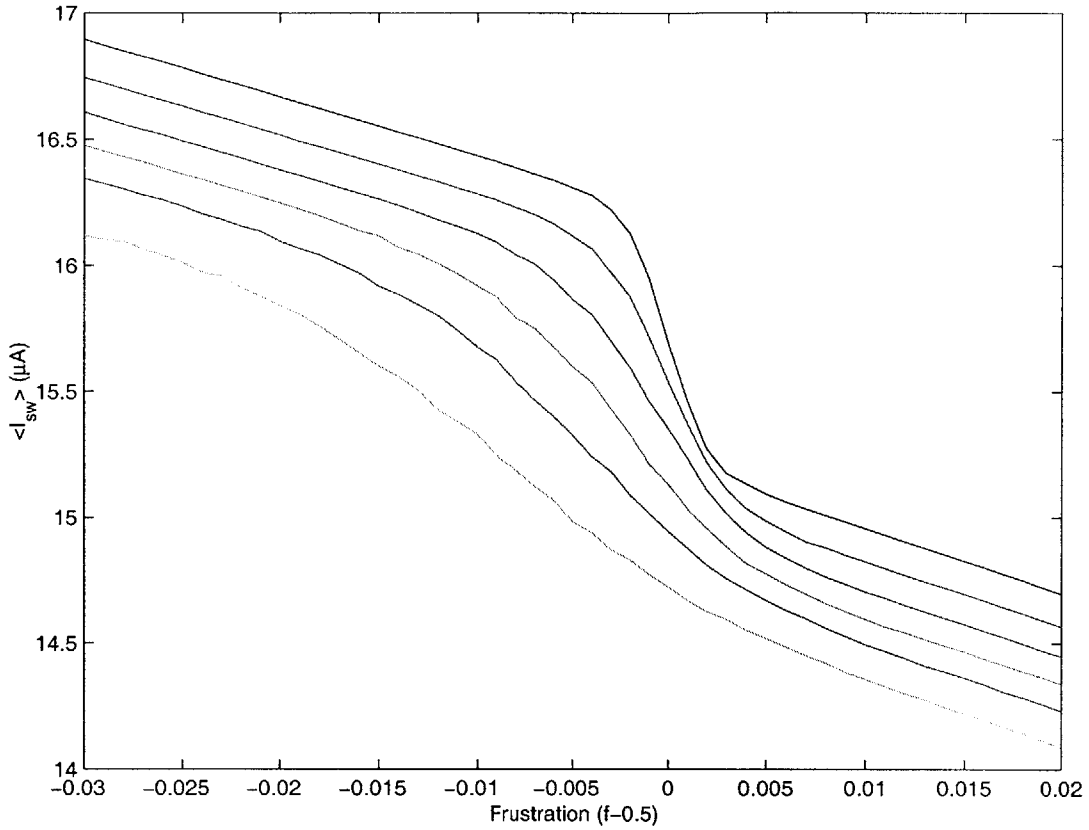

FIGURE 4-12. The temperature dependence of the qubit step signature as calculated in the Monte Carlo simulation. Like in the measurements, as the temperature increases, the qubit step becomes wider and shifts to the left, towards higher magnitude magnetic field.

Additionally, Kenneth Segall has worked out an analytical model of this effect [44]. At the start of the measurement, point ***B*** in Figure 4-10, $P_{\mathbf{R}} = \Gamma_{\mathbf{LR}}/(\Gamma_{\mathbf{RL}}+\Gamma_{\mathbf{LR}})$, which is the steady-state probability for the occupation of $P_{\mathbf{R}}$. He then reasons that the probability of measuring a switching current corresponding to qubit state **R** is $P_{\mathbf{R},meas}=P_{\mathbf{R}}+P_{\mathbf{L}}(1-P_{stay})$. P_{stay} is the probability that the qubit does not change states by the middle of τ_{meas}. $P_{stay} = \exp(-\Gamma_{\mathbf{LR}}\tau_m)$, where τ_m is equal to $\tau_{meas}/2$. This changes the shape of the step, which, when normalized, follows the mean of the circulating current, $\langle I_p \rangle$. $\langle I_p \rangle = I_{p\mathbf{R}}P_{\mathbf{R}} + I_{p\mathbf{L}}P_{\mathbf{L}}$. $I_{p\mathbf{R}}$ is the persistent, circulating current in the qubit when it is state **R**. The value of the persistent current in the **L** state is $I_{p\mathbf{L}}=-I_{p\mathbf{R}}$. Replacing $P_{\mathbf{L}}$ and $P_{\mathbf{R}}$ with $P_{\mathbf{L},meas}$ and $P_{\mathbf{R},meas}$ changes Equation (4-3) to Equation (4-4), resulting in a different shape for the step. In this case, $\langle I_p \rangle$ is not the true value of the mean of the qubit's persistent current value, but the measured value which gives the step. Note that in these equations we assume that the damping parameter, and ω_0, the resonant frequency of the

well, are unaffected by the change in frustration which drives the difference between $\Delta U_{\mathbf{LR}}$ and $\Delta U_{\mathbf{RL}}$. This is a reasonable but not entirely true approximation which can be corrected later. This formulation assumes an essentially digital measurement, and its output depends on whether the state of the qubit changed in the range corresponding to **L** or to **R**.

$$\frac{\langle I_p \rangle}{I_{p\mathbf{L}}} = \frac{\Gamma_{\mathbf{RL}} - \Gamma_{\mathbf{LR}}}{\Gamma_{\mathbf{RL}} + \Gamma_{\mathbf{LR}}} = \frac{\frac{\omega_0}{2\pi}\left[\exp\left(-\frac{\Delta U_{\mathbf{RL}}}{k_B T}\right) - \exp\left(-\frac{\Delta U_{\mathbf{LR}}}{k_B T}\right)\right]}{\frac{\omega_0}{2\pi}\left[\exp\left(\left(-\frac{\Delta U_{\mathbf{RL}}}{k_B T}\right) + \exp\left(-\frac{\Delta U_{\mathbf{LR}}}{k_B T}\right)\right)\right]} = \tanh\left(\frac{\Delta U_{\mathbf{LR}} - \Delta U_{\mathbf{RL}}}{k_B T}\right) \quad \textbf{(4-3)}$$

$$\frac{\langle I_p \rangle}{I_{p\mathbf{L}}} = P_{stay} \tanh\left(\frac{\Delta U_{\mathbf{LR}} - \Delta U_{\mathbf{RL}}}{k_B T}\right) + (P_{stay} - 1) \quad \textbf{(4-4)}$$

The usual means of normalizing the SQUID curve to produce a curve of the qubit's $\langle I_p \rangle$ uses the mean switching current of the SQUID rather than a straight division between **L** signals and **R** signals. This requires the more complicated analysis shown in Equation (4-5).

$$\frac{\langle I_p \rangle}{I_{p\mathbf{L}}} = P_{\mathbf{L}} - P_{\mathbf{R}} + \int_0^{\tau_{meas}} I(t) P_h(t) dt \quad \textbf{(4-5)}$$

Here, $I(t)$ is the bias current of the SQUID at time t, normalized to -1 at the lower switching current and +1 for the higher switching current, such that $I(t)=(I_{SQUID}(t)-I_{center})/\Delta I$, where I_{center} is the midpoint between the lower and higher switching currents, and $2\Delta I$ is the difference between the two switching currents. +1 is equivalent to $I_{p\mathbf{L}}$ and -1 is equivalent to $I_{p\mathbf{R}}$ when mapped from switching current to the qubit's circulating current. $P_h(t)$ is the probability that the qubit will change from **L** to **R** at time t, and is defined in Equation (4-6).

$$P_h(t)dt = (1 - P_{\mathbf{R}}) e^{-\Gamma_{\mathbf{LR}} t} \Gamma_{\mathbf{LR}} dt \quad \textbf{(4-6)}$$

In this formulation, the full definition of $\Gamma=(\Delta U \omega_0 / 2\pi Q k_B T)\exp(-\Delta U / k_B T)$ is applied, where Q is the quality factor. In this equation, the term $(1-P_{\mathbf{R}})$ is the probability that it starts in state **L**, $\exp(-\Gamma_{\mathbf{LR}} t)$ is the probability that it has not switched yet, and $\Gamma_{\mathbf{LR}} dt$ is the probability of switching in a infinitesimal time dt. When the integral in Equation (4-5) has

been solved, one gets Equation (4-7).

$$\frac{\langle I_p \rangle}{I_{p\mathbf{L}}} = P_{\mathbf{L}} - P_{\mathbf{R}} + (1 - P_{\mathbf{R}})\left[\left(\frac{2}{\Gamma_{\mathbf{LR}}\tau_{meas}}\right)[1 - \exp(-\Gamma_{\mathbf{LR}}\tau_{meas})] - 1 - \exp(-\Gamma_{\mathbf{LR}}\tau_{meas})\right] \quad \textbf{(4-7)}$$

Since $P_{\mathbf{L}} + P_{\mathbf{R}} + \int P_h(t)dt = 1$, $P_{\mathbf{L}}=(1-P_{\mathbf{R}})\exp(-\Gamma_{\mathbf{LR}}\tau_{meas})$. Thus Equation (4-7) simplifies to Equation (4-8).

$$\frac{\langle I_p \rangle}{I_{p\mathbf{L}}} = (1 - P_{\mathbf{R}})\left(\frac{2}{\Gamma_{\mathbf{LR}}\tau_{meas}}\right)[1 - \exp(-\Gamma_{\mathbf{LR}}\tau_{meas})] - 1 \quad \textbf{(4-8)}$$

Figure 4-13(a) shows the three step shapes given by Equation (4-3), Equation (4-4), and Equation (4-8). Figure 4-13(b) compares Equation (4-8) with the measured step, which shows a very good match between the shapes. In either form of the equation, the value of $\Delta U(f)$ is needed. Near f=1/2, ΔU's value varies approximately linearly with the flux bias, as shown in Equation (4-9).

$$\begin{aligned} \Delta U_{\mathbf{RL}}(f) &= 2\pi\alpha E_J(f_q - 0.5) + \Delta U_{\mathbf{RL}}(f_q{=}0.5) \\ \Delta U_{\mathbf{LR}}(f) &= -2\pi\alpha E_J(f_q - 0.5) + \Delta U_{\mathbf{LR}}(f_q{=}0.5) \end{aligned} \quad \textbf{(4-9)}$$

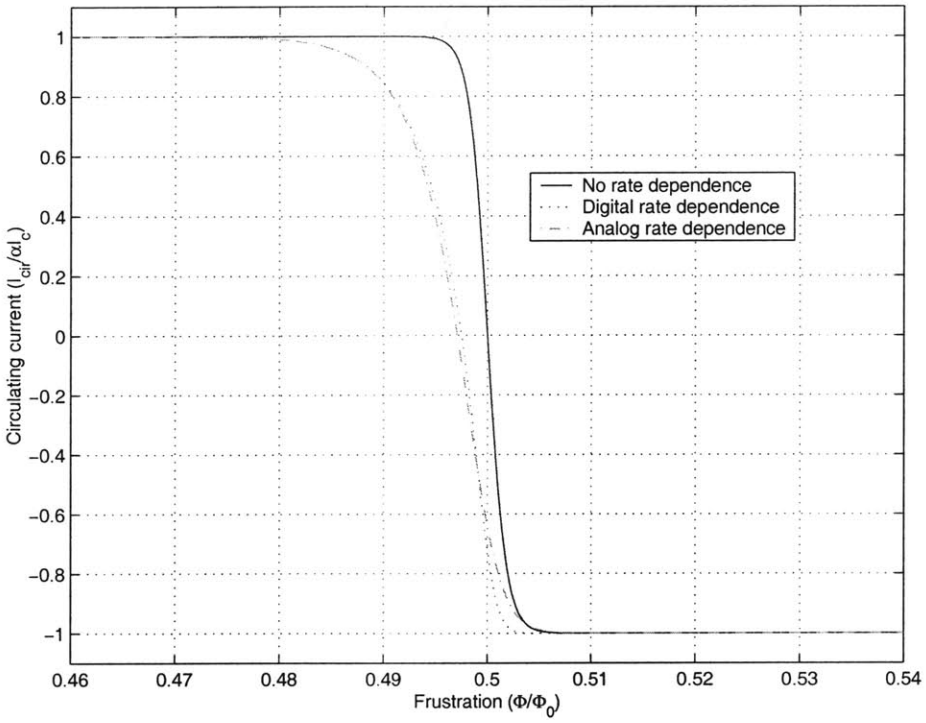

(a)

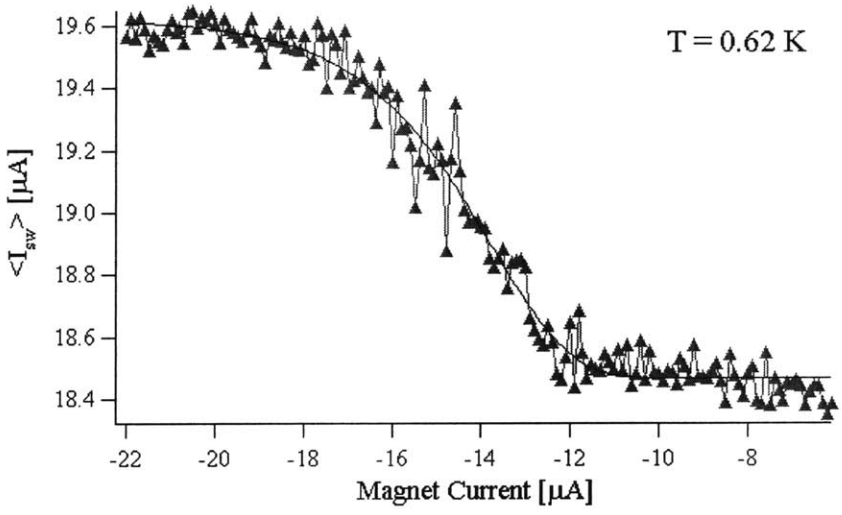

(b)

FIGURE 4-13. (a) These three curves show the shape of the step predicted by the three analytical models. Method 1 does not take into account the time difference between measuring state L and state R. Method 2 assumes a digital read-out that measures L and R with the time difference, but does not allow for anything in-between to affect the average. Method 3 allows for switching in between the states. (b) The curve predicted by Method 3 closely matches the experimentally measured curve.

Tracking the midpoint of the qubit step is a convenient way to distill the data down

to the minimum necessary information. The midpoint location is the magnetic field bias, in units of flux quanta in the qubit, f_z, where $<I_p(f_z)>=0$.

$$f_z = 0.5 - \left[\frac{k_B T}{4E_J}\ln\left(\frac{\Delta U_{LR}(f_z)\omega_0\tau_{meas}}{1.44Qk_BT}\right) - \frac{\Delta U_{LR}(0.5)}{4E_J}\right] \quad \textbf{(4-10)}$$

This equation comes from Equation (4-4), combined with the linear approximation of the barrier height in Equation (4-9). This is a transcendental equation since f_z influences ΔU, but ΔU's influence on f_z is logarithmic. The equation indicates that when thermal activation is predominant, the step's movement is linear in temperature and logarithmic in measurement time.

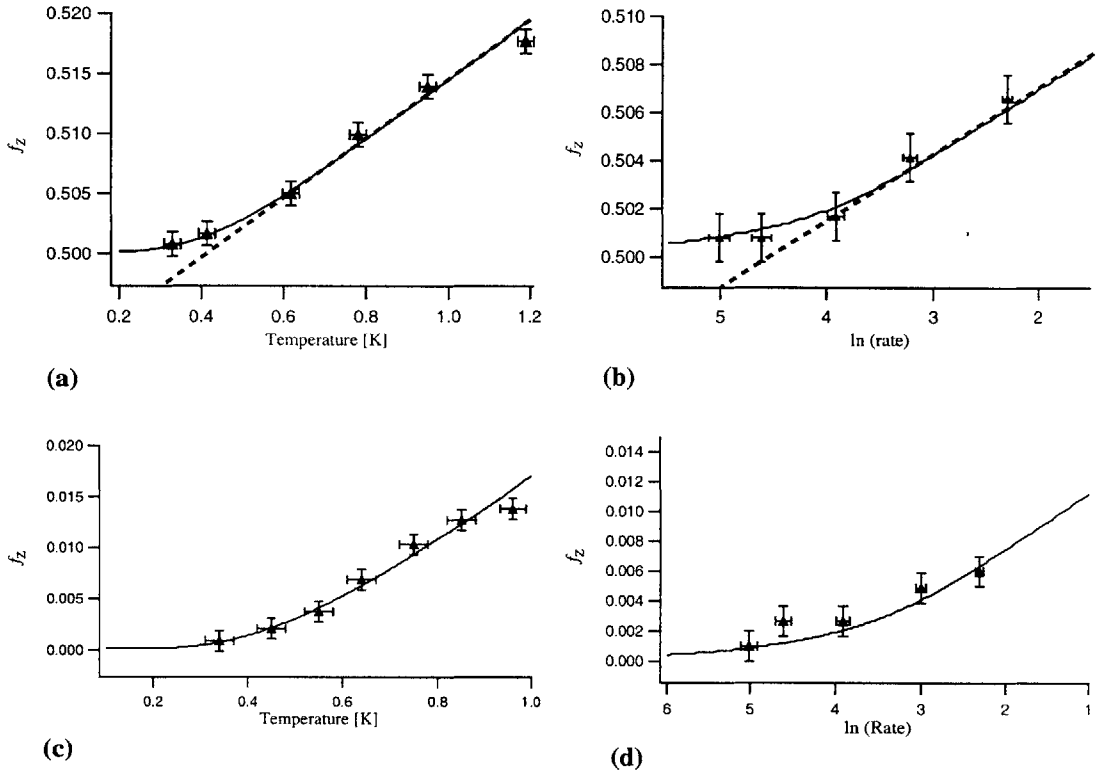

FIGURE 4-14. These curves show the location of the qubit step midpoint in the SQUID curve as a function of temperature or rate for two different samples. The point where it becomes constant in temperature indicates the barrier height. (a) The location of the midpoint for different temperatures in the 730 A/cm^2 sample. (b) The same for different rates in the 730 A/cm^2 sample. (c) The same for different temperatures in the 370 A/cm^2 sample. (d) The same for different rates in the 370 A/cm^2 sample.

Figure 4-14 shows how the midpoint of the step moves both with temperature and ramp rate for two SQUID and qubit samples. Although the layouts are identical, one was fabricated with 730 A/cm^2, while the other was fabricated with 370 A/cm^2. The rate data

is plotted with the logarithm of the rate on the x-axis, while the temperature data has the temperature on the x-axis, which gives roughly equivalent plots. Both graphs follow the Equation (4-10), and are linear at high values of temperature and measurement time, and flat at low values of temperature and measurement time. The curve flattens out when $\frac{k_B T}{E_J} \ln\left(\frac{\Delta U_{\mathbf{LR}}(f_z)\omega_0 \tau_{meas}}{1.44 Q k_B T}\right)$ is small compared to $\frac{\Delta U_{\mathbf{LR}}(0.5)}{4E_J}$.

4.4.3 Deriving Parameters

Equation (4-10) describes the shape of the curves in Figure 4-14. There are four parameters to fit these curves, E_J, E_C, α (the ratio of the small junction to the large junction of the qubit), and Q. ΔU and ω_0 derive from E_J, E_C, and α. We can fit the curves to the data first by using E_J and Q to fit the linear slope in both the rate and temperature data, then by fitting α by using the turning point from flat to linear. E_C is the hardest parameter to fit. If the junctions were ideal, then knowing E_J should give us E_C simply from the geometry of the junctions. While uncertainty about the junction capacitance may alter the estimate of Q by as much as a factor of 3, no other parameter depends strongly on the approximation of E_C. The values which the data suggests for the 730 A/cm^2 sample are E_J=4000 μeV, E_C=6.6 μeV, α=0.58, and Q=1.2x10^6. For the 370 A/cm2 sample, E_J=2400 μeV, E_C=5.5 μeV, α=0.59, and Q=1x10^6. The Q value gives an environmental resistance better than 1 MΩ.

4.4.4 Conclusions for the Thermal Activation Regime

The thermal activation theory accurately explains the qubit's behavior at high temperatures. Not only does the theory correctly predict the change in the step's location as a result of both temperature and measurement rate, it also predicts the shape of the step. Using this data, it is possible to derive two of the four significant parameters of the qubit with high accuracy, and the other two within an order of magnitude. The derived values of Q suggest that these junctions have very good quality for niobium-aluminum oxide-niobium junctions, exhibiting a subgap resistance better than 100 MΩ. In this measurement regime, however, the qubit clearly acts as a classical two-state system. The next question is whether the qubit exhibits quantum behavior as the temperature is lowered and thermal activation is frozen out.

4.5 The Qubit below 300 mK

4.5.1 Initial Measurements

Below 300 mK, the qubit step begins to acquire features which significantly differentiate it from the previous results. As Figure 4-15 shows, as temperatures get lower the step becomes broader and develops distinct peaks and dips. These peaks and dips are not noise, as they are repeatable. Moreover, they develop gradually with changes in temperature and measurement rate.

This first sample, which is shown in Figure 4-15, had an unusually high current density of 730 A/cm^2, so another sample, which had a J_c of 370 A/cm^2 was tested as well. This showed similar results, which will be the focus of this discussion.

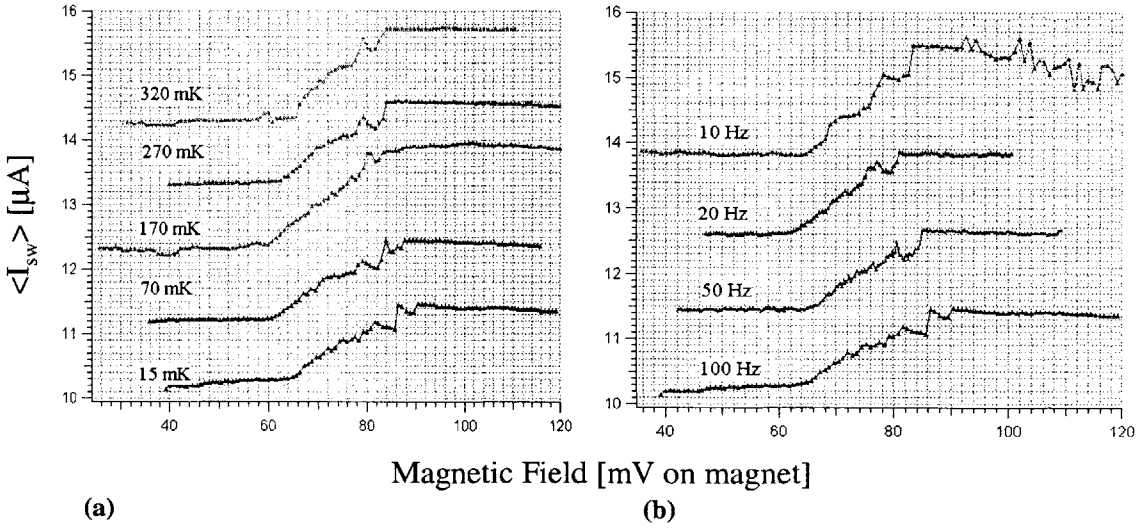

FIGURE 4-15. (a) The step as temperature decreases from 600 mK to 15 mK. The step becomes broader and develops distinct peaks and dips. (b) As the measurement rate is decreased, the step changes similarly to how it would change for increasing the temperature.

While the 730 A/cm^2 sample began to show structure around 300 mK, the 370 A/cm^2 sample showed structure at 400 mK. This seemed unusual since the small critical current should mean a smaller energy barrier for thermal activation, which would make the sample more vulnerable to thermal activation. However, any reduction in the barrier would facilitate quantum tunneling as well, which, since it depends on the quantum energy levels of the qubit, would cause significant structure in the qubit. This will be discussed in more detail in the Analysis in Section 4.5.4.

4.5.2 Design for Hysteresis Measurement

Once the general shape of the step had been measured, it became clear that in order to get more detailed information, we wanted to observe the transition rate in one direction by choosing in which well the qubit started in for each measurement. Each SQUID switching event is expected to reset the qubit (the oscillations of the SQUID while it is in its voltage state randomize the qubit's state), so any preparation of the qubit must occur after the SQUID returns to its zero-voltage state and before it switches to the voltage state. This can be done by pulsing the background magnetic field, flux biasing the qubit such that its potential is a single well, then bringing the qubit back to the double-well potential. The magnetic field pulse resets the qubit by flux biasing it before the SQUID returns to its zero voltage state and remaining so until after it does. Then the potential just needs to return to the flux bias where the measurement is performed before the SQUID switches to the voltage state. Figure 4-16 gives an indication of how this is done. The dotted line in part (a) is the voltage of the SQUID, while the solid line is the background magnetic field. The SQUID switches at both the positive and the negative switching current, resulting in a positive and negative voltage, respectively. We only measure the positive switching current, so before this occurs the pulse in the magnetic field must return to the original background. Once the positive switch occurs, the background magnetic field can be pulsed to its preparation bias and remain there until after the negative voltage state retraps. As long as the SQUID is in its voltage state, the back-action scrambles the state of the qubit, so the magnetic field can only return from its preparation state after the SQUID retraps.

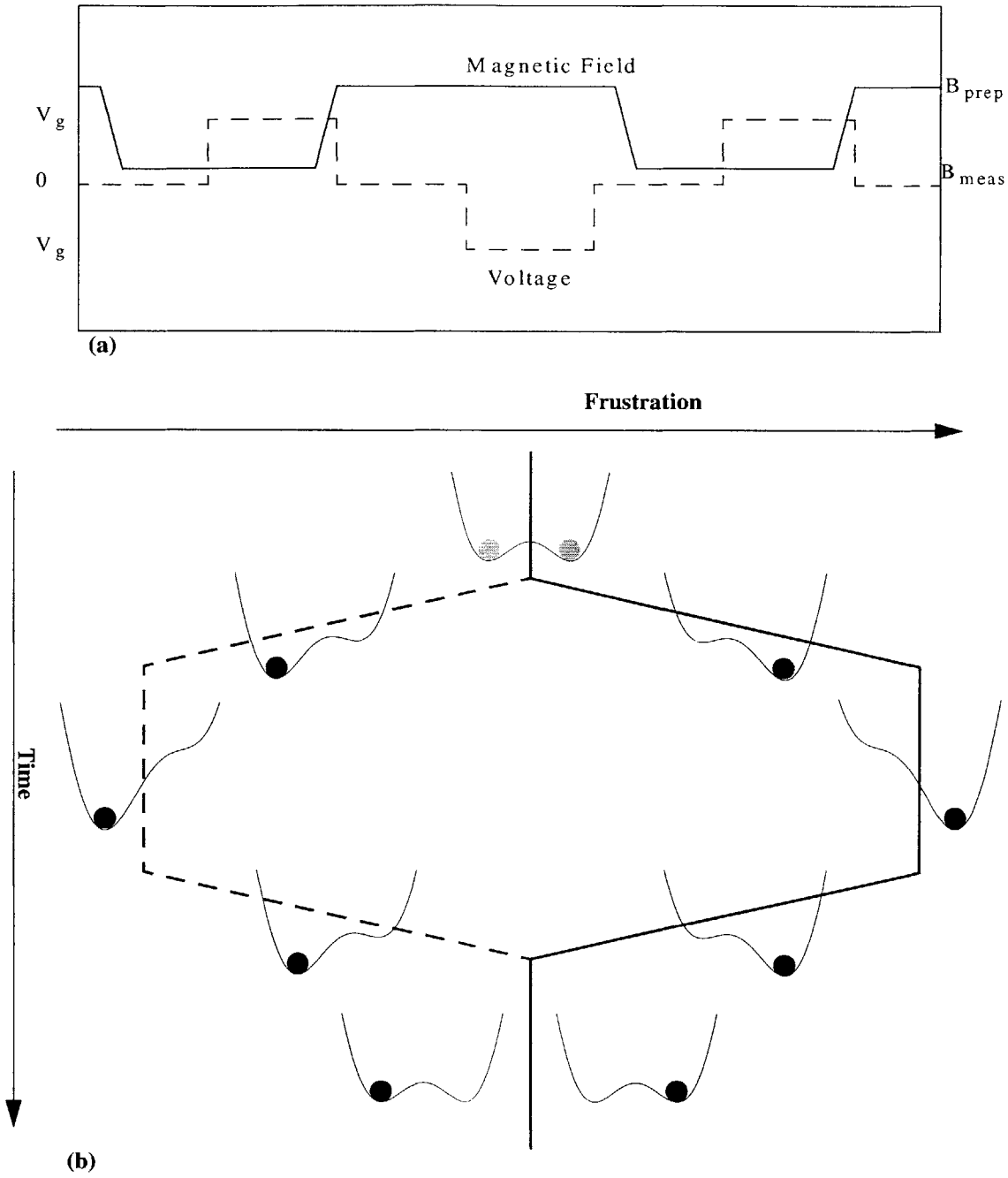

FIGURE 4-16. (a)The voltage of the SQUID and the background magnetic field. While the SQUID is not being measured, the magnetic field is in the preparation state. It returns only when the SQUID is in the superconducting state before the measurement takes place. (b) The qubit potential as it responds to the changing flux bias, for preparing both in the L state and the R state. As the potential shifts such that the left well becomes deeper and the right well becomes shallower, the probability for it being found in the right well decreases, until the right well vanishes altogether and the qubit is 100% in the left well. If it is then moved quickly back to the starting point, it remains in the well it began in.

A diagram of the circuit which does this appears in Figure 4-17. A comparator compares to the SQUID's bias current to a threshold value, and its buffered output serves as a current source in parallel with the magnet's regular current source. The threshold for the comparator is set to just above zero, so that the SQUID has time to retrap from the negative switching event, and the magnetic field can return to the measurement flux bias before the SQUID reaches its switching point. This hysteresis circuit needs to be isolated from the ground of the measurement circuit, and as long as precautions are taken with the ground, the polarity of the magnetic field shift can be altered simply by switching the leads.

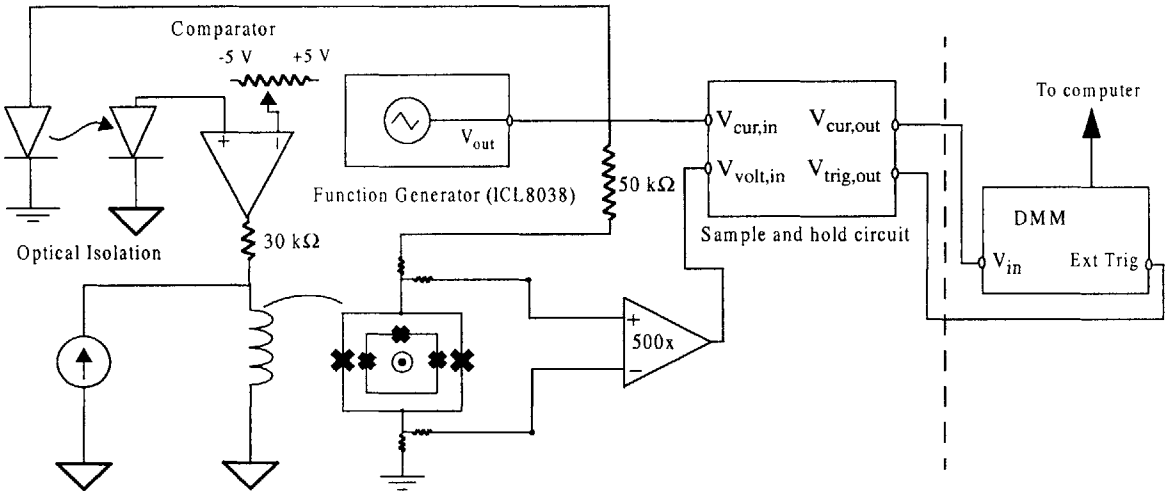

FIGURE 4-17. Setup used to measure switching current of dc SQUID modified to include a synchronous change to the magnetic field. The function generator signal is fed to a comparator through an optical isolator, which is in parallel with the dc bias field. This prepares the qubit in a predetermined state.

4.5.3 Results of the Hysteresis Measurements

Figure 4-18 shows the two curves, the results of measuring the qubit when it is prepared in the **L** state or the **R** state, for the 370 A/cm^2 sample. It is clear that there is hysteresis, which indicates that we are not seeing a superposition of states in this sample. Secondly, while the transition between the states while preparing on one side is smooth, on the other side there are multiple peaks and dips in the curve.

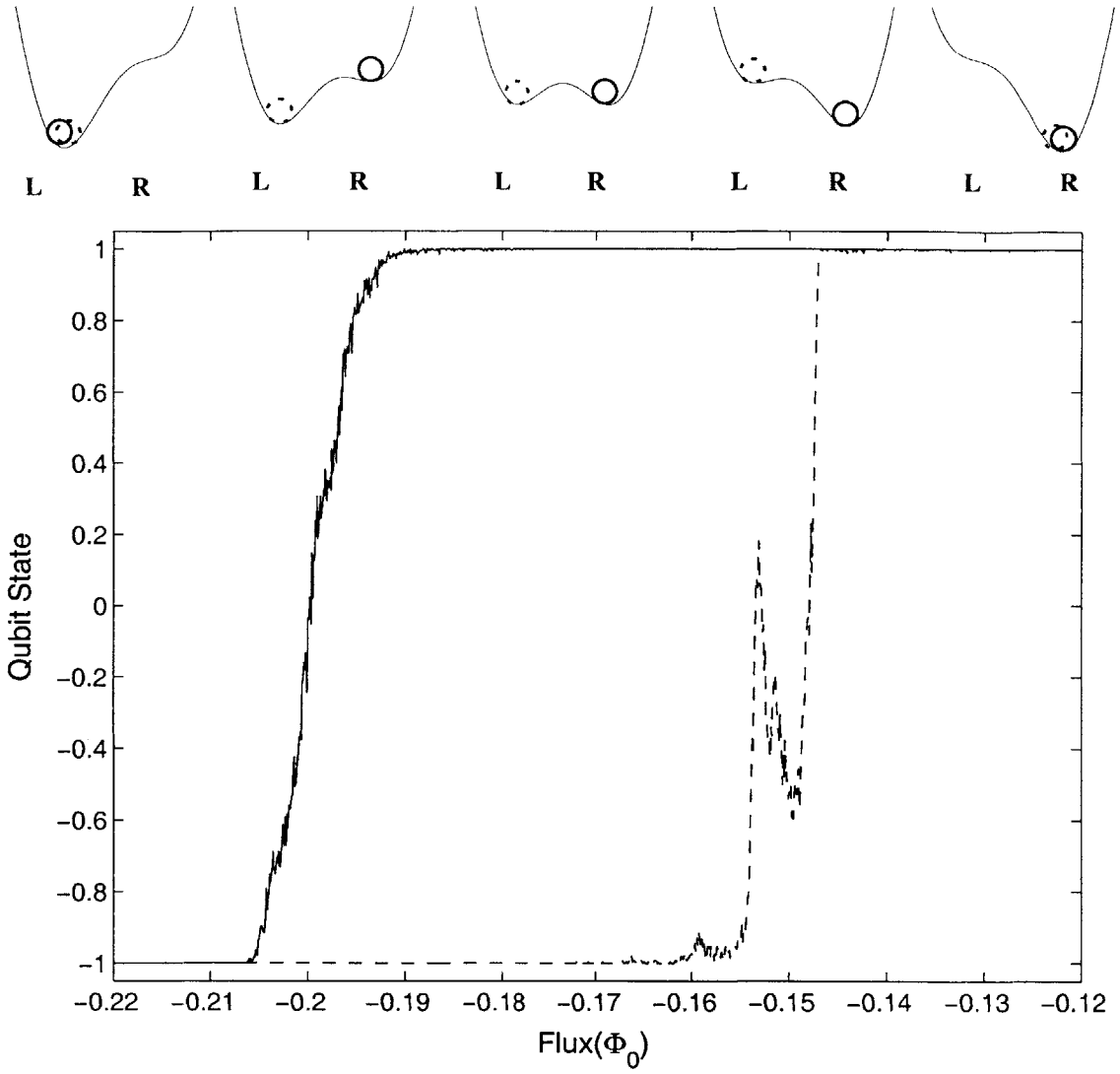

FIGURE 4-18. The hysteresis measurement at 15 mK. The parabolas above the figure show the shape of the double-well potential at the various frustrations. The solid line is for a qubit prepared in the right well, represented in the double-well diagram as a solid circle. The dotted line shows the measured qubit state when it starts off prepared in the left well, corresponding to the dotted circle in the double-well potential diagrams. The dotted line shows numerous peaks and dips, while the solid line's structure is less pronounced. Multiple scans over the same region produce the same results.

When the sample is heated from 15 mK to 500 mK, the hysteresis loop closes. As it does so, the peak and dip structure becomes lost as the critical field for the hysteresis moves towards f_q=0.5.

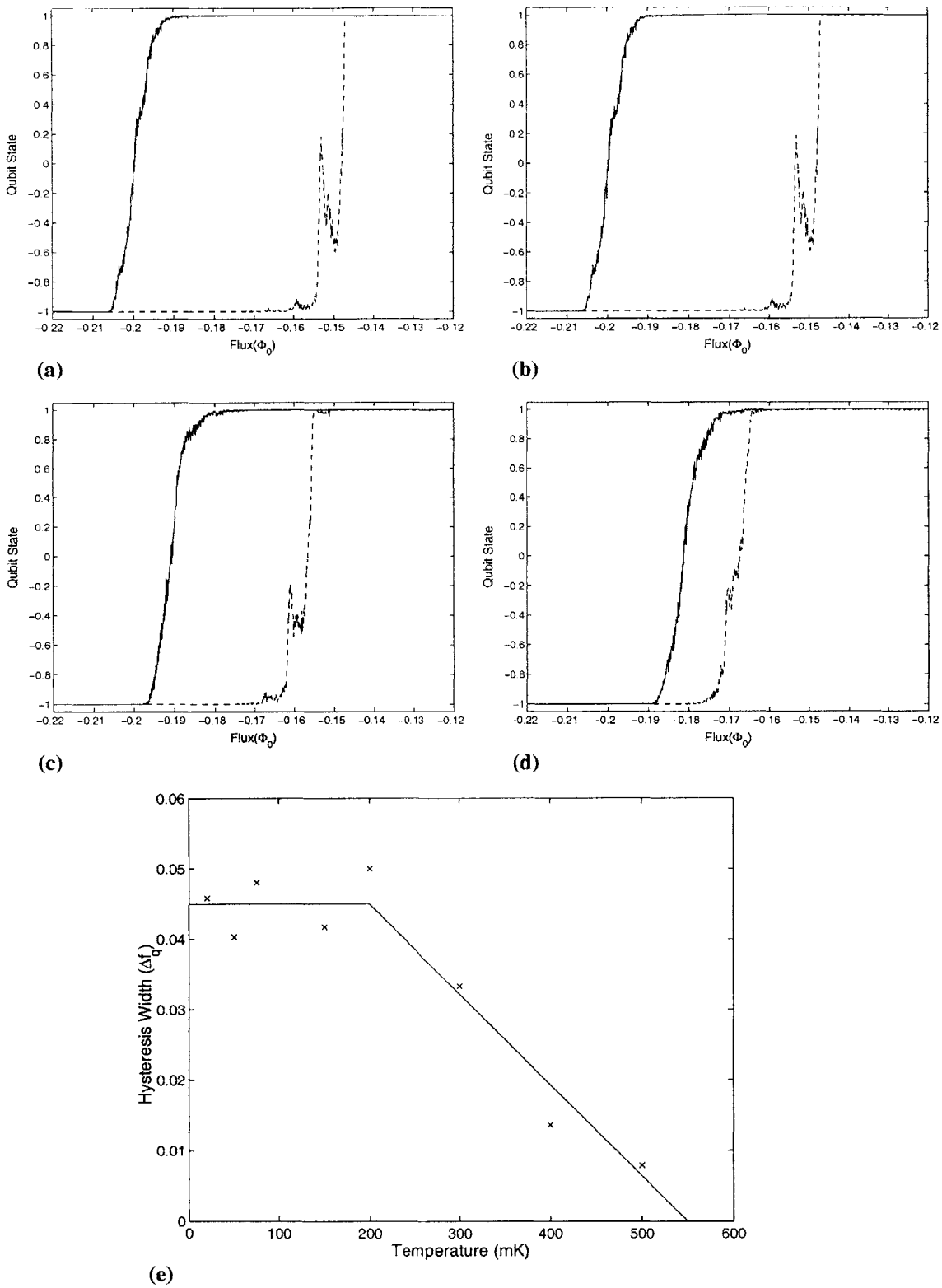

IGURE 4-19. The hysteresis measurement at (a) 15 mK, (b) 200 mK, (c) 300 mK, and (d) 400 mK. e) shows that the hysteresis loop shrinks as the temperature increases, which makes sense for deep ells where thermal excitation can cause the phase particle to escape the well of its prepared state.

Slowing down the measurement has a noticeable result when the qubit is prepared on the left side, as shown in Figure 4-20. The peaks grow increasingly larger while not changing position, indicating that the probability of transition grows due to the slowing of the SQUID ramp rate. This suggests that the rate of transition from the **L** to **R** state is comparable to the SQUID ramp rate

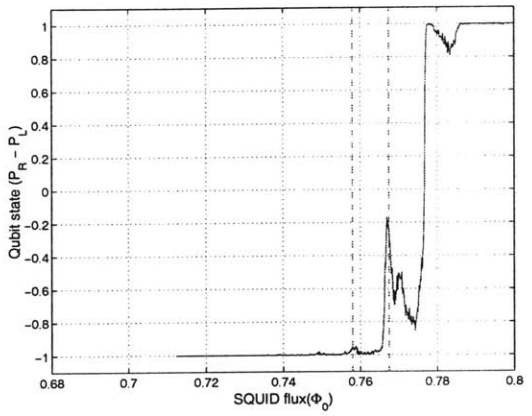

(a)

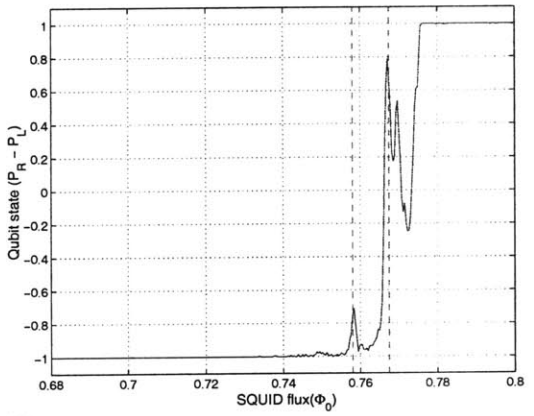

(b)

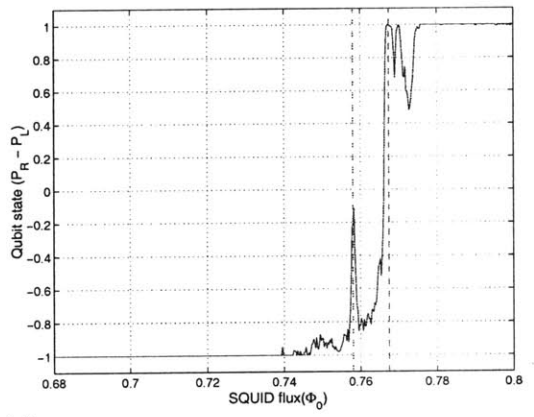

(c)

FIGURE 4-20. The qubit state when the SQUID is ramped at a rate of (a) 60 Hz, (b) 40 Hz, and (c) 12.5 Hz. The slower ramp rate results in a higher probability that the qubit will transition to the R state, as is made clear by the growing peaks marked by the vertical lines.

While the qubit should be symmetrical about f_q=0.5, the structure for the right-well preparation curve, which should match the structure on the left-well preparation curve, is smeared out. The **R** curve at 15 mK shows some hints of peaks and dips, but nowhere near as strongly as the **L** curve. However, a closer look at the data, using contour plots similar to those in Figure 4-7, clarifies the situation. For the qubit prepared in the **L** state, Figure 4-21 shows that there are no switching events in between the peak populations for the SQUID switching current, which correspond to the **L** and **R** state of the qubit. It is the variation in the population between the **L** and the **R** state which results in the peaks and dips in the curve. A peak corresponds to where the **R** population is higher than other flux biases, whereas the dips correspond to points where the **R** population is lower than it is for neighboring flux biases. The contour plot where the qubit is prepared in the **R** state displays stripes of switching events between the two peak switching points, as shown in Figure 4-22. These may, like the events discussed in Section 4.4.2, be the result of qubit transitions in between the **L** and the **R** state. This will be discussed in Section 4.5.4.

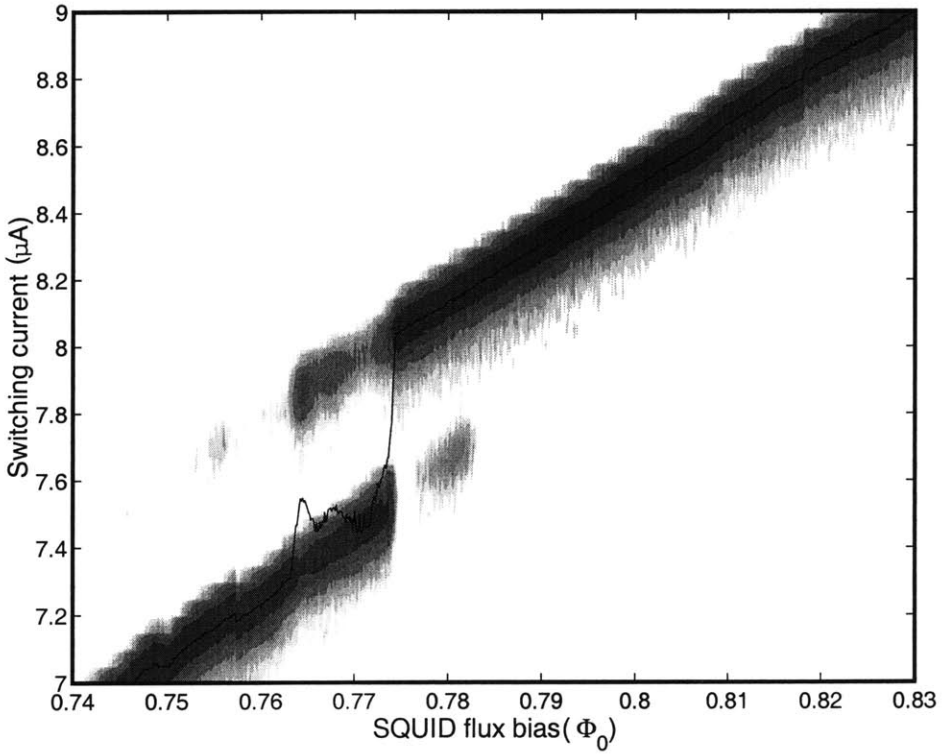

FIGURE 4-21. A contour plot showing the number of switching events at different bias current and magnetic fields for a qubit prepared in the L state. The black line is the mean switching current. The peaks and dips correspond to changes in the population of the two qubit states, but no switching events happen in between the two peaks in switching events.

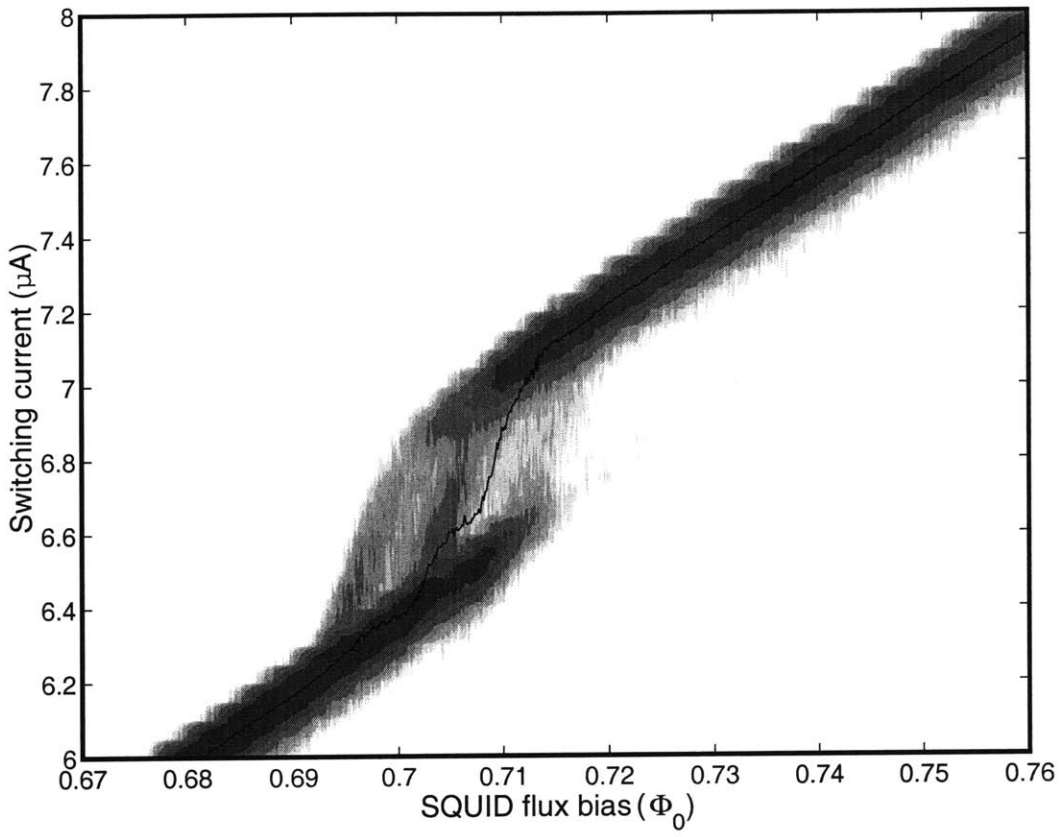

FIGURE 4-22. A contour plot showing the number of switching events at different bias current and magnetic fields for a qubit prepared in the R state. The black line is the mean switching current. The stripes have a similar structure to the peaks and dips which appear in the hysteresis curve where the qubit is prepared in the L state.

4.5.4 Analysis

As the temperature is lowered, the thermal activation is frozen out: this means that the thermal energy is insufficient to excite the phase particle out of the shallow well within the time it takes for the SQUID to reach its switching point. This also explains why the previous, non-hysteresis measurements shown in Figure 4-15 produced a wider step as the temperature decreased. When the thermal activation is high, then the qubit can escape the shallower well and is much more likely to be found in the deeper well. Once the phase particle does escape from the shallow well, returning is even more difficult, as the barrier from the deep to the shallow well is much higher than the other way around. At lower temperatures, though, the qubit is stuck in whichever well it starts in until the well becomes shallow enough for it to escape by thermal activation or quantum tunneling. If

the only means that the qubit can change states is by thermal activation or quantum tunneling, then repeated measurements on the qubit at the same flux bias while the wells are too deep for thermal activation or quantum tunneling should result in the same measurement each time. This is clearly not the case, and the qubit state is apparently randomized with each measurement. The measurement SQUID itself is the most likely cause of this randomization, as its switching to the voltage state causes a strong back-action on the qubit. As temperatures become higher, deeper and deeper wells are escaped and the flux bias region where the qubit is trapped in the shallow well becomes smaller, thus giving the decreasing width of the step with higher temperatures and slower ramp rates, which give the qubit phase particle more time to escape, in Figure 4-15. This directly corresponds to the decreasing size of the hysteresis loop in Figure 4-19. So at higher temperatures, the phase particle escapes the shallow well before the qubit is measured and is unable to return, resulting in a narrower step.

This explains thermal activation and ignores quantum tunneling as the means for the qubit to move from one well to the other. Quantum tunneling depends not only on the height of the barrier, but also on whether there is an energy state on the other side of the barrier into which the phase particle could tunnel. Since the shape of the potential, and relative position of the energy levels in the potential wells, depends on the frustration, the quantum tunneling would only occur at distinct frustrations. It is reasonable to conclude that the peaks and dips in the probability of the two states are indicative of the quantum levels of the qubit, as in Figure 4-25. At certain frustrations, the energy levels line up, and thus it is possible for the phase particle to tunnel across the barrier, creating some probability of finding the phase particle in the other state. Their appearance on only one side has more to do with how the measurement works than with the physical mechanism. In fact, when looking at a histogram of the measurements, it is clear that there are distinct transitions at certain frustrations when it is prepared in the higher state (Figure 4-22). These appear as stripes in the data. Circulating current in the SQUID couples to the qubit and changes its flux bias. Because the circulating current decreases as the current bias of the SQUID increases, the actual flux bias of the qubit, f_q', changes during the SQUID's ramp. Whenever the energy levels on both sides of the qubit barrier line up, there is a distinct possibility of a transition from the **R** state to the **L** state. If this happens after the

SQUID's bias current is already ramped past the switching point for the **L** state of the qubit, then the SQUID will switch immediately. The stripe in the data indicates the line where the combination of the external flux and the SQUID circulating current bias the qubit flux such that the levels line up.

Using the variables f_q to represent the external flux bias of the qubit and f_q' to represent its total flux bias, $f_q'=f_q+MI_{cir}/\Phi_0$. M and I_{cir} are the mutual inductance and circulating current of the SQUID. As the bias current of the SQUID increases, the circulating current decreases. With a lower circulating current, higher background magnetic flux is necessary so that the qubit is at f_q'. From Section 3.2, we have Equation (4-11) for the bias current and circulating current of the SQUID.

$$\begin{aligned} I_{bias} &= 2I_c \cos\varphi_m \sin\varphi_p \\ I_{cir} &= I_c \sin\varphi_m \cos\varphi_p \end{aligned} \tag{4-11}$$

Meanwhile, Equation (4-12) gives the value of φ_m when the SQUID has a significant self-inductance, L_m.

$$2\varphi_m = 2\pi\left(f_S + \frac{L_m I_{cir}}{\Phi_0} + \frac{MI_p}{\Phi_0}\right) + 2\pi n \tag{4-12}$$

There are three equations and three unknowns, I_{cir}, φ_m, and φ_p. I_{bias} is the applied current bias and f_S is the applied flux bias to the SQUID, which is proportional but not identical to the qubit flux bias, f_q. I_p is the persistent current in the qubit, and may either be positive or negative, but is usually approximately αI_c. When solving this equation, it is safe to use I_p for the state in which we prepare the qubit. For the non-hysteresis measurements, we can find the solutions for both values of I_p, since there is some probability for each to be true. n has no effect on the measurable variables and can be ignored. An example of how the circulating current decreases due to the bias current is shown in Figure 4-23.

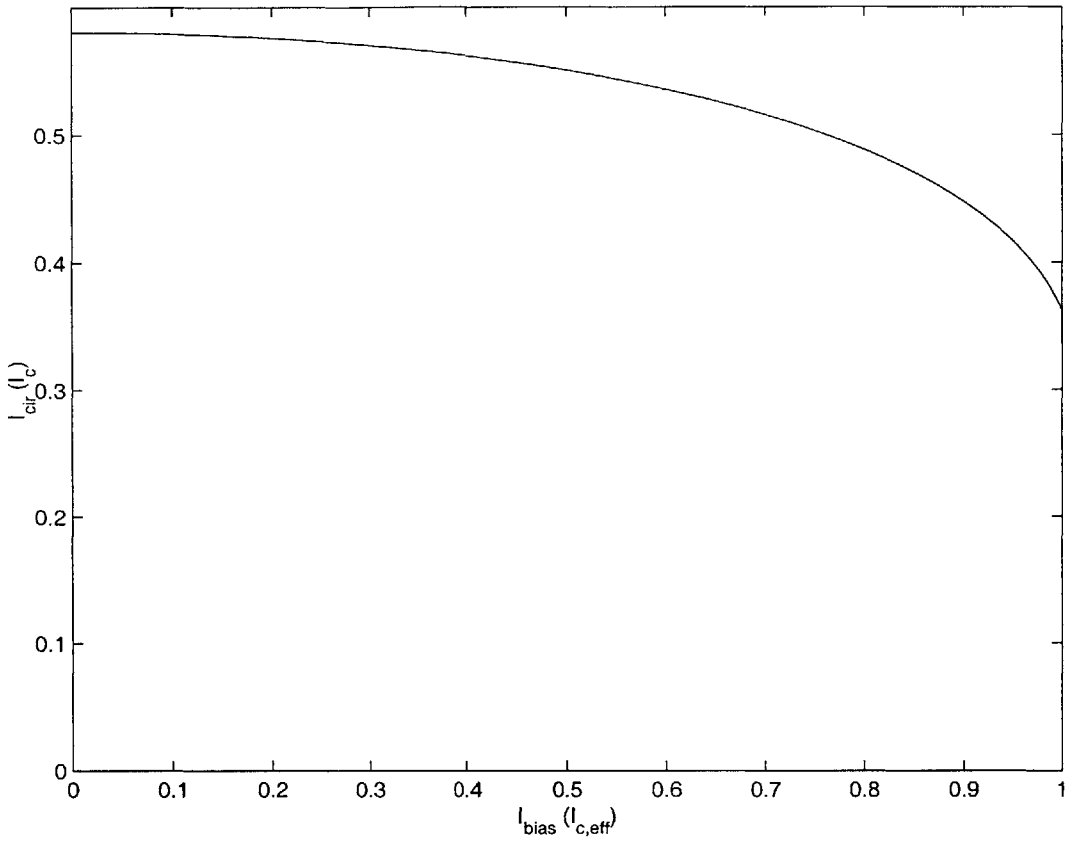

FIGURE 4-23. The circulating current in the SQUID at a frustration of 0.61. As the bias current is increased, the circulating current decreases.

Equation (4-13) describes the value of f_q'. It is not necessary to include the self inductance if it is taken into account in the calculation of the qubit's energy level structure. Figure 4-24 shows the results of this by plotting lines of constant f_q' in the contour plots of the SQUID switching events. When these constant flux contours line up with the stripes in the data, it is clear that we are witnessing transitions from the **R** to the **L** state of the qubit at flux biases which align qubit levels on either side of the barrier.

$$f_q' = f_q + \frac{MI_{cir}}{\Phi_0} \tag{4-13}$$

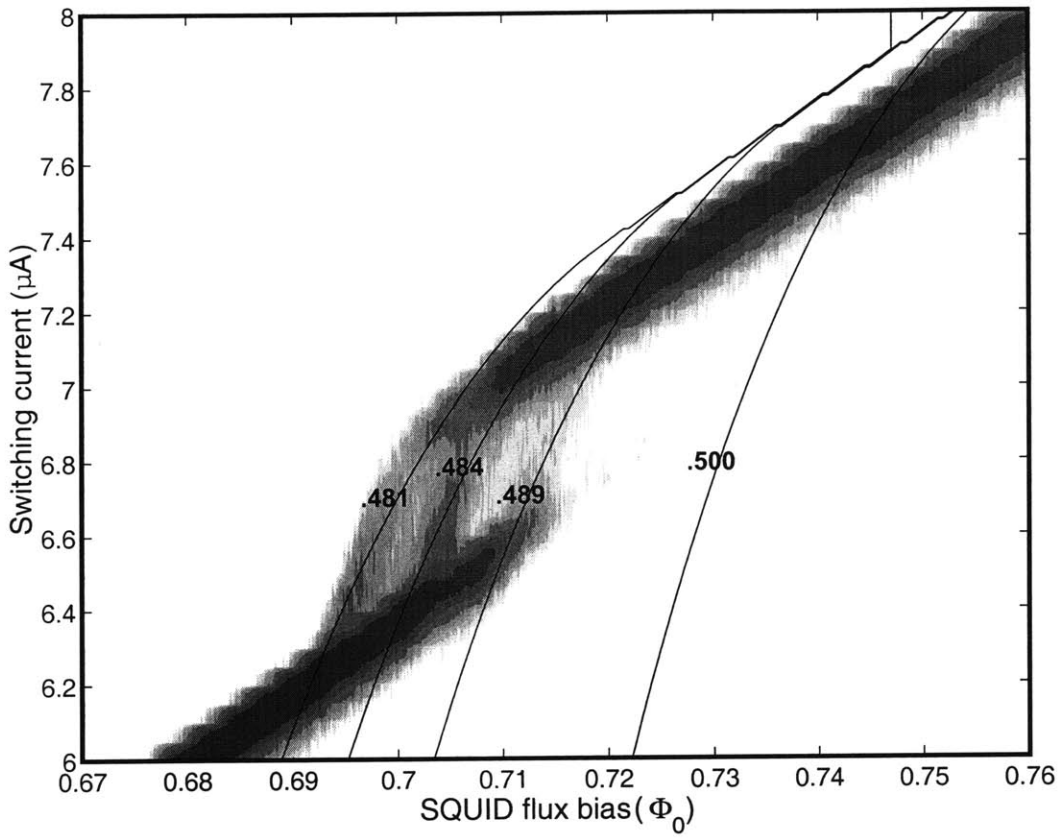

FIGURE 4-24. This contour plot for a qubit prepared in the R state includes lines of constant f_q'. These lines, whose numbers tell the actual value of f_q', mark where the total flux bias of the qubit causes a level alignment and enhanced quantum tunneling. Near some lines, there may be more than one quantum level in close proximity. There are only a few points near the f_q'=0.5 line, indicating deep wells with little quantum tunneling.

We observe the stripes on the hysteresis measurement when the qubit is prepared in the **R** state, but not in the hysteresis measurement where the qubit is prepared in the **L** state, because of the finite measurement time. Consider the qubit potential in Figure 4-25. If the qubit starts in the **L** state, it will be measured in the **L** state unless it tunnels to the **R** state before the SQUID reaches the **L** state's switching current. It cannot tunnel from **L** to **R** after the SQUID has passed the **L** state's switching current because the SQUID would already have switched. Once the qubit phase particle tunnels to the **R** state, it is unlikely to tunnel back since the relaxation time for one of the upper levels of the right well is very short, and it will fall from there to the ground state. In this case, the qubit phase is no longer in an energy level which aligns with an energy level in the other well, so it can no longer transition over. The only place where the qubit could transition back and forth would be at $f_q' = 0.5$, as in Figure 4-25(b), but the barrier is very high here, limiting the

qubit to very few transitions.

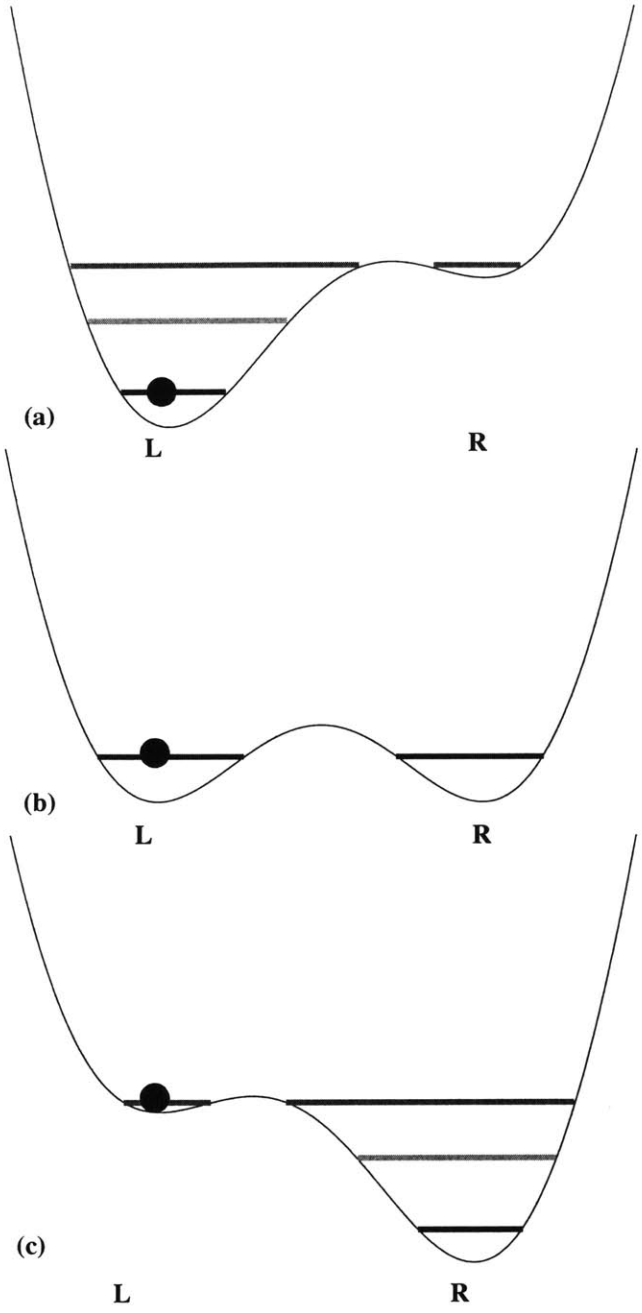

FIGURE 4-25. The qubit has a double-well potential. In the 400 A/cm^2 sample, more than one quantum energy level may be localized in a well. When the sample is prepared on the left side, it remains there as long as the left well is the lower state (f<1/2) and there is no energy state for it to transition to by quantum tunneling, as in (a). In (b), which corresponds to f=1/2, there is a state available for quantum tunneling, but the barrier between the states is still high, and the probability of transition is small. Note that there is only one level in each well at f=1/2. In (c), where f>1/2, more levels form in the right well as it gets deeper, and when the energy levels in the left and right are equal, the probability of a transition is high since the barrier has become smaller. This is where the peaks and dips appear.

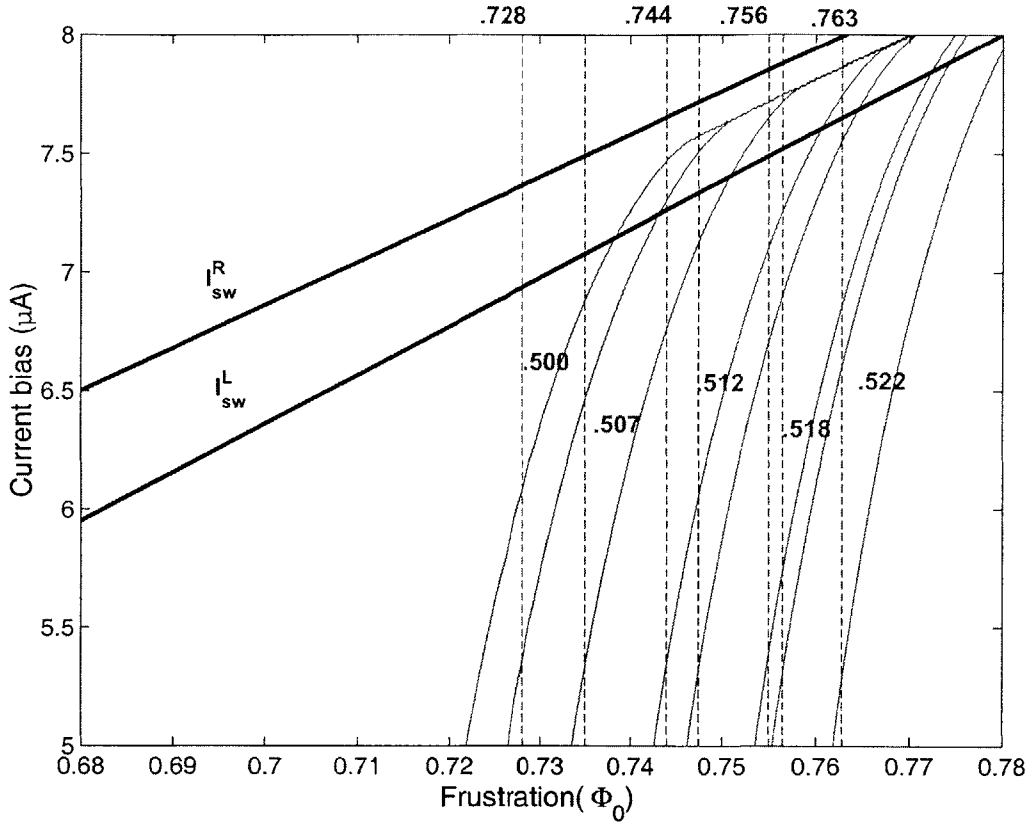

FIGURE 4-26. The thin, solid lines indicate contours of constant effective qubit flux, similar to the lines which aligned with the stripes in Figure 4-24. The dashed lines are the path that a current ramp follows, while the two heavy lines are the mean switching current for the SQUID for each qubit state. Since we are assuming any change in the qubit state occurs before the SQUID reaches the L switching current, any level alignment which we measure must occur before then.

The hysteresis curve for the qubit prepared in the left well is odd not because it has structure, but because of how well-defined the structure is. Since the flux bias which the qubit sees is constantly changing, the sharp peaks in the transition between states indicate not just that the flux bias gives a high tunneling rate, but that the qubit spends a long time at a bias which has a high tunneling rate. Thus, when the current ramp rate is slower, the peaks are higher, which is consistent with Figure 4-20. Given that the circulating current follows the relationship $\sqrt{1-(I_{bias}/I_c)^2}$, as shown in Figure 4-23, the circulating current changes most slowly near the bottom of the current ramp. This would indicate that the sharp peaks would result from when the flux bias causes an energy level alignment near the bottom of the ramp, as shown in Figure 4-26. However, the current bias in this plot starts at 5 μA, rather than 0, since the state preparation magnet pulse does not return to the measurement state until the current bias ramp of the SQUID has begun, which Figure 4-

16(a) shows. Including the external flux bias return as an exponential decay with an RC time of 100 μs gives the total effective flux bias of the qubit during the current ramp in Figure 4-27, where the bias increases to a maximum as the external magnet returns from the preparation pulse, then begins to decrease as the ramping of the SQUID's bias current decreases its circulating current. This curve is tangential to the level crossing at f_q'=0.512 for about 0.2 ms, resulting in the high transition probability which gives the peaks in Figure 4-28.

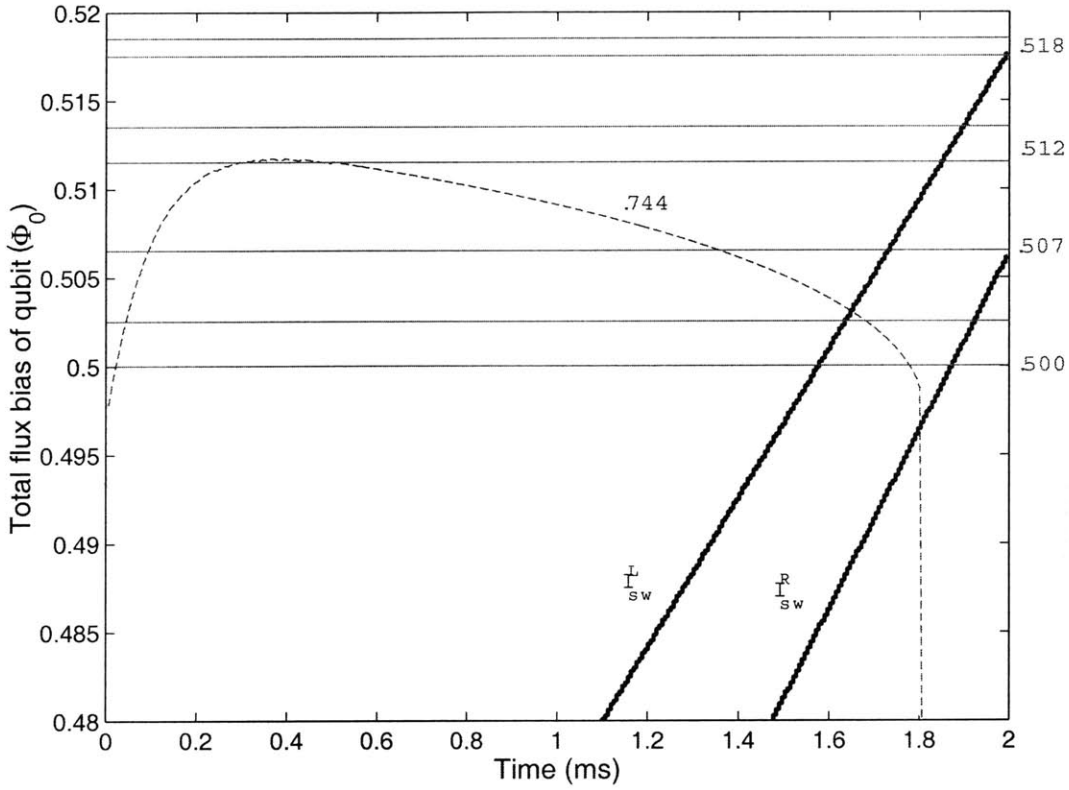

FIGURE 4-27. The thin, solid lines indicate constant effective qubit flux where level alignment occurs. The dashed line is one of the paths that a current ramp follows, specifically the one that occurs when the external flux bias of the SQUID is at $0.744\Phi_0$. The two heavy lines are the mean switching current for the SQUID for each qubit state. The path followed, including the return from the level preparation and the decrease of the circulating current, is briefly tangential with the level alignment at f_q'=0.512.

In order to simulate the effect of the SQUID bias current ramp on the state of the qubit, an equation for the rate of the transition is needed. These measurements resemble those observed by Lukens [12-14], and described theoretically by Averin [15] to give an equation for the rate of transition from the lowest energy level in one well to a high energy

level in the other in Equation (4-14).

$$\tau^{-1} = \frac{\Delta^2 \Gamma_r}{2\Delta^2 + \Gamma_r^2 + 4\varepsilon^2} \tag{4-14}$$

Here Δ and ε are the tunnel splitting and energy bias, while Γ_r is the rate at which the qubit relaxes from the highest energy state in a well to one of the lower states. Δ and ε are a function of the energy bands, and can be calculated from the values which we already know (see Section 4.5.5). Although it technically varies with the current bias of the SQUID, which affects the qubit's coupling to the external circuit environment, we will consider the Γ_r to be a constant, since the peaks occur when the energy levels line up for a relatively short amount of time during the current bias ramp. The relaxation to the lower energy levels is the fitting parameter, with the guideline that the higher the energy level, the more quickly it should relax. Running the simulation of the flux ramps shown in Figure 4-26 gives Figure 4-28(a), which corresponds closely with the data in Figure 4-28(b). Γ_r is for all the levels ranges from 10 μs to 100 μs.

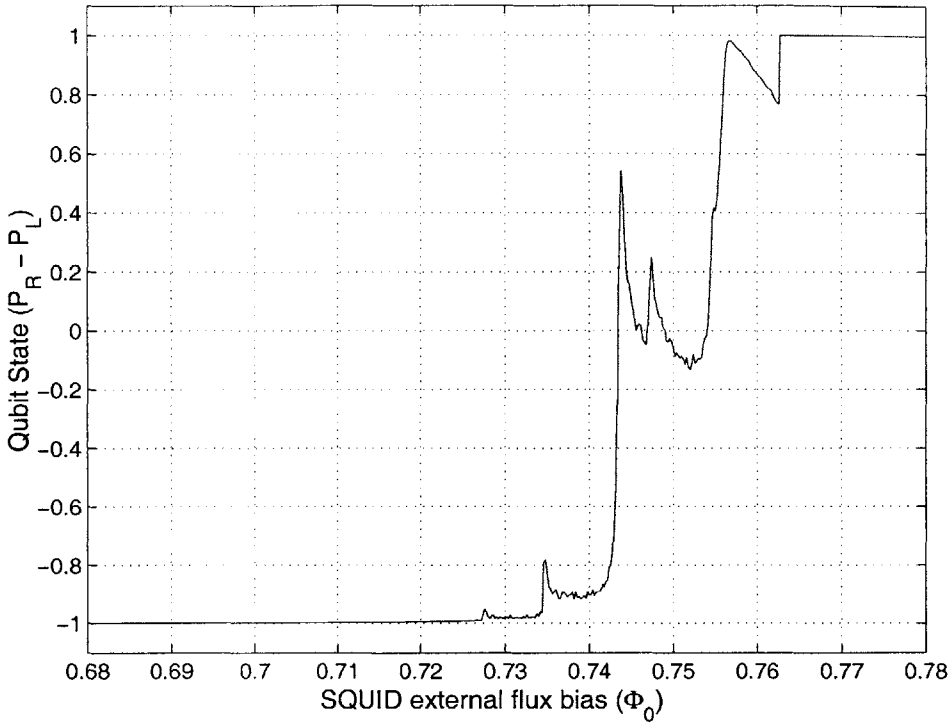

(a)

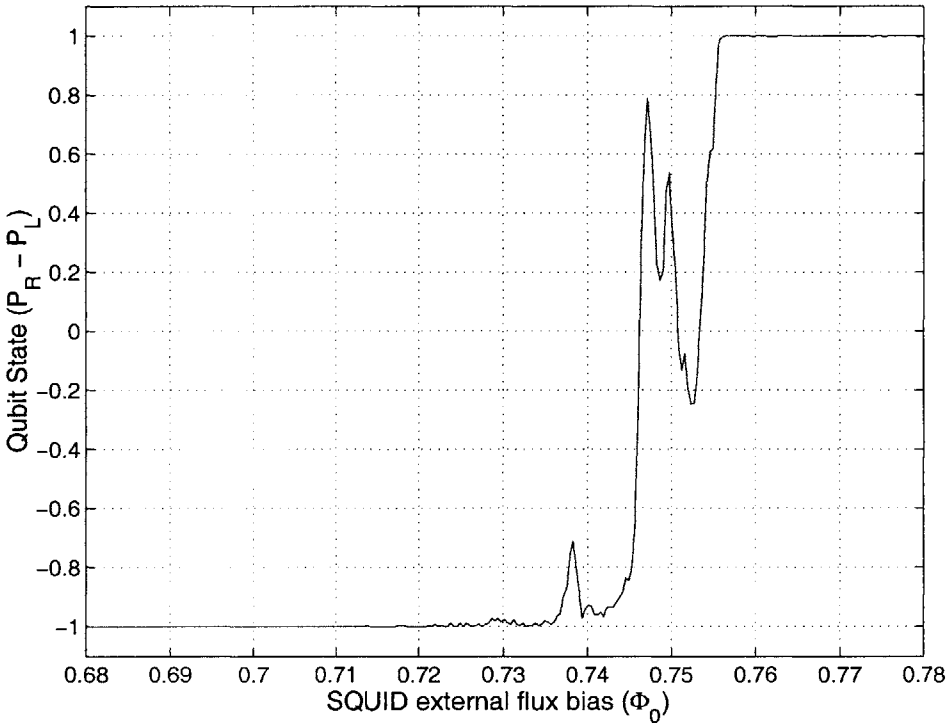

(b)

FIGURE 4-28. (a) The simulation of the current ramp produces the probability of transition shown in this plot. (b) The data gives the result in this plot. Aside from the small downturn at the end, the two are very close.

4.5.5 The Quantum Levels

The experiment shows some, if not all, of the flux biases where the quantum levels line up. Now, it is simply a matter of determining the qubit parameters which best fit the observed level crossing. This strongly depends on E_J, E_C, and α. E_J and α were derived from the time-dependent measurements in Section 4.4.3. While we can estimate the value of E_C in this case, we don't expect it to be very accurate. We know that $E_J=(\Phi_0/2\pi)I_c$, and that $I_c=J_cA$, where J_c is the critical current density and A is the area of the junction. Since we know what J_c is for the chip, E_J should give us A. Further, $E_C = e^2/2C$, and $C=C_0A$. Since we know C_0 for the chip, and A from E_J, we should be able to calculate C and thus E_C.

If this is so, then we should be able to run the quantum simulation of the qubit with these parameters and get energy level crossings which match up with the results in our experiments. However, the results in Figure 4-29 only show two energy crossings within the qubit, one of which is at f=1/2, which we know has no significant tunneling. This leads us to believe that the parameters need to be refined. While E_J and α are necessarily close to their correct values given the results of our experiments, the dependence on E_C was weak. If E_C is smaller than calculated, then the energy gap between the levels in each well is smaller, and there are more levels in each well and thus more level crossings. This is apparent from the fact that ω_m and ω_p are proportional to $(E_JE_C)^{1/2}$, which means that the distance between the energy levels in a single well is also proportional to the square root of E_JE_C as long as the simple harmonic oscillator approximation is accurate.

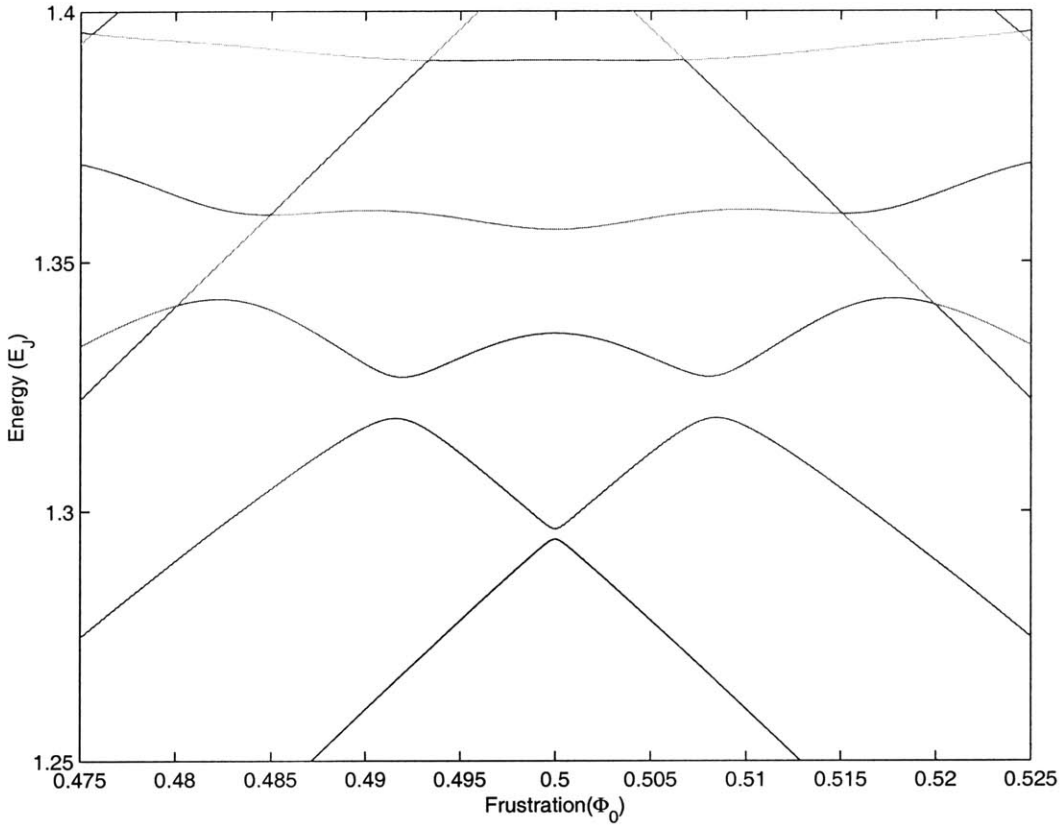

FIGURE 4-29. This energy band diagram is the result of assuming that C_1 = 0 fF/μm^2, while C_0 = 45 fF/μm^2. It is equivalent to saying that the undercut portion of the junction has no capacitance. The only avoided crossings at f=0.49, 0.500, and 0.510.

This does not agree with the capacitance calculated from the junction area which the Josephson energy gives us. However, undercutting may affect the specific capacitance differently than how it affects the critical current density, as explained in Section 2.9.3.4. We can approximate this by using A_d to be the designed area of the larger junctions, and A_u to be the area with undercut. $A_{d,s}$ is the designed area of the smaller junction, while $A_{u,s}$ is the area of the smaller junction with undercutting. The α measured in Section 4.4.3 equals the ratio of $A_{u,s}/A_u$. The capacitance of the junction in the area left after the undercut is C_0A_u, where C_0 is the measured specific capacitance of the junction, which is 45 fF/μm^2. The area A_d-A_u, the area which has been undercut, also has a specific capacitance, which we'll call C_1. For now, we'll treat C_1 as an unknown, but because the undercutting decreases the critical current, this implies that the distance between the electrodes is greater there, so we can assume that the specific capacitance, which equals ε/d, is smaller. So the total capacitance of the larger junction is C_0A_u + $C_1(A_d$-$A_u)$, while that of the

smaller junction is $C_0A_{u,s} + C_1(A_{d,s}\text{-}A_{u,s})$. This gives a ratio, α_C, of $[C_0A_u + C_1(A_d\text{-}A_u)]/[C_0A_{u,s} + C_1(A_{d,s}\text{-}A_{u,s})]$.

When C_1= 20 fF/μm^2, the results are much more in line with those in the measurements, as shown in Figure 4-30. This is the expected result if the undercut gives twice the thickness as the unaltered area of the junction, which means that the undercut area has half the specific capacitance while the critical current density is exponentially smaller. This has an α_C of 0.75, and shows avoided crossings at f=0.484, 0.487, 0.495, 0.500, 0.505, 0.513, and 0.516, which is a good match for the stripes shown in Figure 4-24. The stripe at the edge is where the qubit becomes single well rather than double well, and it occurs at f=0.479 on one side and f=0.521 on the other.

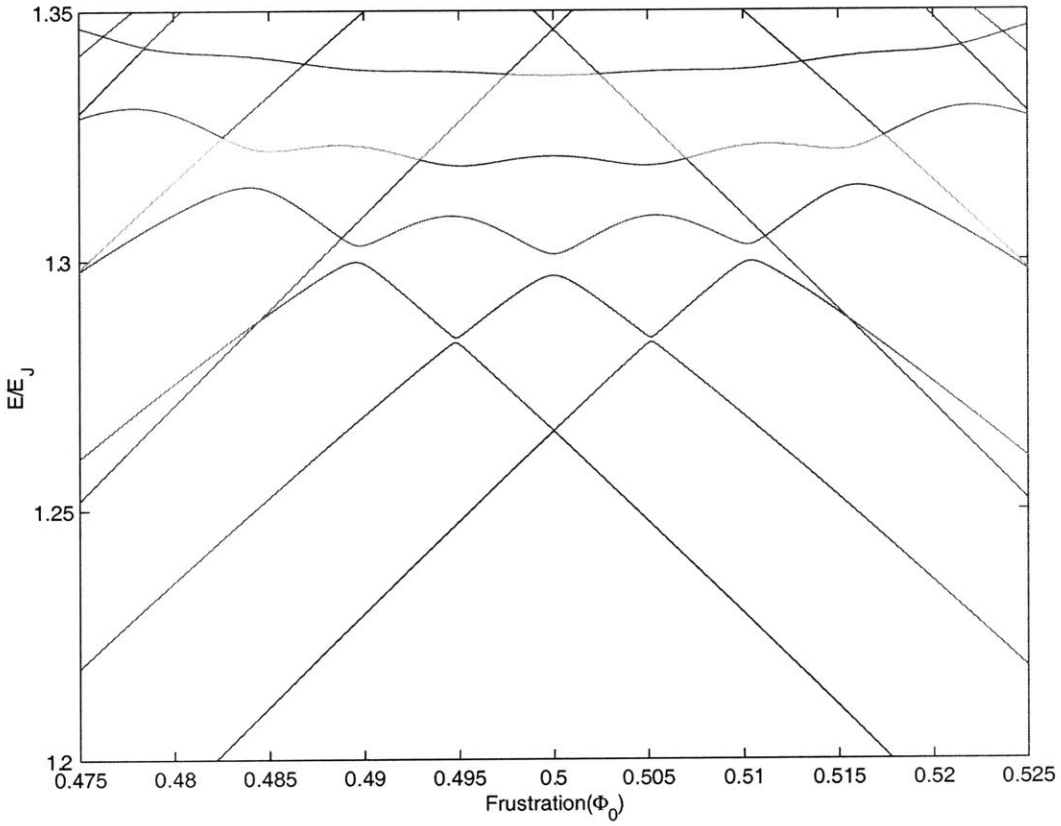

FIGURE 4-30. This energy band diagram is the result of assuming that C_1 = 20 fF/μm^2, while C_0 = 45 fF/μm^2. It shows avoided crossings at f=0.484, 0.487, 0.495, 0.500, 0.505, 0.513, and 0.516.

4.6 Summary

The experiments have demonstrated a quantum system with a double well potential. With the parameters which we have used, the wells are deep enough to contain multiple quantum levels, and we have resonant tunneling between the wells due to these levels. Our measurements have allowed us to extract the parameters of the qubit, measuring, for the 370 A/cm^2 sample, an α of 0.63, an α_C of 0.75, a Q of 3x10^5, an E_J of 2400 μeV, and an E_C of 3 μeV. The larger current density sample has an α of 0.58, a Q of 4x10^5, and an E_J of 4000 μeV. E_C and α_C have not been measured yet for this sample. While these parameters are not suitable for a qubit due to the depth of the wells and lack of significant incoherent tunneling at f=0.5, a new sample fabricated at 67 A/cm^2 should meet the requirements.

Chapter 5

Josephson Junction Oscillators

5.1 Introduction

As we saw in Section 2.7, applying an oscillating input to a persistent-current qubit causes it to rotate between the |0> and |1> state. This can be done using an external oscillator operating at room temperature which we couple to the qubit through coaxial lines, or it can be done by designing an on-chip oscillator using superconducting technology. This chapter begins by showing how the Josephson junction can be used as an oscillator and how the RCSJ model provides a circuit description of a Josephson junction oscillator in Section 5.2. Section 5.3 then covers Shapiro steps and explains how a Josephson junction can be used to measure an rf signal. Next, Section 5.4 presents the SQUID oscillator designed to drive the qubit, with an analysis of its contribution to decoherence and some preliminary measurements. Finally, in Section 5.5, experiments done on Josephson junction arrays are presented in order to give an example of the rf signal generation and detection abilities of Josephson junctions.

5.2 The Josephson Junction Oscillator

An oscillating magnetic field can drive the qubit between its ground state and its first excited state. Using an external microwave oscillator, Caspar van der Wal has demonstrated this driving, mapping out how the resonance changes with frustration [30] and demonstrating level splitting at f=0.5. This experiment had a short decoherence time, however. Performing observable Rabi oscillations requires a longer decoherence time, which requires better filtering of external noise and a reduced magnetic coupling [31]. Better control of decoherence may be possible by building an on-chip oscillator. This eliminates the need to build high speed lines, which can carry noise as well as the desired signal, from the outside world to the qubit. With an on-chip oscillator, the only source of high-frequency noise is from the oscillator itself. While that can be significant, it can also

be calculated with a high degree of accuracy, and possibly engineered in order to reduce the decoherence.

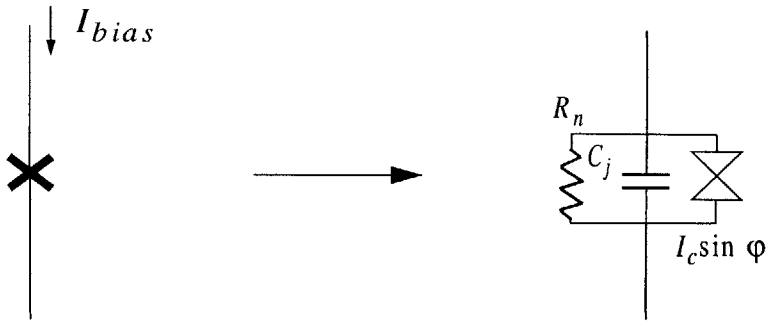

FIGURE 5-1. The Josephson junction and the RCSJ (Resistively-Capacitively-Shunted Junction) circuit model. The hourglass figure is the supercurrent branch, which follows the Josephson relation.

Figure 5-1 substitutes the RCSJ model for the Josephson junction. This circuit model of the Josephson junction has three branches: the Josephson element branch, which follows the Josephson relations and is marked by the hourglass symbol, the capacitive branch, which comes from the physical structure of the junction and acts as a simple capacitance, and the resistive branch, which is due to quasiparticle tunneling across the barrier. In the quantum model of the junction, we were able to ignore the resistive branch, since when the junction is biased below the critical current, the dc voltage is zero and no dc current flows through the quasiparticle channel. When the junction is biased below its gap voltage, then the resistive channel has a very high resistance, greater than 1 MΩ, called the subgap resistance. This depends on the temperature of the sample, since it is proportional to the number of quasiparticles available for tunneling. Above the gap voltage, the junction resistance is equal to the normal resistance, which has no dependence on the number of quasiparticles and instead is equal to $\pi V_g/4I_c$. A number of parameters are important for describing the RCSJ model. As was noted in Section 1.3, the Josephson inductance, $L_J=\Phi_0/2\pi I_c$ approximates the junction for small signal sources at low frequencies. The Stewart-McCumber parameter, β_c, is the ratio of the timescale of the capacitor (R_nC_j) to the timescale of the inductor (L_j/R_n), so $\beta_c=R_n^2C_j/L_J$. A $\beta_c>1$ junction is considered underdamped, while a $\beta_c<1$ junction is overdamped. In an underdamped system, the capacitor discharges slowly. When the current is ramped up past the critical current, the

charge across the capacitor causes the junction to remain in the voltage state until the current bias drops to a retrapping current which is smaller than the critical current. This causes hysteresis in the current-voltage characteristic. In an overdamped system, the capacitor discharges through the Josephson current, and thus does not hold a voltage. While raising the bias current above the critical current will cause the junction to enter the voltage state, lowering below the bias current will return it to the supercurrent branch.

The Josephson relation in Equation (5-1) describes the direct link between the voltage across a junction and the rate at which the phase changes.

$$V = \frac{\Phi_0}{2\pi}\dot{\varphi} \tag{5-1}$$

A constant voltage produces a constant rate of change in the phase. Since the current across the junction, as given in Equation (5-2), depends sinusoidally on the phase, a constantly changing phase produces an oscillating current at a frequency of 483 MHz/μV.

$$I = I_c \sin\varphi \tag{5-2}$$

Unfortunately, it is difficult to voltage bias junctions. A good voltage source has an impedance much smaller than the load, while a good current source has an impedance much higher than the load. Since junctions have a very low impedance, it is more common to current bias than voltage bias junctions. It is relatively easy to find the average dc voltage bias of a junction when $RC<<L_J/R$, which is $V=I_cR_n[(I_{bias}/I_c)2\text{-}1]^{1/2}$. However, the current oscillations intentionally excited in the junction disturb the bias, producing harmonics of the fundamental frequency maintained by the average dc voltage.

As the dc voltage becomes higher, the oscillating current's disturbance of the average voltage becomes less significant, the harmonics die out, and the junction becomes more single frequency. Assuming the resistance dominates the impedance, and $V_{ac}=I_cR_n$, then the amplitude of the harmonics approximately follows the formula in Equation (5-3), where α is the voltage magnitude of the harmonic relative to I_cR_n, ν is V_{dc}/I_cR, and n is the number of the harmonic [39].

$$\alpha = 2\nu[(1+\nu^2)^{1/2}+\nu]^{-n}, \tag{5-3}$$

5.3 Shapiro Steps

In addition to producing an oscillating current from a dc input, Josephson junctions show a dc response to an oscillating signal. When an oscillating voltage is placed across a junction, there is a corresponding decrease in the junction's critical current, as well as the development of constant-voltage current steps [70], called Shapiro steps, in the I-V curve, as in Figure 5-2. These steps are located at voltages which are integral multiples of $V_s=\Phi_0\nu_s$, where ν_s is the frequency of the source, and have a magnitude which depends on the amplitude of the oscillating voltage. Consider the applied voltage to have a dc component and an ac component as in Equation (5-4).

$$V = V_{dc} + V_{ac}\sin(\omega_s t) = \frac{\Phi_0}{2\pi}\dot{\varphi} \tag{5-4}$$

We can discover the Josephson current by integrating the voltage to get the phase and calculating the current from the Josephson relation in Equation (5-2), which gives Equation (5-5).

$$i_J(t) = I_c \sum_{n=-\infty}^{\infty} (-1)^n \left[J_n\left(\frac{2\pi V_{ac}}{\Phi_0 \omega_s}\right)\right] \sin(\varphi(0) + (\omega_J - n\omega_s)t) \tag{5-5}$$

If we want to see the influence of this oscillating current on the dc current-voltage relation, we are interested in the dc current through the junction, which includes not only the dc Josephson current but also the dc current across the resistive branch. $\langle i_J \rangle$ is given by finding the time-invariant components of Equation (5-5), which appear whenever the frequency at which the detector Josephson junction oscillates, ω_J, is an integer multiple of the frequency of the driving source, ω_s, as in Equation (5-6).

$$\langle i_J \rangle = I_c \sum_{n=-\infty}^{\infty} (-1)^n \left[J_n\left(\frac{2\pi V_{ac}}{\Phi_0 \omega_s}\right)\right] \sin(\varphi(0))\delta_{\omega_J, n\omega_s} \tag{5-6}$$

The dc current in the resistive branch is simply V_{dc}/R, which is clear from Equation (5-7).

$$i_R(t) = \frac{V_{dc}}{R} + \frac{V_{ac}}{R}\sin(\omega_s t) \tag{5-7}$$

The total dc current is given in Equation (5-8).

$$\langle i_R \rangle = \frac{V_{dc}}{R} + I_c \sum_{n=-\infty}^{\infty} (-1)^n \left[J_n\left(\frac{2\pi V_{ac}}{\Phi_0 \omega_s}\right)\right] \sin(\varphi(0))\delta_{\omega_J, n\omega_s} \tag{5-8}$$

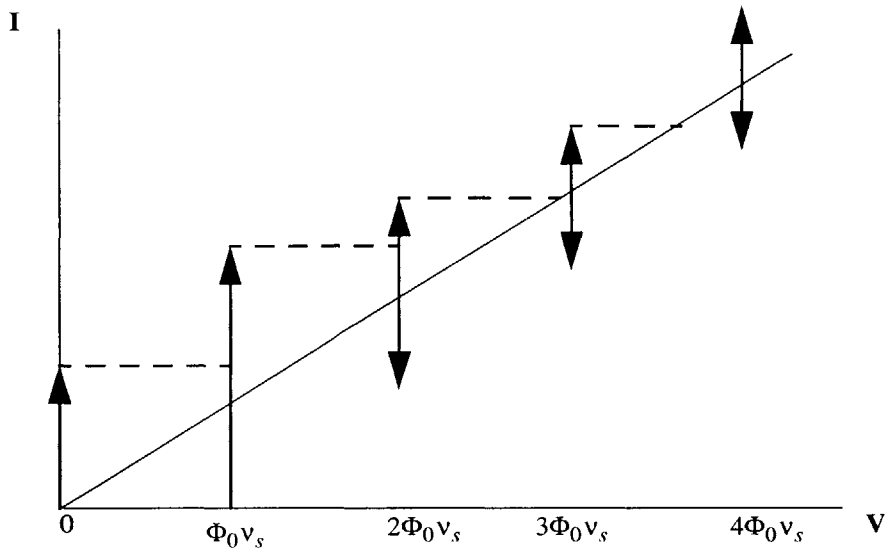

FIGURE 5-2. I-V curve of a voltage biased junction driven by an oscillating voltage. Note that a number of constant-voltage current steps appear at multiples of the driving frequency, ν_s. The dotted line indicates the path which a current biased measurement would follow.

This result is shown in Figure 5-2. While this gives a nice solution, there are two differences between this calculation of the dc current-voltage characteristic and the typical real world measurement. First, the oscillating source rarely approaches an ideal voltage source. However, the model will work as long as the current produced by the junction's own oscillations are much smaller than the current oscillations it is measuring. Second, rather than holding the junction at a dc voltage and observing the range of current which can be added without altering the voltage, the current-voltage characteristic is usually measured by ramping a dc current across the junction and measuring the voltage. The steps are still produced, but the height of the steps are no longer equal to the Bessel function solution. Notice that in Figure 5-2, there are certain current values where two or more voltages are possible. Rather than observing these multiple values, the current biased detector junction I-V follows a smooth curve, as in Figure 5-3. In addition, the steps are rounded by high temperature fluctuations. These can be calculated, as [69] shows. The current appears to follow the path indicated by the dotted line in Figure 5-2, such that it does not observe complete steps, but rather goes to the closest available voltage value once it reaches the top of the step, but there is no good analytical solution for this problem [71]. For this reason, calculating exact power output from Shapiro steps is quite difficult. Notice, however, that the critical current of the detector junction also changes with the

oscillating signal (n=0 and V_{dc}=0 in Equation (5-8)), and since the full critical current can always be observed (except for what is lost due to thermal noise), this provides the best approximation of total power.

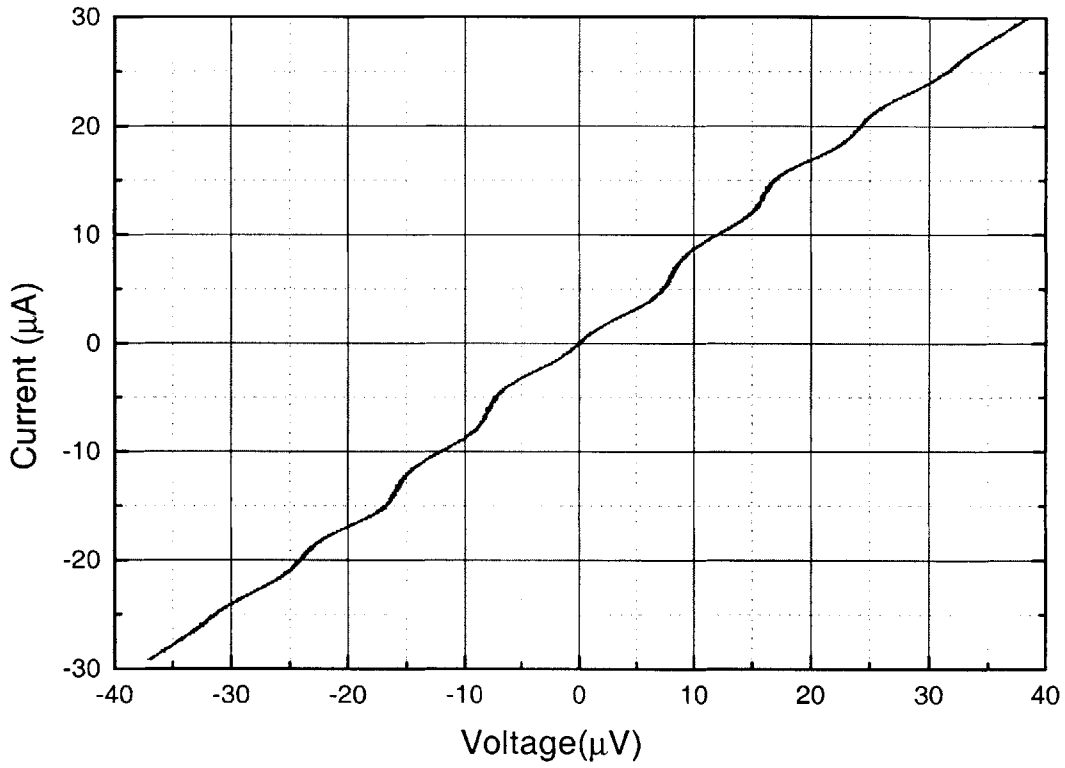

FIGURE 5-3. Measured I-V curve of a current biased junction driven by an oscillating current. Note that the critical current is nearly completely suppressed, and the visible steps are rounded. There is no hysteresis in this I-V curve.

These approximations can allow for a first order calculation of the power from the detector junction response. However, a more exact solution requires a simulation of the junction I-V with a current bias and an oscillating input signal. Even this simulation does not account for the whole problem, since it does not simulate the effect of temperature in rounding the steps.

For an overdamped junction, the shape of the step rounding due to thermal noise for the critical current can be written as Equation (5-9) when $\gamma=k_BT/E_C<<1$.

$$\langle V\rangle = 2I_cR_n\sqrt{1-\left(\frac{I}{I_c}\right)^2}\sinh\left(\frac{\pi I}{I_c\gamma}\right)\exp\left(-\frac{U_0}{k_BT}\right) \qquad \textbf{(5-9)}$$

R_n is the resistive branch, U_0 is the barrier seen by the phase particle. When $\gamma>>1$ in an overdamped junction, the curve follows the expression in Equation (5-10) [71].

$$\langle V \rangle = 2I_c R_n \left(\frac{I}{I_c} - \frac{I/I_c}{2((I/I_c)^2 + \gamma^2)} \right) \tag{5-10}$$

At the higher-order steps (any step but the critical current itself), the curvature of the step is different because the height of the step is not I_c. This gives a different value for γ, called γ_1, in Equation (5-11).

$$\gamma_1 = 2\gamma \frac{I_c}{\Delta I} \frac{R_d}{R} \left(1 + \frac{I_c^2}{2I^2} \right) \tag{5-11}$$

This value can now be plugged into the above equations and used to calculate the curvature of each step. R_d is the dynamic resistance of the junction at the current bias point if there is no applied oscillating current, and ΔI is half the amplitude of the Shapiro step [71].

5.4 The SQUID Oscillator

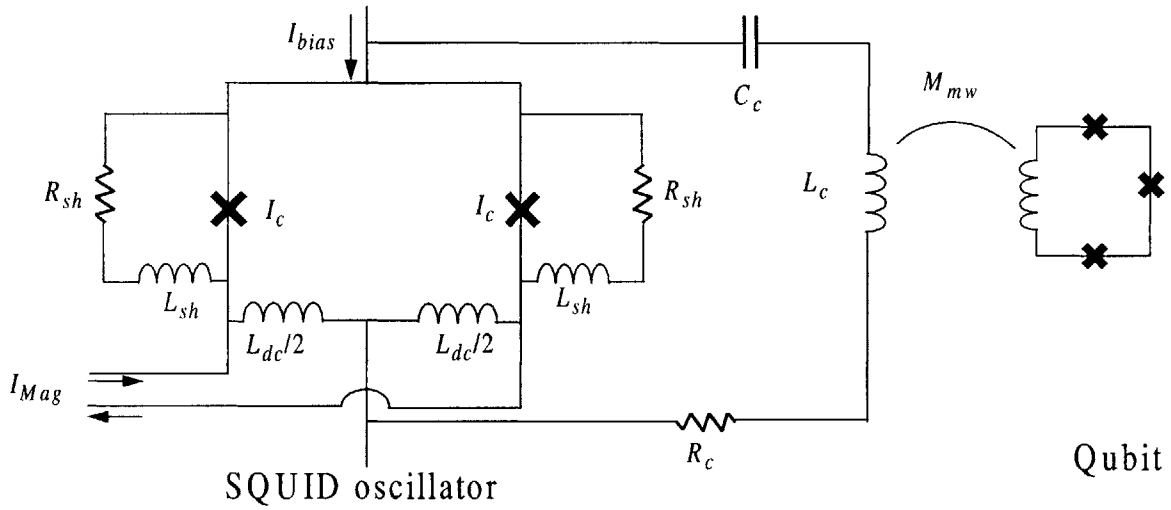

FIGURE 5-4. Circuit diagram of the SQUID oscillator.

A simple oscillator based on an overdamped dc SQUID was designed to drive the qubit, as shown in Figure 5-4. This is the simplest oscillator design which has two controls, current bias and flux bias, in order to adjust the frequency and amplitude of the SQUID. The two are not completely independent, however, and it may take experimenta-

tion to map out the appropriate flux and current biases to specify the desired amplitude and frequency. In this design, the dc SQUID oscillator is placed on a ground plane to minimize any field bias from the external source which biases the qubit. In order to flux bias the SQUID, direct injection is used, where an extra current, I_{Mag} in the figure, flows along a segment of the superconducting wire in the SQUID, adding flux through the loop without changing the bias of the junctions.

The output of the oscillator is inductively coupled to the qubit, so that it is the oscillating magnetic field which drives it. Not only does the oscillator need to provide sufficient amplitude at the right frequency to drive the qubit, it needs to do this without decohering the qubit. Fortunately, this can be modeled with the spin-boson model, and the oscillator can be engineered in order to reduce this noise.

5.4.1 Decoherence

The spin-boson model for relaxation and dephasing times may be applied to the persistent current qubit [46]. The relevant equations give dephasing and decoherence times in terms of the spectral density of the noise [33]. A version of this method was described in Section 3.7.1. We repeat Equation (3-21) in Equation (5-12) for clarity.

$$\tau_r^{-1} = \frac{1}{2}\left(\frac{\Delta}{\nu}\right)^2 J(\omega)\coth\left(\frac{\hbar\omega}{2k_BT}\right) \quad \tau_\phi^{-1} = \frac{\tau_r^{-1}}{2} + \frac{1}{2}\left(\frac{\varepsilon}{\nu}\right)^2 \lim_{\omega\to 0}\left[J(\omega)\coth\left(\frac{\hbar\omega}{2k_BT}\right)\right] \tag{5-12}$$

τ_r and τ_ϕ are the relaxation and dephasing times, respectively. The ω in the relaxation rate is the frequency corresponding to the energy difference (ν) between the two states. Δ and ε are the tunnel splitting and energy bias, respectively, and $J(\omega)$ is the environmental spectral density function. This is calculated from the fluctuations in the energy bias, $J(\omega)=<\delta\varepsilon\ \delta\varepsilon>_\omega/\hbar^2\coth(\hbar\omega/2k_BT)$, which in turn depends on oscillations of the magnetic flux in the qubit due to Johnson-Nyquist noise in the environment. These values are well known from our circuit model, and for an inductive line (L_c) which magnetically couples to the qubit with a mutual inductance M_{mw}, $J(\omega)$ can be written as in Equation (5-13).

$$J(\omega) = \frac{4}{\hbar\omega}\left(\frac{M_{mw}I_p}{L_c}\right)^2 Re\{Z_t(\omega)\} \tag{5-13}$$

Here $Z_t(\omega)$ is the impedance of the circuit environment, in this case the SQUID oscillator which couples to the qubit. We will use the linearized circuit model of the oscillator as the

environmental impedance. Since the relevant noise is the Johnson noise across the inductance from other noise sources, $Z_t(\omega)$ is the inductance, L_c, in parallel with the rest of the circuit. I_p, meanwhile, is the circulating current in the qubit. This formula gives a means of calculating the decoherence and dephasing rates from the impedance of the circuit, making design of the appropriate circuit straightforward.

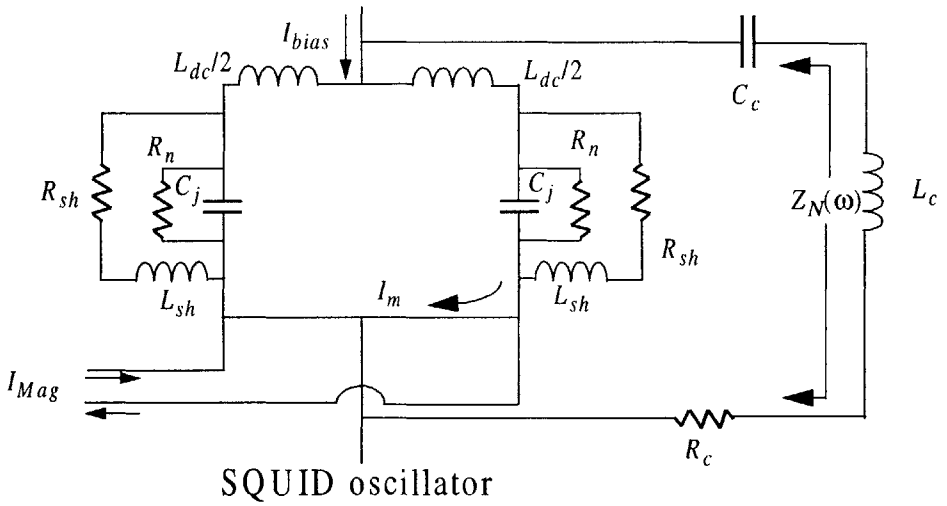

FIGURE 5-5. Circuit diagram of the SQUID oscillator. The junctions have been replaced by the RCSJ model where the Josephson element is removed, giving the Norton equivalent circuit.

5.4.2 Circuit design

There are three requirements for the on-chip oscillator. First, it must deliver an oscillating signal from 10 to 20 GHz with an amplitude of at least $0.001\Phi_0$. Second, the signal must be clean--harmonic frequencies must be minimized. Third, the relaxation and dephasing times need to be greater than 1 μs.

A circuit model from which decoherence can be calculated uses the RCSJ model for the junctions in the SQUID. When the junctions are rotating, they look like independent current sources, and thus may be treated as open circuits in the impedance calculation. The circuit model is shown for this circuit in Figure 5-5. At first, we consider the inductor to be the load, and we calculate the Norton impedance, $Z_N(\omega)$, in Equation (5-14).

$$Z_N(\omega) = \frac{1/2}{j\omega C_j + \frac{1}{R_n} + \frac{1}{R_{sh} + j\omega L_{sh}}} + \frac{1}{j\omega C_c} + R_c \qquad \textbf{(5-14)}$$

Then, placing the inductor in parallel with this circuit, we get $Z_t(\omega)$ in Equation (5-15).

$$Z_t(\omega) = \left[(Z_N(\omega))^{-1} + \frac{1}{j\omega L_c}\right]^{-1} \quad \textbf{(5-15)}$$

This is the impedance which appears in the spectral density calculation in Equation (5-13).

The impedance is a complex function, but it is readily apparent that the real impedance in parallel with the inductor, L_c, should be large. (This comes from the fact that our primary interest is current across the inductor, and although a large impedance means greater voltage noise, it results in smaller current noise.) There is, however, a conflict here, as a small shunt resistance is necessary to reduce the I_cR product so that it is smaller than the voltage which gives 10 GHz, namely 20 μV. Fortunately, a compromise is possible if a damping resistor is used in the coupling loop.

The maximum amplitude of magnetic flux oscillation is at the resonance of the LC circuit. Unfortunately, this is at the maximum throughput for the noise as well. In order to achieve a balance between flux amplitude and noise, we designed the resonance to be slightly off from the target frequencies of the oscillator. In this case, the LC resonance occurs at about 8.6 GHz. By using an LC resonance below the operating frequency, higher frequency harmonics are reduced. With some work, a suitable set of parameters has been found.

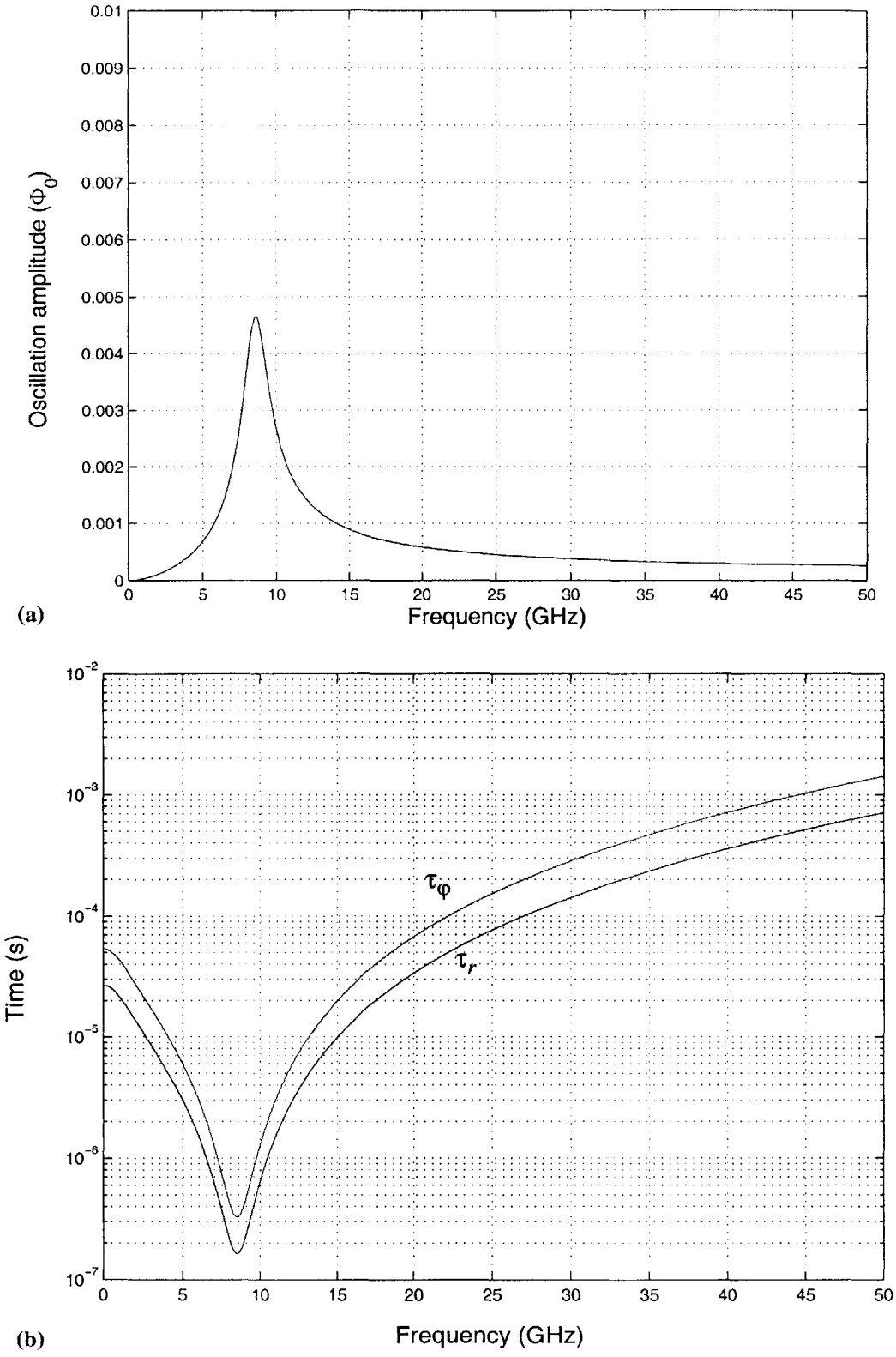

FIGURE 5-6. (a) The amplitude of the SQUID oscillator at various frequencies. (b) The decoherence times of the SQUID oscillator at various frequencies.

I_c	R_n	C_j	R_{sh}	L_{sh}	R_c	C_c	L_c	M_{mw}
81 μA	23.4 Ω	4.84 pF	0.19 Ω	0.38 pH	0.73 Ω	4.6 pF	75 pH	0.6 pH

For 10 GHz, which is near the resonance frequency, the calculated flux oscillation has a maximum of $0.0027\Phi_0$, while the computed relaxation and dephasing times are 0.63 μs and 1.2 μs, respectively. Within 1 GHz, however, the amplitude has dropped to $0.0018\Phi_0$ and the relaxation and dephasing times have increased to 1.5 and 3 μs. By 20 GHz, the oscillation is $0.00058\Phi_0$ and the times are 34 μs and 67 μs. This circuit has been fabricated at Lincoln Laboratory in their niobium trilayer process. It is coupled to a qubit created by the same process.

5.4.3 Simulation

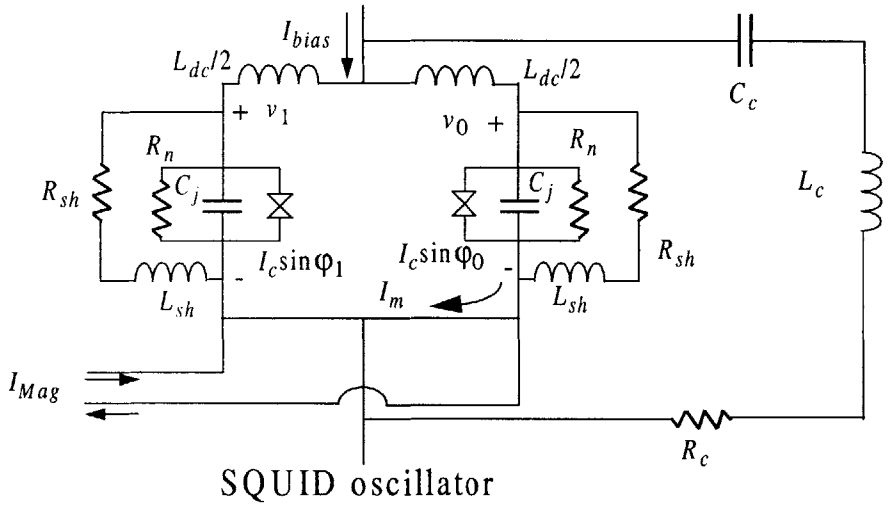

FIGURE 5-7. Circuit diagram of the SQUID oscillator.

The dc SQUID oscillator can be simulated using the RCSJ model, the Josephson relations, and flux quantization. The voltage across the load is simply $V_{load} = \frac{v_0 + v_1}{2}$, where v_0 and v_1 are the voltages across junctions 0 and 1 respectively. The voltage across the load is the average of these, since it is tapped off the middle of the loop, which divides the inductance equally between the two branches. Since the voltage difference around the loop (v_0-v_1+$L_{dc}dI_m/dt$) must be equal to zero according to Kirchoff's voltage law, this means that $V_{load} = v_0+.5L_{dc}dI_m/dt = v_1 - .5L_{dc}dI_m/dt = (v_0+v_1)/2$.

Flux quantization requires Equation (5-16) to be true, where f_{osc} is the external flux bias of the oscillator which I_{mag} produces.

$$I_m = \frac{\Phi_0(\varphi_1 - \varphi_0 + 2\pi f_{osc})}{2\pi L} \tag{5-16}$$

Flux enters and leaves the loop by 2π changes in φ_0 and φ_1. Equation (5-17) describes the current in each branch of the SQUID.

$$\begin{aligned} i_0 &= \frac{I_{bias} - I_{load}}{2} + I_m \\ i_1 &= \frac{I_{bias} - I_{load}}{2} - I_m \end{aligned} \tag{5-17}$$

The rest of the equations follow from the Josephson relations and basic circuit element equations. The voltage-phase relation ($V=(\Phi_0/2\pi)d\varphi/dt$) gives

$$\frac{\partial \varphi_k}{\partial t} = \frac{2\pi}{\Phi_0} v_k \tag{5-18}$$

The Josephson current-phase relation ($I = I_c \sin\varphi$) combined with Ohm's law and the capacitance current-voltage relationship ($i = CdV/dt$)gives Equation (5-19).

$$\frac{\partial v_k}{\partial t} = \frac{i_k - v_k/R_n - I_c \sin(\varphi_k) - i_{sh,k}}{C_j} \tag{5-19}$$

The current across the resistive shunt for junction k is $i_{sh,k}$, which changes in time according to Equation (5-20) according to the inductance current-voltage relationship ($V=LdI/dt$).

$$\frac{\partial i_{sh,k}}{\partial t} = \frac{v_k - i_{sh,k} R_{sh}}{L_{sh}} \tag{5-20}$$

The current across the load follows this inductance current-voltage relationship as well when we calculate the portion of the voltage across the inductor, as shown in Equation (5-21).

$$\frac{\partial I_{load}}{\partial t} = \frac{V_{load} - V_{cap} - I_{load} R_c}{L_{load}} \tag{5-21}$$

Finally, the voltage change across this capacitance depends on this current, as in Equation (5-22).

$$\frac{\partial V_{cap}}{\partial t} = \frac{I_{load}}{C_c} \tag{5-22}$$

Since we can determine the time-rate of change of each of these variables in terms of their

present values, it is straightforward to solve numerically as long as we have the correct starting conditions (I_{bias}=0, f=0, φ_1=φ_2=0, v_1=v_2=0, $i_{sh,1}$=$i_{sh,2}$=0). At each point in time, the current values of the variables are used to determine their rate of change, multiplied by Δt, and added to the current values. Matlab's integration subroutines, such as ODE45, further improve the solution by calculating enough intermediate steps to avoid discretization errors. I_{bias} and f_{osc} are considered constants since they change slowly enough to allow the others to reach a steady-state solution. This steady-state solution is mostly sinusoidal once the average voltage is past I_cR, which is the desired operating regime of the SQUID.

These simulations allow a more exact determination of the frequency and amplitude of the oscillations seen by the qubit. First, Figure 5-8 shows the I-V curve, both simulated and measured. Figure 5-9 shows a contour plot, where the horizontal axis is the bias current on the SQUID, the vertical axis is the frequency, and the colors indicate the amplitude of the signal, so that each vertical slice shows the amplitude spectrum at a particular current bias. The flux bias is kept constant at f=0. Unlike the array in Section 5.5, the maximum output of the SQUID oscillator occurs at f=0, since the two junctions contribute symmetrically to the load. Figure 5-10 shows the amplitude of the dominant signal versus the bias current of the oscillator. The frequency of this signal changes with the current bias. This simulation allows a good estimation of the signal produced by the oscillator at different values of I_{bias} and f_{osc}.

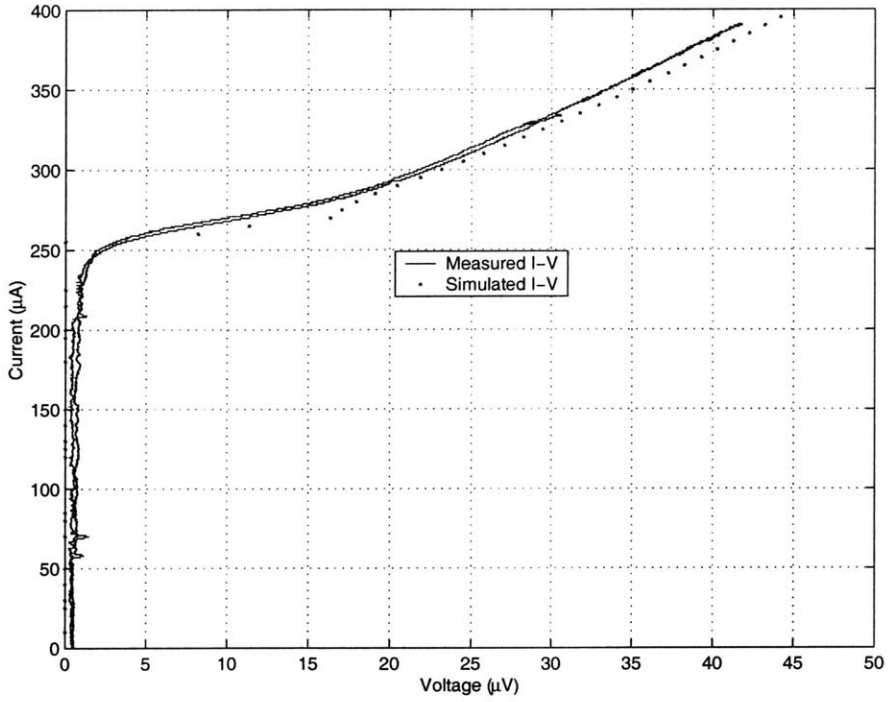

FIGURE 5-8. The I-V curve of the oscillator, both measured and simulated. f_{osc}=0.

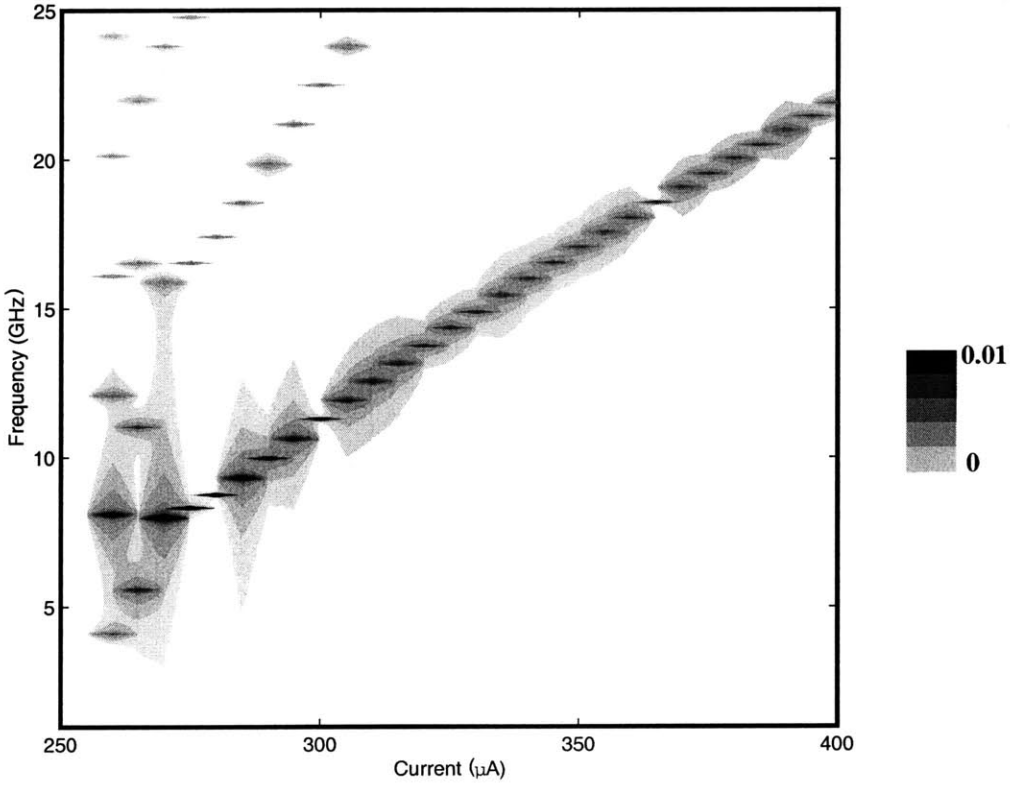

FIGURE 5-9. A contour plot showing the frequency and amplitude of the oscillator as the bias current is varied. f_{osc}=0.

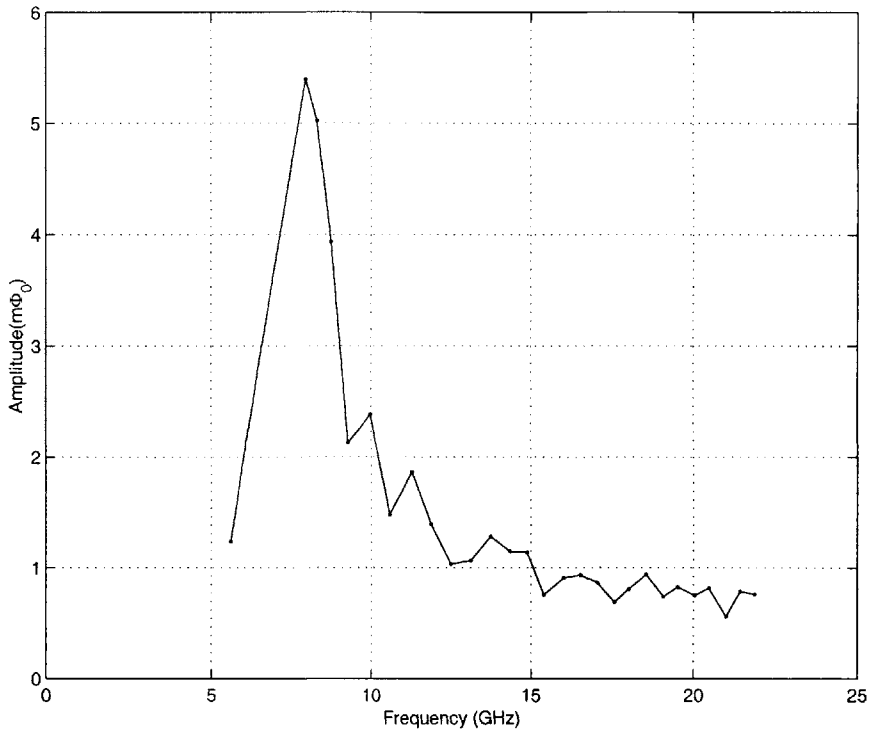

FIGURE 5-10. The amplitude of the dominant frequency coming out of the oscillator at varying bias currents. f_{osc}=0.

5.4.4 Measurements

Measurements have been performed on the oscillator at 300 mK. It has not yet been tested at dilution refrigerator temperatures, so there are no measurements of qubit rotation. However, the current-voltage characteristic has been measured, as shown in Figure 5-8. Moreover, the oscillator produces suppression in the critical current of the measurement SQUID when it is on, as shown in Figure 5-11. This indicates that power is being delivered to the measurement SQUID through magnetic coupling, and by extension to the qubit.

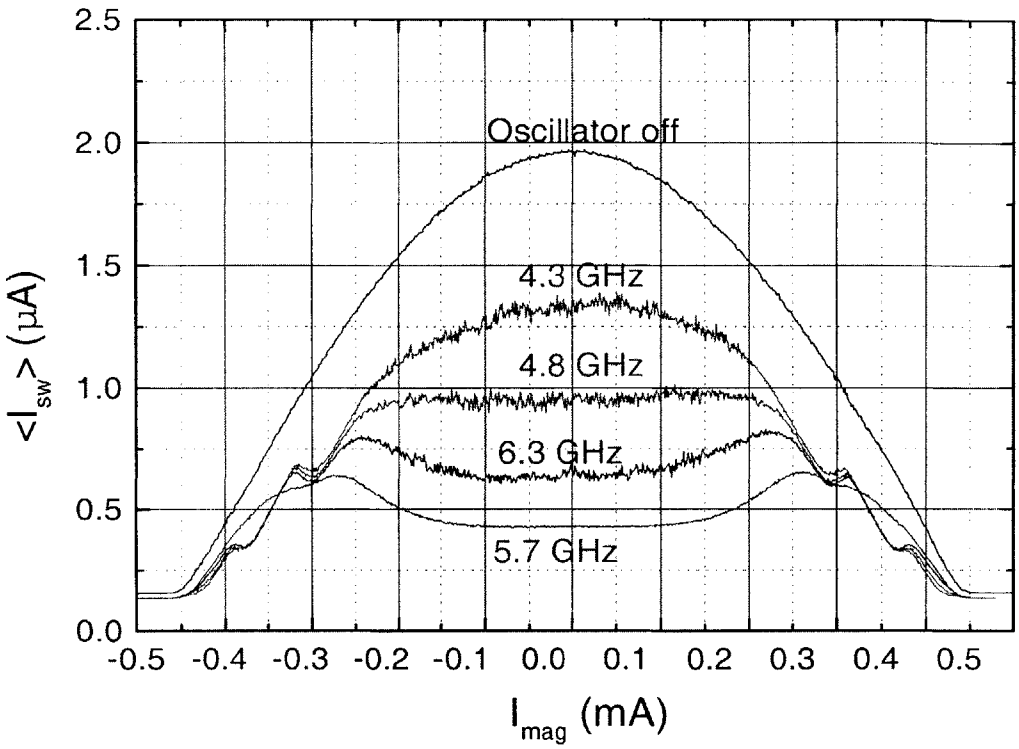

FIGURE 5-11. The mean switching current for the measurement SQUID when the SQUID oscillator is at various frequencies. The magnetic field bias of the oscillator is kept at f_{osc}=0.26, while the current bias is changed to produce different oscillation frequencies.

When the oscillator is on, the SQUID's switching current standard deviation becomes broader even as the curve shape is distorted, as shown in Figure 5-12. This makes it difficult to detect the qubit step and measure it. With enough averaging and comparison to a SQUID lobe without a qubit step, it should be possible, however. This experiment has not been run at this time due to problems with the samples.

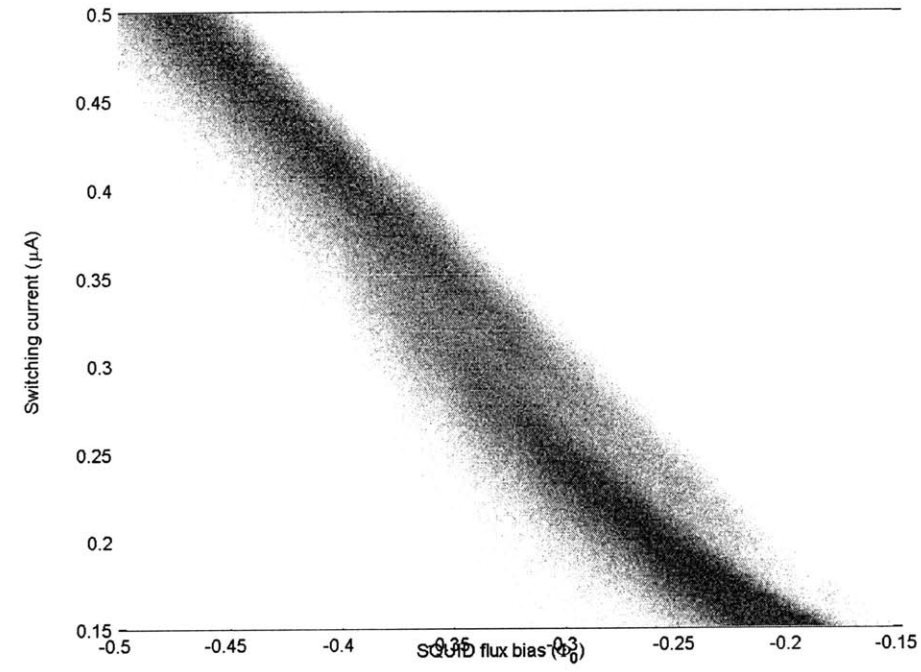

(a)

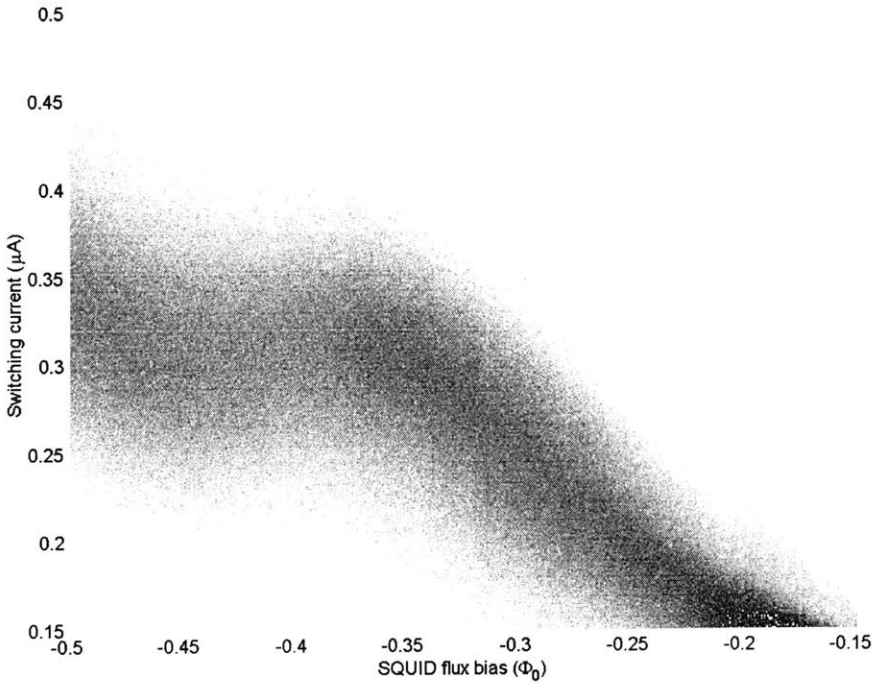

(b)

FIGURE 5-12. The contour plots showing the number of switching events. The qubit step is clearly visible in (a), where the oscillator is off, but it is washed out in (b), when the oscillator is on at 4.9 GHz. As above, f_{osc}=0.26.

5.5 Arrays

Arrays of parallel Josephson junctions can operate as tunable oscillators [35]. When the array is current biased such that it has a non-zero voltage, V_{arr}, each junction oscillates with a period of $T=\Phi_0/V_{arr}$. In a shunted array, a single frequency wave solution is applicable when the array is biased such that $V_{arr}>I_cR$ (R is the total resistance of the junction, $R_n||R_a$, the junction's normal resistance and its shunt resistance, respectively) with frequency $\omega=(2\pi/\Phi_0)V_{arr}$. Then each junction can be modeled as an independent, sinusoidal current source, whose phase differs from its neighbor by $2\pi\Phi_{ext}/\Phi_0$, where Φ_{ext} is the applied external flux per cell of the array. Using this model, we can design a load that is impedance matched to the array for maximum power output [36]. For testing purposes, a single, overdamped Josephson junction can detect the power delivered to it as the load.

What is not apparent is that the same single frequency model is useful when $V_{arr}<I_cR$. Despite the fact that the periodic, ac current of each junction is distinctly non-sinusoidal, if one considers each harmonic individually, this approximation still works. This will be shown by a series of nonlinear simulations.

5.5.1 Nonlinear simulation

Consider a parallel array consisting of 54 junctions, as shown in Figure 5-13(a). Each cell of the array has a mesh inductance calculated from the cell geometry using a program called FastHenry [37]. The RCSJ model is substituted for each Josephson junction in the array. In this experiment, the junctions are resistively shunted, and both the resistance and the inductance of the shunt are included in the model [68]. The complete array is modeled in a numerical simulation which solves for flux quantization and Kirchhoff's voltage and current laws. Typical parameters for each junction are the following: I_c=120 μA, R_n=8.6 Ω, and C_j=300 fF. The cell inductance, L_s=15.2 pH, gives a value of L_J/L_s=0.177. The shunt resistance for each junction is R_a=2.6 Ω (the inductance of the loop it forms with the junction is L_a=1.28 pH), which gives a Stewart-McCumber parameter of β_c=0.5.

5.5.2 Linear circuit model, $V_{arr} > I_c R$

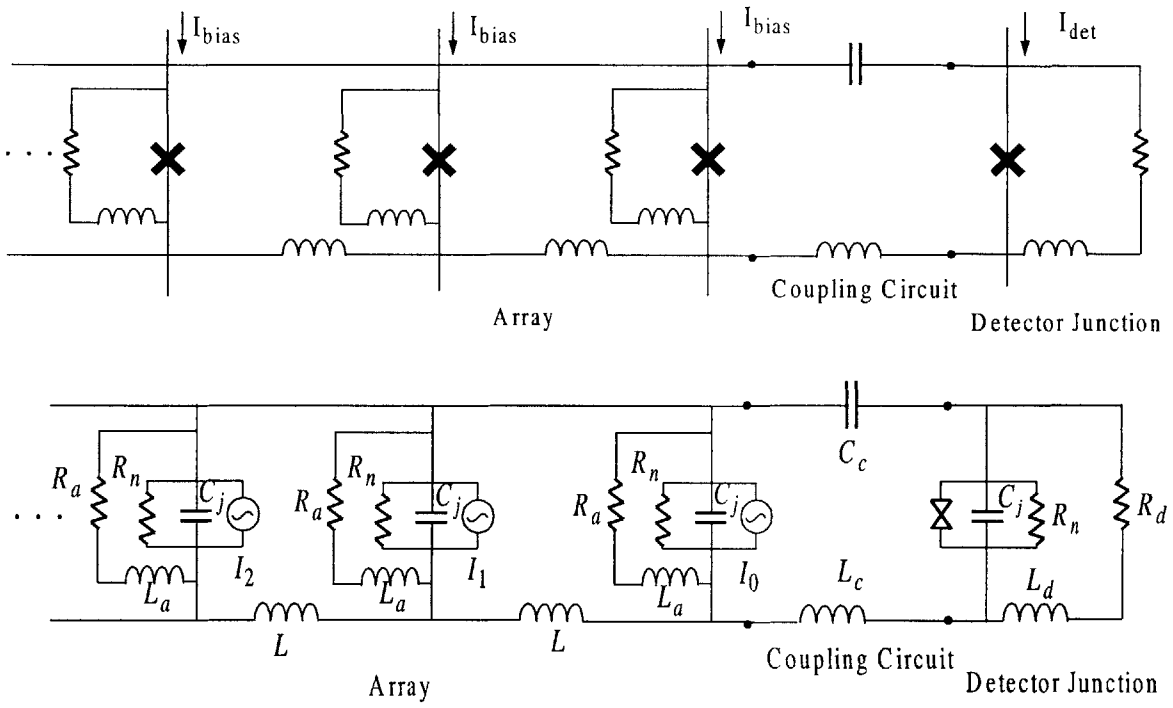

FIGURE 5-13. (a) Schematic of array. (b) Diagram of circuit used to model array. $I_i=\alpha I_c \sin(\omega t+\theta_i)$, where $\theta_i=2\pi if$.

When the bias current of the array, I_{bias}, is high enough that $V_{arr}>I_cR$, a traveling wave solution is apparent. At this bias, each of the array's junctions is in a whirling mode [38], in which each junction is continuously rotating through phase. This produces a periodic and approximately sinusoidal current of magnitude I_c. Modeling the Josephson current of each junction as an independent source, which has an amplitude of I_c at a frequency of $\omega=(2\pi/\Phi_0)V_{arr}$, and which differs in phase by $2\pi\Phi_{ext}/\Phi_0$ per cell, allows a fairly simple circuit model utilizing the RCSJ junction model, as shown in Figure 5-13(b). This linearized model can be solved analytically. From this linear circuit network, we can calculate the equivalent impedance of the array. First, each individual junction has an impedance of

$$Z_{j,a} = \frac{1}{\frac{1}{R_n} + j\omega C_j + \frac{1}{R_a + j\omega L_a}}. \qquad \textbf{(5-23)}$$

These parameters are labeled in Figure 5-13(b). For an array with many junctions, adding

one more junction and its cell inductance should not change the overall impedance of the array. Thus, the impedance of the array can be calculated recursively, so that the equivalent impedance at one end is the recursive solution in parallel with the final junction:

$$Z_r = j\omega L + \sqrt{(j\omega L)^2 + 4j\omega L Z_{j,a}}$$
$$Z_{arr} = \left(\frac{1}{Z_{j,a}} + \frac{1}{Z_r}\right)^{-1} \quad \textbf{(5-24)}$$

Furthermore, the circuit model allows the calculation of how the power delivered to the load varies with frustration, $f=\Phi_{ext}/\Phi_0$. One would normally assume that the power is maximum when all the junctions are in phase, $f=0$. This need not be the case, however, when the inductance of the cell induces a current lag between the junctions. This means that the currents from two neighboring junctions are in phase only if the phase difference compensates for the current lag. In fact, when the inductance is paired with the resistor and capacitor of the RCSJ model, it forms a low pass filter. The load, at one end of the array, will not see a power equal to the sum of all the junctions' output, but rather the total power will asymptotically approach a finite level as more junctions are added to the array. The number of junctions where this levels off is dependent on the parameters of the array, but here it is about 10. Nonlinear simulations show that this model is effective. The phase difference between the junctions is approximately as predicted (Figure 5-14(a)), as is the current amplitude (Figure 5-14(b)).

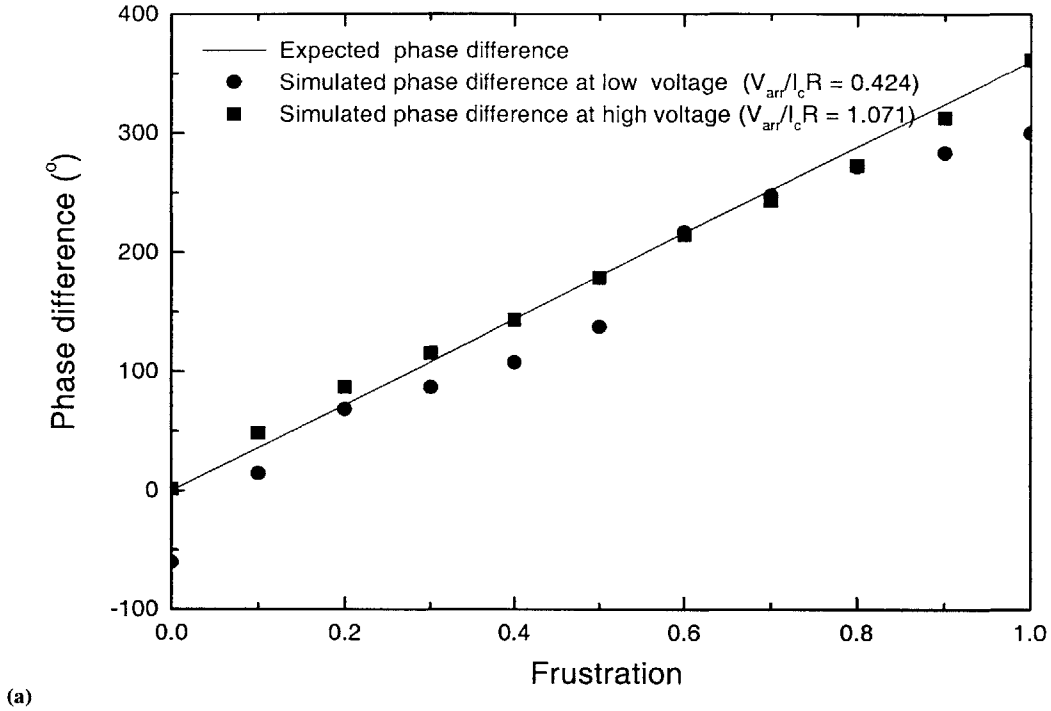

(a)

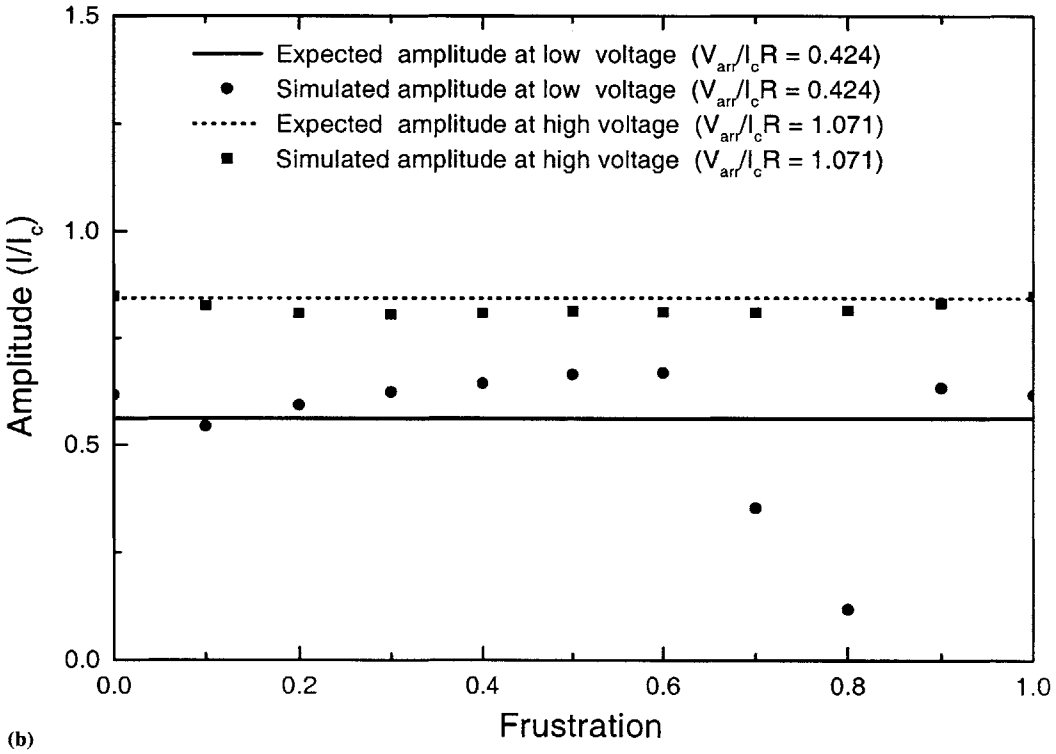

(b)

FIGURE 5-14. A comparison of simulations of the array biased at high and low voltage: (a) the phase difference between adjacent junctions, and (b) the amplitude of the oscillation.

5.5.3 Linear circuit model, $V_{arr}<I_cR$

When the voltage is significantly smaller than I_cR, each junction's Josephson current is non-sinusoidal. Despite this, the model may still be used if each harmonic is examined individually. The magnitude of each harmonic for a resistively shunted junction is given by

$$\alpha = 2v[(1+v^2)^{1/2}+v]^{-n}, \tag{5-25}$$

where n is the order of the harmonic, and $v = V_{arr}/I_cR$ [39]. As can be seen in Figure 5-14(a) and (b), the phase difference and magnitude follow the same trend. There are, however, some obvious outliers near f=0.8.

5.5.4 Impedance matching the load

When the junctions are modeled by simple impedances, it is possible to impedance match the detector junction as the load of the oscillator. The detector junction in this experiment is a single junction, identical to the junctions in the array, and shunted by a resistance. The junction parameters are determined by our choice of critical current and critical current density rather than our desire to match the impedances. Thus it is the shunt resistance and inductance that are adjusted to match the array impedance. The detector's impedance is given by

$$Z_{j,d} = \frac{1}{\frac{1}{R_n} + j\omega C + \frac{1}{R_d + j\omega L_d}} \tag{5-26}$$

It is separated from the array by a capacitor to block dc current, which forms a loop with an inductance. This coupling has an impedance of

$$Z_c = j\omega L_c + \frac{1}{j\omega C_c} \tag{5-27}$$

Note that this impedance is purely imaginary. Thus while the detector junction's parameters are adjusted to match the real part of the array's impedance, the coupling circuit's capacitance and inductance can be adjusted until the imaginary part of the impedance is matched, thus achieving the matching requirement: $Z_{arr}=(Z_c+Z_{j,d})^*$. The parameters of the detector junction itself are identical to the junctions in the array, but its shunt resistance and inductance can be varied. In order to impedance match the detector to the array, R_d=2.6 Ω and L_d=1.36 pH are used with a coupling capacitor and inductance of C_c=200 fF

and L_c=50 pH.

Even in the full simulations, it is apparent that the impedance matching which was accomplished using the linear model works well. Although it is not clear that the power transfer is optimized, the voltage delivered to the load is a clean sinusoidal voltage, even at low V_{arr} where the array produces many harmonics. At the least, this indicates that the impedance matching is much better within the target frequency range than at the harmonics of the signal.

5.5.5 Experiments

Experiments have been performed on Nb arrays manufactured by HYPRES. 3x3 μm^2 junctions were used, which had a critical current of 120 μA. Figure 5-15(a) shows a current-voltage curve of the array, specifying where the bias point is which gives the Shapiro step in Figure 5-15(b).

When the rf power from the array is delivered to the detector junction, it develops Shapiro steps at voltages corresponding to multiples of the frequency of the rf source, ω_s. As [40] and [41] show, we need the full nonlinear simulations to determine the power which the detector junction sees. These full simulations give the Shapiro step height and critical current suppression corresponding to different amplitudes of independent sources, and then we can map those values to our measured I-V curves. We have considered the height of the first step and the suppression of the critical current independently, allowing two estimates of the power. Only the calculation from the step height is shown. The power calculated from the critical current suppression, while not identical, has the same qualitative shape.

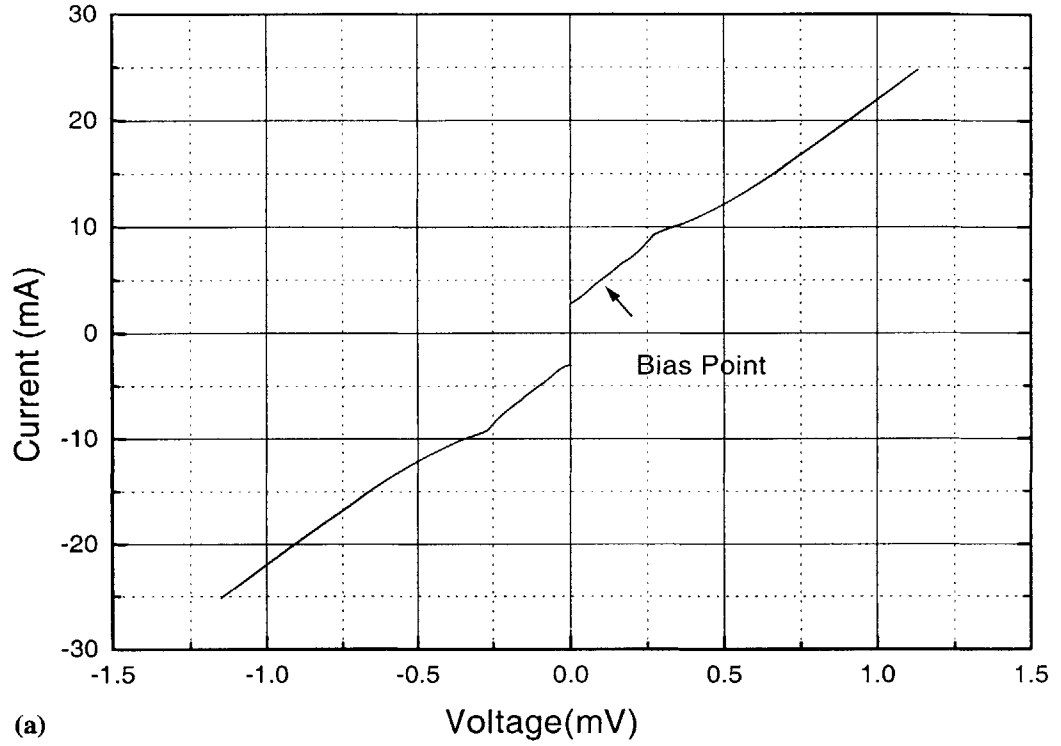

(a)

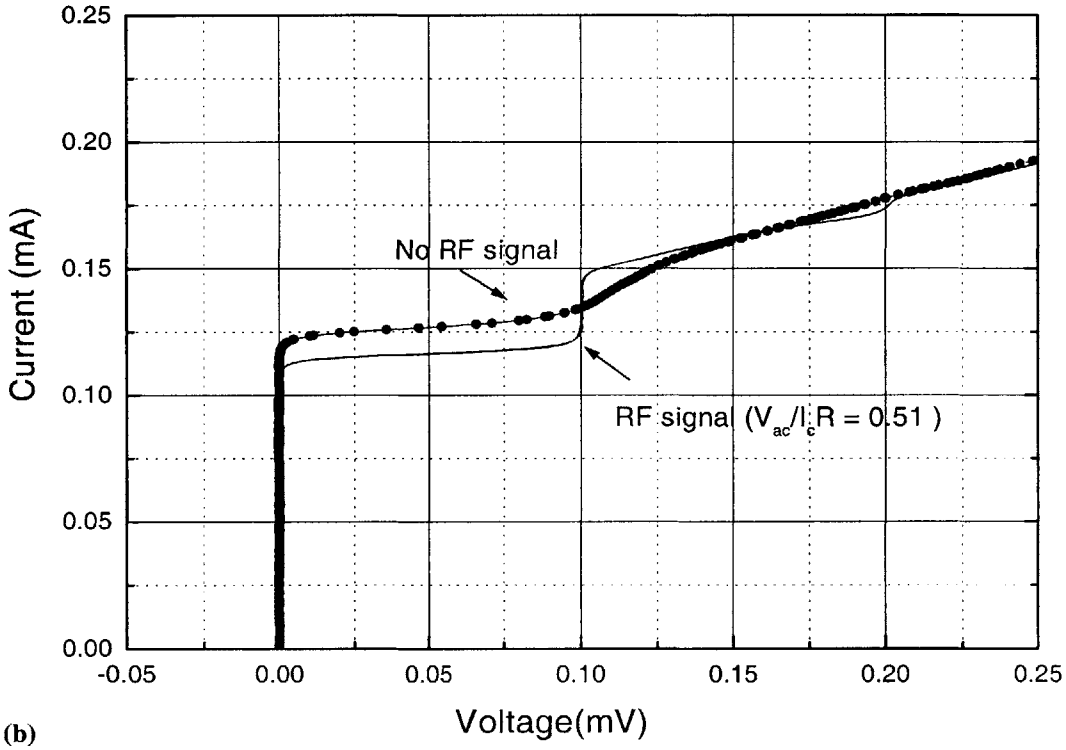

(b)

FIGURE 5-15. (a) Measured current versus voltage of the array at 7.0 K. The bias voltage which gives a 50 GHz output is indicated, V_{arr} = 0.1035 mV=0.42 I_cR. (b) Measured current vs. voltage curves of detector junction at 7.0 K, showing the curve both with and without an rf source of 50 GHz (V_{arr} = 0.1035 mV).

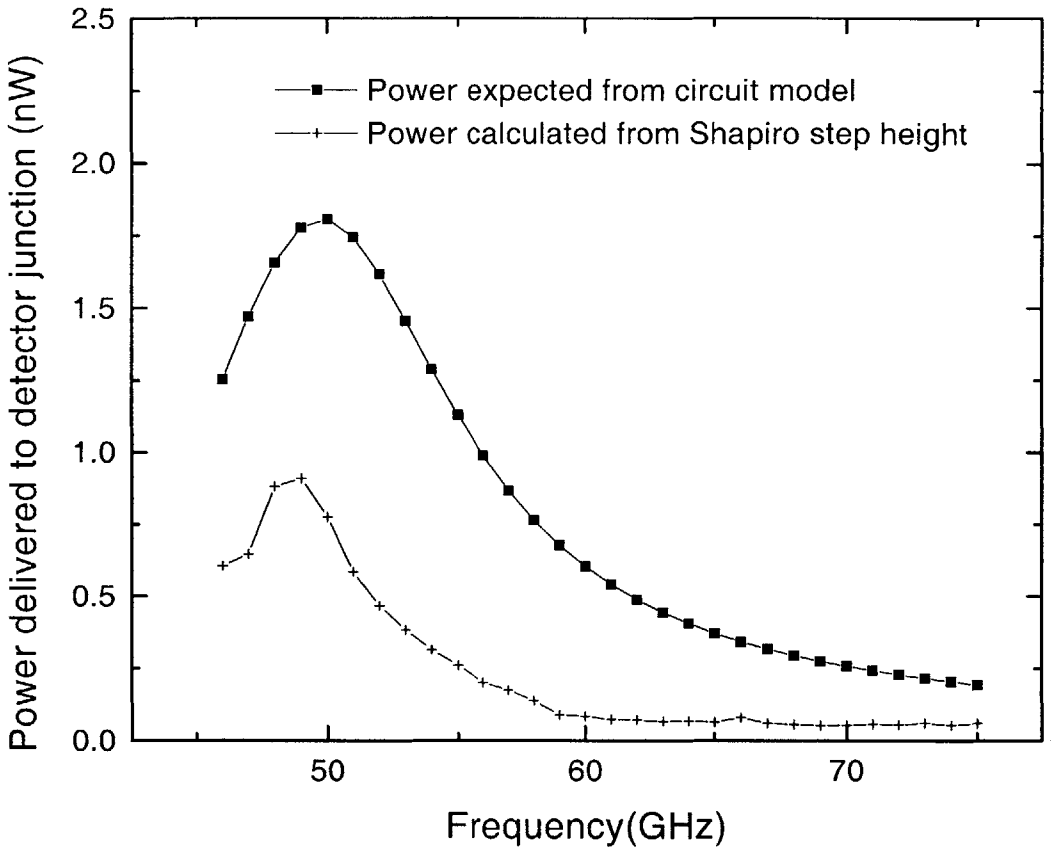

FIGURE 5-16. Power delivered to the detector junction varying with the applied frequency. The frequency is determined by the bias point of the array's voltage. $v=V_{arr}/\Phi_0$. The top curve is the power expected analytically, while the measured power is roughly half of that.

Figure 5-16 shows power delivered to the load versus the frequency of the array, indicating the frequency response of the coupling to the detector junction. While the measured power is roughly half of that expected analytically, the circuit shows the correct frequency response, indicating successful impedance matching.

Figure 5-17 shows the variation of power with frustration. In this experiment, even though the array was current biased, the voltage, V_{arr}, was held constant through a feedback loop. The power is periodic in frustration and can be tuned from its maximum value of about 1 nW to near zero, while the frequency (voltage) of the array is maintained at a constant value. Similar dependencies are found at other frequencies. The expected power is shown from both the linear circuit model (+) and the nonlinear simulations (o). The solid line is a fit through the nonlinear simulation points. Results differ from the predicted

values in three significant ways. First, the measured power is less than the predicted power by approximately a factor of 2 (in Figure 5-17, the predicted power is shown reduced by this factor in order to more clearly show the match in the shape). Second, the offset of the maximum differs from that predicted (0.7 rather than 0.8). Third, the peak in the power is broader than expected. Notice that the shape of the nonlinear simulation prediction is closer to the experimental results than the linear circuit mode.

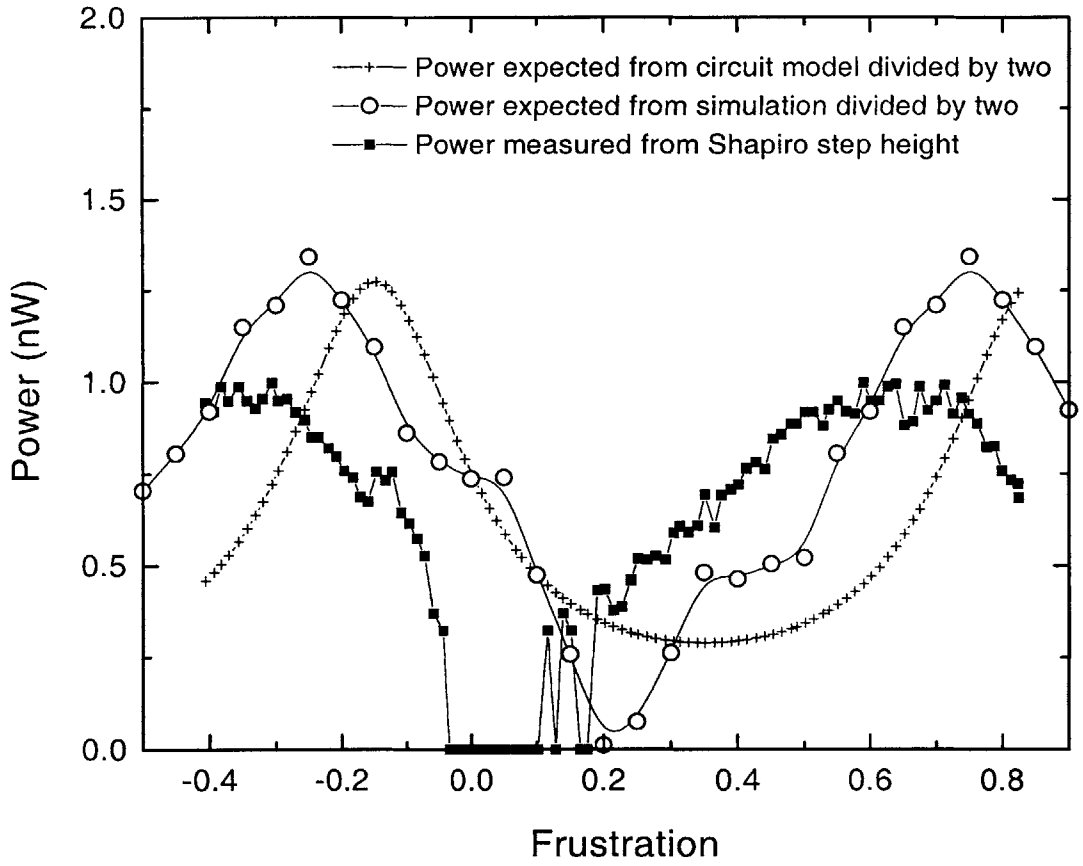

FIGURE 5-17. The power produced by the array, experimental measurements compared to nonlinear simulation and linear circuit model predictions. The array is biased at V_{arr}=0.1035 mV.

The linear circuit model has proven useful in predicting the qualitative shape of the array output and, more importantly, in allowing an impedance match between the array and the junction. The experiments further confirm that amplitude and frequency can be modified independently using frustration and bias current, resulting in a tunable rf source. The low power output may be due to two factors. First, the detector junction influences the oscillator in the same way that the oscillator influences the detector junction. In other

words, we have an active element as the detector, and its influence on the oscillator is significant. This can be reduced by using a detector junction with a much smaller critical current, and thus less signal, than the array's junctions. Second, the leads connected to the array provide an alternative path for the power. This can be alleviated by creating high impedance barriers in the leads close to the oscillator.

5.6 Conclusion

Engineering on-chip control of the qubit requires hitting a moving target at this stage of the project. Although we design in order to provide coherent control according to the most recent theoretical analysis, the theory is constantly changing as we refine our model of the qubit. We have designed a device which is connected to the qubit, and our experiments on this device will refine our model, improve the theory, and allow for better design. We can determine that the oscillator delivers power to the qubit. This oscillator is just the first step in the iterative process which will hopefully result in reliable, coherent on-chip quantum computation.

Chapter 6

RSFQ Circuits

6.1 Introduction

This chapter introduces the concept of Rapid Single Flux Quantum (RSFQ) superconducting digital logic in Section 6.2, and explains how its various components perform their operations. This logic is potentially useful for performing on-chip control of quantum devices. Section 6.3 covers the coupling between quantum devices and RSFQ control in more detail, adapting our method of accounting for circuit environment decoherence to RSFQ. The Variable Duty Cycle Oscillator which we designed in collaboration with the University of Rochester is discussed in Section 6.4. This device repeats a fixed frequency oscillation which lasts for a programmable length of time. This frequency can drive the qubit, and it might be useful in observing Rabi oscillations. Finally, a more conservative circuit based on external timing control and designed for a lower critical current density is described in Section 6.5.

6.2 RSFQ Concepts

CMOS (Complementary Metal-Oxide-Semiconductor) logic forms the basis for modern silicon technology. Pairs of transistors either block or transmit current depending on the charge on their gate inputs, thus storing information and processing logical operations in units of charge. It is difficult to use charge as the basic measure of information in superconductors, since they transmit charge much more readily than they block it. This is apparent even in the names: a *semi*conductor can either conduct or not conduct, while a *super*conductor always conducts charge. Because of this difficulty, it is natural to look to the complement of charge, namely magnetic flux, as the basic logical unit in superconducting technology. In superconductors, information is stored not by charge stored on a capacitor, but by charge circulating in a loop to store magnetic flux. Information is stored and processed by conducting magnetic flux rather than charge.

In CMOS technology, it is difficult to perform logic with only a single electron. Instead, a large number of electrons are stored on a capacitor, enough for it to reach the arbitrary voltage at which the logic operates. This means that the number of electrons can vary with the size of the capacitor. As silicon processing technology pushes the size of those capacitors smaller and smaller, CMOS logic approaches the point where computing is done with quantized electrons, rather than a large, imprecise number of them.

The flux quantum is quantized by the superconductor: it is the amount of flux which produces a phase difference of 2π around a superconducting loop. From the start, superconducting flux logic has dealt with units of flux quanta. Thus this type of logic is called RSFQ, or rapid single flux quantum, technology. Josephson junctions can serve to redirect flux quanta, providing the logic necessary for RSFQ. The components described below differ little from those described by Likharev in his groundbreaking paper [60].

6.2.1 The Josephson Transmission Line

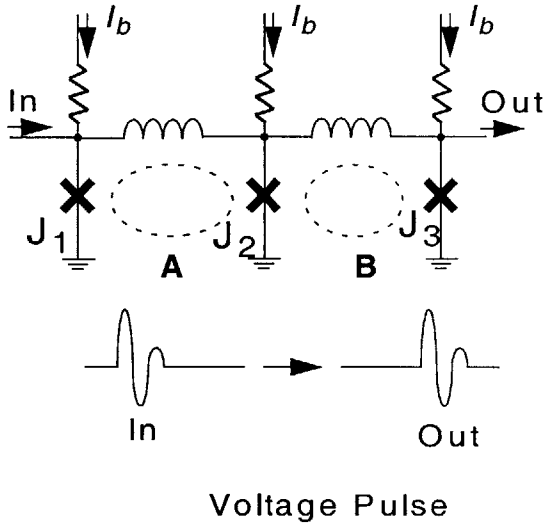

FIGURE 6-1. A Josephson transmission line.

The first component of RSFQ logic is simply a line which can transmit the flux quantum from one end to another, as shown in Figure 6-1. This is called the Josephson transmission line. This line is active, propagating the flux through overdamped Josephson junctions which are each biased near their critical currents. The damping is necessary, since the junctions must return to their initial states while remaining biased.

Consider a flux quantum in loop A, inducing a current in the clockwise direction. The induced current flows in the opposite direction from the bias current across the junction to the left, J_1, so that junction is well below the critical current. However, for the junction on the right, J_2, the sum of the induced current and the bias current is greater than the critical current of the junction, causing it to enter the voltage state. If it were to remain in the voltage state, it would oscillate continuously, but in this case the voltage across the junction looks like a pulse, as shown in the figure. As soon as J_2 enters the voltage state, the current finds an easier path, continuing down the line into the inductor in loop B. The pulsed junction returns to its state just below the critical current, only now the circulating current is in loop B, so the induced current subtracts from the total current in J_2. The junction to the far right, J_3, now has a current greater than the critical current, and it flips. In this way, the flux quantum propagates to the right, travelling through the junctions along the way. The JTL reinforces the pulse, assuring that it reaches the end at full strength, but there is a time delay for the pulse to travel that distance.

6.2.2 The T-Flip-flop

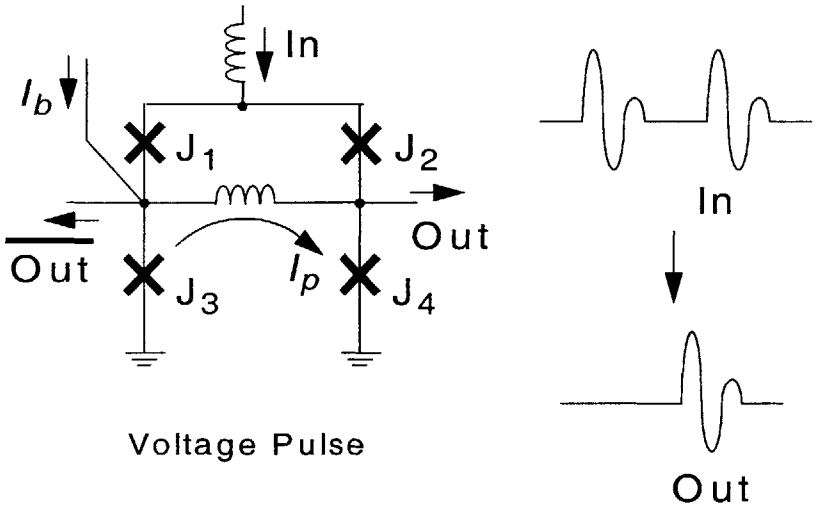

FIGURE 6-2. The SFQ T-flip-flop.

The T-flip-flop, as shown in Figure 6-2, is a basic memory element in both CMOS and RSFQ. The single input serves to both set, reset, and read the cell. When the cell starts out in the 0 state, then an input signal changes it to a 1, and a flux quantum comes out at the $\overline{OUT}$ terminal. When the cell is in the 1 state, then an input resets it to 0 and

sends a voltage pulse to OUT. I_p, the persistent current in the bottom loop, stores the information. When the persistent current flows clockwise and the bias current is such that J_4 is closer to its critical current than J_3, and a pulse at the input will cause J_4 to flip. With a voltage across J_4, the path across J_3 remains superconducting, and the circulating current changes direction. The voltage pulse at J_4 exits the T-flip-flop at Out. Thus the clockwise circulating current corresponds to 1. Once the persistent current starts flowing counterclockwise, an incoming pulse will cause J_3 to flip, since it is closer to its critical current than J_4 is, and the circulating current will reverse direction again, while the voltage pulse is sent to $\overline{\text{Out}}$. The counterclockwise circulating current corresponds to 0.

The properties of the T-flip-flop make it a very useful component. By putting three T-flip-flops in series, one can send signals to the first T-flip-flop, and the state of the three registers will progress from 000, through 100, 010, 110, 001, 101, 011, 111, and back to 000, with an output signal from the last T-flip-flop. If one reads the register of T-flip-flops in the opposite direction, one gets 000, 001, 010, 011, 100, 101, 110, 111, and 000. In other words, these three T-flip-flops form a counter, outputting a pulse every time the counter turns over.

6.2.3 The Non-Destructive Read Out Memory Cell

The T-flip-flop is an example of a DRO, or Destructive Read Out, memory cell. Sending a signal to the input will give an output indicating the current value in the cell, but it will also change the state of the cell to its opposite. An Non-Destructive Read Out (NDRO) cell can output the bit in memory without changing its state. In its most flexible form, an NDRO has 3 inputs. The Set changes the value of the bit to one, or leaves it alone if it's already one. The Reset acts similarly, forcing the state to zero. The Read sends a pulse to Out if the bit is one, sends no output if the bit is zero, and does not change the state of the cell either way.

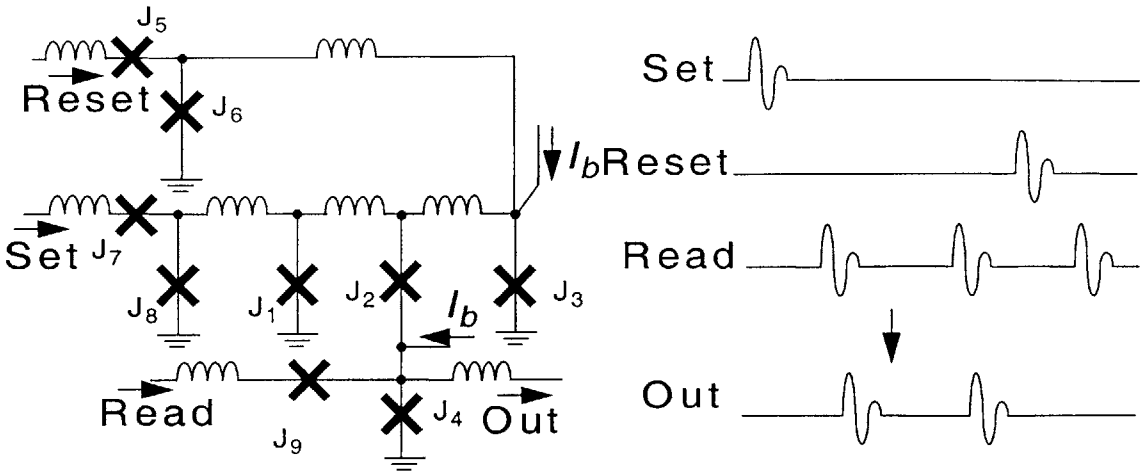

FIGURE 6-3. The SFQ NDRO memory cell.

The information bearing circulating current is contained in the J_1-J_3 loop. If J_2 has a small critical current, it does not significantly effect the circulating current. However, a circulating current in the loop, the "1" state, does force both J_2 and J_4 close to $\pi/2$ due to fluxoid quantization, causing J_4 to switch when a READ signal comes in. When there is no circulating current in the J_1-J_3 loop, then J_2 and J_4 are phase biased near 0, and the READ input does not cause J_4 to switch. Set and Reset behave similarly to how the two branches of the T-flip-flop behave.

6.2.4 The Inverter

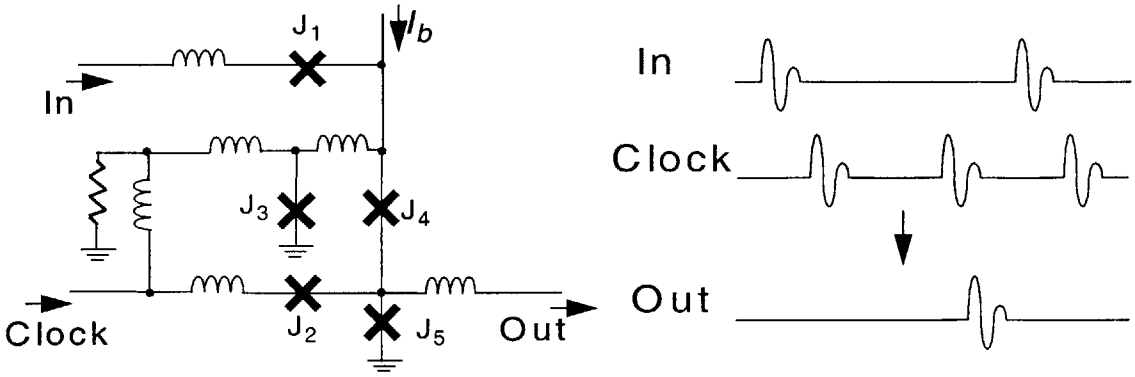

FIGURE 6-4. The SFQ Inverter.

The Inverter outputs an SFQ pulse at each clock signal unless it has received an SFQ pulse at its input since the last clock signal.

In the inverter, the main loop around which flux is quantized is composed of J_3, J_4, and J_5. When an SFQ signal comes in on the In line, the J_1 junction undergoes a 2π flux leap if the circulating current in the loop is counter-clockwise. If the current is clockwise, then the J_4 junction is biased near its critical current and it pulses into the voltage state. J_5 remains superconducting since it has a larger critical current. When this happens, the current goes from clockwise to counter-clockwise. In this case, a pulse on the Clock input causes a 2π phase jump in J_2 rather than J_5. Any signal coming in on the Clock input also resets the J_3-J_4-J_5 loop to clockwise circulating current by causing a 2π phase jump in J_3 if the current is counter-clockwise.

If no input comes in on the Input line, the circulating current remains clockwise, and an input on the Read causes J_5 to pulse (since it is biased near its critical current), sending a signal to the output.

6.2.5 The DC-to-SFQ converter

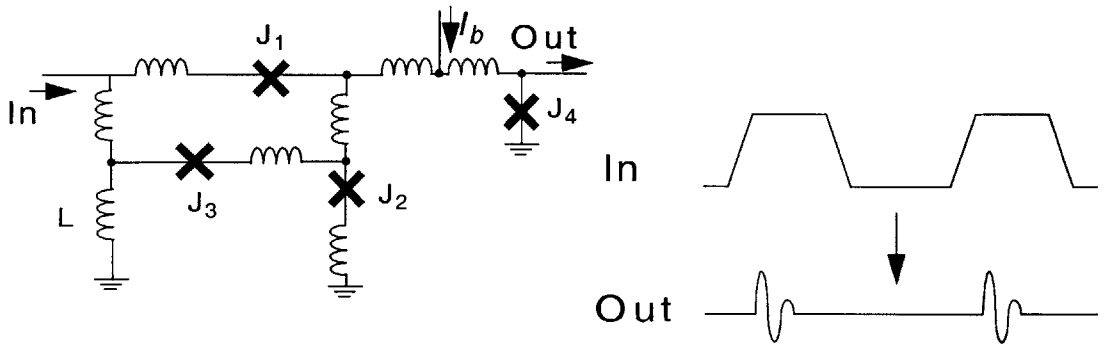

FIGURE 6-5. The DC-to-SFQ Inverter.

In order for an RSFQ logic circuit to be useful, it needs to be able to communicate to the outside world. Therefore, it needs some way to convert CMOS signals, where a high voltage corresponds to "1" and a low voltage corresponds to "0", into SFQ pulses, where the presence of a pulse is "1" and its absence is "0". The DC-to-SFQ converter produces an SFQ pulse at the rising edge of a CMOS signal, so that every time the input current (converted from a voltage) rises past the trigger current, the converter outputs one pulse and then stops [72].

In the above circuit, the J_1-J_3 loop looks like a single junction, and L-(J_1-J_3)-J_2 acts

like an rf SQUID. When the current going into the SQUID exceeds the critical current of J_2, it flips, sending a pulse to the output and trapping an anti-fluxon in the L-(J_1-J_3)-J_2 loop, such that there is now circulating current in the loop flowing counter-clockwise. This brings J_2 below its critical current, so there are no more pulses on the output. (This is identical to what happens when you increase the flux through an rf SQUID and the SQUID changes states at $f = 0.5$.) When the current from In is decreased, the flux escapes through J_3, which is smaller than J_2, then through J_1, which is the same size as J_2.

6.2.6 The SFQ-to-DC converter

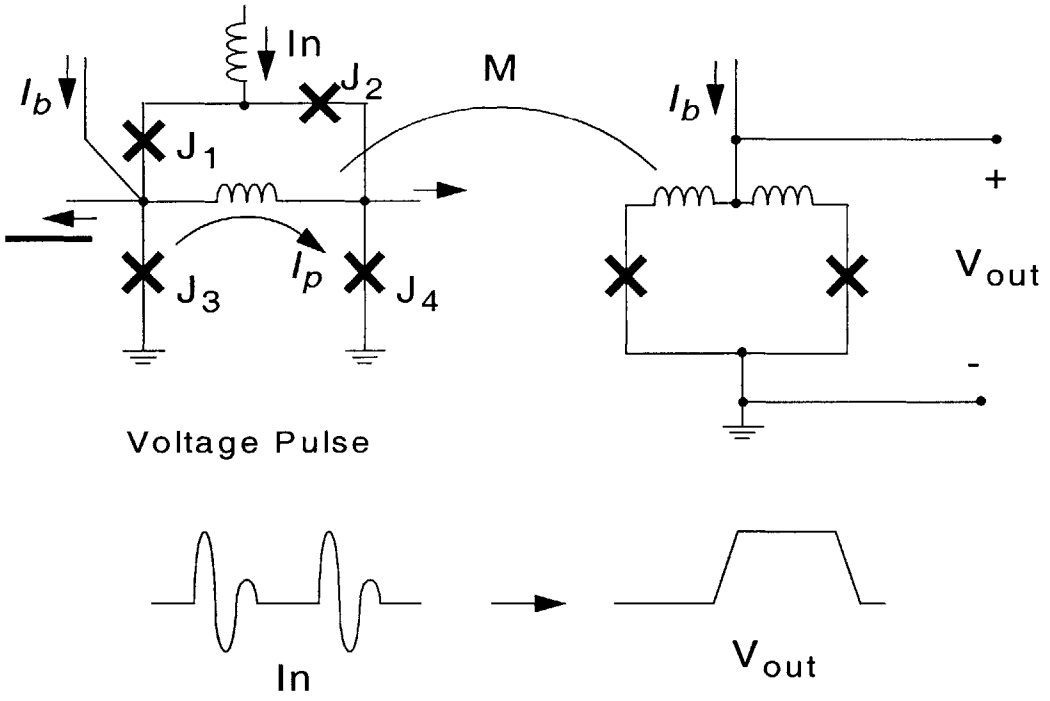

FIGURE 6-6. The SFQ-to-DC converter. It consists of a T-flip-flop and an overdamped dc SQUID.

The easiest way to convert a signal from SFQ to DC is to use a T-flip-flop and an overdamped dc SQUID. The T-flip-flop stores a current either going clockwise("1") or counterclockwise("0") around the J_3-J_4 loop, oscillating between them with each input pulse it receives. A overdamped dc SQUID can measure the flux stored in this loop. If the SQUID is biased just below its switching current when the state of the T-flip-flop is "0," it will switch to the voltage state when the T-flip-flop goes to "1," and return to the zero voltage state when the T-flip-flop again changes to "0." This is shown in Figure 6-6.

For greater coupling over a ground plane, the dc SQUID can be directly coupled to the T-flip-flop by sharing a superconducting line in the storage loop.

6.3 Decoherence from RSFQ circuitry

We used the method in [46], discussed in Section 3.7.1, to estimate and minimize the contribution which the RSFQ electronics make to decoherence in the qubit. In this method, the spin-boson model determines the influence of noise on the relaxation and dephasing times, producing the equations in Equation (6-1).

$$\tau_r^{-1} = \frac{1}{2}\left(\frac{\Delta}{\nu}\right)^2 J(\omega)\coth\left(\frac{\hbar\omega}{2k_BT}\right) \quad \text{and} \quad \tau_\phi^{-1} = \frac{\tau_r^{-1}}{2} + \frac{1}{2}\left(\frac{\varepsilon}{\nu}\right)^2 \lim_{\omega\to 0}\left[J(\omega)\coth\left(\frac{\hbar\omega}{2k_BT}\right)\right] \tag{6-1}$$

τ_r and τ_ϕ are the relaxation and dephasing times, respectively. Δ and ε are the tunnel splitting and the energy bias, which relate to the energy difference ν by $\nu^2=\Delta^2+\varepsilon^2$. Finally, $J(\omega)$ is the spectral density due to the Johnson-Nyquist noise in the resistor, and its value can be derived from the impedance of the RSFQ circuit as shown in Equation (6-2).

$$J(\omega) = \frac{4}{\hbar\omega}\left(\frac{M_{mw}I_p}{L_c}\right)^2 \Re\{Z_t(\omega)\} \tag{6-2}$$

Here, I_p is the qubit's persistent current, M_{mw} is the mutual inductance between the qubit and the RSFQ circuit's coupling loop, whose inductance is L_c, and $Z_t(\omega)$ is the total impedance of the RSFQ circuit in parallel with L_c. The last stage of the RSFQ circuit before it is coupled to the qubit is a Josephson transmission line, as shown in Figure 6-7. A good approximation of the RSFQ circuit's impedance can be reached using only this last stage, since there are generally enough stages in the JTL line for it to be considered infinite. A linearized circuit model of the junction, based on the RCSJ model, was used to calculate the impedance of this stage, which, in series with the resistor and capacitor of the RLC filter, gives $Z_{RSFQ}(\omega)$. The total impedance seen by the qubit is $Z_t(\omega) = Z_{RSFQ}(\omega)\|j\omega L_c$. This formulation gives an estimate of τ_r =2.6 μs and τ_ϕ =5.3 μs as the contribution from the oscillator. Since experimental measurements on a similar qubit without the RSFQ components extract a decoherence time on the order of 50 ns [30], the contribution by the RSFQ circuit should be small compared to other qubit sources. This accounts for circuit noise, but a greater concern is the possibility of heating by the RSFQ

circuitry. The junctions in an RSFQ circuit are current biased near their critical current, and the bias is maintained by resistors which divide an externally applied bias between junctions. These resistors dissipate heat equal to I^2R, and it is unclear how well that heat can be extracted from the chip. Some simulations done by the Bocko and Feldman group at the University of Rochester indicate that the heat load is manageable, while calculations and measurements done by the Lukens group at the State University of New York at Stonybrook indicate otherwise. At this point, it is too early to tell without doing more extensive measurements, ideally by testing RSFQ and qubits running concurrently on the same chip.

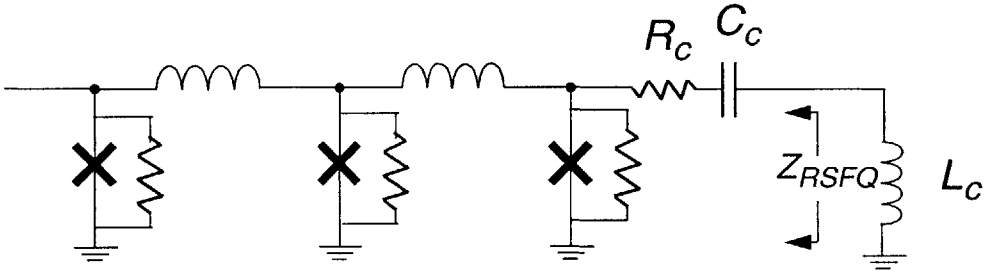

FIGURE 6-7. A Josephson transmission line which couples to the qubit.

6.4 A Variable Duty Cycle Oscillator

An on-chip oscillator can provide a magnetic field at the resonant frequency in order to perform a σ_x rotation of arbitrary phase. One such oscillator was described in Section 5.4. The rate of rotation depends on the oscillator amplitude, so that the degree of rotation depends both on the amplitude and the time duration of the driving signal. For this reason, a useful on-chip oscillator needs, at the least, control of its duration while its amplitude is fixed to a rate much faster than the decoherence rate and its frequency is fixed to the resonant frequency. The design described here has a variable duty cycle, which allows on-chip control of the duration of driving oscillations.

Figure 6-8 shows the block diagram of the oscillator circuit. The 8 GHz clock (consisting of a JTL ring) serves as an always-on RSFQ oscillator. Its signal is sent to the Read input of the NDRO (Non-Destructive Read Out) memory cell every 125 ps. If there is a 1 in the memory cell, then a pulse is sent to the JTL and is transmitted to the qubit

after filtering. If there is a 0 in the memory cell, no pulse is sent. The Set and Reset on the memory cell are controlled by two counters, each of which is made up of a chain of 13 T-flip-flops which increment at each pulse of the 8 GHz clock from 0 to 2^{13}-1, or 8191. With a 125 ps clock period, the counters have a period of about 1 μs. When the counter connected to the Set input of the memory cell overflows, turning over from 8191 to 0, it sends the overflow pulse to the NDRO in order to store a 1 in the cell. Likewise, the other counter will reset the NDRO cell when it overflows. We can set the initial states of the two counters to create an offset which determines the on-time of the NDRO cell. If the Set counter fills up 10 pulses before the Reset counter does, the circuit will transmit 10 pulses to the qubit, then stop until the next time the Set counter overflows.

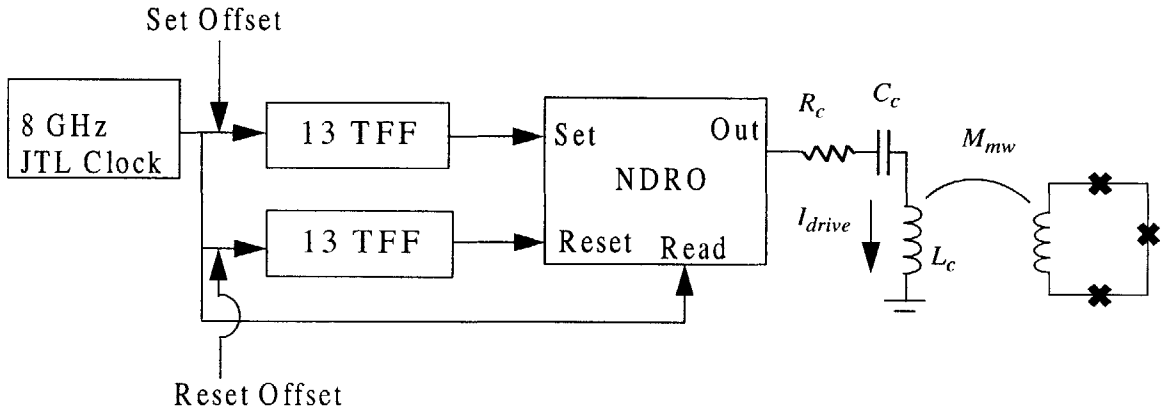

FIGURE 6-8. An RSFQ Variable Duty Cycle Oscillator. It has a 1 μs period, any portion of which can have the 8 GHz oscillator on.

The oscillator may thus be adjusted to transmit anywhere from 1 to 8191 pulses to the qubit every counter period, corresponding to the number of counts by which the two TFF chains are out-of-phase. This fine degree of control is advantageous for causing controlled oscillations in the qubit. The signal coming out of the NDRO goes through an RLC filter before reaching the qubit, preventing harmonics in the signal from reaching the qubit, where they would cause unwanted transitions and subsequent decoherence. The filter has parameters of R_c=1.8 Ω, L_c=68 pH, and C_c=10 pF, such that the resonant frequency is 6.8 GHz, and the Q is 2.1. The qubit sees an oscillating magnetic field corresponding to $M_{mw}I_{drive}$. Figure 6-9(a) shows the series of pulses which travel down the JTL as calculated by JSIM, while Figure 6-9(b) shows the sinusoidal current which couples magnetically to the qubit. This magnetic field's effect on the qubit can be simulated using the

technique discussed in Section 2.7. We can thus predict the rate of the Rabi oscillation and the influence of any higher harmonics.

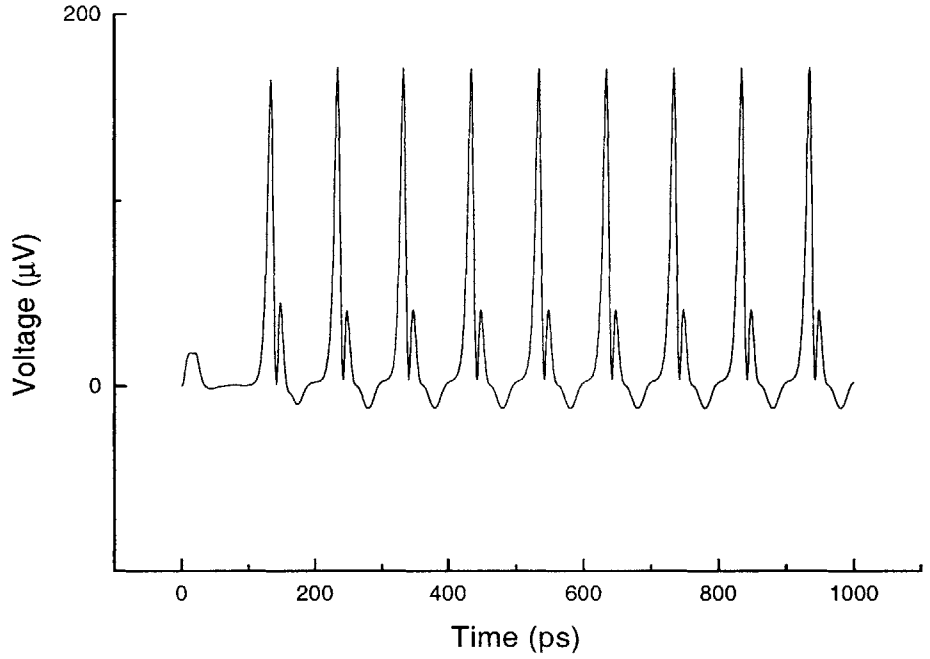

(a)

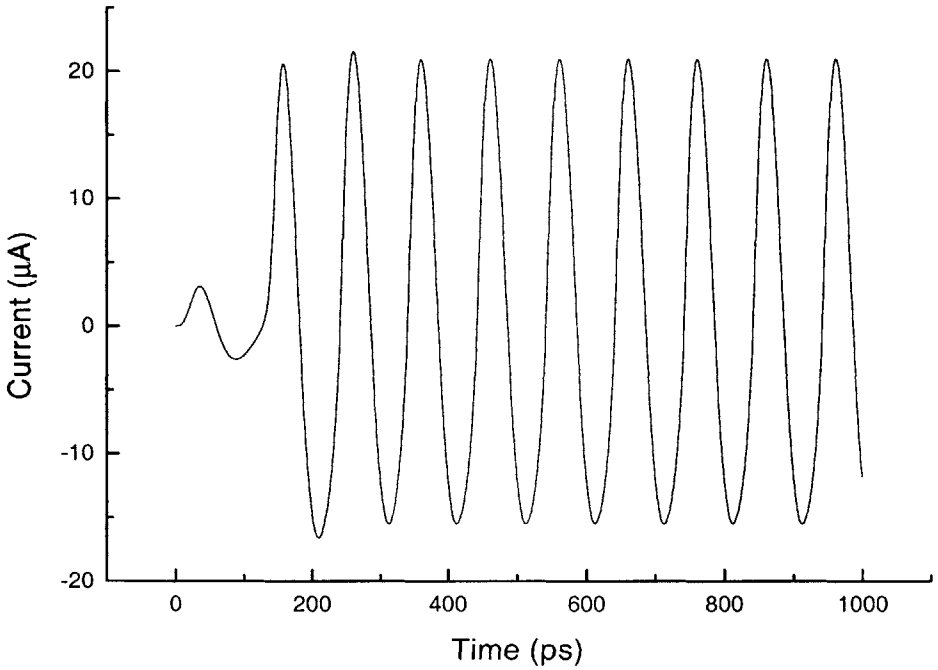

(b)

FIGURE 6-9. (a) The signal which travels down the JTL. Here voltage pulses are clearly non-sinusoidal. (b)Once it passes through an RLC filter, the signal from the NDRO produces a nearly sinusoidal current across the inductor, which magnetically couples this signal to the qubit as a flux oscillation.

Once the rate and fidelity of the Rabi oscillation is established, an experiment to observe Rabi oscillations may be possible. The oscillator drives the qubit to rotate between |0> and |1> as shown in Figure 6-10. Since the qubit also decoheres, it tends towards a 50-50 mixture of the |0> state and the |1> state if the oscillator is continuously on due to dephasing, and completely decays to the |0> state when the oscillator is turned off due to relaxation.

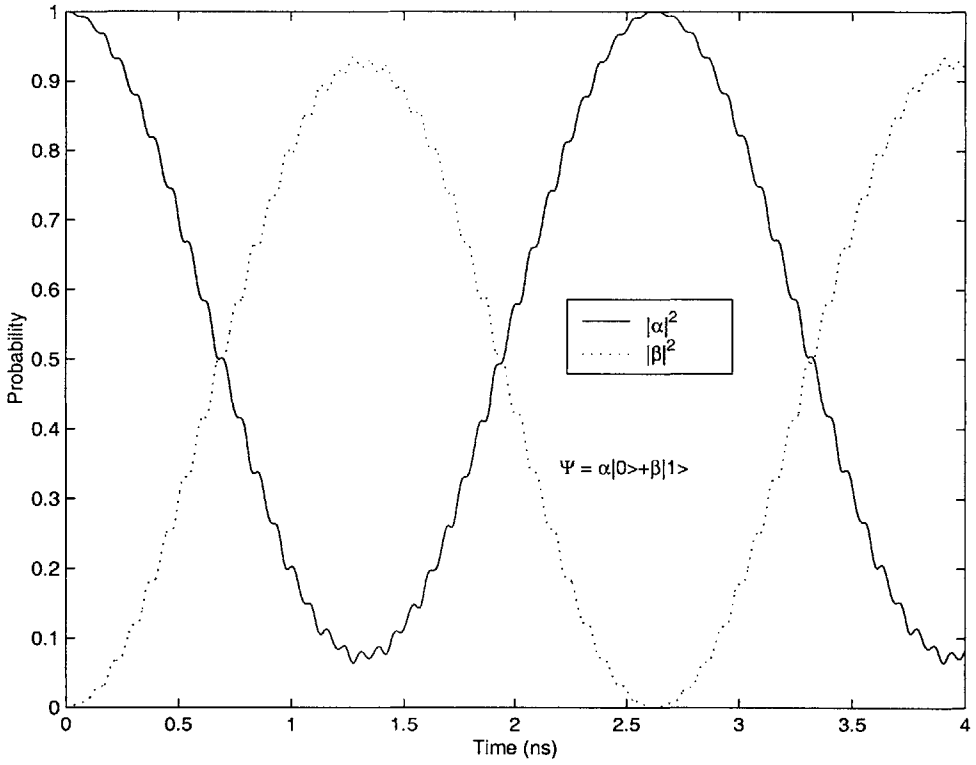

FIGURE 6-10. The population of the qubit's first two energy levels as a function of time in response to driving at the energy splitting. The total wavefunction is $\alpha|0\rangle+\beta|1\rangle$.

An unshunted DC SQUID is used to detect the field of the persistent current qubit, reading out the circulating current and thus the qubit's state [43]. If the RSFQ oscillator described in this paper drives the qubit, the slow measurement process now in use cannot be synchronized with the fast rate of the RSFQ circuit. The actual result of the measurement is now difficult to determine. If the qubit is undergoing continuous Rabi oscillations, then the measurement will presumably catch the qubit somewhere in its oscillations, and a single measurement will give |0> half the time and |1> the other half. Only when a large ensemble of measurements is taken will it become clear what percentage of time the qubit spends in each state. If the RSFQ oscillator is run at some duty cycle less than 50% and

the relaxation time is less than 100 ns, the qubit will essentially reset between pulses of the oscillator. Figure 6-11(a) shows the oscillator with 50% on-time, while (b) displays the qubit response to this driving, assuming a 100 ns relaxation and dephasing time. The oscillator can be set to deliver any arbitrary rotation during its on-time, including a $\pi/2$-pulse, a π-pulse, or a 2π pulse. In Measurement A, the qubit is rotated by a 2π pulse, and an ensemble measurement of the qubit should produce $|0\rangle$ with just a slight perturbation should the measurement catch the qubit during its rotation. In Measurement B, the qubit is rotated by a π pulse, then the measurement should read something much closer to $|1\rangle$ than in Measurement A, even allowing for the rapid rate of relaxation to lower the probability of catching the qubit in $|1\rangle$ with the measurement. Following this reasoning gives the plot of measured qubit value versus duty cycle in Figure 6-12. Note that the fine resolution can show Rabi oscillations in the ideal case. Even if dephasing and the slow measurement make it impossible to see the Rabi oscillations themselves, it should still be possible to get relaxation time from this circuit by observing the rate at which the qubit decays to the $|0\rangle$ state.

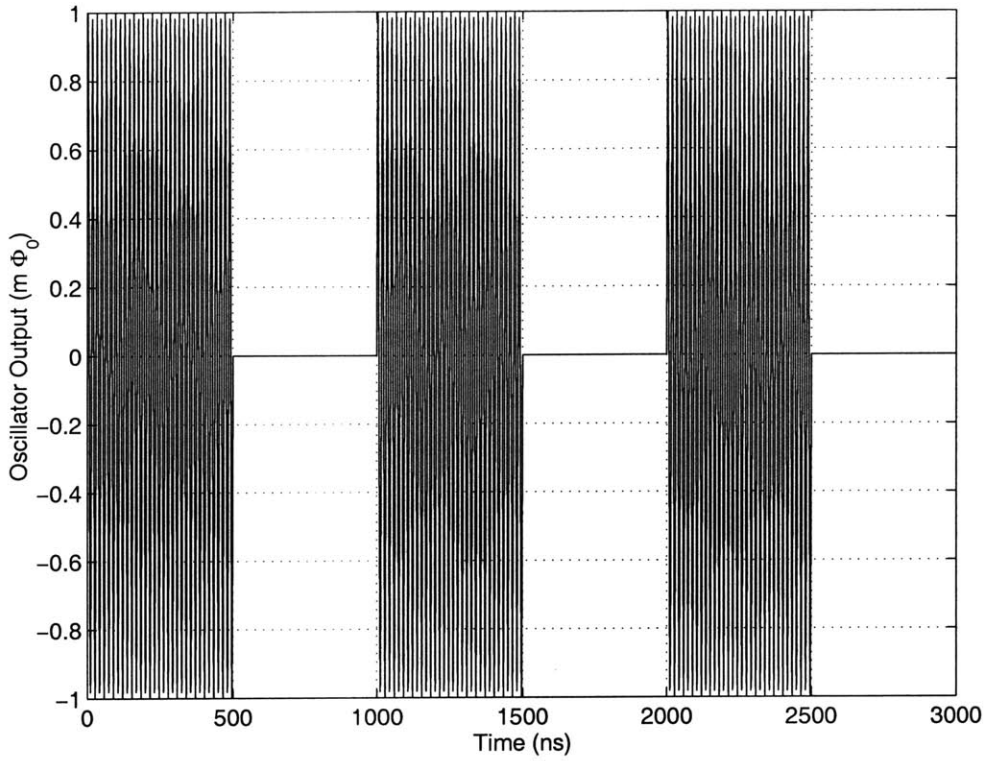

(a)

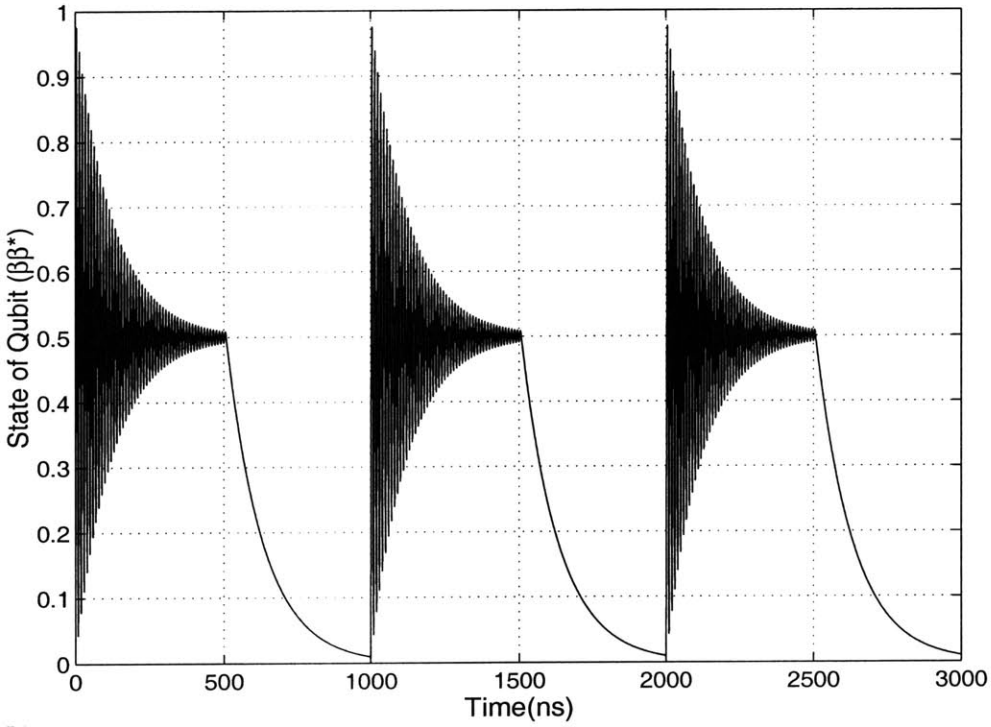

(b)

IGURE 6-11. (a) This is the output of the oscillator at 50% duty cycle, in units of magnetic flux een by the qubit. The oscillations in this figure are aliased at 64 MHz in order to make the plot ore readable. (b) This is the qubit response to the signal in (a). Here, the relaxation and ephasing times are both assumed to be ~100 ns.

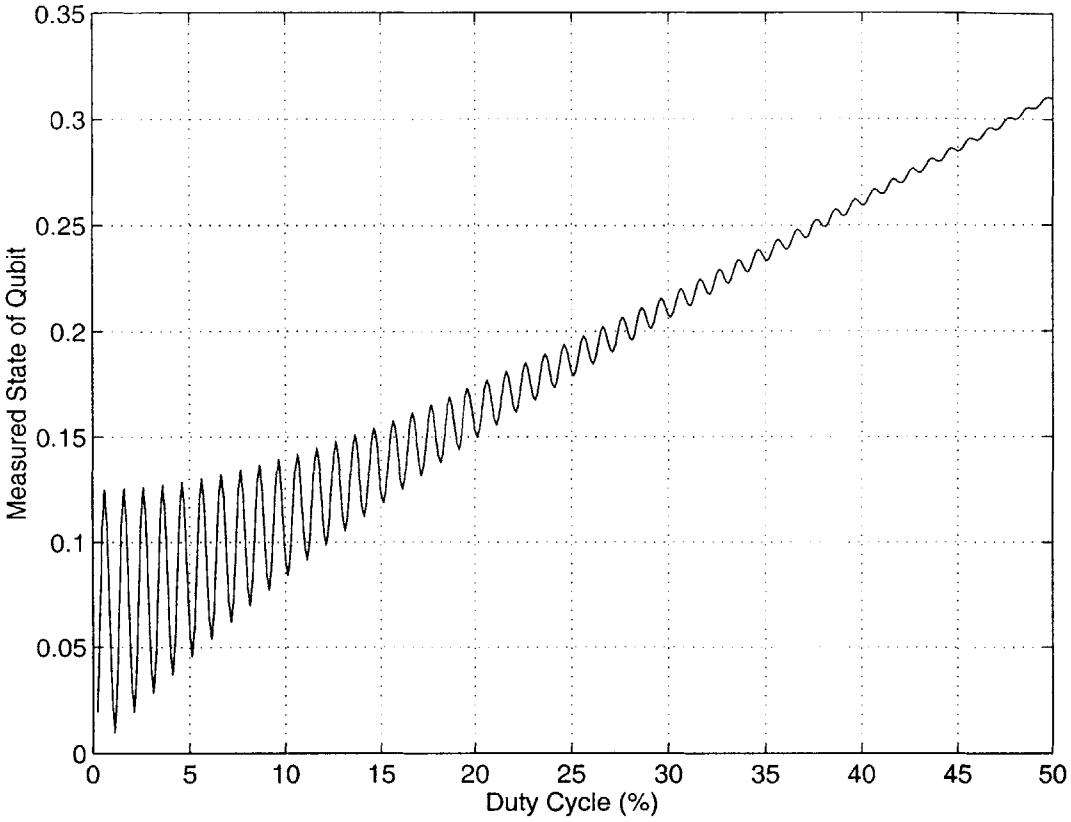

FIGURE 6-12. As the duty cycle of the oscillator is varied, the mean value of the qubit response varies. The mean of Figure 6-11(b) corresponds to 50% duty cycle, for example. If an ensemble measurement of the qubit produces the mean, then changing the duty cycle will produce this plot for the mean of the ensemble measurement. Rabi oscillations are observable in this type of measurement.

6.5 An RSFQ Oscillator with Off-chip Timing

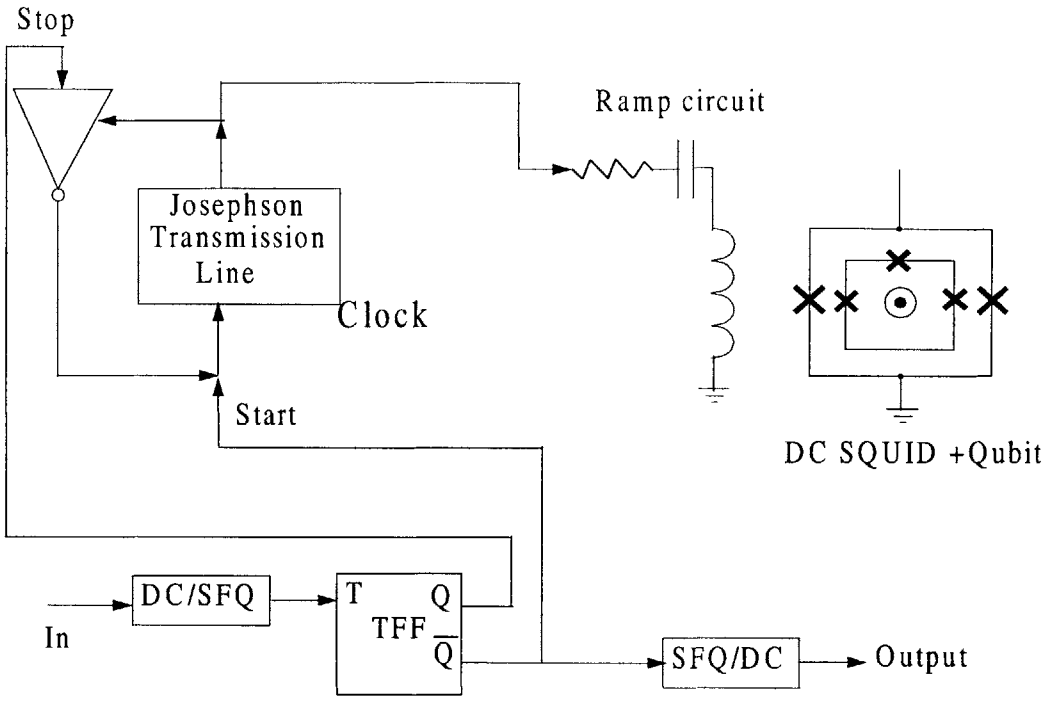

FIGURE 6-13. An RSFQ oscillator which may be turned on and off by an external signal.

The Variable Duty Cycle Oscillator in Section 6.4 is useful for the described experiment, but it has two weaknesses. First, the timing used for the oscillator is on-chip and self-contained, while the timing for the dc SQUID which measures the qubit state is off-chip. There is no way to synchronize the two. Second, the oscillator was designed for a 500 A/cm^2 technology, while the qubit works best at 100 A/cm^2. To meet these requirements, a new circuit design is necessary.

The new circuit, shown in Figure 6-13, is designed for off-chip control, so it can be synchronized with the off-chip measurement. In an effort to minimize the number of high-speed leads, one line sends the signal which turns on and turns off the oscillator. The oscillator is a JTL ring interrupted by an inverter. The JTL provides the clock signal to the inverter, and unless the inverter has received a signal, the inverter outputs a pulse with each clock signal it receives from the JTL. That pulse is sent back to the JTL, completing the ring, which cycles the pulse at 3 GHz. If a pulse is sent to the input of the inverter, no signal is outputted when the inverter receives the clock signal, and the clock stops.

The signal which starts the clock, and which stops it, comes from a single T-flip-flop, which receives its input from a DC-to-SFQ converter. The DC-to-SFQ converter, described in Section 6.2.5, outputs a pulse at each rising edge it reads. The T-flip-flop then divides the incoming pulses, sending the first pulse to start the clock, the second pulse to stop it, the third pulse to start it again, *et cetera*. Thus a single line is sufficient to control the oscillator. The pulses from the oscillator go through filtering similar to that seen by the VDCO, and for the same reasons: to clean the signal and to reduce stray noise. This circuit has been designed, but not yet fabricated.

6.6 Conclusions

RSFQ technology can potentially integrate complex digital electronics on the same chip as qubits. We've designed and have begun fabrication on a few simple circuits which can be useful even in this early phase of superconducting quantum computation. Additionally, we've calculated the decoherence due to the direct coupling of the qubits and the RSFQ circuits and shown that the decoherence times are on the order of a few microseconds, which is longer than decoherence due to the measurement SQUID. This indicates that the directly coupled noise from RSFQ can be reduced to the point where it will not unduly influence the SQUID. A more significant concern is the effect of heating in the RSFQ electronics. While the junctions themselves are generally in the superconducting state and only dissipate energy briefly as they perform 2π phase jumps, they current biasing of the junctions are done using bias resistors. It is unclear how much of the heat dissipated in these resistors will influence the qubit. The heating may be reduced by using smaller resistors, and smaller Josephson junctions which require less current to bias. A great many more experiments are necessary to fully explore the viability of RSFQ controlling superconducting qubits.

Chapter 7

Conclusion

7.1 Results

7.1.1 Characterizing the Persistent Current Qubit

The experimental procedure gives a method to determine the qubit's parameters by examining its classical response to temperature and measurement rate. Moreover, much of this information can be determined at higher temperatures, which can be reached with a Helium-3 refrigerator, and thus does not require a dilution refrigerator as the low temperature measurements do. This provides a means of testing samples and determining their parameters in order to determine whether they will behave quantum mechanically prior to cooling them down in the dilution refrigerator. The one piece of information which cannot be found at Helium-3 temperatures is E_C, which is necessary to determine what frequencies are necessary to drive the qubit.

These measurements produce significant information about the qubit. First, the information gives the exact areas of the qubit's junctions, and confirmed the extent of the undercut. This undercut is expected, due to what is known about the fabrication process, but its exact extent was difficult to determine. Due to the unpredictability of the exact size of the junctions, along with a similar unpredictability in hitting the exact critical current density, it is difficult to design a qubit exactly using today's niobium trilayer fabrication processes. Nevertheless, it is possible to hit a reasonable range of values, and the Lincoln process continues to undergo improvements which, while they reduce the repeatability of qubit designs, should eventually lead to a more efficient, reliable, and predictable process, greatly improving design efficiency and yield. For now, however, a certain robustness must be built into the qubit design to account for the inevitable variation in parameters. Second, the results from the measurement give us an indication of the junction's quality factor, which is on the order of 10^6, which points to a subgap resistance better than 100 MΩ. Since the subgap resistance is always shunted by some environmental resistance, we

can only set a lower bound.

7.1.2 The Nature of the Quantum System

At temperatures below 300 mK, the quantum nature of the qubit becomes clearer. At this point, thermal activation does not make a significant contribution to the qubit's evolution, and macroscopic quantum tunneling is the cause of the qubit's change of state. Distinct features in the histogram data provide strong evidence that the qubit is tunneling at certain magnetic fields, which correspond to the alignment of levels in each of the two wells. State preparation clearly shows that while macroscopic quantum tunneling from the shallower well to the deeper well is likely, there is no significant probability of tunneling from the deeper to the shallower well. This indicates rapid relaxation to the lowest state in each well. Moreover, no significant quantum tunneling appears to take place at f=0.5, where the two wells are of equal depth. This indicates that the barrier between the two potential wells is larger at this point than what is necessary to achieve a coherent superposition of states. That our samples show this is not surprising, since they are at a higher critical current density than for which the qubit was designed, and thus have an E_J/E_C value on the order of 1000.

7.1.3 Circuit Environment Decoherence of the Qubit

We make good use of the theory which maps spin-boson decoherence onto the circuit environment of the qubit such that the decoherence can be calculated directly from the impedance. It allows the circuit designer to take decoherence into account in design as a criteria and a trade-off. Its results mirror the obvious intuition that the better isolated the system is, the less the decoherence, but the accuracy of this theory has yet to be experimentally tested. The designer is advised to overdesign, considering this theory qualitative rather than quantitative until it has been confirmed by measurements.

7.1.4 The DC SQUID Oscillator

The oscillator is designed to be monolithically integrated with the qubit, so it is designed for the same fabrication process with the same critical current density. The design takes into account the decoherence, and thus it is designed with an RLC filter

which isolates the oscillator from the qubit, and the oscillator is designed to operate slightly off resonance, since the driving frequency is where the impedance most needs to be high in order to minimize relaxation. The design should be able to deliver sufficient signal over the desired frequency range of 10 to 20 GHz while keeping the decoherence times longer than 1 μs. This demonstrates the feasibility of designing on-chip control with long decoherence times using our theory which derives decoherence times from the circuit impedance. (Once again, measurements of decoherence times are necessary to determine the accuracy of this theory.) Measurements show that the oscillator is indeed delivering considerable signal (as shown by the response of the measurement dc SQUID), but it has not yet been tested at a temperature where it would be expected to drive the qubit, due to the temporary unavailability of a dilution refrigerator.

7.1.5 RSFQ Designs

The circuits designed to use Rapid Single Flux Quantum logic are ambitious, but they do not have to work perfectly in order to give useful information. Getting components designed at 500 A/cm^2 to work at all, which Jonathan Habif has already demonstrated, shows progress in reaching a critical current density value where both RSFQ and qubits can work reliably. Designs have since been pushed to operate at 100 A/cm^2, which will, if successful, demonstrate the ability to build RSFQ circuits in the ideal critical current density regime for flux qubits. The RSFQ electronics designed at these lower critical current densities also have critical currents half the value of the original designs, which reduces power dissipation in the bias resistors, equal to I^2R, by a factor of four. The circuits we are building in those regimes, oscillators with precise timing control, are useful circuits even for this early stage of quantum experimentation. Even if the experiments for which they were designed do not perform as hoped, the mere presence of RSFQ electronics on the same chip as flux qubits should tell us a lot about the influence of the RSFQ flux noise and heating on the qubit's decoherence, giving us a clearer sense of how much it adds to the qubit's decoherence and what means must be taken to isolate it.

7.2 Future Work

7.2.1 Refining the Measurement of the Qubit

Some of the greatest challenges of this experiment are the shortcomings of the measurement device, in particular its slow measurement time and the strong effect the measurement dc SQUID has on the qubit prior to actually performing the measurement. While we have been able to make use of both of these weaknesses to get useful information out of the qubit, they are still limitations. The slow measurement time makes observing a Rabi oscillation very difficult. For this reason, an important criteria for future work is to develop a faster measurement device. The timed measurement discussed in Section 3.6 is one example of improving the measurement. It measures the qubit much more quickly than the present process, using a very fast ramp on the SQUID, which requires soft coaxial lines to send the signal and extract the output. It does not require a new on-chip design and fabrication run, since the changes are purely external. As such, it does little to limit the feedback of the SQUID, and instead relies on speed. The SQUID feedback can only be reduced by measuring at a SQUID bias where its circulating current is smaller and thus changes less as the SQUID is ramped up (the SQUID is kept biased closer to an integral number of flux quanta) and by measuring lower critical current density samples (samples which have a lower critical current in the SQUID). Since the lower critical current density makes our qubit design more quantum mechanical, the next samples to be measured will certainly be at a lower critical current density.

The very quick ramp-up is beneficial if it can catch the qubit in its present state, meaning that it is best if the ramp-up is either non-adiabatic or low feedback. As a non-adiabatic ramp-up requires a much faster rate than we can produce off-chip using the soft coaxial line, low feedback on the ramp-up is best. Alternatively, we can ramp-up prior to the actual measurement, then perform a measurement which only triggers the switching in the SQUID when the qubit changes states. If the qubit oscillates rapidly between states, then what we will see is similar to that observed in the experiments of Yu *et al.* in [52]: a periodic change in the escape rate of the SQUID as the qubit oscillates between the two states. This requires preparation of the qubit, a timing device with a resolution of nanoseconds, a signal to the qubit with a ramp time of a few nanoseconds, and a high band-

width measurement of the SQUID's switch to the voltage state such that the signal is sharp within the resolution of the measurement, which, as already stated, must be on the order of nanoseconds. This should be possible with soft coaxial lines to the dc SQUID in the dilution refrigerator, and all the other components are already in place. This experiment is currently being pursued by Yang Yu and Bhuwan Singh.

Another improved method of measurement uses an rf SQUID biased at its superconducting branch. The qubit state changes the flux bias of the SQUID, which in turn, alters its effective inductance. This can be measured by designing a resonant circuit and testing the circuit for changes in its resonance due to the changing state of the qubit. This has the advantage of keeping the SQUID in its superconducting branch and only using small-signal measurements to determine its state, thus minimizing the feedback to the qubit. The measurements can also be performed quite rapidly, using a driving frequency on the order of 100 MHz and needing only a few oscillations to determine the resonant frequency. Janice Lee is working to develop this measurement technique.

Finally, it may be possible to use very high speed measurements that work on the timescale of 100 ps. This uses a component called a flux comparator, which can detect the small difference between the two circulating currents of the qubit and, due to that difference, switch to one state or another. Since the fast measurement of the qubit has already taken place, the state stored in the comparator may be read at leisure, using a dc SQUID for example. This component may also be useful for integrating to RSFQ technology. This technique is being explored by Karl Berggren and William Oliver at Lincoln laboratory.

7.2.2 Refining the Qubit

The samples on which the bulk of the measurements were performed are not ideally suited for quantum computation. While people have successfully tested flux qubits with multiple levels in their wells [29], performing measurements require that the flux-state of the qubit changes. Our preferred mode of operation is to induce oscillations between the lowest state in one well and the lowest state in the other, a difficult proposition if the barrier between the wells is so high that multiple levels are present in each well.

This is a direct result of having an E_J/E_C of 1000, whereas this ratio should be closer to 100. The newest samples have a much smaller critical current density, about 67 A/cm^2, which should give an E_J/E_C of about 200, which gives a single level in each well as long as their are two wells and a much smaller barrier between them.

Additionally, the qubit which we've been measuring has a high inductance in order to strongly couple it to the dc SQUID. As has already been discussed, this strong coupling needs to be reduced. Additionally, a large self-inductance of the qubit makes it less like the model we developed for the qubit by introducing an additional degree of freedom, as discussed in Section 2.5. Reducing this makes the qubit more closely resemble the simulated device, but it also makes the qubit signal smaller and harder to measure.

The most difficult aspect of improving the qubit is the fabrication process. In the fabrication, the two primary challenges are solving the undercut and critical current density variation. Missing the critical current density target alters the E_J of the qubits linearly. While this is undesirable, it is not fatal. The qubits can still function as qubits even if E_J is off by 10% or more. It does affect the barrier height and level splitting, but as long as these remain close to their intended values, there are few experiments at this stage which small variations in E_J rule out. The slight difference in E_J only becomes catastrophic if the variation among junctions on the same wafer is large, which is not the case. Moreover, Lincoln laboratory is continually improving the accuracy and variance of J_c, and it is reasonably expected that they will eventually achieve great reliability on that front. The more difficult problem to overcome is the undercutting. This affects E_J, E_C, and α. E_J equals $\Phi_0 J_c A/2\pi$, where A is the area of the junction, while E_C equals $e^2/2C_0A$. Assuming that the area seen by the Josephson energy equals the area seen by the charging energy, then the critical parameter, E_J/E_C is proportional to A^2. However, it is entirely possible that the area used to determine the junction's capacitance is not the same as the area used to determine the critical current, and indeed, the experiments seem to suggest this (Section 4.5.5). Additionally, the difference between the critical current reduction and the capacitance reduction requires two different values for the ratio between the junctions, one of which, α, is for the critical current, and the other one of which, α_C, is for the capacitance. While this complicates matters, it is perfectly possible to incorporate these separate variables into

the qubit Hamiltonian, and in fact, one of the earliest simulations, programmed by Lin Tian, allows for different values for these two variables. In the end, it looks unlikely that the undercut problem will be solved in the near future. However, if the exact amount of undercut is known for each junction size, and for both the critical current and capacitance calculation, then it is simply an engineering problem to design a qubit with the right parameters. So far, our experiments show that even with the undercut, the achievable range of E_J, E_C, α, and α_C, should be sufficient to design a qubit. It is merely a problem of achieving a reliable precision in the undercut, which is one of Lincoln Laboratory's ongoing fabrication refinements.

7.2.3 Testing the DC SQUID oscillator

The observed effect of the oscillator on the measurement SQUID shows that it is delivering power to the SQUID, and presumably to the qubit, but how much has not yet been determined. Additionally, spectroscopy has not yet been performed. Presumably, spectroscopy will be a simple matter of sweeping the flux bias on the SQUID and qubit while running the oscillator at different frequencies. The mean switching current measured will exhibit peaks and dips corresponding to the frustrations where the oscillator frequency excites the qubit, as in [30]. This has not been observed yet, but there's ample reason to believe that these quantum effects will manifest once the device is cooled to temperatures below 100 mK. There are three potential problems which need to be resolved, however. Firstly, the oscillator perturbs the measurement SQUID as well as the qubit (the perturbation of the SQUID is what has been observed so far), and that may make it difficult to distinguish the qubit excitation from the SQUID's perturbation. Secondly, the large current through the oscillator (about 200 μA) may result in some heating of the sample. This was not observed at 350 mK in the Helium-3 probe, but the cooling power of the dilution refrigerator at 15 mK is smaller than the cooling power of the Helium-3 probe at 350 mK. It may be that the sample will warm up, but currents of 600 mA have already been tested in the dilution refrigerator with only minimal heating, so the oscillator, which has a critical current of about 200 μA, should be manageable. Finally, the amplitude of the flux oscillations which the oscillator transmits to the qubit is not constant with frequency, and it is unclear whether the range of frequencies which the oscillator transmits

will be able to map out the desired energy levels. There is some adjustability in the oscillator's amplitude, however, so it should be possible to turn up the amplitude to the level necessary to drive the qubit.

7.2.4 Testing the RSFQ Circuitry

The RSFQ circuitry requires a different kind of measurement procedure. The measurement SQUID can be used in the same way as before, but the RSFQ circuitry has many more lines, both for control and input/output than any on-chip device tested so far. The Superconducting Digital Electronics group at the University of Rochester has the expertise to test the RSFQ circuitry. At MIT, we have developed the expertise to measure the qubit itself. The challenge will be for these two groups to combine their expertise and perform the measurement, while at the same time learning what it takes to run RSFQ electronics in a dilution refrigerator.

7.2.5 Measuring Rabi Oscillations

More than anything else, measuring Rabi oscillations requires precise timing. While it may be possible to observe the average effect of Rabi oscillations as described in Section 6.4, a truer Rabi experiment with a better chance of working requires stopping the oscillator, then quickly measuring the state of the qubit before it has an opportunity to relax to its ground state. As that time is expected to be in the microseconds, a very quick measurement is required, probably using one of the techniques described in Section 7.2.1. Once a suitable measurement technique is found, then it is simply a matter of synchronizing the excitation of the qubit, whether off-chip or on-chip, with the measurement of the qubit, whether off-chip and on-chip. The duration of the excitation can be adjusted, then quickly measured by the oscillator. The state of the qubit versus the duration of the excitation will give the qubit's Rabi oscillations.

7.3 The Prospects for Niobium

Niobium has several advantages over aluminum, including its high critical temperature, its well-developed fabrication technology, and the extensive research in developing on-chip electronics in that material system. In the application of quantum computation,

the requirements are somewhat different. The temperatures at which the devices behave quantum mechanically is already below one kelvin, so niobium's ability to work at liquid helium temperatures is not as much of an advantage. The higher critical temperature can still be an advantage, since it means a smaller proportion of quasiparticles for any given temperature. However, the primary question is whether its junction quality is sufficient for use in quantum computation. Aluminum-aluminum oxide-aluminum junctions, whether they are formed by shadow evaporation or a trilayer process, are higher quality than niobium-aluminum oxide-niobium junctions [57]. While the niobium junctions may still be of high enough quality for use in quantum computation, aluminum is clearly the better of the two. The second difficulty is that the fabrication process for niobium has difficulty reliably fabricating small junctions, whereas aluminum junctions, especially when fabricated with shadow evaporation, can be made extremely small.

Our experiments show that the Lincoln Laboratory's low current density junctions are of a very high quality with a subgap resistance in excess of 100 MΩ. Refining the junction size so that junctions can be reliably made smaller is a continuing project. The more predictable undercutting is, the smaller the junctions can be designed, even if undercutting is not entirely eliminated.

Appendix I

Expansion of the Qubit with Inductance

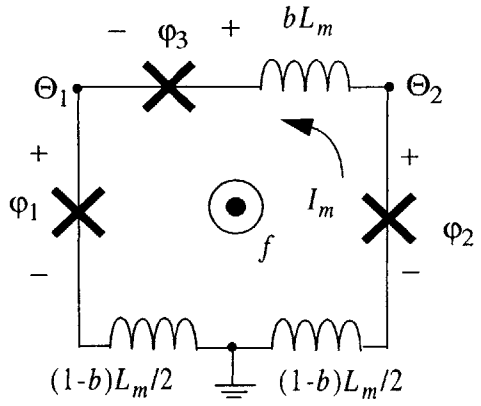

FIGURE I-1. The three junction qubit with inductance. The inductance has been distributed on all three branches. Doing this, and using branch as opposed to junction phases, the three dimensional model reduces to a simpler form, the sum of the two dimensional model, a simple harmonic oscillator, and a correction term.

Recall that we used the definitions in Equation (I-1):

$$\begin{aligned}
\varphi_1 &= \Theta_1 - \frac{1-b}{2}\left(\frac{2\pi}{\Phi_0}\right)(L_m I_m + \Phi_{ext}) \\
\varphi_2 &= \Theta_2 + \frac{1-b}{2}\left(\frac{2\pi}{\Phi_0}\right)(L_m I_m + \Phi_{ext}) \\
\varphi_3 &= \Theta_2 - \Theta_1 - b\left(\frac{2\pi}{\Phi_0}\right)(L_m I_m + \Phi_{ext}) \\
b &= \frac{1}{1+2\alpha}
\end{aligned} \tag{I-1}$$

From these we derived the variables ere $M_p = 2\left(\frac{\Phi_0}{2\pi}\right)^2 C_j$, $M_m = (2+4\alpha)\left(\frac{\Phi_0}{2\pi}\right)^2 C_j$, $\Theta_p = \frac{\Theta_1 + \Theta_2}{2}$, and $\Theta_m = \frac{\Theta_1 - \Theta_2}{2}$. We found it convenient to add to these definitions the variable $\Theta_m = \Theta_m - (1-b)2\pi f$. This left us with the kinetic energy in Equation (I-2) and the potential energy in Equation (I-3).

$$= \frac{1}{2}M_p\dot{\Theta}_p^2 + \frac{1}{2}M_m\dot{\Theta}_m^2 + \frac{\alpha}{1+2\alpha}C_j L_m^2 \dot{I}_m^2 \tag{I-2}$$

$$U = E_J\Big[2+\alpha-2\cos\Theta_p\cos\Big(\tilde{\Theta}_m-\frac{\alpha}{1+2\alpha}\Big(\frac{2\pi}{\Phi_0}\Big)L_mI_m\Big)- \alpha\cos\Big(2\tilde{\Theta}_m+2\pi f+\frac{1}{1+2\alpha}\Big(\frac{2\pi}{\Phi_0}\Big)L_mI_m\Big)\Big]+\frac{1}{2}L_mI_m^2 \quad \textbf{(I-3)}$$

We can now expand the cosine terms, neglecting the second order terms.

$$\cos\Big(\tilde{\Theta}_m-\frac{\alpha}{1+2\alpha}\Big(\frac{2\pi}{\Phi_0}\Big)L_mI_m\Big) = \cos\tilde{\Theta}_m+\frac{\alpha}{1+2\alpha}\Big(\frac{2\pi}{\Phi_0}\Big)L_mI_m\sin\tilde{\Theta}_m \quad \textbf{(I-4)}$$

$$\cos\Big(2\tilde{\Theta}_m+2\pi f+\frac{1}{1+2\alpha}\Big(\frac{2\pi}{\Phi_0}\Big)L_mI_m\Big) = \cos(2\tilde{\Theta}_m+2\pi f)-\frac{1}{1+2\alpha}\Big(\frac{2\pi}{\Phi_0}\Big)L_mI_m\sin(2\tilde{\Theta}_m+2\pi f) \quad \textbf{(I-5)}$$

This gives us the potential energy in Equation (I-6).

$$U = E_J[2+\alpha-2\cos\Theta_p\cos\tilde{\Theta}_m-\alpha\cos(2\tilde{\Theta}_m+2\pi f)] + L_mI_mI_c\Big(\frac{\alpha}{1+2\alpha}\Big)(\sin(2\tilde{\Theta}_m+2\pi f)-2\cos\Theta_p\sin\tilde{\Theta}_m)+\frac{1}{2}L_mI_m^2 \quad \textbf{(I-6)}$$

We can approximate the value of the second term by replacing Θ_p and $\tilde{\Theta}_m$ with $\langle\Theta_p\rangle$ and $\langle\tilde{\Theta}_m\rangle$, and then completing the square by defining $\tilde{I}_m \equiv I_m + I_c\Big(\frac{\alpha}{1+2\alpha}\Big)(\sin(2\langle\tilde{\Theta}_m\rangle+2\pi f)-2\cos\langle\Theta_p\rangle\sin\langle\tilde{\Theta}_m\rangle)$. Since $\dot{\tilde{I}}_m = \dot{I}_m$, This does not affect the kinetic energy. This gives a potential of

$$U = E_J[2+\alpha-2\cos\Theta_p\cos\tilde{\Theta}_m-\alpha\cos(2\tilde{\Theta}_m+2\pi f)] + \frac{1}{2}L_m\tilde{I}_m^2-\frac{1}{2}L_mI_c^2\Big(\frac{\alpha}{1+2\alpha}\Big)^2(\sin(2\langle\tilde{\Theta}_m\rangle+2\pi f)-2\cos\langle\Theta_p\rangle\sin\langle\tilde{\Theta}_m\rangle)^2 \quad \textbf{(I-7)}$$

The complete Hamiltonian has the form given in Equation (I-8).

$$H = \frac{1}{2}M_p\dot{\Theta}_p^2+\frac{1}{2}M_m\dot{\tilde{\Theta}}_m^2+E_J[2+\alpha-2\cos\Theta_p\cos\tilde{\Theta}_m-\alpha\cos(2\tilde{\Theta}_m+2\pi f)] + \Big(\frac{\alpha}{1+2\alpha}C_jL_m^2\dot{\tilde{I}}_m^2+\frac{1}{2}L_m\tilde{I}_m^2\Big)-\frac{1}{2}L_mI_c^2\Big(\frac{\alpha}{1+2\alpha}\Big)^2(\sin(2\langle\tilde{\Theta}_m\rangle+2\pi f)-2\cos\langle\Theta_p\rangle\sin\langle\tilde{\Theta}_m\rangle)^2 \quad \textbf{(I-8)}$$

The first line is the original qubit Hamiltonian. The next two terms form an Harmonic oscillator, while the final term is a correction to the shape of the energy bands.

References

[1] A.J. Leggett and A. Garg, "Quantum Mechanics versus Macroscopic Realism: Is the flux there when nobody looks?", *Phys. Rev. Lett.* **54**, p. 857, 1985.

[2] A.J. Leggett, "Macroscopic Quantum Systems and the Quantum Theory of Measurement," *Progress of Theoretical Physics* **69**, p. 80, 1980.

[3] A.J. Leggett, "Macroscopic Quantum Tunneling and Related Maters," *Jpn. J. Appl. Phys.* (1) Supplement **26-3**, p. 1986, 1987.

[4] A.J. Leggett, S. Chavrakarty, A.T. Dorsey, M.P.A. Fisher, A. Garg, and W. Zwerger, "Dynamics of the Dissipative Two-State System," *Rev. of Mod. Phys.* **59**, p. 1, 1987.

[5] A.O. Caldeira and A.J. Leggett, "Quantum Tunneling in a Dissipative System," *Annals of Physics* **149**, p. 374, 1983.

[6] A.J. Leggett, "Macroscopic Quantum Tunneling -- An Overview of the Background," *J. Appl. Phys.* **73**, p. 6715, 1993.

[7] C.D. Tesche, "Superconducting Measurement Circuit for an EPR Experiment with an rf SQUID," *Physica B* **165**, p. 925, 1990.

[8] C.D. Tesche, "Can a noninvasive measurement of magnetic flux be performed with superconducting circuits?", *Phys. Rev. Lett.* **64**, p. 2358, 1990.

[9] M.H. Devoret, J.M. Martinis, and J. Clarke, "Measurements of Macroscopic Quantum Tunneling out of the Zero-Voltage State of a Current-Biased Josephson Junction," *Phys. Rev. Lett.* **55**, p. 1908, 1985.

[10] J.M. Martinis, M.H. Devoret, and J. Clarke, "Energy -Level Quantization in the Zero-Voltage State of a Current-Biased Josephson Junction," *Phys. Rev. Lett.* **55**, p. 1543, 1985.

[11] Y-C. Chen, "Macroscopic Quantum Tunneling in a dc SQUID," *J. Low Temp. Phys.* **65**, p. 133, 1986.

[12] S. Han, J. Lapointe, and J.E. Lukens, "Observation of Incoherent Relaxation by Tunneling in a Macroscopic Two-State System," *Phys. Rev. Lett.* **66**, p. 810, 1991

[13] R. Rouse, S. Han, and J.E. Lukens, "Observation of Resonant Tunneling between Macroscopically Distinct Quantum Levels," *Phys. Rev. Lett.* **75**, p. 1614, 1995.

[14] S. Han, R. Rouse, and J.E. Lukens, "Observation of Cascaded Two-Photon-Induced Transitions between Fluxoid States of a SQUID," *Phys. Rev. Lett.* **84**, p. 1300, 2000.

[15] D.V. Averin, J. R. Friedman, and J.E. Lukens, "Macroscopic resonant tunneling of magnetic flux," *Phys. Rev. B*, vol. 62, p. 11802, 2000.

[16] M. Matters, W.J. Elion, and J.E. Mooij, "Influence of Controlled Quantum-Mechanical Charge and Phase Fluctuations on Josephson Tunneling," *Phys. Rev. Lett.* **75**, p. 721, 1995.

[17] L. Grover, "Quantum Mechanics Helps in Searching for a Needle in a Haystack," *Phys. Rev. Letters* **79**, p. 325, 1997.

[18] P. Shor, "Algorithms for Quantum Computation: Discrete Log and Factoring," in *Proceedings of the 35th Annual Symposium on Foundations of Computer Science*, S. Goldwasser, Ed., IEEE Computer Society, Los Alamitos, CA, p. 124, 1994.

[19] N.A. Gershenfeld and I.L. Chang, "Bulk Spin-Resonance Quantum Computation," *Science* **275**, p. 350, 1997.

[20] Y. Mahklin, G. Schön, and A. Shnirman, "Josephson-junction qubits with controlled couplings," *Nature* **398**, p. 305, 1999.

[21] D. Deutsch, A. Barenko, and A. Ekert, "Universality in Quantum Computation," *Proc. R. Society London A* **449**, p. 669, 1995.

[22] D.P. DiVincenzo, "Topics in Quantum Computers," in *Mesoscopic Electron Transport (NATO Asi Series. Series E, Applied Sciences, No. 345)*, L.L Sohn *et al.*, Eds., Kluwer Academic Publishers, p. 657, 1997.

[23] J. E. Mooij, T. P. Orlando, L. Levitov, L. Tian, C. H. van der Wal, and S. Lloyd, "Josephson Persistent-Current Qubit," *Science* **285**, p. 1036, 1999.

[24] T.P Orlando, J.E. Mooij, L. Tian, C.H. van der Wal, L. Levitov, S. Lloyd, and J.J. Mazo, "A Superconducting Persistent Current Qubit," *Phys. Rev. B* **60**, p. 15398, 1999.

[25] D.P. DiVincenzo, "Quantum Computation," *Science* **270**, p. 255, 1995.

[26] Y. Nakamura, Y.A. Pushkin, J.S. Tsai, "Coherent control of macroscopic quantum states in a single-Cooper-pair box," *Nature* **398**, p. 786, 1999.

[27] Alexander Shnirman, Gerd Schön, and Ziv Hermon, "Quantum manipulations of small Josephson junctions," *Phys. Rev. Letters* **79**, p. 2371, 1997.

[28] M.F. Bocko, A.M. Herr, and M.F. Feldman, "Prospects for Quantum Coherent Computation Using Superconducting Electronics," *IEEE Trans. Appl. Supercond.* **7**, p. 3638, 1997.

[29] J.R. Friedman, V. Patel, W. Chen, S.K. Tolpygo, and J.E. Lukens, "Quantum superposition of distinct macroscopic states," *Nature* **406**, p. 43, 2000.

[30] C.H. van der Wal, A.C.J. ter Haar, F.K. Wilhelm, R.N. Schouten, C.J.P.M. Harmans, T.P. Orlando, S. Lloyd, and J.E. Mooij, "Quantum superposition of macroscopic persistent-current states," *Science* **290**, p. 773, 2000.

[31] I. Chiorescu, Y. Nakamura, C.J.P.M. Harmans, and J.E. Mooij, "Coherent Quantum Dynamics of a Superconducting Flux Qubit," *Science* **299**, p. 1869, 2003.

[32] In principle, this can always be done for such circuits. A general proof can be given in terms of topological matrices. See E. Trías, *Vortex motion and dynamical states in Josephson arrays*, Ph.D. thesis, MIT, p. 35, 2000.

[33] M. Grifoni, E. Paladino, and U. Weiss, "Dissipation, decoherence and preparation effects in the spin-boson system", *Eur. Phys. J. B* **10**, p. 719, 1999.

[34] A.J. Leggett, "Macroscopic quantum tunneling and related effects in Josephson systems," *Percolation, localization, and supeconductivity*, Plenum Press: New York, 1984.

[35] A.K. Jain, K.K. Likharev, J.E. Lukens, and J.E. Sauvageau, "Mutual phase-locking in Josephson arrays," *Phys. Rep.* **109**, p. 309, 1984.

[36] E. Trías, T.P. Orlando, A.E. Duwel, and S. Watanabe, "Circuit models for arrays of Josephson oscillators with loads," *IEEE Trans. Appl. Supercond.* **9**, p. 4316, 1999.

[37] M. Kamon, M.J. Tsuk, J.K. White, "FastHenry – a multipole accelerated 3-D inductance extraction program," *IEEE Trans. on Microwave Theory and Techniques* **42**, p. 1750, 1994.

[38] S. Watanabe, S.H. Strogatz, H.S.J. van der Zant, and T.P. Orlando, "Whirling modes and parametric instabilities in the discrete Sine-Gordon equation: experimental tests in Josephson rings," *Phys. Rev. Lett.* **74**, p. 379, 1995.

[39] J.E. Lukens, "Josephson arrays as high frequency sources," in *Superconducting Devices*, S.T. Ruggiero and D.A. Rudman, Eds., Boston, MA: Academic Press, Inc., 1990, p. 135.

[40] A.M. Kadin, *Introduction to Superconducting Circuits*. New York, NY: John Wiley&Sons, Inc., 1999.

[41] Y. Taur, P.L. Richards, and F. Auracher, "Application of the Shunted Junction Model to Point-Contact Josephson Junctions," in *Low Temperature Physics--LT-13*, vol. 3, K.D. Timmerhaus, W.J. O'Sullivan, and E.F. Hammel, Eds., New York: Plenum Press, 1974, pp. 276-280.

[42] R.C. Rey-de-Castro, M.F. Bocko, A.M. Herr, C.A. Mancini, and M.J. Feldman, "Design of an RSFQ control circuit to observe MQC on an rf-SQUID," *IEEE Trans. Appl. Supercond.* **11**, p. 1014, March 2001.

[43] K. Segall, D. Crankshaw, D. Nakada, B. Singh, J. Lee, N. Markovic, S. Valenzuala, T.P. Orlando, M. Tinkham, and K. Berggren, "Two-state dynamics in a superconducting persistent current qubit," *IEEE Trans. Appl. Supercond.*, accepted for publication.

[44] K. Segall, D. Crankshaw, D. Nakada, T.P. Orlando, L.S. Levitov, S. Lloyd, N. Markovic, S.O. Valenzuela, M. Tinkham, K.K. Berggren, "Impact of time-ordered measurements of the two states in a niobium superconducting qubit structure," *Physical Review B Rapid Communications*, 2003, accepted for publication.

[45] K.K. Berggren, E.M. Macedo, E.M. Feld, J.P. Sage, "Low T_c superconductive circuits fabricated on 150-mm wafers using a doubly planarized Nb/AlO_x/Nb process," *IEEE Trans. Appl. Supercond.* **9**, p. 3271, 1999.

[46] T. P. Orlando, L. Tian, D. S. Crankshaw, S. Lloyd, C. H. van der Wal, J. E. Mooij, and F. Wilhelm, "Engineering the quantum measurement process for the persistent current qubit," *Physica C* **368**, p. 294, 2002.

[47] C.H. van der Wal, F.K. Wilhelm, C.J.P.M. Harmans, and J.E. Mooij, "Engineering decoherence in Josephson persistent-current qubits: Measurement apparatus and other electromagnetic environments," *Eur. Phys. J. B* **31**, p. 111, 2003.

[48] P.G. De Gennes, "Boundary Effects in Superconductors," *Rev. Mod. Phys.* **36**, p. 225, 1964.

[49] J.I. Cirac and P. Zoller, "Quantum Computations with Cold Trapped Ions," *Phys. Rev. Lett.* **74**, p. 4091, 1995.

[50] Loss and D.P. DiVincenzo, "Quantum Computation with Quantum Dots," *Phys. Rev. A* **57**, p. 120, 1998.

[51] S.Y. Han, Y. Yu, X. Chu, S.I. Chu, and Z. Wang, "Time-resolved Measurement of Dissipation-induced Decoherence in a Josephson Junction," *Science* **293**, p. 1457, 2001.

[52] Y. Yu, S. Han, X. Chu, S. Chu, and Z. Wang, "Coherent Temporal Oscillations of Macroscopic Quantum States in a Josephson Junction," *Science* **296**, p. 889, 2002.

[53] L. Tian, S. Lloyd, and T.P. Orlando, "Decoherence and Relaxation of a Superconducting Quantum Bit during Measurment," *Phys. Rev. B* **65**, p. 144516, 2002.

[54] Y. Nakamura, Y.A. Pashkin, J.S. Tsai, "Rabi Oscillations in a Josephson-Junction Charge Two-Level System," *Phys. Rev. Lett.* **87,** p. 246601, 2001.

[55] Y. Nakamura, Y.A. Pashkin, T. Yamamoto, J.S. Tsai, "Charge Echo in a Cooper Pair Box," *Phys. Rev. Lett.* **88**, p. 47901, 2002.

[56] J.R. Kirtley, C.D. Tesche, W.J. Gallagher, A.W. Kleinsasser, R.L. Sandstrom, S.I. Raider, and M.P.A. Fisher, "Measurement of the Intrinsic Subgap Dissipation in Josephson Junctions," *Phys. Rev. Lett.* **61**, p. 2372, 1988.

[57] M.A. Gubrud, M. Ejrnaes, A.J. Berkley, R.C. Ramos, Jr., I. Jin, J.R. Anderson, A.J. Dragt, C.J. Lobb, and F.C. Wellstood, "Sub-Gap Leakage in Nb/AlO_x/Nb and Al/AlO_x/Al Josephson Junctions," *IEEE Trans. on Appl. Super.* **11**, p. 1002, 2001.

[58] A.T. Johnson, C.J. Lobb, and M. Tinkham, "Effect of Leads and Energy Gap upon the Retrapping Current of Josephson Junctions," *Phys. Rev. Lett.* **82**, p. 2417, 1999.

[59] A. Steane, "Error Correcting Codes in Quantum Theory," *Phys. Rev. Lett.* **77**, p. 793, 1996.

[60] K.K. Likharev and V.K. Semenov, "RSFQ Logic/Memory Family: A New Josephson-Junction Technology for Sub-Terahertz-Clock-Frequency Digital Systems," *IEEE Trans. on Appl. Supercond.* **1**, p. 1, 1990.

[61] J. Sage, *Lincoln Laboratory DPARTS Process Design Rules.*

[62] D. Nakada, K.K. Berggren, E. Macedo, V. Liberman, and T.P. Orlando, "Improved Critical-Current-Density Uniformity by Using Anodization," *IEEE Trans. on Appl. Supercond.*, accepted for publication.

[63] Z. Bao, M. Bhushan, S. Han, and J.E. Lukens, "Fabrication of High Quality, Deep-Submicron Nb/AlO_x/Nb Josephson Junctions using Chemical Mechanical Polish," *IEEE Trans. on Appl. Supercond.*, **5**, p. 2731, 1995.

[64] L. Tian, *A Superconducting Flux QuBit: Measurement, Noise, and Control*, Ph.D. Thesis, MIT, 2002.

[65] D.S. Crankshaw, E. Trias, T.P. Orlando, "Magnetic flux controlled Josephson array oscillators," *IEEE Trans. on Appl. Supercond.* **11**, p. 1223, 2001.

[66] D. S. Crankshaw and T. P. Orlando, "Inductance effects in the persistent current qubit," *IEEE Trans. on Appl. Supercond.* **11**, p. 1006, 2001.

[67] U. Klein, S. Schröder, and J.H. Hinken, "Calculation of the Shapiro Step Amplitudes in Two-Dimensional Josephson Tunnel Junctions," *IEEE Trans. on Instr. and Meas.* **40**, p. 291, 1991.

[68] A.B. Cawthorne, C.B. Whan, and C.J. Lobb, "Influence and Evaluation of Parasitic Inductance in Shunted Josephson Junctions," *IEEE Trans. on Appl. Supercond.* **7**, p. 2355, 1997.

[69] R.L. Kautz, R.H. Ono, and C.D. Reintsema, "Effect of thermal noise on Shapiro steps in high-T_c Josephson weak links," *Appl. Phys. Lett.* **61**, p. 342.

[70] P. Somervuo and Y. Serkeinen, "Simple method of determining the external signal voltage in Josephson junctions," *Journal of Appl. Phys.* **46**, p. 1415, 1975.

[71] K. K. Likharev, *Dynamics of Joesphson junctions and Circuits*, Philadelphia, PA: Gordon and Breach Scientific Publishers, 1986.

[72] A. Rylyakov, "DC to SFQ Converter," http://pavel.physics.sunysb.edu/RSFQ/Lib/AR/dcsfq.html.